DEPARTAMENTO DE FÍSICA TEÓRICA Y DEL COSMOS

Universidad de Granada

# A study of the near-ultraviolet emission in Seyfert nuclei

Victor Manuel Muñoz Marín

**Memoria de Tesis**
presentada para optar al grado de
Doctor por la Universidad de Granada
en la especialidad de Astrofísica

dirigida por
**Rosa María González Delgado**

preparada en
Instituto de Astrofísica de Andalucía, (IAA-CSIC)

Junio 2011

Editor: Editorial de la Universidad de Granada
Autor: Victor Manuel Muñoz Marín
D.L.: GR 628-2012
ISBN: 978-84-694-6945-3

A mis padres,
cuyo amor y ejemplo
me han hecho lo que soy

# Resumen

Esta memoria de tesis doctoral recoge nuestro trabajo sobre una muestra de galaxias con actividad nuclear de tipo Seyfert, en el que abordamos el estudio de la coexistencia de un objeto compacto supermasivo central y la formación estelar circumnuclear desde varios puntos de vista.

Los núcleos activos de tipo Seyfert se encuentran entre los fenómenos más energéticos del universo local. En el modelo generalmente aceptado se explica este fenómeno como la caída de material en un disco de acrecimiento en torno a un objeto compacto supermasivo, probablemente un agujero negro de masa entre un millón y mil millones de veces la del Sol, con la consiguiente transformación de parte de la energía potencial gravitatoria en radiación. En este proceso el agujero negro está ganando masa y por lo tanto creciendo. Pero esto no sería más que una etapa en la vida de las galaxias, ya que actualmente se piensa que la mayoría de las galaxias a partir de un cierto tamaño, si no todas, tienen en su centro un objeto masivo, que vendría en la forma de un agujero negro para las más masivas, o un cúmulo compacto de estrellas en las menores. Además se ha descubierto recientemente que las propiedades del objeto central se correlacionan con otras propiedades del bulbo galáctico que lo contiene. Esto hace probable una relación entre elementos a escalas físicas muy distintas, cuya posible causalidad está por determinar. Por otro lado, una serie de trabajos avalan la presencia de fenómenos de formación estelar violenta en las regiones circumnucleares de galaxias activas de diversos tipos. Ya que la formación estelar es uno de los principales procesos por los que crecen los bulbos galácticos, los objetos en los que ambos procesos se den a la vez son laboratorios perfectos para estudiar la posible conexión entre el crecimiento del bulbo y del objeto central.

Nuestra aproximación a este problema ha sido construir una muestra de 75 galaxias Seyfert que hemos estudiado con el Telescopio Espacial Hubble, lo que nos ha proporcionado una sensibilidad y una resolución extraordinarias, eligiendo la banda del ultravioleta cercano como base. Estos datos han sido complementados con imágenes ópticas y en infrarrojo cercano, también del Telescopio Espacial, y constituyen un atlas pancromático de referencia para las regiones nucleares de este tipo de objetos. El trabajo presentado en esta tesis se estructura en tres partes. En una primera presentamos el atlas de la muestra y realizamos su estudio morfológico y fotométrico, comparando los resultados entre tipos de actividad, identificando la población de cúmulos estelares y determinando la fracción de la emisión total que se puede atribuir a estos. En una segunda parte seleccionamos una submuestra para la cual poseemos imágenes en banda estrecha ([OIII]$\lambda\lambda$5007), y nos centramos en la componente de luz difusa en el ultravioleta cercano. Para cada objeto, con una combinación de cálculos teóricos y medidas experimentales, intentamos determinar la contribución de cada posible componente a esta emisión extendida. Finalmente, en una tercera parte nos centramos en la componente de emisión compacta. Eligiendo como ejemplo la galaxia NGC 5135 desarrollamos y optimizamos una metodología para el estudio de la población de cúmulos estelares en este tipo de objetos, la cual podrá ser usada en una muestra mayor para determinar cómo afecta la proximidad del núcleo activo a la formación y disrupción de los cúmulos. Para terminar hemos añadido una presentación de las líneas de investigación que estamos desarrollando, y que consisten principalmente en la extensión del trabajo a núcleos activos de baja luminosidad.

# Contents

# List of Figures

# List of Tables

### Chapter 1

# Introduction

This thesis report compiles our work on a sample of galaxies with Active Galactic Nuclei of the type called Seyfert, addressing the issue of the coexistence of a nuclear compact massive object with nuclear and circumnuclear star formation in the galaxies. It is therefore needed a short introduction of the concepts involved, including why the evolution of the nuclear object and the star formation in the host galaxy itself is thought to be interrelated, and the technics we use to explore this relation. This will be addressed along the present chapter.

## 1.1 The characteristics of Nuclear Activity

The first clues to unusual activity in the center of some galaxies date back to the discovery by Fath (1909) of emission line spectra of some 'spiral nebulae', such as NGC 1068, and the later first systematic studies of these nuclear spectra in the 40s (Seyfert, 1943). With the development of radioastronomy and the discovery of quasars and blazar objects during the 60s and 70s, came the definitive take off of the field.

Under the term Active Galactic Nucleus (AGN) we group a variety of objects that share a particular set of phenomenological elements, among others: a bright non-resolved nucleus, a very high bolometric luminosity, variability in short timescales, non-thermal emission in a broad range of frequencies, radio and X-ray cores, extended and collimated radio emission in the form of jets, presence of broad (thousands of km/s) permitted emission lines, presence of narrow (hundreds of km/s) permitted and forbidden emission lines, a polarized continuum.

Each particular class of AGN may show some of the former properties but not all. A first step in the understanding of the AGN phenomenology was a taxonomy based in these observables, leading to a numerous set of different types: Seyfert 1 and Seyfert 2 galaxies, Low Ionization Nuclear Emission-line Region (LINER), Radio galaxies (grouping broad and narrow-line objects), quasars, blazars (BL Lac objects plus Optical Violently Variable quasars), etc. It was soon realized that different AGN types shared some similarities, and some schemes were designed to group the different types of objects with a few degrees of freedom (see for example the excellent review by Lawrence, 1987, on the first unification schemes). To a certain point, our understanding of the AGN phenomenon has been conditioned by the classification of objects made in the first term, and much effort has been put in gaining a global view of the energy source and the interrelation of it with the host galaxy.

The main observational features (variability timescale, gas dynamics, overall energy budget, etc.) imply the existence of a mass of the order $10^6$–$10^9\,M_\odot$, in a region smaller than 0.1 pc in diameter. Nowadays, the only theoretical model that can explain such mass density, together with some relativistic effects (observed for example in the X-ray Fe K line), while staying stable over time, is a super massive black hole or SMBH (see Ferrarese & Ford, 2005, for a review on the observational evidence for it).[1]

Within this frame, most of the AGN phenomenology is explained by accretion of material onto the SMBH, with the subsequent emission of radiation, through the unified model (Antonucci, 1993; Urry & Padovani, 1995). Before falling to the SMBH, the material forms an accretion disk, which is surrounded by an obscuring structure, possibly a clumpy dusty torus. AGN are classified as type 1 or 2 depending on the presence or absence of broad emission lines in their optical and UV spectra. Broad and narrow lines are originated in regions of different physical conditions. The Broad Line Region (BLR), origin of the broad permitted emission lines visible in the spectra of the type 1 AGN, are high density gas clouds located in the inner 0.1 pc. The Narrow Line Region (NLR) is a set of low density gas clouds extending ∼100 pc from the galactic center, where the narrow component of the emission lines, including forbidden ones, are originated. These are both photoionized by a non-thermal central radiation source. In the unification scheme, type 1 and type 2 AGN are regarded as intrinsically similar, although by an orientation effect the dusty torus hide from our direct sight the BLR in type 2 AGN. The model explained successfully the occurrence of broad emission lines in polarised light in the spectra of some Seyfert 2 galaxies (Antonucci & Miller, 1985; Miller & Goodrich, 1990), as well as the existence of high-excitation gas extending out from the nucleus with conical and biconical morphology (e.g. Wilson et al., 1988; Tadhunter & Tsvetanov, 1989; Pérez et al., 1989).

This is an elegant model with few free parameters, but some studies question the absolute validity of it. There seems to be a population of true Seyfert 2 nuclei, this is, galaxies which lack a BLR, or that are unabsorbed and compton-thin in nature (Tran, 2001; Panessa & Bassani, 2002). Malkan et al. (1998) found a statistical difference between the morphology of the host galaxy of Seyfert 1 and 2. Some environmental studies show differences in the abundance of companions between types (Dultzin-Hacyan et al., 1999). Taking into account also stellar population studies, it has been suggested an evolutionary sequence among Seyfert types, from starburst to Sy2 and then to Sy1 (Storchi-Bergmann et al., 2001; Oliva et al., 1999;

---

[1] Despite this is not a direct detection, but rather indirect evidence, it is widely accepted and commonly used in the literature the term super massive black hole (SMBH) instead of the more precise super-massive compact object. Throughout this work we will preserve the standard notation, as we are not interested in the exact nature of the central engine itself, but in the impact in its environment and the interrelation with it.

Koulouridis et al., 2008). Moreover, mid-IR observations of Ramos Almeida et al. (2011) find that differences between Seyfert 1 and 2 galaxies would arise mostly due to intrinsic properties of the absorber than merely to an orientation effect, assuming a clumpy torus model. In addition, the existence of the torus is generally accepted throughout the literature, however, some studies stress the difficulty of maintaining a stable optically thick cold rotating structure, and point to a warped disk as the main absorber (see Lawrence & Elvis 2010, and references therein). Added to all this, there is the puzzling rapid change of spectral Seyfert type documented for several objects (e.g. Tran et al., 1992b), that may originate in a scale much smaller than the clumpy torus (Puccetti et al., 2007).

It seems that the unification model is part of the story, but not everything (e.g. see Trump et al., 2011, and references therein). Despite the insight gained with the unification scheme, comparison studies between AGN of types 1 and 2 are needed today as much as they were two decades ago, in order to clarify this long-standing debate.

While quasar density decreases notably from redshift $z \sim 2$, being absent nowadays, Seyfert galaxies dominate the AGN emission, and therefore the SMBH growing, in the local universe. In this study we will concentrate in local Seyfert galaxies. In this way, we will be able to achieve the necessary resolution to study in detail the circumnuclear region of the AGN.

## 1.2 The ubiquity and role of Super Massive Black Holes

So accretion onto a SMBH is most probably the energy source of quasars, which are common at $z \gtrsim 2$, but where have all these objects gone? They obviously must be common as quiescent remnants in nowadays galactic nuclei. This was one of the first arguments for the ubiquity of SMBH. By means of gas and star dynamics it has been possible to detect the existence of very massive dark compact objects also in the center of local quiescent galaxies (e.g. Kormendy & Richstone, 1995), and not only in active nuclei. It is today widely accepted, that a super massive black hole resides in the very centre of every bright galaxy with a well developed bulge (Magorrian et al., 1998).

Early studies discovered a relation between the inferred mass of the SMBH and the total luminosity of the host galaxy or galactic bulge (Kormendy & Richstone, 1995; Magorrian et al., 1998; Kazantzidis et al., 2005), but with a large scatter in the relation. More recently, stronger observational correlations have been found between the black hole mass and the velocity dispersion of the host bulge (Gebhardt et al., 2000; Ferrarese & Merritt, 2000; Tremaine et al., 2002), and also with other magnitudes as bulge mass (Marconi & Hunt, 2003), light concentration (Graham et al., 2001), etc. Although the relation $M_{BH} \propto \sigma^{\alpha}$ in the local universe is today well established, there are details which need further consideration. For example, some particular galaxies seem to fall bellow the relation, such as narrow-line Seyfert 1, galaxies with bars or pseudobulges (e.g. Mathur et al., 2011; Graham & Li, 2009).

It has been suggested that the cited relation is in fact an upper limit (King, 2010). It is also being investigated at higher redshift in search for a possible evolution (e.g. Salviander et al., 2006).

Observed correlations imply a direct relation between the formation and evolution processes of the central SMBH and those of the host bulge. It must be noted however, the extremely different physical scales involved: up to several kpc for the galactic bulge and a fraction of a pc for the SMBH gravitational influence. The theoretical interpretation of these correlations is not trivial. There are currently four main models to explain this issue. One model states that the formation of the SMBH could depend on the dynamical properties of the host bulge through the rate of gas supply. The second option claims that feedback between the bulge and the SMBH regulates the accretion and growing of the central object (Silk & Rees, 1998). Another possibility is that both bulge and SMBH grow together through major mergers (Haehnelt & Kauffmann, 2000). At last, there is the possibility that the correlation arrises from stochastic processes, assuming the existence of primordial black holes as seeds for the current ones (Dokuchaev & Eroshenko, 2003).

An interesting piece of this puzzle are the massive star clusters found at the nuclei of spirals (Carollo et al., 2002; Böker et al., 2002), early type galaxies (Côté et al., 2006) and Low Luminosity AGNs (González Delgado et al., 2008). The nuclear star clusters, also known as stellar nuclei, have been studied spectroscopically and characterized by Walcher et al. (2006) and Rossa et al. (2006). These are massive compact star clusters whose mass seems to be correlated with the luminosity of the host bulge following the same slope than that for SMBH. Recent results support the view that SMBH and stellar nuclei have close similarities in their formation and evolution histories (Ferrarese et al., 2006). Everything suggests that they both are intimately linked to the evolution of the galactic bulge.

## 1.3 A connection between star formation and Nuclear Activity

The correlations explained above indicate that in the past, the AGN phenomenon must have coexisted with violent star-formation, but to what extent this is happening today and whether there is a causal connection between them is something that needs to be better understood.

Clues for this emerged first from the study of the Ultra-Luminous Infrared Galaxies (ULIRGs). These galaxies harbor a powerful radiation source which is heavily absorbed by dust. This dust is heated and re-emit strongly in the infrared. ULIRGs are well known for usually hosting powerful starbursts and showing evidence of merging, and often harboring an active galactic nucleus (Díaz-Santos et al., 2010, and references therein). Evidence has been accumulating for an evolutionary connection between ULIRGs and quasars (Sanders et al., 1988; Sanders, 1999; Kormendy & Sanders, 1992; Joseph, 1999). The nuclear concentrations of dense gas in ULIRGs would feed the AGN, which would then expel the nuclear gas and dust, appearing as luminous quasars. These processes constitute an example of feedback between star formation (SF) and AGN activity.

On the other hand, it appears to be a delay between the triggering of a starburst and the onset of the nuclear activity (Davies et al., 2007; Schawinski et al., 2009; Wild et al., 2010), or in other words, between the peak of the star formation rate and the peak of the SMBH accretion rate. If this is the case, then the violent starburst environment may not be the best place to prove the AGN-SF feedback. Veilleux et al. (2005) or Krug et al. (2010) find mixed results in those environments. Post-starburst systems may be more useful to this regard (Tremonti et al., 2007; Humphrey et al., 2010; Dunn et al., 2010; Feruglio et al., 2010).

Looking for star formation signatures in Seyfert galaxies have yielded important clues in the matter. Direct observational evidence that an important fraction of the total UV light detected in Seyfert 2 galaxies is emitted by star formation processes comes from high resolution UV images of these objects (Heckman et al., 1997; Colina et al., 1997; González Delgado et al., 1998). Powerful circumnuclear starbursts have been unambiguously identified in 40% of nearby Sy 2 galaxies (González Delgado et al., 2001; Cid Fernandes et al., 2001, 2004a). These starbursts were originally detected by means of either UV or optical spectroscopy of the central few 100 pc. Several spectroscopic works have detected features of young and intermediate age stellar population (Heckman et al., 1997; González Delgado et al., 1998, 2001; Storchi-Bergmann et al., 2000), suggesting that these populations are significant, if not dominant, in the nuclear region of many Sy2 galaxies.

There are clues that AGN activity and starbursts are associated but the physical mechanisms linking them are still uncertain. The circumnuclear star clusters are very good tracers of this process. This is because the occurrence of star clusters is a common phenomenon in star forming environments. Hubble Space Telescope studies of starburst galaxies (e.g. Meurer et al., 1995) have identified compact knots of star-formation and a difusse component, which is believed to originate via disipation of aging star clusters (Tremonti et al., 2001; Chandar et al., 2005). Most of the stars are in fact thought to be born in clusters (Fall et al., 2005; Lada & Lada, 2003). Stellar clusters are the building blocks of the star formation process, and therefore, the study of cluster population is one of the best tools to approach this issue.

## 1.4 Aim and outline of this thesis

In few words, our aim is understanding better the nature of the near-UV light in the circumnuclear region of Seyfert galaxies, as well as the connection between the AGN and starbursts processes. High resolution imaging combined with a high sensitivity is needed in order to resolve the nuclear star cluster population and to disentangle the distribution of extended emission related to the active nucleus and the star forming-regions. In order to do that, we have based our work in a snapshot survey of a sample of Seyfert galaxies with the Advanced Camera for Surveys (ACS) of the

Hubble Space Telescope (HST) in its High Resolution Configuration, with the filter F330W, which is a near-ultraviolet band (HST Proposal 9379, Schmitt et al.). The use of HST is crucial to get the needed resolution and image stability, unattainable from the ground. Observations from outside the Earth atmosphere also allows a major improvement in near-UV sensitivity, band which is severely affected by atmospheric absorption. At this wavelength the young stellar population appears bright, as well as the post-sturburst stellar population ($\sim$100 Ma), which is fainter at shorter wavelengths. As far as they are not heavily affected by dust extinction, they should also be easier to disentangle from the older and redder population of the host bulge (see Figure 1.1). In summary, this configuration is optimal to detect faint young and middle-aged star-forming regions around these nuclei, and separate their light from the underlying bulge emission. The images of this proposal complement optical and near-IR images available in the HST archive providing a panchromatic atlas of the inner regions of these objects.

This thesis is structured over three complementary works, combined to pose a reasonably complete approach to the subject exposed in this introductory chapter. These parts consist in: first, a general morphologic and photometric study of a large sample of Seyfert galaxies and comparison among types; second, focussing on the understanding of the different components of the extended emission; last, tackling the problem of characterizing the population of star clusters and compact knots of star formation. An extra chapter has been included where we outline the extension of the work to a sample of lower luminosity objects (Low-Luminosity AGN), that we are carrying out with complementary data.

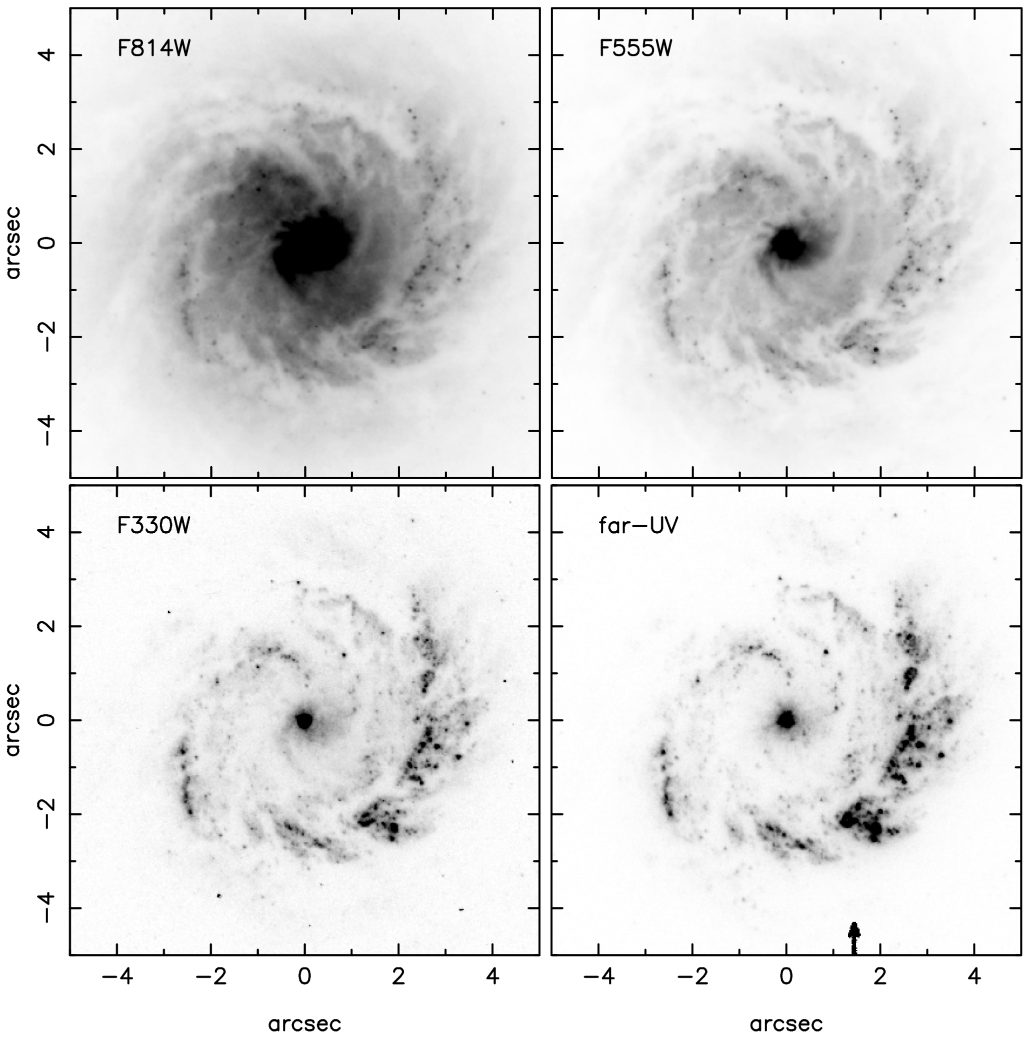

Figure 1.1: The four panels show the center of NGC 4303 in the bands F814W (I), F555M (V), F330W (U), with ACS, and far-UV with STIS. This figure show how nuclear and circumnuclear stellar clusters can be more easily detected at shorter wavelengths, due to the lower contribution of the host bulge.

# Chapter 2

# Data source, software, and analysis overview

---

## Contents

---

This chapter provides a general introduction to the data used in this work, and the technics and software needed for the data reduction and analysis. The analysis technics covered in this chapter are intended to be general and common to most of the data set. A more detailed insight in some steps that are relevant only in particular cases will be given in its corresponding chapter, for example the correction for Charge Transfer Inefficiency.

## 2.1 The Hubble Space Telescope

The Hubble Space Telescope (HST) is a cooperative program between NASA and ESA, consisting in a reflecting telescope in a low-Earth orbit (600 km), that was launched in April 1990. The telescope has a primary mirror of 2.4 meters, with a Ritchey-Chretien Cassegrain design, and working at f/24. This gives a plate scale on axis of 3.58 arcsec/mm, with a FWHM of the Point Spread Function (PSF) of 0.043 arcsec. Despite the obvious expenses in budget and technological difficulties, placing a telescope on-orbit brings several advantages over the ground-based observatories due to the avoidance of the Earth's atmosphere:

- The optical system, if good enough, is able to work close to the diffraction limit, allowing for a tremendous improvement in resolution over a large field of view.
- The stable environmental conditions yield quite a reproducible PSF, which is important for studies like those of star clusters.
- Access to a larger wavelength range, like for example the near-UV band, which is severely affected by atmospheric absorption.
- Reduction of the sky background, making possible very deep observations.

These characteristics combined make a small to medium size telescope on-orbit outperform the largest telescopes on the ground, in many working situations. For this reason the HST has produced a number of ground-breaking results in many fields in astronomy, and also constitutes the optimal choice for our work.

### 2.1.1 Description of the Snapshot Mode

When designing an observational program with HST there are mainly two types of observing proposals: General Observer (or GO) and Snapshot programs (leaving apart other kind of proposals with special requirements, such as Guaranteed Time Observer, Director's Discretionary and Calibration programs). The main difference between GO and Snapshot is that in the former the observer requests a number of orbits of the telescope, while in the latter the observer requests a number of targets. Most of the observing programs are of the GO kind. Time is allocated with an algorithm, which commonly results unable to fill completely the weekly observing schedule with GO targets. The gaps left are filled with observations from Snapshot programs. These programs consist in separate and short observations of an object list, generally of less than 45 minutes duration and distributed over the entire sky. There is no guarantee that any specific target is selected, and in general only a fraction of targets will be finally observed, depending on the availability of appropriate schedule gaps. Despite this last disadvantage, this strategy may favor some observing proposals over others.

Our work presented in this thesis is mostly based in a Snapshot program, proposal ID 9379 (P.I. Schmitt), which is explained in more detail in Chapter 3. With

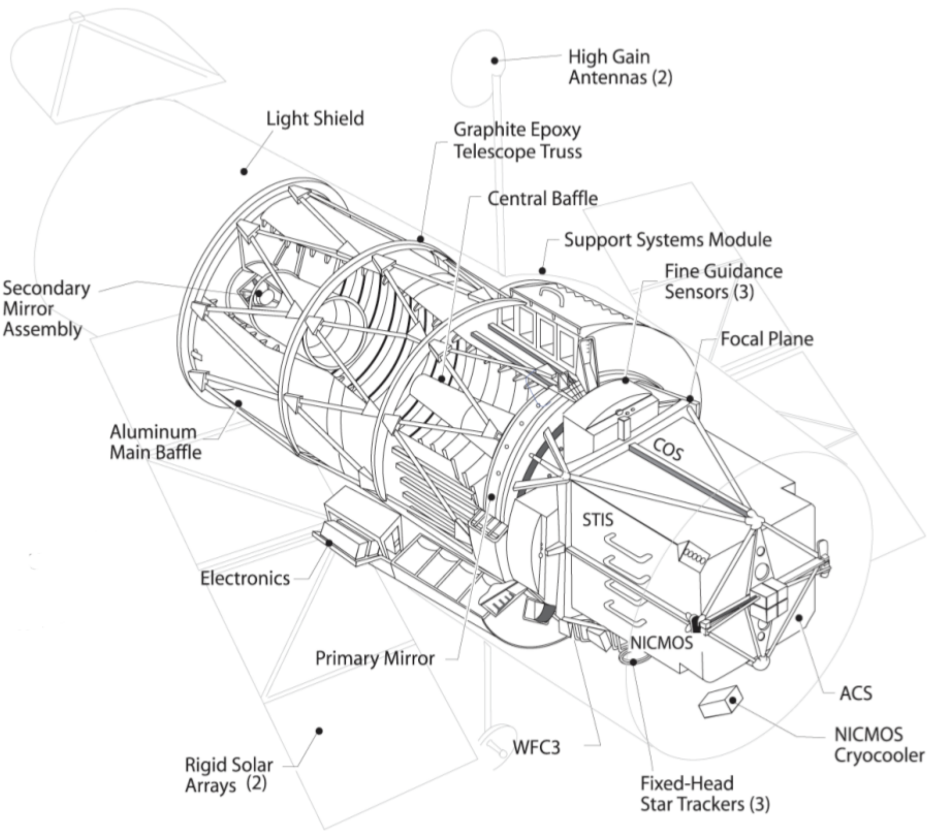

Figure 2.1: The image shows the major components of the Hubble Space Telescope after the last Servicing Mission. (Source: STScI)

the intention to extend the work to active nuclei of lower luminosity, our group wrote another Snapshot proposal, ID 10548 (P.I. González Delgado), for observing during HST cycle 14 (during 2005-2006). This proposal illustrates very well the process explained above. In June 2006 the Advanced Camera for Surveys suffered a failure in the electronics of its power supply. A redundant set of electronics allowed to resume observations before a definitive failure in 2007, but the camera was temporarily down. Therefore the observing time had to be re-scheduled, and some observing proposals were affected. As a consequence only 11 out of the 59 requested galaxies in the Snapshot ID 10548 could be finally observed.

### 2.1.2 The HST Data Archive

This is perhaps the most valuable legacy of the HST mission. All science and calibration data of each observation, together with many engineering data, are automatically placed in the HST Data Archive. The Principal Investigator of an observing program, and those designed by him, have exclusive access to the science data during a proprietary period. This period is normally one year, but the proposers may request a shorter proprietary period, or even waive this right altogether for the possible benefits to the scientific community. Once the proprietary period has expired the data become public, and any researcher has access to the Archive with just registering as a user. Data and calibration files can be retrieved through a web interface[1] that allows simple and user-friendly searches. The data is then reprocessed on-the-fly with the most up to date calibration files and may be accessed by FTP.

## 2.2 Instrumentation used on-board HST

The HST was designed with the idea of on-orbit servicing missions every 2.5 years and a total duration of the observations of 15 years. In total, 5 successful servicing missions have been carried out with the Space Shuttle, last one in 2009[2], expanding Hubble's lifetime for more than 20 years. These have the aim of refurbishment with new instrumentation, changing aging or spoiled solar panels or gyroscopes, replenishment of cryogen for the instrumentation, etc. The instrumentation on-board HST has been thus changing and evolving with the successive servicing missions. In this work we have used data of first (FOC), second (WFPC2, NICMOS), and third generation (ACS) instruments, each one with different technology and performance. Figure 2.1 shows an schematic plan of the main components of the HST after the last Servicing Mission in 2009.

---

[1] Multimission Archive at Space Telescope Science Institute webpage is currently at: `http://archive.stsci.edu/index.html`

[2] No more servicing missions are planned for the future, as the Shuttle program has been closed down by NASA.

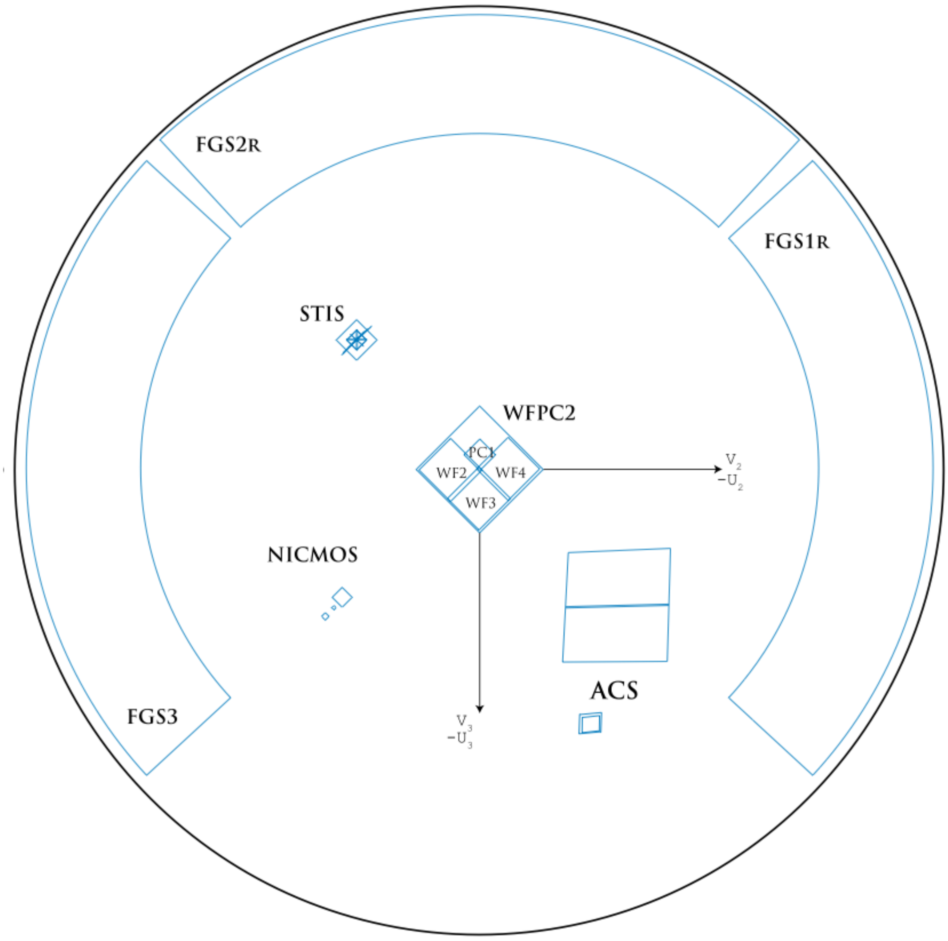

Figure 2.2: The image shows the focal plane of the Hubble Space Telescope before the last Servicing Mission, with the position of the detectors that provided data for this work. (Source: STScI)

### 2.2.1 Advanced Camera for Surveys

The Advanced Camera for Surveys (ACS) is a third generation instrument, installed during the fourth servicing mission in 2002. It has three different channels: Solar Blind Channel, Wide Field Channel, and High Resolution Channel. The only one used in our study has been the High Resolution one (HRC). This mode allowed[3] for near-UV to near-IR imaging (from ∼1700 Å to ∼11000 Å). The HRC detector was a 1K by 1K, thinned and backside-illuminated, SITe CCD with a near-ultraviolet optimized coating and $21{\times}21\,\mu$m pixels, that provided ∼0.028×0.025 arcsec/pixel spatial resolution.

This configuration had a PSF that was critically sampled at 6300 Å and undersampled by a factor 3 at 2000 Å, although it could be reconstructed with well-dithered observations. Another characteristic of HRC images is a dark shadow produced by the occulting finger used for coronography, such as studies of circumstellar disks, search for planetary companions, etc. The occulting finger may pose a problem for some photometric studies, although its position is well-known and can be masked easily.

A further particularity of ACS is its high geometric distortion. The HST primary mirror has a well-known problem of spherical aberration, which was discovered after launch. Second and third generation instruments were thus designed with an internal corrective optics. In particular, ACS optics was designed with the minimum number of optical components in order to correct for the spherical aberration and maximize throughput. For this reason the components are off-axis, the detector is tilted respect to the optical axis, and the field of view is rhombus-shaped when projected on the sky (see Figure 2.2). Therefore the scale and pixel area also varies across the detector, resulting in a complicated distortion correction

### 2.2.2 Wide Field Planetary Camera 2

The Wide Field Planetary Camera 2 (WFPC2) is a second generation instrument that was retired during last servicing mission. Its focal plane was a mosaic of four CCDs, three of them “wide-field” (called WF2, WF3 and WF4), and a higher resolution one as the Planetary Camera (called PC). All four CCD had 800×800 pixels, and were sensitive from 1150 to 11000 Å. The WF chips provided a pixel size of $0\rlap{.}''1$ for a total FoV of $2\rlap{.}'5$ side, and the PC chip had a pixel size of $0\rlap{.}''0455$ with a FoV of $35''\times35''$. So the PC provided higher resolution and reduced field, and the WFC chips the complementary. The four chips shared a common vertex, producing the typical stair-like shape of the whole FoV. They were exposed at the same time, yielding four different images that could be later combined into a mosaic. The object could be placed anywhere in the field, depending on the study to be carried out and the resolution or field needed to achieve that goal.

As in the case of ACS, WFPC2 undersamples the PSF, by a factor of 2 for the PC chip, and a factor of four for the WFC chips in the visible. The design of

---

[3] Since January 2007 the HRC is not working and could not be recovered in last servicing mission.

the camera and its location in the center of the focal plane produces a negligible field aberration in this case. These data have a special problem that is the partial vignetting of the inner edges between chips, due to the splitting of light in the internal optical design. However, this haven't affected our data, as our objects were commonly centered in the PC, and more rarely in WF3.

### 2.2.3 Near-Infrared Camera and Multi-Object Spectrograph

This camera, called NICMOS in short, was installed in February 1997 and has continued working ever since. It provides near-IR imaging, from 8000 to 25000 Å, through three independent channels, that image contiguous fields-of-view. Each channel has its own detector, which are 256×256 HgCdTe Rockwell arrays. The pixel size and FoV are 0″.043 and 11″×11″ for Camera 1 (called NIC1), 0″.075 and 19″.2×19″.2 for Camera 2 (NIC2), and 0″.2 and 51″.2×51″.2 for Camera 3 (NIC3). Both NIC1 and NIC2 provide diffraction-limited images, while NIC3 does not. NIC2 channel has a occulting circular spot that allows for coronography, but introduces an extended artifact in the image that has to be masked. The chips are divided in 4 quadrants, which are read independently (each with an amplifier), and the pixel charge is not transfered in this kind of detectors, so they do not suffer from Charge Transfer Inefficiency or bleeding, unlike CCDs. However they have their own problems, as the matching of the bias level for the four quadrants that produces the pedestal effect, as we will see in next section.

### 2.2.4 Faint Object Camera

This was one of the 4 original instruments on-board HST after launch, and was retired during the fourth servicing mission. FOC was designed to provide high-resolution images of small fields, through two independent channels that magnified the input beam by a factor of four (f/96) and two (f/48). In addition, a variety of prisms and polarizers were available, and the f/48 relay also had a longslit spectrograph. The camera detectors were not CCD, but photon-counting photocathodes, with a wavelength sensitivity from 1200 to 6000 Å.

The performance of this instrument was marked by the aberration of Hubble's primary mirror. All the data taken before the first servicing mission suffer from this problem, and as a result is difficult to work with them. There are tools however to deconvolve the data, recovering some of the expected resolution, but creating many image artifacts. During the first servicing mission a corrective optics was installed (COSTAR), so later data recover most of the image quality. COSTAR changed the f/ratio of HST's optical assembly, raising the two channels to f/75.5 and f/151. In addition high voltage instabilities were detected, limiting the use of the f/48 relay to mainly long-slit spectroscopy, and making the f/96 camera the almost exclusive choice. When corrected by COSTAR, the FoV and pixel size of the f/96 camera were 7″×7″ (512×512 format) and 0″.014×0″.014, respectively; a field of 14″×14″ could be used with the 512×1024 pixel format and a rectangular pixel size of $0\farcs028\times0\farcs014$. Without COSTAR in the beam, the corresponding parameters for the f/96 camera were: $11''\times11''$ FoV in the 512x512 format with pixel size $0\farcs0223\times0\farcs0223$, and full-format field of $22''\times22''$ with $0\farcs0446\times0\farcs0223$ pixels.

### 2.2.5 Space Telescope Imaging Spectrograph

The Space Telescope Imaging Spectrograph (STIS) was installed in February 1997, and provides ultraviolet and optical spectroscopy and imaging through three channels. STIS can be used to obtain spatially resolved, long-slit (or slitless) spectroscopy over the 1150–10300 Å wavelength range at spectral resolving power of R ∼ 500 to 17,500; and echelle spectroscopy over the 1150-3100 Å wavelength range at spectral resolving powers of R ∼ 30,000 and 114,000, covering broad spectral ranges of $\Delta\lambda\sim800$ Å and 200 Å, respectively. STIS can also be used for optical and solar-blind ultraviolet imaging. Three detectors, each with a 1024×1024 pixel format, support spectroscopy and imaging as follows. The STIS/FUV-MAMA far ultraviolet channel uses a solar-blind, CsI, Multi-Anode Microchannel detector Array (MAMA), with a FoV of $25''\times25''$, a plate scale of 0.025 arcsec/pixel, and covers the wavelength region from 1150–1700 Å. The STIS/NUV-MAMA near-ultraviolet channel uses a $Cs_2Te$ MAMA detector with the same FoV and plate scale, and covers the 1600–3100 Å wavelength region. For the 1650–11000 Å optical wavelength region, the STIS/CCD detector is a thinned and backside-illuminated SITe CCD with a near-ultraviolet optimized coating. The FoV is $52''\times52''$ and the plate scale is 0.05 arcsec/pixel.

## 2.3 Main Software used during this work

The wide range of needs for the analysis of the images have required the use of several software tools and packages, from very specialized software, designed for a particular step in the data reduction process, to programs coded by us in a general programming environment. The main software packages used along this work are: IRAF, Python, Synphot and TinyTim.

### 2.3.1 IRAF

The Image Reduction and Analysis Facility[4] (IRAF) constitutes the most popular basic tool of image analysis for astronomers. It contains numerous packages of programs that perform multiple and varied tasks, like reading data in FITS format, managing tables, image and spectra reduction and analysis, etc. It works with the image visualization tool SAOImage-DS9. In addition, it is built in a way that allows the integration of external packages, like the Space Telescope Data Analysis

---

[4] IRAF (Image Reduction and Analysis Facility) is distributed by the National Optical Astronomy Observatories, which are operated by AURA, Inc., under cooperative agreement with the National Science Foundation.

System (STSDAS). This last uses IRAF as its core, and includes most of the tools specifically developed to reduce and analyze HST data. IRAF allows to write scripts in order to automatize some tasks, or an interactive use through a command line.

This software have been used for so many porpoises during this thesis that it wouldn't have sense to explain them all in detail here. Some of the applications are, among others: visualization of HST data; reprocessing some of the images with the STSDAS tools; image manipulation such as cropping, image registration and alignment, rotation, scale transformation and rebinning, image arithmetics, statistics of regions, etc; spectra visualization and line measurement; identification of sources; photometry...

There is also an IRAF version prepared to work under Python, called Pyraf. This is useful, as it allows to use IRAF tasks within Python programs. It is also needed in order to use some of the tasks for reprocessing ACS data.

### 2.3.2 Python

Python is an object oriented programing language. Despite being very powerful it is also easy to learn, intuitive, and quick to use, with a command line that allows an interactive use akin to Matlab. In addition, its code is Open Source and it is distributed under free license, with a large support community. It works under the three more common platforms: Windows, Linux and MacOS; so the developed software is easily portable to any new working conditions. For all these reasons we have chosen Python as our usual working software, although during the first year of work we used also other tools (such as IDL) that we later abandoned.

We have used Python for these main tasks: as a graphical tool, for the results visualization and plot creation; as a script generator combining IRAF (Pyraf) tasks and Python proper functions; and to program particular data analysis in some more complicated code, such as photometry and verification of results with Synphot.

### 2.3.3 Synphot

Synphot is a package of synthetic photometry of the STSDAS system, and thus it is oriented toward photometry with the HST. It works integrated in either IRAF or Pyraf environment as a external package. Synphot allows to simulate photometric and spectral data, as observed with HST. It can be used to plot HST sensitivity curves or filter transmission curves, predict count rates and simulate any instrument mode, compute the photometric calibration for any instrument mode, or compute the transformation between different photometric systems.

### 2.3.4 TinyTim

TinyTim[5] is a software package to simulate HST Point Spread Functions. It is written in C and works through the command line. It can simulate the PSF of any

---

[5] `http://www.stsci.edu/software/tinytim/`

instrumental configuration, although with some caveats. We have used TinyTim in several occasions along this work to simulate observations of artificial star-clusters, calculate aperture corrections, or degrade several bands to a common resolution.

## 2.4 Data reduction and image analysis

The instruments on-board HST, as all the astronomical detectors, produce raw data that need to be prepared and calibrated previous to any scientific measurement. This is the so-called data reduction process. The STScI has put much effort in automatizing this procedure, and making the extraction of scientific data from the images a very efficient process.

When downloading the data from the Archive there is the possibility to do it with the 'on the fly' calibration option. This performs the usual correction to the images from bias, dark and flat-field subtraction with the most up-to-date reference files and bad pixel tables. When the exposures are split in several of shorter exposure time, the automatic pipeline rejects the most severe cosmic rays, combining the frames in a single image. Each instrument has an associated group of routines that confront optimally its particularities. The final products are both astrometrically and photometrically accurate.

For most scientific applications the images produced by the pipeline may suffice. However, one may desire more control over the measurements, and sometimes a partial re-calibration of the data is required by certain circumstances. One example of this are NICMOS data. It has been explained above that the detectors of NICMOS are divided in 4 quadrants which are read with 4 different amplifiers. This camera suffers from a problem of stability in the bias level among the different quadrants, that may vary during the exposure. This is known as the *pedestal effect*, and produces the print of the flat field image in the final data. As a consequence, part of the reduction process has to be redone, with the previous use of a special IRAF routine called 'pedsub', that with an iterative algorithm allows to correct for the effect. With NICMOS data we have found also a problem with the sky over-substraction when combining several exposures of objects occupying a large fraction of the FoV. Some parameters were changed in the reduction routines that allowed for a later manual subtraction of the sky in these cases. In general, the automatic calibration does not combine images from different datasets. This has to be done manually with special tasks provided by STSDAS. The precision of the absolute astrometry with HST is around 1 arcsec, so when combining different images they have to be previously registered, with special care needed for ACS data, which has a strong geometric distortion.

In this work STIS data were used exclusively as a support for the nebular continuum estimation in Chapter 4. The spectra used were already calibrated and published by Spinelli et al. (2006), so we did not have to confront any data reduction for this instrument.

### 2.4.1 Cosmic rays removal

As an orbital observatory, the HST is heavily exposed to cosmic rays (CRs). Each single event hitting the detector may affect to more than one pixel, either by an oblique impact or by charge diffusion. The counts in the affected pixels are very high, and may spoil the measurement of the target. This problem is much worse with HST than with ground-based telescopes. For ACS, for example, an integration of 1000 seconds may yield between 1 and 3 % of the pixels affected by CRs.

The best strategy to remove CRs is to split the exposure in several of less integration time, adding a dither pattern in order to remove also the hot pixels (pixels which give systematically an abnormally high number of counts). If the observations are not well planned the CRs may be an issue, depending on the nature of the target. For an extended diffuse object, for example, the cosmic rays may be easily removed with a median-based filter. In the cases when we attempted to measure star clusters this step had to be performed with care.

We have found that the standard parameters of the pipeline were not sufficient to clean completely the ACS frames. The undersampling problem, with the very small size of point-like objects made difficult to distinguish them from clumps of bad pixels. This depends also in the S/N ratio of the image, so in some cases was worse than others. We tried several tasks with different parameter sets in order to remove the cosmic rays from the ACS images, but finally we decided that the only way to ensure that we wouldn't remove the cluster cores was to do it by hand. This is quite effective after familiarizing with the data, for telling real features from artifacts, although it was time-consuming as well. For WFPC2 data, of better S/N as they were optical instead of UV, this problem was relieved. In particular, when several exposures were available for an object, the CR removal was straightforward when combining the images. Regarding NICMOS images we found easy to create artifact-free data from them.

### 2.4.2 Photometry

#### 2.4.2.1 Magnitude systems

A magnitude system is a decimal logarithmic scale to measure brightness in the next way:

$$m = -2.5 \log \frac{f_i}{F_i},$$

where $f$ is the monochromatic flux density in the band $i$, and $F$ is a reference flux in that band. This is a definition that has been kept mostly by historical reasons, and different magnitude systems have emerged based in it. The problem is that the reference flux may be dependent on the wavelength, and its calibration may change over time, as happened with systems based in Vega. In addition, the flux density may be expressed per unit wavelength or per unit frequency. All this makes that the conversion between different systems may not always be straightforward and color terms appear. Some of the most widely used systems (Figure 2.3) are:

- VEGAMAG: this photometric system uses the spectrum of the star Vega ($\alpha$ Lyrae) as the reference flux, in a way that the color of Vega in any two given bands are equal to 0 and V= 0.03.
- ABMAG: the reference spectrum is one of constant flux density per unit frequency, normalized so that the magnitude at V band is approximately zero, in the next way:
$$\mathrm{ABMAG} = -2.5 \log F_\nu - 48.6,$$
where $F_\nu$ is expressed in $\mathrm{erg\,cm^{-2}\,s^{-1}Hz^{-1}}$.
- STMAG: the reference spectrum is one of constant flux density per unit wavelength, normalized so that the magnitude at V band is approximately zero, in the next way:
$$\mathrm{STMAG} = -2.5 \log F_\lambda - 21.1,$$
where $F_\lambda$ is expressed in $\mathrm{erg\,cm^{-2}\,s^{-1}\text{Å}^{-1}}$.

The magnitude scale is based in the logarithmic response of the eye. Although our modern detectors are linear, the use of magnitudes is so widespread in the field that we will stuck to the usual procedure. However, we consider wise to use a more physical magnitude system than the classical based in Vega. Both STMAG and ABMAG systems are flux-based, and therefore are directly related to physical units. Conversion of magnitudes between them is straightforward, due to the simple relation between $F_\lambda$ and $F_\nu$, although one has to be careful when using the average flux density in a bandpass, instead of the monochromatic flux density. We have decided to use STMAG system for all our analysis along this thesis.

#### 2.4.2.2 Absolute photometry

With a small FoV, as those of HST, it is difficult to get standard stars in the same field for comparative photometry, and pointing the telescope to several calibration stars would be too time-consuming and expensive. Thus, the most efficient working procedure is absolute photometry. This depends strongly on a good calibration of the instrumentation used. STScI provides a very precise calibration of most of the instruments, allowing to perform a highly accurate absolute photometry.

The data products created by the calibration pipeline come in counts (WFPC2) or counts per second (NICMOS, ACS). Transforming one to the other is trivial, known the image exposure time. Given the linear response of the detectors, an alternative way to express the magnitude in a passband P is:

$$m(P) = -2.5 \log(\mathrm{total\,counts/s}) + \mathit{zeropoint},$$

where *zeropoint* is the magnitude of an object which produces a detection rate of one count per second. When using the STMAG system, the most straightforward way to convert the data in the images to physical fluxes or magnitudes is using the header keywords PHOTZPT (photometric zero point of the magnitude scale),

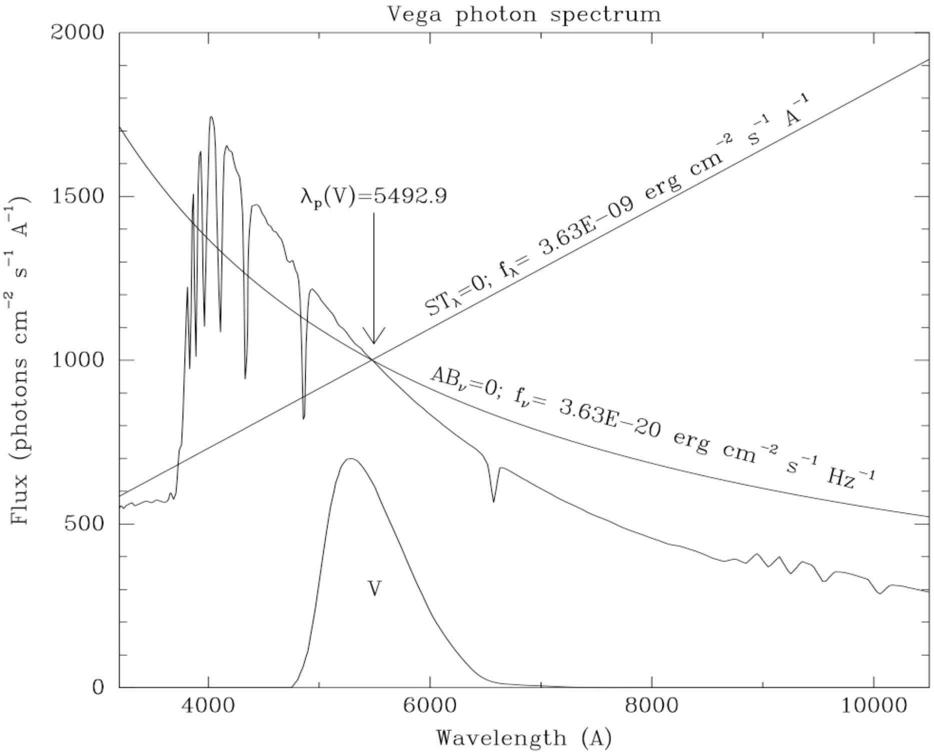

Figure 2.3: The plot shows the spectra of zero monochromatic magnitude for VEGAMAG, STMAG and ABMAG systems. They are defined to cross at the pivot wavelength of the Johnson V passband, i.e. to produce the same count-rate in the V band. Source: STScI)

and PHOTFLAM (inverse sensitivity), which is the mean flux density in units of $\mathrm{erg\,cm^{-2}\,s^{-1}\,\mathring{A}^{-1}}$ that produces one count per second in the detector. When retrieved from the Archive, the headers of the images are populated with the most up-to-date calibration keywords. In this way we can use the next equation to transform from counts (DN) to magnitude in a passband P:

$$m(P) = -2.5\log\left(\frac{PHOTFLAM \cdot DN}{EXPTIME}\right) - PHOTZPT \tag{2.1}$$

#### 2.4.2.3 Photometric software tools

The software presented in Section 2.3 has been applied to our photometric studies as follows.

**IRAF** It provides several packages which are very helpful for photometric applications and image analysis. Among them we can cite the next, which we have mostly used along the work:
- apphot: aperture photometry package, which is useful to derive surface brightness profiles, sky determination, etc.
- daophot: stellar photometry package meaningful for crowded fields, finding compact objects, etc.
- isophote: package for fitting elliptical isophotes.
- imexamine: performs simple photometry measurements on images.
- imstat: computes pixel statistics of images or rectangular regions.

**Synphot** It is a package specially developed for photometry with HST, so it was an essential working tool. It served also as a source of the filter transmission curves to check for possible emission line contamination, and it provided the photometric parameters of each instrumental configuration, such as the average wavelength of the filter or its equivalent width. A large base of external Single Stellar Population spectra was transformed into Synphot format, what allows its internal use. With this we could construct the color diagrams and transform between coordinate systems in order to compare with other works.

**Python** For photometry we have used Python only as an auxiliary tool, running Pyraf programs combined with further Python analysis. We have performed synthetic photometry, convolving synthetic spectra with HST transmission curves, and applying numerically a reddening law. This allowed a double-check of the results obtained with Synphot.

### 2.4.3 Point Spread Function

The Point Spread Function, or PSF, is basically the image of a point source as registered with the instrument. This takes into account from the whole optical system to the interaction of the light with the different detector layers. It is complicated to model, depending on many things, such as the wavelength (and thus on combination of the Spectral Energy Distribution and the filter transmission curve), the position on the detector, focus changes due to thermal variations of the telescope structure, etc.

Along this work we have frequently needed to use a simulated PSF for several instrumental configurations. For this we have used the software tool TinyTim, developed at STScI by John Krist. Due to the reasons explained above, the artificial simulation of the PSF has some caveats, and the agreement with the real PSF may be limited. Using a TinyTim PSF to subtract a point-like object may certainly leave residuals, that have to be interpreted with caution. For the same reason, one should never use the diffraction spikes seen around a bright point-like object in order to scale the PSF to the object brightness, but the wings or the core of the PSF should be used instead.

The best approach to this is inferring the PSF from your own image, but when instrumental configurations with a small FoV are used, getting appropriate stars in the field may not be possible. A wise use of the synthetic PSF, knowing the caveats of its usage, may well serve as well as an experimental one for many scientific porpoises. Avoiding very small apertures, such as 2 pixels or less, eliminates most of the problems cited, for the precision we need in our work. However we have checked the effect of using a broadened PSF when we thought it was required.

### 2.4.4 Spectral synthesis models

The spectra of individual stars are well known to depend on a reduced set of parameters, mainly the star mass, its age, and metallicity. Acknowledging some intrinsic uncertainties in some late phases of the stellar evolution, as well as the effect of stellar rotation, binarity, etc., it is possible to construct a synthetic spectrum of a whole population of stars. The main ingredients for this are: a model of how the stellar spectrum for a given mass changes with age (stellar evolutionary tracks), an assumption of how is the distribution of stellar mass for new-born stars (initial mass function, or IMF), and the rate at which new stars have been forming (history of the star formation rate). In the simplest case an instantaneous burst of star formation can be assumed, with all the individual stars that make up the resulting spectrum having the same age. This is called a Single Stellar Population, or SSP. Most of the star clusters are a reasonably resemble an SSP. Therefore, individual star cluster properties, such as its total mass, age and affecting reddening, can be inferred by comparison of its integrated light (broad band photometry) with similar photometry of SSP models.

In this thesis we use SSP models in Chapters 4 and 5, for a detailed analysis of a star cluster population, and helping us to constrain the nature of extended emission. There exist a variety of synthesis models, which are improving at the pace at which our knowledge of stellar evolution and stellar atmospheres is increasing: PÉGASE (Fioc & Rocca-Volmerange, 1997), Girardi et al. (2002), Bruzual & Charlot (2003), etc. Some members of our group have been also involved in the work of developing evolutionary synthesis models for long (Cerviño & Mas-Hesse, 1994; Leitherer et al., 1999; González Delgado et al., 2005). In this work we have decided to use the Bruzual & Charlot (2003, BC03) and Starburst99 (Leitherer et al., 1999) models, as against those developed by our group because the former extent to longer wavelengths (J and H bands) that we need for our analysis, and besides we don't need the high spectral resolution of the latter models, optimized for espectroscopic analysis. These models however give a limited ability to determine metallicities, due to the incompleteness of the stellar libraries they use (González Delgado & Cid Fernandes, 2010). Despite of that, considering also metallicity would imply too many free parameters, and thus our approach has been working with a limited set of metallicities or assuming solar. Altogether, we have considered that they pose an adequate choice for our work.

## Chapter 3

# An Atlas of the circumnuclear regions of 75 Seyfert galaxies in the near-ultraviolet

Contents

## 3.1 Introduction

There is a rule of thumb when designing a study in extragalactic astronomy: the smaller your sample is, the deeper you can study it, but at the same time the possible results will be hardly generalizable. One has to bear in mind also the ultimate goal of your project, which in our case is to investigate the nature of the near-UV light in these objects, its relation to the circumnuclear starburst phenomenon, and the connection of this to the evolution and growth of the galaxy bulge and central black hole.

In this chapter, we present an atlas of the central regions of 75 Seyfert galaxies imaged in the near-UV with the Advanced Camera for Surveys of the Hubble Space Telescope at an average resolution of ∼10 pc. High resolution imaging combined with a high sensitivity is needed in order to resolve the nuclear star cluster population and disentangle the distribution of extended emission related to the active nucleus and the star forming-regions. This is why the use of the HST is the best observational choice for our project. The wavelength chosen is optimal to detect faint young and middle-aged star-forming regions around these nuclei, and separate their light from the underlying bulge emission. These data complement archival high resolution data from the Space Telescope at optical and near-IR wavelengths, creating an extremely valuable dataset for astronomers with a broad range of scientific interests, with the role of a panchromatic atlas of the inner regions of these objects. The size of the sample allow us to perform a detailed analysis and, at the same time, to draw statistically significant conclusions.

Along the chapter we characterize the near-UV emission of the galaxies in the sample. We present a morphological and photometric analysis of the objects, in which we estimate the size and the luminosity of the emitting regions, extract the luminosity profile, and determine the presence of unresolved compact nuclei. In addition, the circumnuclear stellar cluster population is identified, and the contribution of the stellar clusters to the total light, at this wavelength, is estimated. The results are compared among Seyfert types. The analysis presented in this chapter pose a self-consistent work that, together with the sample and the images of the objects, have been published in the Astronomical Journal (Muñoz Marín et al., 2007).

## 3.2 Constructing the Atlas: sample and data reduction

### 3.2.1 Selection of the sample

We have selected all the Seyfert (Sy) galaxies in the HST archive that had images in these three bands: near ultraviolet with ACS/HRC F330W, near infrared with NICMOS F160W and optical WFPC2 F606W (in most cases, but also F555W or F547M). The sample is composed by the galaxies imaged as part of the proposal ID 9379 (P.I. Schmitt), which is an HST cycle 11 ACS snapshot, plus NGC 7212 and NGC 5728 from the proposal ID 9681 (P.I. Kraemer). These two galaxies have not been imaged with NICMOS, but are included in this work because they improve our UV study of Seyfert nuclei with their F330W images. The instrumental configuration of the observations is described in more detail in section 3.2.3

The list of objects for proposal ID 9379 was constructed from the sample presented in Quillen et al. (2001), consisting in all the Sy observed with NICMOS F160W, which is itself a heterogenous sample made up from several proposals.

Only objects with also WFPC2, most of them in F606W (Malkan et al., 1998), were included in the proposal 9379 list. From the original list of 101 objects, 73 were observed during the snapshot, making a total of 75, that will allow us to carry out a statistical study for different types of Sy. From the final sample of 75 objects, 47 (63%) are classified as Seyfert 2 (Sy2), 14 (∼19%) as intermediate types Sy1.8-1.9, and 14 (∼19%) as Seyfert 1 and Sy1.2-1.5. Along the work we will group together the objects Sy 1, Sy 1.2 and Sy 1.5, that hereafter will be referred to as Sy1.

### 3.2.2 Sample properties and discussion of possible biases

In Table 3.1 we list the basic properties of the whole sample extracted from NED[1]. For the calculation of the distance we have used the Hubble law with $H_0 = 75$ km s$^{-1}$, and the radial velocity data from NED, with the exception of objects with radial velocity $V_r \leq 1200$ km s$^{-1}$. For those, we used values of the literature determined by other means, which are: M81 (NGC 3031) 3.6 Mpc (Freedman et al., 1994); Circinus, 4 Mpc (Freeman et al., 1977) and for the objects: NGC 3486 (7.4 Mpc), NGC 4395 (3.6 Mpc), NGC 3982 (17 Mpc), NGC 4258 (6.8 Mpc), NGC 5005 (21.3 Mpc), NGC 5033 (18.7 Mpc), NGC 5194 (7.7 Mpc), NGC 5273 (21.3 Mpc) and NGC 6300 (14.3 Mpc) we used the values from Tully (1988).

---

[1] The NASA/IPAC Extragalactic Database operated by NASA/IPAC, Caltech. (`http://nedwww.ipac.caltech.edu/`)

Table 3.1: Main properties of the whole galaxy sample

| Galaxy Name (1) | Alternative Name (2) | Spectral Class (3) | Hubble Type (4) | vel. [km s$^{-1}$] (5) | Scale pc/$''$ (6) | B_T [mag] (7) | E(B–V) [mag] (8) | axial ratio (b/a) (9) | $L_{[OIII]}$ (10) | Ref. (11) | FIR [10e11 $L_\odot$] (12) | IRAS $F_{12}/F_{25}$ (13) | IRAS $F_{25}/F_{60}$ (14) |
|---|---|---|---|---|---|---|---|---|---|---|---|---|---|
| CGCG 164-019 | | Sy2 | Sa | 8963 | 579 | 15.3 | 0.026 | 0.875 | 41.4 | dG92 | <0.672 | 0.735 | 0.436 |
| Circinus | ESO 97-G13 | Sy2 | SA(s)b | 449 | 19 | 12.1 | 1.455 | 0.435 | 40.21 | ol94 | 0.135 | 0.275 | 0.275 |
| ESO 103-G35 | | Sy2 | SA0 | 3983 | 257 | 14.7 | 0.076 | 0.364 | 40.75 | mw88 | 0.428 | 0.246 | 1.04 |
| ESO 137-G34 | | Sy2 | SAB(s)0/a?. | 2747 | 178 | 12.21 | 0.335 | 0.786 | 41.35 | fe00 | <0.2597 | 0.392 | 0.325 |
| ESO 138-G1 | | Sy2 | E-S0 | 2740 | 177 | 14.7 | 0.2 | 0.5 | 40.12 | li88 | <0.186 | 0.273 | 0.664 |
| ESO 362-G8 | | Sy2 | Sa | 4785 | 309 | 13.6 | 0.032 | 0.5 | 41.22 | mu96 | <0.156 | <0.316 | 0.297 |
| Fairall49 | IR 18325-5926 | Sy2 | Sa | 6065 | 392 | 13.2 | 0.065 | – | 41.25 | dG92 | 1.006 | 0.431 | 0.427 |
| IC 2560 | ESO 375-G4 | Sy2 | SB(r)bc | 2925 | 189 | 12.53 | 0.095 | 0.625 | 40.51 | gu06 | 0.2097 | 0.437 | 0.246 |
| IC 4870 | ESO 105-IG11 | Sy2-HII | Pec | 889 | 57 | 13.89 | 0.113 | 0.563 | –[a] | | <0.0073 | – | <0.391 |
| IC 5063 | ESO 187-G23 | Sy2 | SA(s)0+ | 3402 | 220 | 12.89 | 0.061 | 0.667 | 41.28 | sc03 | 0.6409 | 0.302 | 0.642 |
| Mrk 6 | IC 450 | Sy1.5 | SAB0+ | 5640 | 365 | 15.0 | 0.136 | 0.625 | 42.10 | wh92 | <0.3635 | <0.456 | 0.607 |
| Mrk 40 | Arp151 | Sy1 | S0-pec | 6323 | 409 | 16.8 | 0.014 | 0.429 | 41.18 | wh92 | – | – | – |
| Mrk 42 | UGC 8058 | Sy1 | SBb | 7385 | 477 | 15.28 | 0.029 | 0.983 | 40.55 | wh92 | – | – | – |
| Mrk 231 | | Sy1 | SA(rs)c?-pec | 12642 | 817 | 14.41 | 0.010 | 0.769 | 41.91 | da88 | 29.716 | 0.212 | 0.254 |
| Mrk 334 | UGC 6 | Sy1.8-HII | Pec | 6582 | 425 | 14.38 | 0.047 | 0.7 | 40.254 | li88 | <1.05 | <0.238 | 0.246 |
| Mrk 461 | UGC 8718 | Sy2 | S | 4856 | 314 | 14.61 | 0.024 | 0.714 | 40.327 | cg94 | – | – | – |
| Mrk 471 | UGC 9214 | Sy1.8 | SBa | 10263 | 663 | 14.54 | 0.010 | 0.667 | 40.66 | da88 | <0.935 | – | <0.500 |
| Mrk 477 | | Sy2 | Compact | 11310 | 731 | 15.2 | 0.011 | 0.709 | 43.02 | wh92 | <1.47 | <0.463 | 0.4 |
| Mrk 493 | UGC 10120 | Sy1 | SB(r)b | 9392 | 607 | 14.6 | 0.025 | 0.714 | 40.595 | li88 | <0.684 | <0.926 | 0.422 |
| Mrk 516 | | Sy1.8 | Sc | 8519 | 551 | 15.3 | 0.060 | 0.833 | 39.91 | os81 | <0.915 | – | 0.221 |
| Mrk 915 | | Sy1 | Sb | 7228 | 467 | 14.82 | 0.063 | 0.833 | 42.07 | wh92 | <0.569 | 1.625 | 0.711 |
| Mrk 1210 | UGC 4203 | Sy2 | Sa; | 4046 | 262 | 14.34 | 0.030 | 1.0 | 42.58 | fa98 | 0.401 | 0.263 | 1.136 |
| NGC 449 | Mrk 1 | Sy2 | (R’)S? | 4780 | 309 | 15.01 | 0.060 | 0.625 | 41.85 | wh92 | <9.727 | <2.24 | 0.348 |
| NGC 1144 | | Sy2 | S-pec | 8648 | 559 | 13.78 | 0.072 | 0.636 | 40.256 | li88 | 2.426 | 0.371 | 0.132 |
| NGC 1320 | Mrk 607 | Sy2 | Sa: sp | 2663 | 172 | 13.32 | 0.047 | 0.316 | 40.71 | wh92 | <0.135 | 0.306 | 0.458 |
| NGC 1672 | | Sy2 | (R’_1:)SB(r)bc | 1331 | 86 | 10.28 | 0.023 | 0.833 | 38.53 | gu06 | 0.5334 | 0.365 | 0.116 |
| NGC 2639 | | Sy1.9 | (R)SA(r)a: | 3336 | 216 | 12.56 | 0.024 | 0.611 | 39.45 | ho97 | <0.212 | – | <0.195 |
| NGC 3031 | M 81 | Sy1.8-L | SA(s)ab | -34 | 17 | 7.89 | 0.080 | – | 39.306 | li88 | 0.0041 | 0.878 | 0.106 |
| NGC 3081 | | Sy2 | (R_1)SAB(r)0/a | 2385 | 154 | 12.85 | 0.055 | 0.762 | 41.58 | wh92 | – | – | – |
| NGC 3227 | | Sy1.5 | SAB(s)-pec . | 1157 | 75 | 11.1 | 0.023 | 0.667 | 40.84 | wh92 | 0.0755 | 0.385 | 0.218 |
| NGC 3362 | | Sy2 | SABc | 8290 | 536 | 13.48 | 0.031 | 0.898 | 41.38 | wh92 | – | – | – |
| NGC 3393 | | Sy2 | (R’)SB(s)ab | 3750 | 242 | 13.09 | 0.075 | 0.909 | 41.98 | sc03 | <0.2398 | <0.352 | 0.298 |
| NGC 3486 | | Sy2 | SAB(r)c | 681 | 36 | 11.05 | 0.022 | 0.732 | 37.96 | ho97 | <0.0096 | <1.115 | 0.0568 |
| NGC 3516 | | Sy1.5 | (R)SB(s)0 | 2649 | 171 | 12.5 | 0.042 | 0.765 | 41.35 | wh92 | 0.1223 | 0.489 | 0.529 |
| NGC 3786 | Mrk 744 | Sy1.8 | (R’)SAB(r)a-pec | 2678 | 173 | 13.50 | 0.024 | 0.591 | 40.59 | wh92 | – | – | – |
| NGC 3982 | | Sy2 | SAB(r)b | 1109 | 82 | 11.78 | 0.014 | 0.882 | 40.06 | wh92 | 0.0719 | 0.571 | 0.1214 |
| NGC 4253 | Mrk 766 | Sy1.5 | (R’)SB(s)a: | 3786 | 245 | 13.70 | 0.020 | 0.8 | 41.77 | wh92 | 0.3934 | 0.297 | 0.340 |
| NGC 4258 | M 106 | Sy1.9-L | SAB(s)bc | 448 | 33 | 9.10 | 0.016 | 0.387 | 41.02 | ho97 | – | – | – |
| NGC 4303 | M 61 | Sy2-HII | SAB(rs)bc | 1566 | 101 | 10.18 | 0.022 | 0.892 | 40.24 | li88 | <0.3227 | – | <0.0259 |
| NGC 4395 | | Sy1.8-L | SA(s)m | 319 | 17 | 10.64 | 0.017 | 0.833 | 39.47 | ho97 | – | – | – |
| NGC 4565 | | Sy1.9 | SA(s)b? sp | 1230 | 80 | 10.42 | 0.015 | 0.116 | 38.71 | ho97 | <0.848 | <1.89 | 0.0778 |
| NGC 4593 | Mrk 1330 | Sy1 | (R)SB(rs)b | 2698 | 174 | 11.67 | 0.025 | 0.744 | 40.82 | wh92 | 0.1637 | – | <0.327 |
| NGC 4725 | | Sy2 | SAB(r)ab pec | 1206 | 78 | 10.11 | 0.012 | 0.710 | 38.76 | ho97 | <0.214 | – | <0.284 |
| NGC 4939 | | Sy2 | SA(s)bc | 3110 | 201 | 11.9 | 0.041 | 0.509 | 41.847 | li88 | <0.183 | – | <0.253 |
| NGC 4941 | | Sy2 | (R)SAB(r)ab: | 1108 | 72 | 12.43 | 0.036 | 0.528 | 40.17 | wh92 | <0.0172 | – | <0.425 |
| NGC 5005 | | Sy2-L | SAB(rs)bc | 946 | 103 | 10.61 | 0.014 | 0.483 | 39.42 | ho97 | 0.31 | 0.602 | 0.0576 |

Continued on Next Page...

Table 3.1 – Continued

| Galaxy Name (1) | Alternative Name (2) | Spectral Class (3) | Hubble Type (4) | vel. [km s$^{-1}$] (5) | Scale pc/$''$ (6) | B_T [mag] (7) | E(B–V) [mag] (8) | axial ratio (b/a) (9) | $L_{[OIII]}$ (10) | Ref. (11) | FIR [10e11 $L_\odot$] (12) | IRAS $F_{12}/F_{25}$ (13) | IRAS $F_{25}/F_{60}$ (14) |
|---|---|---|---|---|---|---|---|---|---|---|---|---|---|
| NGC 5033 | | Sy1.9 | SA(s)c | 875 | 91 | 10.75 | 0.011 | 0.467 | 39.36 | ho97 | 0.1878 | 0.733 | 0.0789 |
| NGC 5135 | | Sy2 | SB(l)ab | 4112 | 266 | 12.88 | 0.060 | 0.692 | 41.28 | wh92 | 1.599 | 0.270 | 0.153 |
| NGC 5194 | M 51 | Sy2-HII | SA(s)bc pec | 463 | 37 | 8.96 | 0.035 | 0.616 | 39.14 | wh92 | 0.0787 | 0.571 | 0.0744 |
| NGC 5256 | Mrk 266 | Sy2 | Pec | 8353 | 540 | 14.00 | 0.013 | – | 41.08 | wh92 | <2.987 | <0.471 | 0.140 |
| NGC 5273 | | Sy1.9 | SA(s)0 | 1064 | 103 | 12..4 | 0.010 | 0.893 | 39.48 | wh92 | <0.0272 | – | <0.417 |
| NGC 5283 | Mrk 270 | Sy2 | S0? | 3119 | 202 | 14.20 | 0.020 | 0.909 | 41.22 | wh92 | – | – | – |
| NGC 5347 | | Sy2 | (R')SB(rs)ab | 2335 | 151 | 13.4 | 0.021 | 0.765 | 39.96 | sc03 | 0.8233 | 0.315 | 0.639 |
| NGC 5548 | | Sy1.5 | (R')SA(s)0/a | 5149 | 333 | 13.3 | 0.020 | 0.929 | 41.91 | wh92 | 0.35 | 0.474 | 0.731 |
| NGC 5674 | | Sy1.9 | SABc | 7474 | 483 | 13.70 | 0.036 | 0.909 | 41.27 | gu06 | <0.704 | – | <0.24 |
| NGC 5695 | Mrk 686 | Sy2 | SBb | 4225 | 273 | 13.58 | 0.017 | 0.715 | 41.09 | wh92 | <0.152 | – | <0.525 |
| NGC 5728 | | Sy2 | (R_1)SAB(r)a | 2788 | 180 | 12.81 | 0.101 | 0.581 | 41.526 | li88 | <0.352 | <0.395 | 0.096 |
| NGC 5940 | | Sy1 | SBab | 10172 | 658 | 14.32 | 0.041 | 1.0 | 41.30 | wh92 | <0.88 | – | <0.316 |
| NGC 6300 | | Sy2 | SB(rs)b | 1109 | 69 | 10.98 | 0.097 | 0.667 | 39.84 | sp89 | 0.1112 | 0.344 | 0.153 |
| NGC 6814 | | Sy1.5 | SAB(rs)bc | 1563 | 101 | 12.06 | 0.183 | 0.933 | 40.26 | wh92 | 0.0985 | 0.559 | 0.104 |
| NGC 6951 | | Sy2-L | SAB(rs)bc | 1424 | 92 | 11.64 | 0.366 | 0.564 | 38.99 | ho97 | 0.170 | 0.385 | 0.0867 |
| NGC 7130 | IC 5135 | Sy2-L | Sa pec | 4842 | 313 | 12.98 | 0.029 | 0.933 | 41.27 | sp90 | 2.083 | 0.294 | 0.128 |
| NGC 7212 | | Sy2 | Sab | 7984 | 516 | 14.78 | 0.072 | – | 42.34 | wh92 | <1.35 | <0.466 | 0.245 |
| NGC 7319 | | Sy2 | SB(s)bc pec | 6747 | 436 | 14.11 | 0.079 | 0.765 | 41.17 | wh92 | – | – | – |
| NGC 7469 | | Sy1.2 | (R')SAB(rs)a | 4892 | 316 | 13.0 | 0.069 | 0.733 | 41.84 | wh92 | 3.599 | 0.237 | 0.203 |
| NGC 7479 | | Sy2-L | SB(s)c | 2381 | 154 | 11.60 | 0.112 | 0.756 | 38.44 | dG92 | 0.474 | 0.226 | 0.274 |
| NGC 7496 | | Sy2 | (R')SB(rs)bc | 1649 | 107 | 11.91 | 0.010 | 0.909 | 39.60 | gu06 | 0.134 | 0.178 | 0.178 |
| NGC 7674 | Mrk 533 | Sy2-HII | SA(r)bc pec | 8671 | 560 | 13.92 | 0.059 | 0.909 | 42.26 | wh92 | 3.188 | 0.375 | 0.345 |
| NGC 7743 | | Sy2 | (R)SB(s)0+ | 1710 | 111 | 12.38 | 0.070 | 0.867 | 39.60 | ho97 | <0.031 | – | <0.433 |
| UGC 1214 | Mrk 573 | Sy2 | (R)SAB(rs)0+ | 5174 | 334 | 13.68 | 0.023 | 1.0 | 42.30 | wh92 | <0.3358 | <0.363 | 0.630 |
| UGC 1395 | | Sy1.9 | SA(rs)b | 5208 | 337 | 14.18 | 0.075 | 0.769 | 40.89 | wh92 | <0.308 | – | <1.8 |
| UGC 2456 | Mrk 1066 | Sy2 | (R)SB(s)0+ | 3605 | 233 | 13.64 | 0.132 | 0.588 | 41.20 | wh92 | 0.763 | 0.216 | 0.221 |
| UGC 6100 | | Sy2 | Sa? | 8844 | 572 | 14.30 | 0.012 | 0.617 | 41.53 | sc03 | <0.623 | – | <0.426 |
| UGC 12138 | | Sy1.8 | SBa | 7487 | 484 | 14.24 | 0.085 | 0.875 | 41.40 | sc03 | <0.633 | – | 0.477 |
| UM 625 | | Sy2 | S0 | 7492 | 484 | 17.43 | 0.062 | 0.848 | 41.48 | Te91 | – | – | – |

Col. (1): Galaxy name. Col. (2): Alternative name. Col. (3): Spectral class. (LINER = L). Col. (4): Hubble type. Col. (5): Radial velocity. Col. (6): Angular scale calculated from the distance. Col. (7): Total asymptotic magnitude in B, B_T, from RC3 catalogue. Col. (8): Reddening, E(B-V). Col. (9): Axial ratio (b/a). (All these quantities, but the scale, were extracted from NED.) Col. (10): Logarithm of [OIII]λ5007 luminosity in units erg/s. Col. (11): References for column (10); cg94: Cruz-González et al. (1994); da88: Dahari & De Robertis (1988); dG92: de Grijp et al. (1992); fa98: Falcke et al. (1998); fe00: Ferruit et al. (2000); gu06: Gu et al. (2006); ho97: Ho et al. (1997); li88: Lipovetsky et al. (1988); mw88: Morris & Ward (1988); mu96: Mulchaey et al. (1996); ol94: Oliva et al. (1994); os81: Osterbrock (1981); sc03: Schmitt et al. (2003); sp89: Storchi Bergmann & Pastoriza (1989); st90: Storchi-Bergmann et al. (1990); te91: Terlevich et al. (1991); wh92: Whittle (1992); Col. (12): IR luminosity from IRAS fluxes calculated with the formula from Sanders & Mirabel (1996). Col. (13) and (14): IRAS flux ratios, $F_{12}/F_{25}$ and $F_{25}/F_{60}$.

[a] IC4870 is a Wolf-Rayet galaxy

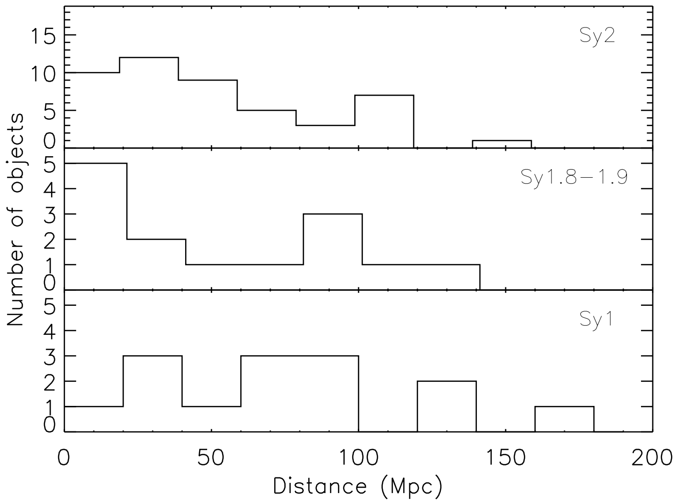

Figure 3.1: The upper, middle and lower panel show the distribution of the distance for the Sy2, Sy1.8-1.9, and Sy1 galaxies, respectively.

In order to understand the possible biases of our sample we compare the general properties of our galaxies with those in two bona-fide samples of Sy galaxies in the literature, the CfA and RSA Seyfert subsamples. From the 48 Sy galaxies in the CfA catalogue presented in Huchra & Burg (1992) (see also McLeod & Rieke, 1995), 24 are in our sample as well. On the other hand, 38 out of 75 of our galaxies belong to the extended RSA Sy sample compiled by Maiolino & Rieke (1995) (sample D in their work). We thus explore 50% of CfA and 42% of RSA, with only 10 of our galaxies occurring in both of them. As CfA has been shown to lack some bright Seyferts, some of which are in our sample, we have used instead the extension to the CfA sample presented in Alonso-Herrero et al. (2003), in which they add a total of nine galaxies previously classified as LINER. From now on we will name these subsamples CfA and RSA respectively. The mean distance, d, of our sample is in between both comparison ones, as $<d_{RSA}>= 34$ Mpc and $<d_{CfA}>$ is three times larger than this (Maiolino & Rieke, 1995), while the mean distance of our sample is $<d>= 57$ Mpc. As in most of the Sy samples in the literature, in our sample Sy1 are, on average, more distant than Sy2. The origin of this bias is that the luminosity of the nucleus compared to the host bulge luminosity is smaller in Sy2 than in Sy1 AGNs. Still, the distance distribution of the galaxies looks homogeneus up to 100 Mpc (Figure 3.1). The standard deviation of the distribution is 41 Mpc, indicating that the range of distances is quite large. With ACS we are able to achieve a much better resolution than any ground-based study. The scale of our images ranges from less than 1 $\mathrm{pc\,pixel^{-1}}$ for the nearest objects to about 20 $\mathrm{pc\,pixel^{-1}}$ for the furthest, with a mean value of 6 $\mathrm{pc\,pixel^{-1}}$.

We have checked for possible bias in the distribution of Hubble types among different types of Sy. This is plotted in Figure 3.2. Peculiar galaxies and those classified as uncertain, are excluded. As it is widely known, Seyfert nuclei are found mostly in spiral galaxies, with preference for early types (see e.g. Moles et al., 1995, and references therein). The histograms do not seem to differ much. In Figs. 3.3 and 3.4 we have plotted a comparison of CfA and RSA samples, finding a good agreement between our sample and the ones we have used for comparison. In order to quantify both statements above, we used the de Vaucouleurs classification from RC3 catalogue (T), that is S0$= -1$, S0a$= 0$, Sa$= 1$, Sab$= 2$, etc. The resulting mean, median and standard deviation of the spiral types for our sample and the comparison ones are summarised in Table 3.2. Our three subsamples of Seyfert activity show quite similar values of mean and median T. This is enough to ensure that the differences we find among groups of activity type do not arise from differences in the Hubble morphology. Applying the same classification to the other samples we get a good matching with our own sample, although CfA galaxies tend to be of a bit earlier type.

Table 3.2: Statistics of Hubble Type; comparison among samples

| | **Sample** | | | **RSA** | | | **CfA** | | |
|---|---|---|---|---|---|---|---|---|---|
| | mean | median | $\sigma$ | mean | median | $\sigma$ | mean | median | $\sigma$ |
| **Sy1** | 1.6 | 2 | 2.3 | 2.0 | 2 | 2.0 | 1.3 | 1 | 1.9 |
| **Sy1.8-1.9** | 2.8 | 3 | 2.6 | 2.8 | 3 | 2.6 | 2.2 | 1 | 3.3 |
| **Sy2** | 2.4 | 2 | 2.3 | 2.0 | 2 | 2.2 | 2.1 | 3 | 2.0 |

The table shows the mean, median and standard deviation of Hubble type for each subsample, following a de Vaucouleurs classification. All the subsamples are represented, on the mean, by early type spirals (Sa=1, Sab=2, Sb=3, etc.)

Finally, we have obtained the distribution of the axial ratio, that is, the minor over the major axis of the galaxy (b/a). This gives an idea of the inclination angle of the galaxy, with high values for objects seen nearly face-on, and low values for edge-on ones. Due to internal galactic absorption more objects with high b/a are expected, leading to a power law distribution for a magnitude-limited sample (Maiolino & Rieke, 1995). Thus, most samples, including ours, are biased against edge-on galaxies. In Figure 3.5 we plot the distribution of the axial ratio for the three samples. Ours is in between the less biased RSA and the CfA (more affected by this effect). This happens naturally because our sample has a mean distance in between the other two. Maiolino & Rieke (1995) find that Sy1 tend to occur more often in face-on than the intermediate type Sy. Within our data also a slight trend in the distribution of Seyfert activity with inclination is observed (Figure 3.6). This effect is not very severe, as the median value of b/a does not change much among groups, with 0.85 for Sy1, 0.75 for Sy1.8-1.9 and 0.75 for Sy2 galaxies.

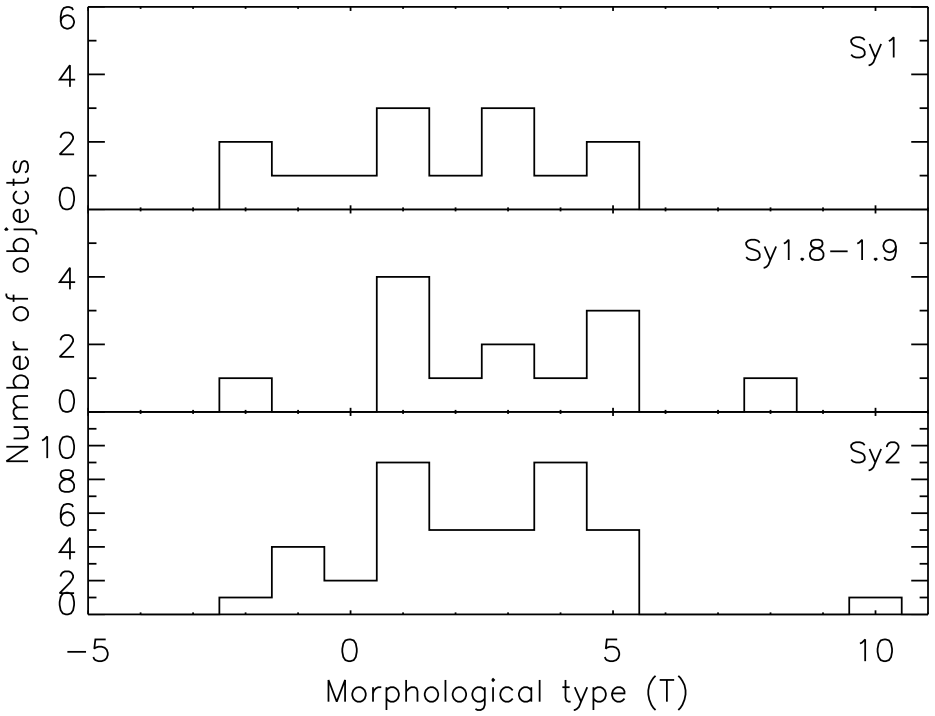

Figure 3.2: Distribution of Hubble types for the different subsamples of Sy activity class. The de Vaucouleurs classification (T) is used: e.g. S0=–1, S0a=0, Sa=1, Sab=2, Sb=3, etc. The T $< -1$ stand for ellipticals. The three subsamples are equivalent on average and median values.

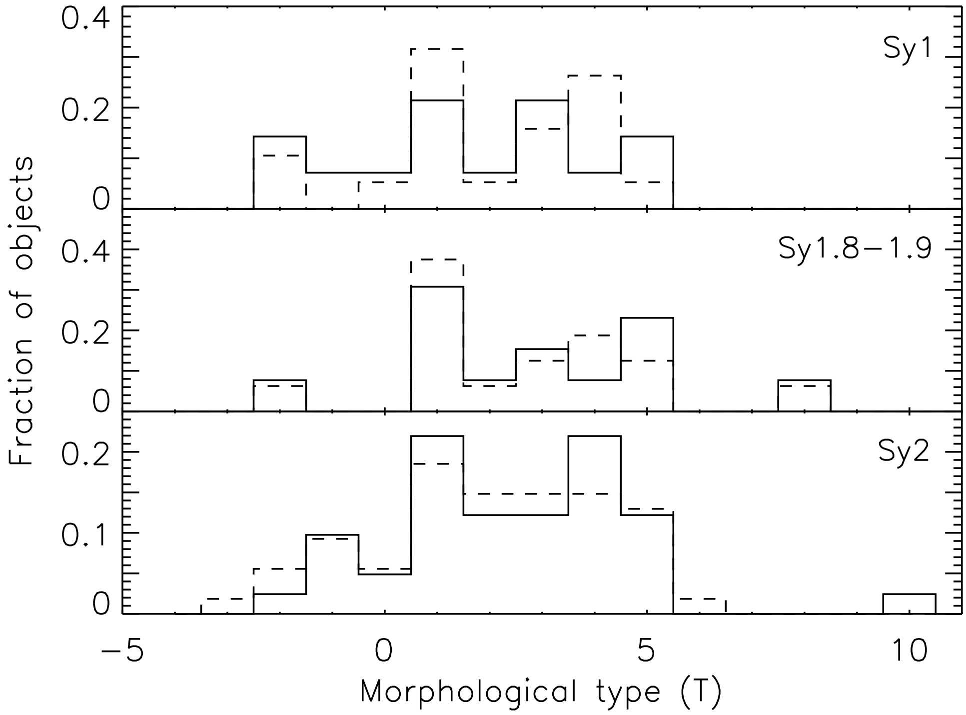

Figure 3.3: Comparison between the distribution of morphological types of our sample (full lines) and the RSA sample (dashed lines). The histograms do not differ much. On average both samples are equivalent (see discussion in text).

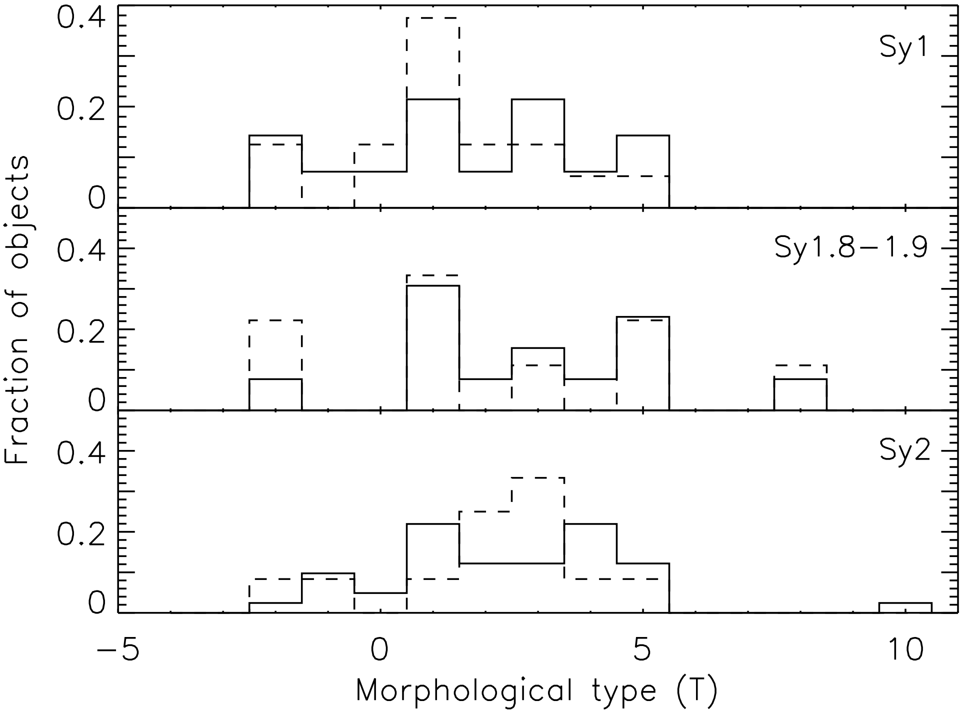

Figure 3.4: Same comparison as in Figure 3.3 for our sample (full lines) and CfA galaxies (dashed). The two distributions are very similar as well.

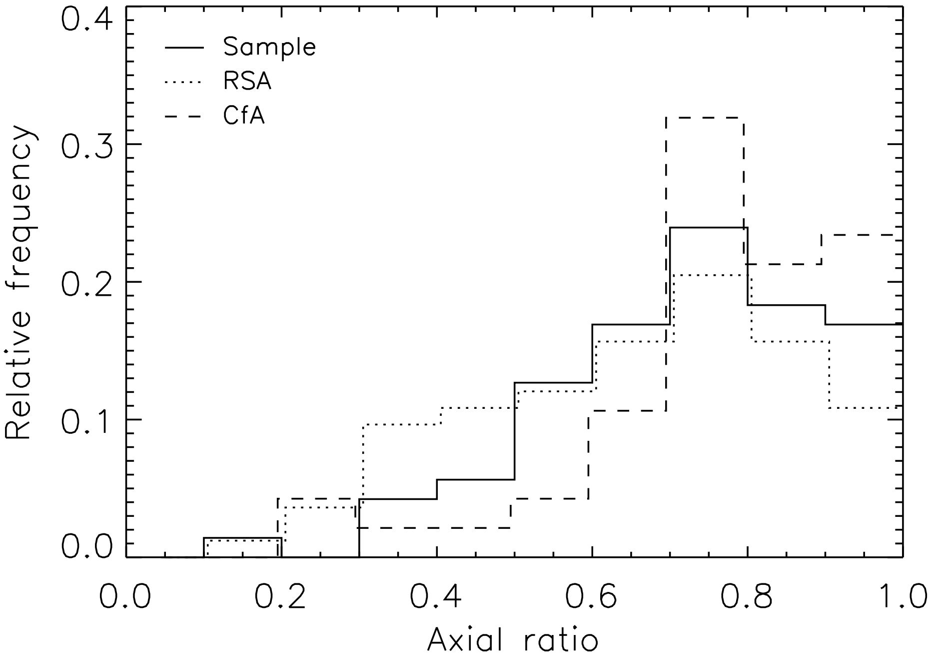

Figure 3.5: Compared histogram of the axial ratio (b/a) of the galaxies of the three different samples. Numbers are relative to the total number of objects in each sample. Our sample seems to lay in between the CfA and the RSA, and it is less biased against edge-on galaxies than CfA.

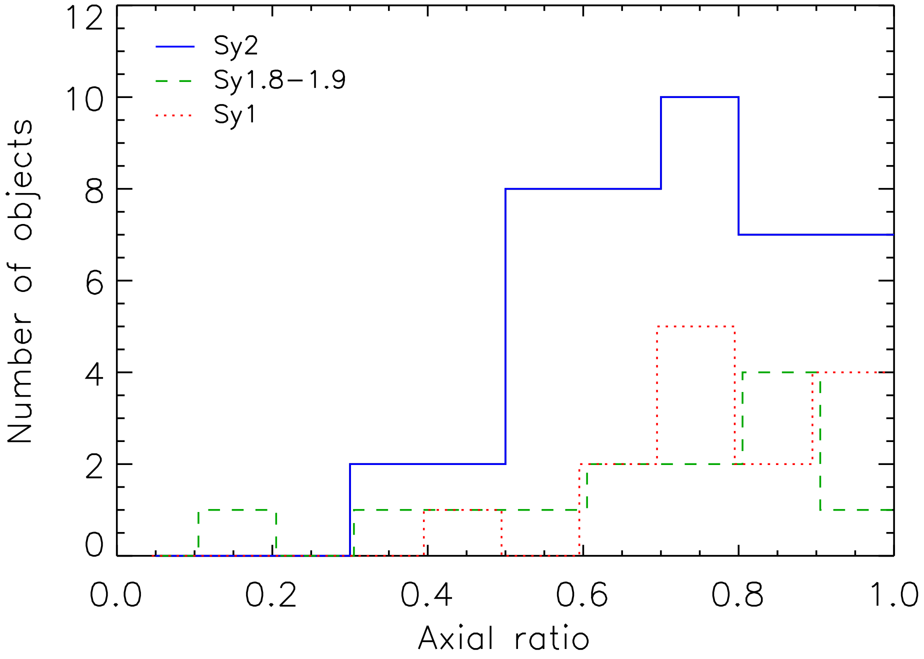

Figure 3.6: Distribution of the axial ratio (b/a) for the three activity classes. The typical trend of less objects at low inclinations is seen for this sample, although no clear trend with Sy type is observed.

### 3.2.3 Observations and data reduction

The sample was imaged with the Advanced Camera for Surveys (ACS) in its high resolution configuration (HRC), which provides a pixel size of 0.025 arcsec. The filter chosen is F330W, that from the UV filters of ACS, has the highest throughput, negligible red leak and minimal contamination by line emission. A higher red leak, as that from F220W, would result in a higher background level with lower S/N detection for young star clusters. The filter F330W has a bandwidth of $\sim 400$ Å centred around 3300 Å, therefore the only strong emission lines contributing to this filter are [NeV]$\lambda\lambda$3346,3426. This type of emission will be normally extended, thus is not a problem for measuring compact objects such as clusters (see Section 3.4.4).

To allow an easier removal of cosmic rays (CRs) two exposures of 10 min each where made for a total of 1200 s. For 19 of the brightest galaxies the exposure was further split in 1140 s and 60 s exposures, in order to be able to study the possible saturated core. In these cases we have used the longest exposure when possible, for this part of the work. The only exceptions are NGC 7212 and NGC 5728, that have 2550 s exposure.

We downloaded the images from the HST archive with the calibration 'on the fly' option, that corrects the images with the most up-to-date ACS reference files and bad pixel tables, and corrects for geometric distortion. Also the most severe CRs are rejected and the exposures combined in a single image. The final products are both astrometrically and photometrically accurate. The pipeline CRs removal task uses very mild values for the parameters, avoiding to remove by mistake the centre of bright stars or galactic nuclei. We found that many of the images had conspicuous artifacts, such as CRs that were not removed by the pipeline. We tried out several IRAF tasks for the identification and removal of the CRs. Due to the small FWHM of the PSF (1.8 pix) and the low S/N in some of the images we could not get a satisfactory result with these routines. Finally we had to remove the artifacts by hand from the region of interest, after comparing the images with those from WFPC2 to help us to discern the CRs from small star clusters.

The background for every object was determined with the IRAF task FITSKY. The mean value and the standard deviation of the background ($\sigma_s$) was measured from several apertures in the outer regions of the image. The values of $\sigma_s$ have a very low scatter (0.004-0.005 counts $\mathrm{s}^{-1}$) due to the constant instrumental configuration and the similar exposure time in different images. The larger scatter of the background values (from 0.0015 to 0.005 counts $\mathrm{s}^{-1}$, equivalent to 21–22.5 mag/arcsec$^2$) suggests that in some cases this is not a real sky determination, but background light from the galaxy itself. As an example of this there are some cases in which the galaxy fills the field of view (e.g. M81).

When imaging very bright objects, as some Seyfert nuclei, the possible effects of saturation have to be accounted for. The detector can reach physical saturation when more charge is released in a single pixel than what it can accumulate, resulting in charge being spilled to adjacent pixels and some flux getting lost. In particular, the default gain value of the HRC chip falls short of sampling the full well depth (∼165,000 $e^-$) by some 22%. There are 11 objects that overcome this threshold. The core-saturated objects are: Mrk 231, NGC 3227, NGC 3516, NGC 4593, NGC 5548, NGC 7469, UGC 12138 (with a 60s image), and Mrk 493, Mrk 915, NGC 5273, NGC 6814 (without a 60s image). In the case of the objects with a 60s image the correction to be made can be calculated by comparing the photometry between the long and short exposures. See below for further discussion.

## 3.3 Visual Atlas and object description

Figs. 3.7–3.9 show the images of the central near-UV emission of all the galaxies in the sample. We have chosen the field of view and scaling in order to enhance the most interesting features. In addition, for some galaxies we show a nuclear close-up in Figure 3.10. We have divided the objects in Seyfert types, in order to better appreciate the common characteristics of each type. In the Appendix A we compile the images of the whole HRC field of view for all the objects. Many have useful morphological information of the Kpc scale, and serve as a complement of this section.

The morphology of the objects is as irregular as varied. There are many different features within the sample: star-forming rings, spirals, clumpy diffuse light emission, plain PSF-dominated objects, complete lack of compact nucleus, etc. From the figures it can be seen that every Sy1-1.5 possesses a bright star-like nucleus, which precludes the observation of the inner morphology. In several cases regions of star-formation and rings can be seen in the images as well. The morphology of intermediate type Sy is more varied. Some objects have a compact nucleus. The morphology can be clumpy or diffuse, and some objects show dust absorption features or ionization cones. For the Sy2 galaxies the morphology is mostly clumpy, with frequent star-formation regions. These are often arranged in rings or spiral arms. There are some objects showing instead a biconical or symmetrical structure as ionization cones. When a very bright nucleus is present, as in the images of galaxies from Sy1 to Sy1.9, some artifacts may appear, such as inner rings or clumps very close to the nucleus. These are caused by the instrumental PSF, that shows not only the diffraction spikes, but also clumpy ring-like wings that can be confused with actual star-forming rings (e.g. see image of Mrk 42, Mrk 493 or Mrk 915).

In the next subsections, we comment on the main morphological components of these galaxies, offering a brief description and notes on individual objects. The descriptions refer to the F330W images unless it is said otherwise.

### 3.3.1 Individual description of Seyfert 1, 1.2 & 1.5

- **Mrk 6:** This object is a Sy1.5 with a very bright saturated core with some extended emission around.

- **Mrk 40:** This galaxy shows just a plain point-like bright source.

- **Mrk 42:** A very bright compact nucleus with a very tight wound spiral of star formation of ∼300 pc of radius. Many stellar clusters are individually resolved.

- **Mrk 231:** This is a very powerful galaxy with a bright nucleus and some diffuse circumnuclear emission. There is an arc of star formation about 2 Kpc to the south. This object falls next to the limit of its classification as a Quasar, and is also an IRAS galaxy, very luminous in the FIR (e.g. Soifer et al., 1987). It shows as well a powerful megamaser emission first detected by Baan (1985).

- **Mrk 493:** Its morphology resembles that of Mrk 42, with a very bright nucleus and a tight wound spiral of star formation. However, the distance to this object is 50% higher than the distance to Mrk 42, so the individual stellar clusters are poorly resolved.

- **Mrk 915:** This galaxy is a prototypical Sy1, with a very bright nucleus surrounded by diffuse emission.

- **NGC 3227:** This Sy1.5 shows a bright saturated nucleus and an off-centered bar of star forming regions, which is misaligned with the main galactic bar. This feature is probably caused by a close interaction with the dwarf elliptical NGC 3226. There is a star forming region 100 pc to the north that is also visible in [OIII] images (Schmitt & Kinney, 1996). X-ray variability from its nuclear source has also been reported (Gondoin, 2004).

- **NGC 3516:** There is diffuse light surrounding the bright nucleus of this galaxy up to several hundred pc away. There is also evidence of obscuration by dust to the south and to the north of the nucleus. The northern dusty patches trace a spiral pattern.

- **NGC 4253:** This is a barred spiral with several bright star-forming knots and star clusters. An important part of the star formation seems to be associated to the east part of the bar. The bar itself is visible in the UV image.

- **NGC 4593:** Apart of the bright nucleus, there is a spiral structure of 1 Kpc width with many individually resolved star clusters.

- **NGC 5548:** This is a face-on spiral with a very bright nucleus. Several hundred parsecs to the north of the nucleus there is an arc of star formation, plus several scattered and relatively isolated stellar clusters still further away.

- **NGC 5940:** This is a face-on barred spiral with many star clusters and star forming regions tracing the bar and spiral arms. Due to the combination of size and distance, most of this structure is included in the ACS-HRC field of view.

- **NGC 6814:** In this image there is not much visible apart of the plain PSF of the nucleus and some faint structure of the outer face-on spiral.
- **NGC 7469:** This is very interesting object, with a faint spiral that becomes a conspicuous ring of star formation in the inner some hundred pc. Many stellar clusters are individually resolved within this region.

### 3.3.2 Individual description of Seyfert 1.8 & 1.9

- **Mrk 334:** This is a peculiar-HII galaxy with irregular nuclear structure, and strong star formation. It is also a strong IR source.
- **Mrk 471:** It is very obscured by dust. The UV image shows only a point-like nucleus and many scattered star-forming blobs and star clusters. In the optical image the barred spiral structure is better distinguished, with many dust lanes tracing the bar.
- **Mrk 516:** This galaxy is classified as a Sc. Although it looks quite regular in the IR, at the U band is clearly asymmetric, with a star-forming arm to the south that has not counterpart to the north. The nucleus, that looks double in WFPC2 image, is at the limit of the resolution and clearly separated from a bright blob right next to the north (∼100 pc).
- **NGC 2639:** The nucleus is heavily obscured and no compact source is seen in the images. However, the main spiral structure is visible, with many stellar clusters in the outer region (several Kpc away from the centre).
- **NGC 3031 (M81):** This is the largest galaxy of one of the nearest groups. It is a typical Sa, with a big bulge that fills the whole field of view of the camera. Some dust lanes are seen in the inner region, although no young star clusters are clearly visible in the UV image. Ho et al. (1995) describe it as a LINER.
- **NGC 3786:** This galaxy shows a nuclear ring of a few hundred pc radius in HST optical images that is incomplete in the UV. An ionization cone coming from the compact nucleus, to the southeast, is clearly detected.
- **NGC 4258 (M106):** The compact nucleus is resolved in our observation. There are many stellar clusters that can be studied individually, and there is a vast amount of absorption by dust in the southwest half of the image. This galaxy hosts a water masing disk that led to the second best determination of the mass of a super-massive black hole (SMBH), after the one in the Milky Way (Miyoshi et al., 1995).
- **NGC 4395:** This is one of those objects for which the nucleus is at the limit of resolution. It is the object of the latest Hubble type in our sample (Sm). With such a small contribution of the bulge, only several scattered stellar

clusters are seen apart from the nucleus and a region of diffuse light 10-20 pc to the west of it.

- **NGC 4565:** This is a nearby edge-on galaxy. The nuclear region is thus very obscured at this wavelength with neat dust absorption. The nucleus appears partially resolved.

- **NGC 5033:** The galaxy shows an unresolved nucleus together with an ionization cone open to the east (see Mediavilla et al., 2005). Heavy absorption to the west may be responsible for this asymmetry. There is an interesting feature consisting in a bright bar of light coming from the nucleus and extending 2 arcsec to the north. This might be scattered light from the AGN or part of the Extended Narrow Line Region.

- **NGC 5273:** This is a lenticular galaxy with the typical morphology of an early type galaxy. It shows a point-like nucleus with extended light emission within the central 100 pc. There are some bright areas and dark lanes. The morphology seen with F606W is very similar, suggesting that the dark lanes are caused by thick dust clouds.

- **NGC 5674:** Although classified as barred spiral in the RC3 catalog, this galaxy clearly shows a ring in UV light. The nuclear morphology is very interesting, with several clumps and stellar clusters embedded in a diffuse emission in the central few hundred pc.

- **UGC 1395:** This object shows a partially resolved nucleus and a circular shell of ∼200 pc radius.

- **UGC 12138:** It shows a bright point-like nucleus and diffuse emission adjacent to the north. To larger scales (several Kpc) it shows a faint filamentary structure.

### 3.3.3 Individual description of Seyfert 2

- **CGCG 164-019:** This Sy2 galaxy shows a bright nucleus and a wide open spiral pattern. Some star clusters and knots are visible within the inner Kpc region, as well as diffuse light that might come from an unresolved stellar component.

- **Circinus:** This is a nearby spiral with a heavily obscured nucleus. The most prominent feature is a central ring of diffuse light and a star-forming blob 200 pc to the south. The galactic latitude of this object is very low, so the image may suffer from foreground stars contamination. This galaxy is known to host a nuclear water masing disk in a sub-parsec scale (Greenhill et al., 2003) and to have a kiloparsec scale ionization cone (Marconi et al., 1994).

- **ESO 103-G35:** No compact nuclear source is seen in the UV image, but only diffuse light and some blobs. The nuclear region is crossed by dust lanes, what gives it its chaotic structure.

- **ESO 137-G34:** Neither the UV nor the optical image show an evident nucleus for this object. It has a patchy and chaotic structure with abundant dust lanes and some bright blobs. It is by far the worse contaminated object in the sample by foreground stars, what results evident from the WFPC2 image. With a scale plate of 5 $\mathrm{pc\,pixel^{-1}}$ it is difficult to distinguish a star cluster from a foreground star.

- **ESO 138-G1:** It has a compact nucleus close to our limit of resolution, and a bright asymmetric circumnuclear zone of diffuse light. The east part looks like an ionization cone or scattered light from the AGN.

- **ESO 362-G8:** This object shows extended light emission around its resolved nucleus, with dusty patches. No stellar clusters or blobs are seen in the circumnuclear region.

- **Fairall49 (IRAS1832-594):** Within the central Kpc, this object shows a wound spiral that ends up in an asymmetric ring of star-forming knots. Several separated star clusters are seen, as well as a bright resolved nucleus. Malkan et al. (1998) found a non-resolved nuclear source in the IR. We can resolve the nucleus in our UV image. Maiolino & Rieke (1995), have reclassified it as a Sy1.8, although we have considered here the traditional classification as Sy2.

- **IC 2560:** A dust spiral is better seen in the optical images. In the UV an irregular extended emission surrounds the resolved nucleus.

- **IC 4870:** Some extended filaments as well as a lot of faint star clusters are seen in this nucleus. There are also some bright clusters and a very bright point-like source in the center. This object may be in fact an extragalactic HII region with an unusually high ionization lines (Malkan et al., 1998), and the point-like source might actually be a field star.

- **IC 5063:** It shows very bright compact but resolved blobs within the nuclear region and some bright filaments along the southeast-northwest direction. Those could be scattered light from the AGN.

- **Mrk 461:** This galaxy shows a resolved nucleus and a faint spiral structure of some Kpc wide.

- **Mrk 477:** This compact galaxy hosts a very luminous Sy2 nucleus that has been proved by spectropolarimetry to have a hidden Sy1 (Tran et al., 1992a). Heckman et al. (1997) have shown that it hosts a very compact nuclear starburst. The galaxy is interacting with a companion 50 arcsec to the north.

The nucleus is extended and it shows a bright blob close to the northeast. There is as well an arc of star formation further, in the same direction.

- **Mrk 1210:** This is a compact face-on spiral. The tight wound spiral structure is visible in our image more like a ring, as traced by star forming regions. The bright nucleus appears double at close inspection. Tran et al. (1992a) showed, by spectropolarimetry, the presence of a hidden BLR.
- **NGC 449:** This object shows a bright resolved nucleus and several stellar cluster and knots. Star forming regions and dust lanes trace a highly inclined spiral.
- **NGC 1144:** It belongs to an interacting pair of galaxies (NGC 1143/1144). It shows a very distorted spiral structure with a circumnuclear ring traced out by dust lanes and bright regions. The nucleus is crossed by dark patches of dust.
- **NGC 1320:** Although resolved, it possesses a bright compact nucleus. Most of the light is confined to a region of less than 100 pc wide. There is also a remarkable bright and narrow filament extending to the north-west. Dust lanes and extended emission trace a tight spiral patter, although no stellar clusters are clearly detected in our image.
- **NGC 1672:** This barred spiral harbors a very intense starburst within the inner Kpc. Many bright stellar clusters are individually resolved in the near-UV image. The star formation is mostly arranged in a ring, inside which there is also an extended diffuse emission. The dust distribution seems completely asymmetrical, with heavy absorption to the north-east half of the nuclear region.
- **NGC 3081:** This is a peculiar ringed-galaxy, with two nested rings, the smaller of which is shown in our F330W image. It has a bright resolved compact nucleus, with a bright ionization cone extending to the north. There is as well an important star forming region ∼300 pc to the south-east of the nucleus.
- **NGC 3362:** Many stellar clusters and star forming regions trace out a wide open spiral pattern. The nucleus is resolved, elongated and have an extension to the west in the form of a bright filament.
- **NGC 3393:** Kondratko et al. (2006) have recently detected signatures of a water masing disk in the sub-parsec scale, around the central SMBH. The image shows an s-shaped bright symmetric filament, what seems to be an ionization cone from the central engine.
- **NGC 3486:** This is a border-line object between Seyfert and LINER, classified as Sy2 by Ho et al. (1997). It has a bright nucleus and an extended emission with dust patches spiraling inwards.

- **NGC 3982:** Although this galaxy was classified as ringed in the RC3 catalog, in our Hubble images this feature results clearly identified as a spiral of star-forming regions, star clusters and dust lanes.

- **NGC 4303 (M61):** It has been reclassified as a Low Luminosity AGN, although in the original proposal was included as Sy2. The nucleus is known to host a compact star cluster as the main source of ionizing radiation (Colina et al., 2002). This nucleus is unresolved in our F330W image. It posses a conspicuous star-forming ring at ∼250 pc radius, with many clusters individually resolved.

- **NGC 4725:** The nuclear morphology of this early type spiral shows not many features apart of the bright resolved nucleus surrounded by an extended emission with a clear exponential profile.

- **NGC 4939:** The most noticeable feature of this nucleus is a biconical ionization structure coming out from the central source.

- **NGC 4941:** It shows an extended emission crossed by dark dust lanes. The nucleus has a compact clumpy structure with a bright compact core.

- **NGC 5005:** The nucleus has both clumpy and diffuse emission, with a very broad dust lane obscuring the north part of the image. An spiral arm is visible to the south with several isolated star clusters and richer star-forming regions.

- **NGC 5135:** This is a nice example of a very strong nuclear starburst, with many bright star clusters individually resolved and two wide open spiral arms, traced by star-forming regions.

- **NGC 5194 (M51):** The nucleus is completely obscured and surrounded by a bright extended emission and crossed by dark dust lanes. The inner several hundred parsecs show some few isolated star clusters, while the outer regions are richly crowded with clusters and star-forming regions.

- **NGC 5256:** This object is in fact a merging system with a double nucleus separated by ∼5 pc. We have studied the northeastern nucleus, that is outstandingly brighter in our near-UV image than its southwestern companion. Actually, this nucleus has been classified as a LINER in the literature (Osterbrock & Dahari, 1983). The structure of the nucleus is compact, clumpy and irregular.

- **NGC 5283:** The nucleus is bright and clumpy, with several almost adjacent objects. It shows filamentary structure of gas extending from the nucleus to the northeast.

- **NGC 5347:** This is a ringed and barred spiral, although in our image only the inner 100 pc are distinguishable. The nucleus is very bright and conical opening to the northeast. There is also an extended and quite homogeneous emission more obvious to the north side of the nucleus.

- **NGC 5695:** The nucleus is compact but resolved, with a blob 0.2 arcsec to the north. There is a faint diffuse emission around it that follows a de Vaucouleurs profile.
- **NGC 5728:** This is peculiar galaxy with a neatly distorted ring of star-forming regions. The nucleus is completely obscured and it shows an obvious ionization cone opening to the east.
- **NGC 6300:** This galaxy is heavily obscured, so only a faint diffuse emission can be appreciated in our image.
- **NGC 6951:** This object shows a very regular ring of star-forming regions and stellar clusters. Inside the ring the surface brightness remains constant. The nucleus is diffuse and extended, with a couple of brighter blobs.
- **NGC 7130:** It shows an interesting morphology, with a ring and an inner bar. It is very rich in star-forming knots and stellar clusters, with a very bright region that is off-center the ring. We have chosen as the galaxy center the centroid of the brightest of these blobs. The morphology of the center in F330W coincides with that of F210M presented in González Delgado et al. (1998).
- **NGC 7212:** This galaxy belongs to a compact group of interacting galaxies. Spectropolarimetric studies have shown the presence of a hidden BLR (Tran et al., 1992a). It shows a clumpy nuclear morphology and irregular diffuse emission.
- **NGC 7319:** This object has the lowest measured UV flux in the sample. The nucleus is faint and shows an ionization cone opening to the north.
- **NGC 7479:** The nucleus is small and resolved and there are some scattered star clusters throughout the field of view. It is remarkable a chain of bright clusters 5 arcsec to the south of the nucleus, that has a north-south alignment.
- **NGC 7496:** This barred spiral hosts a very powerful starburst in its center. In the image many star clusters can be seen embedded in a diffuse emission. The center has been chosen as the brightest object in the field.
- **NGC 7674:** An obvious spiral structure with many star-forming regions. The nucleus is very bright and embedded in a extended diffuse emission and surrounded by an arc of star formation.
- **NGC 7743:** This galaxy is classified as an SB, although in our near-UV image no signs of the spiral structure can be detected. The nucleus is bright and it is surrounded by a diffuse emission that appears brighter to the south.

- **UGC 1214:** The nucleus is very bright and is is surrounded by a Kpc-scale symmetrical structure that seems to be an ionization cone.

- **UGC 2456:** It has a bright clumpy nucleus and S-shaped extended emission with three bright stellar clusters in it.

- **UGC 6100:** Although the S/N in the image is low, a spiral pattern with several star-forming regions is detected. The nucleus is extended and diffuse.

- **UM 625:** This galaxy has a very bright compact nucleus that is partially resolved in our image. It also possesses a bright star cluster ∼150 pc directly to the west. Apart from this, the emission is diffuse and compact, as most of the light is enclosed within 1 arcsec from the nucleus.

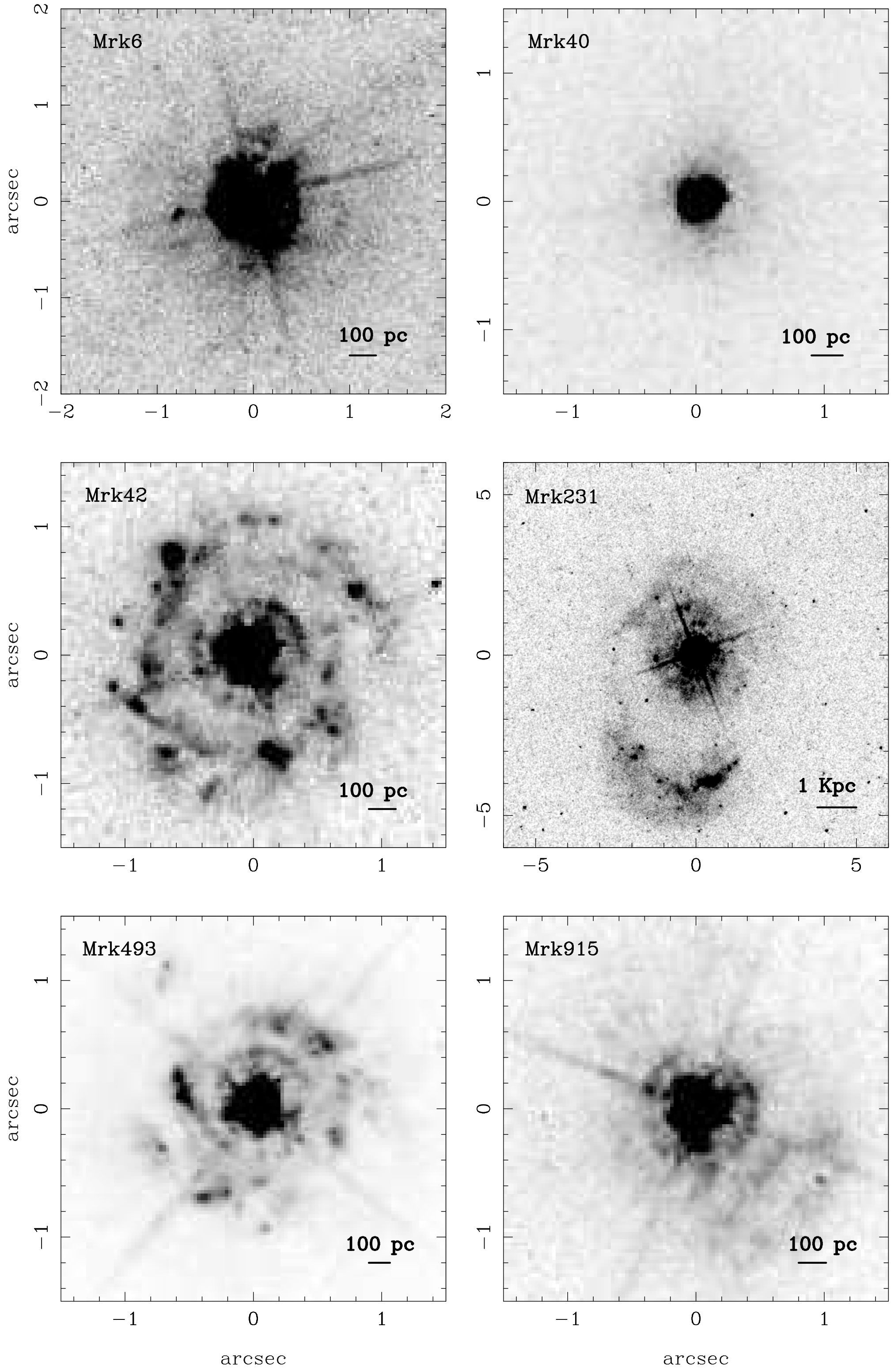

Figure 3.7: Images of the Sy1 galaxies of the sample. The field of view and contrast is chosen to show the most interesting parts and structure of every object. North is up and East to the left in all the figures.

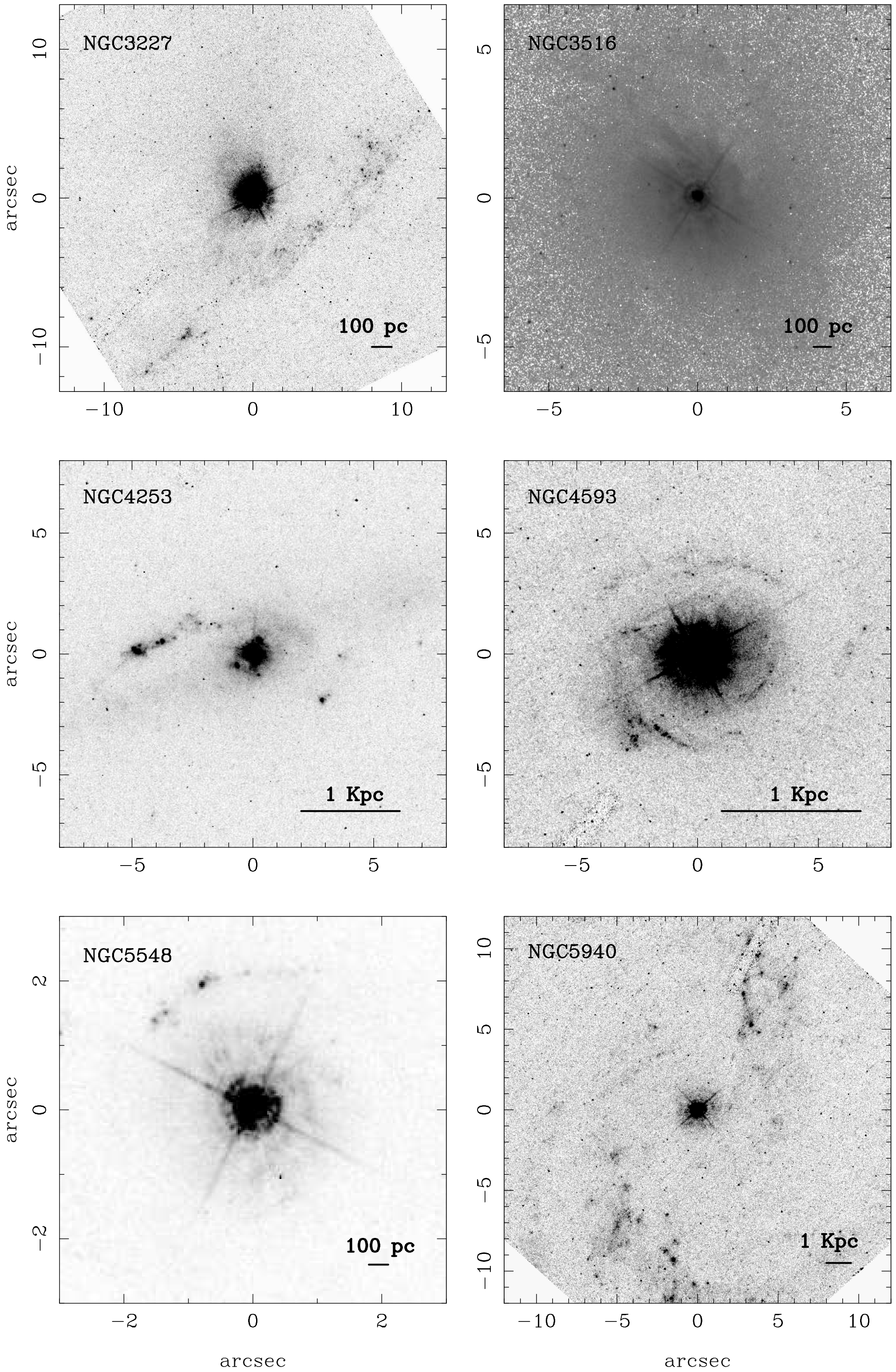

Figure 3.7: Images of the Sy1 galaxies of the sample –continued

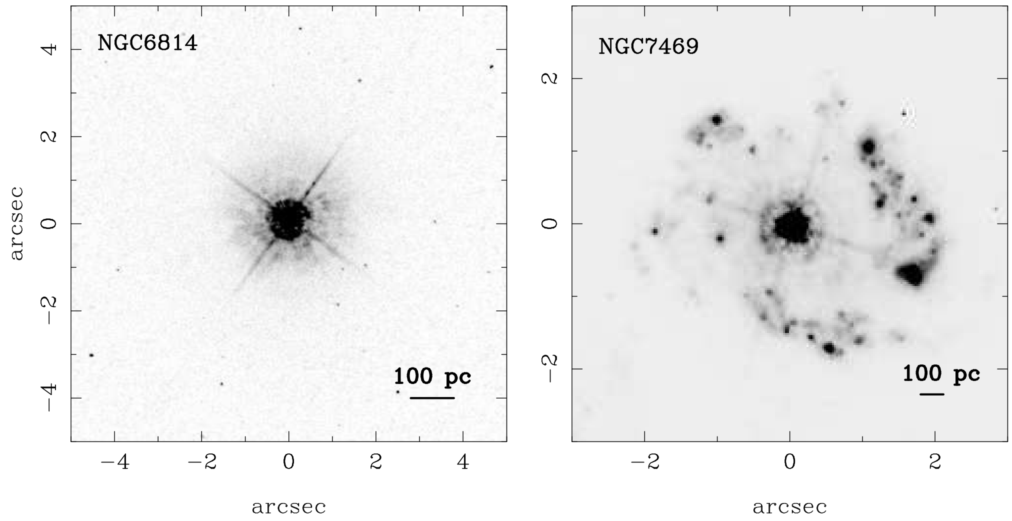

Figure 3.7: Images of the Sy1 galaxies of the sample –continued

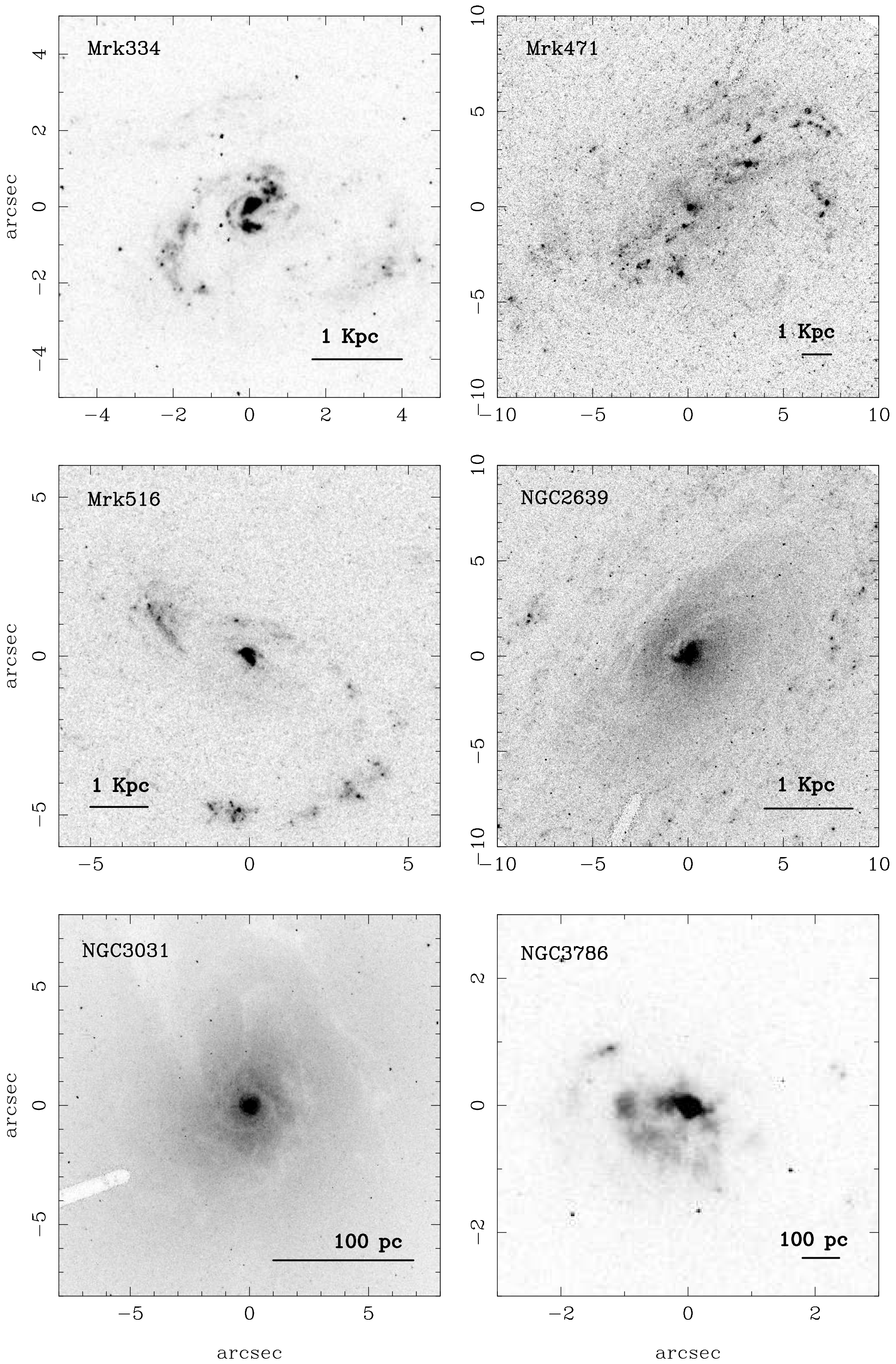

Figure 3.8: Images of intermediate Sy type galaxies (Sy1.8-1.9)

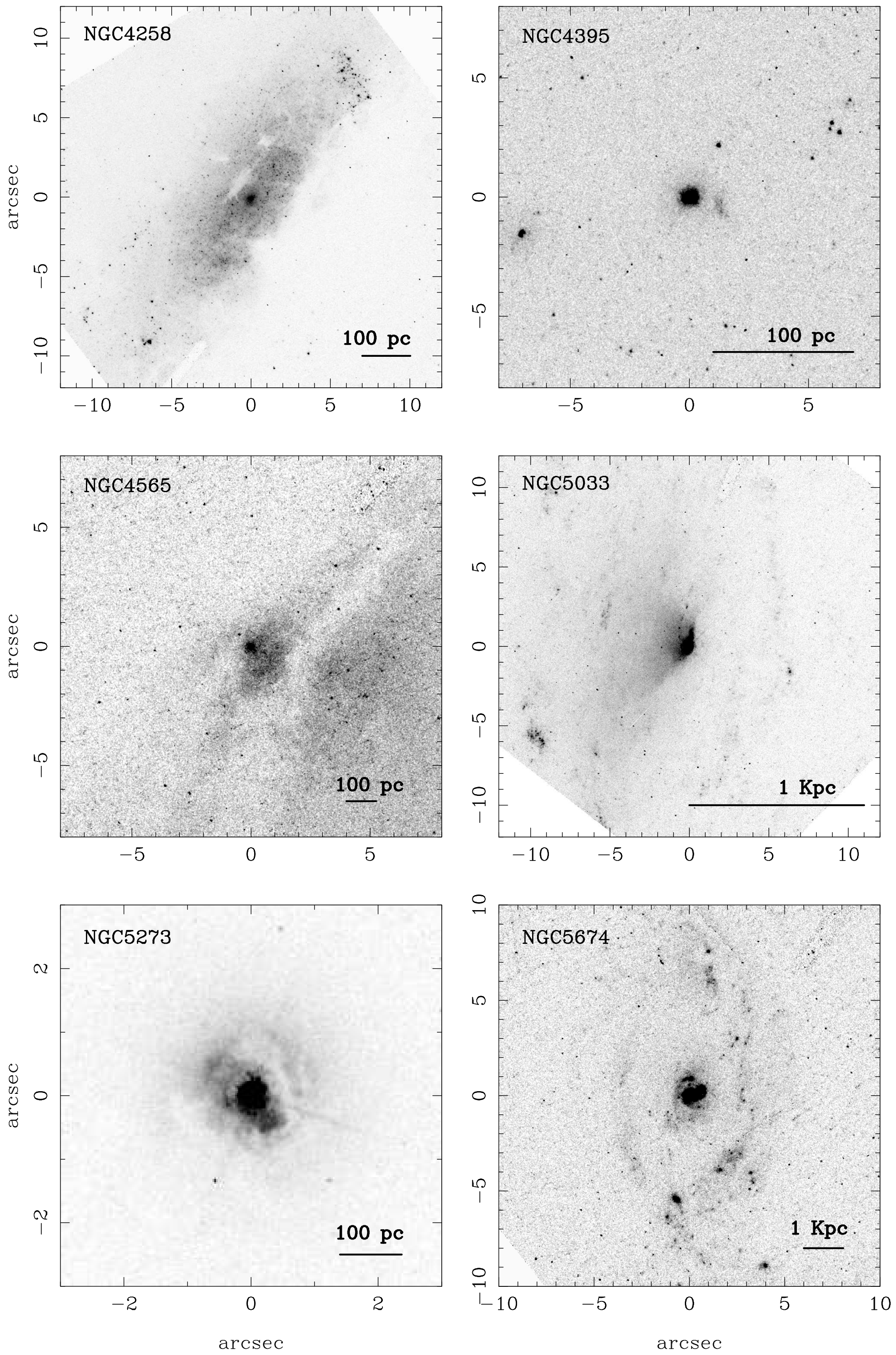

Figure 3.8: Images of Sy1.8-1.9 galaxies –continued

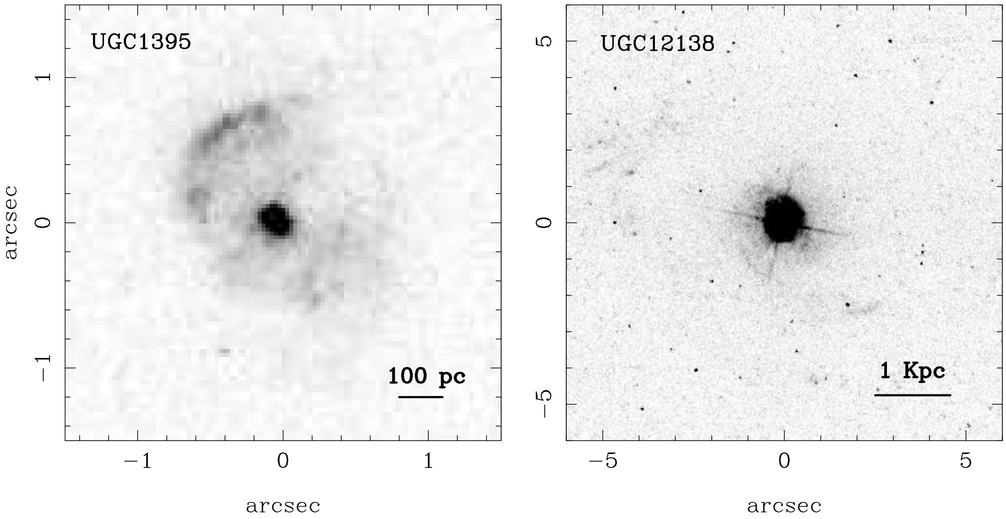

Figure 3.8: Images of Sy1.8-1.9 galaxies –continued

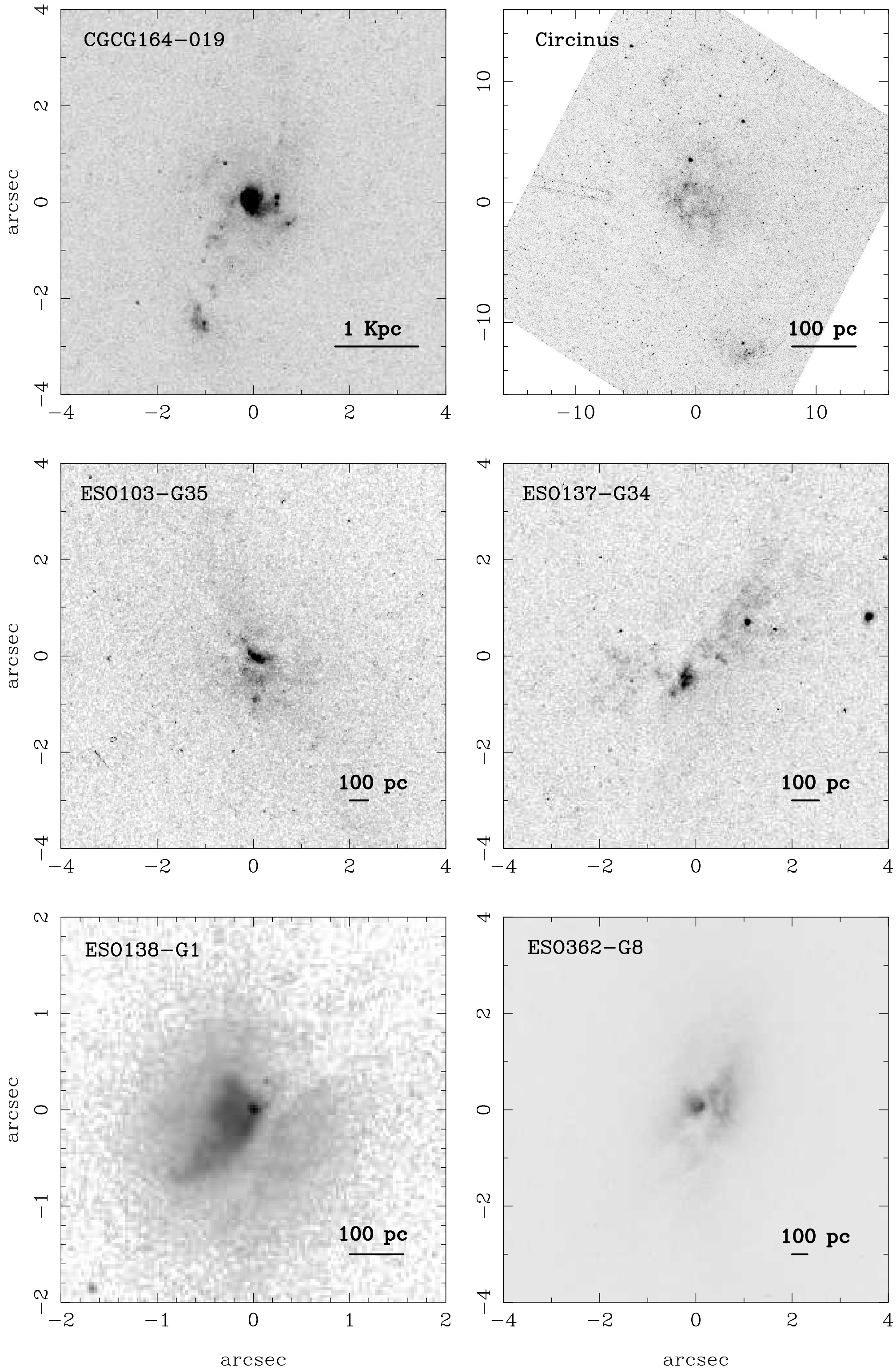

Figure 3.9: Images of the Sy2 galaxies

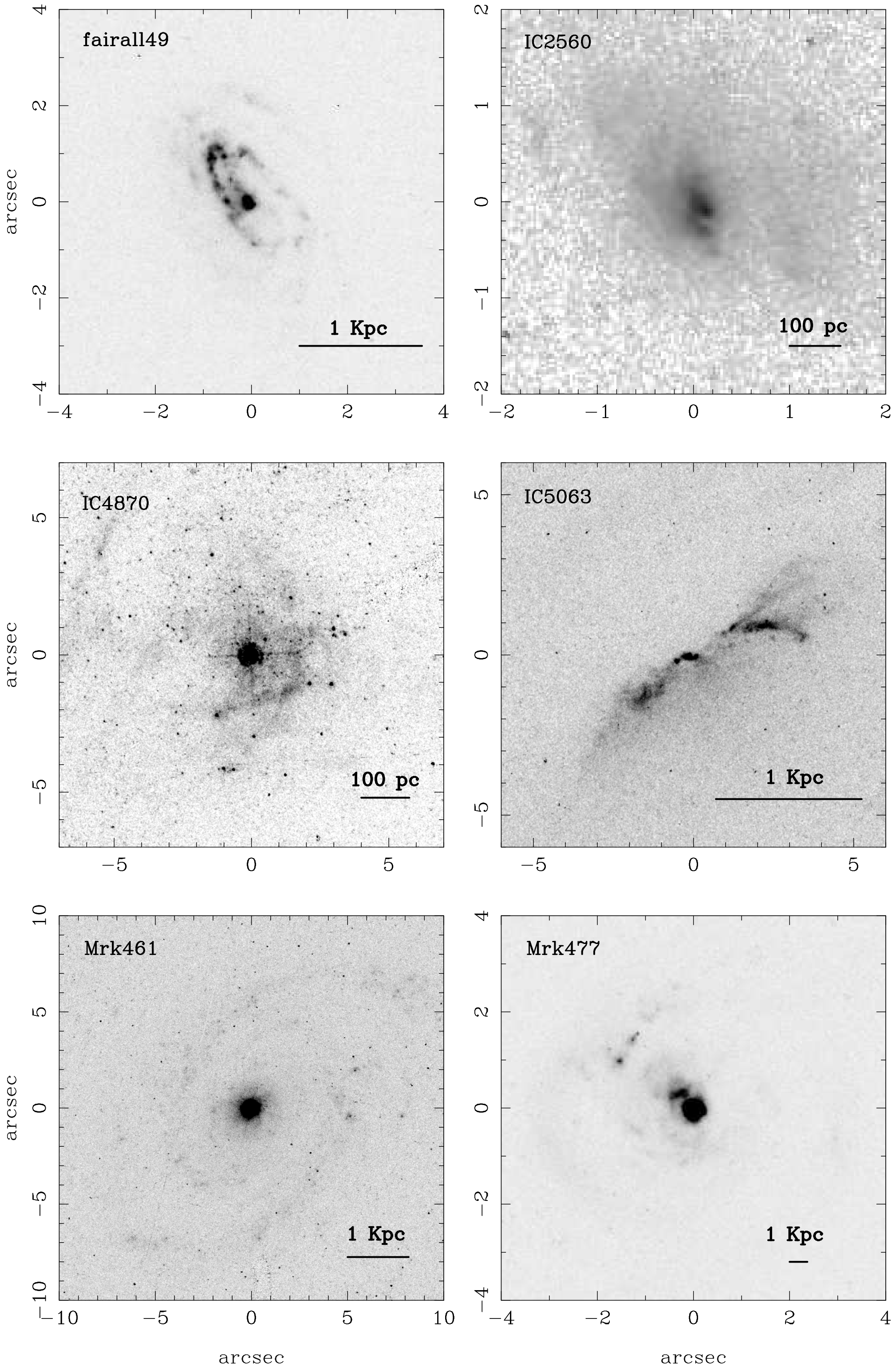

Figure 3.9: Images of the Sy2 galaxies –continued

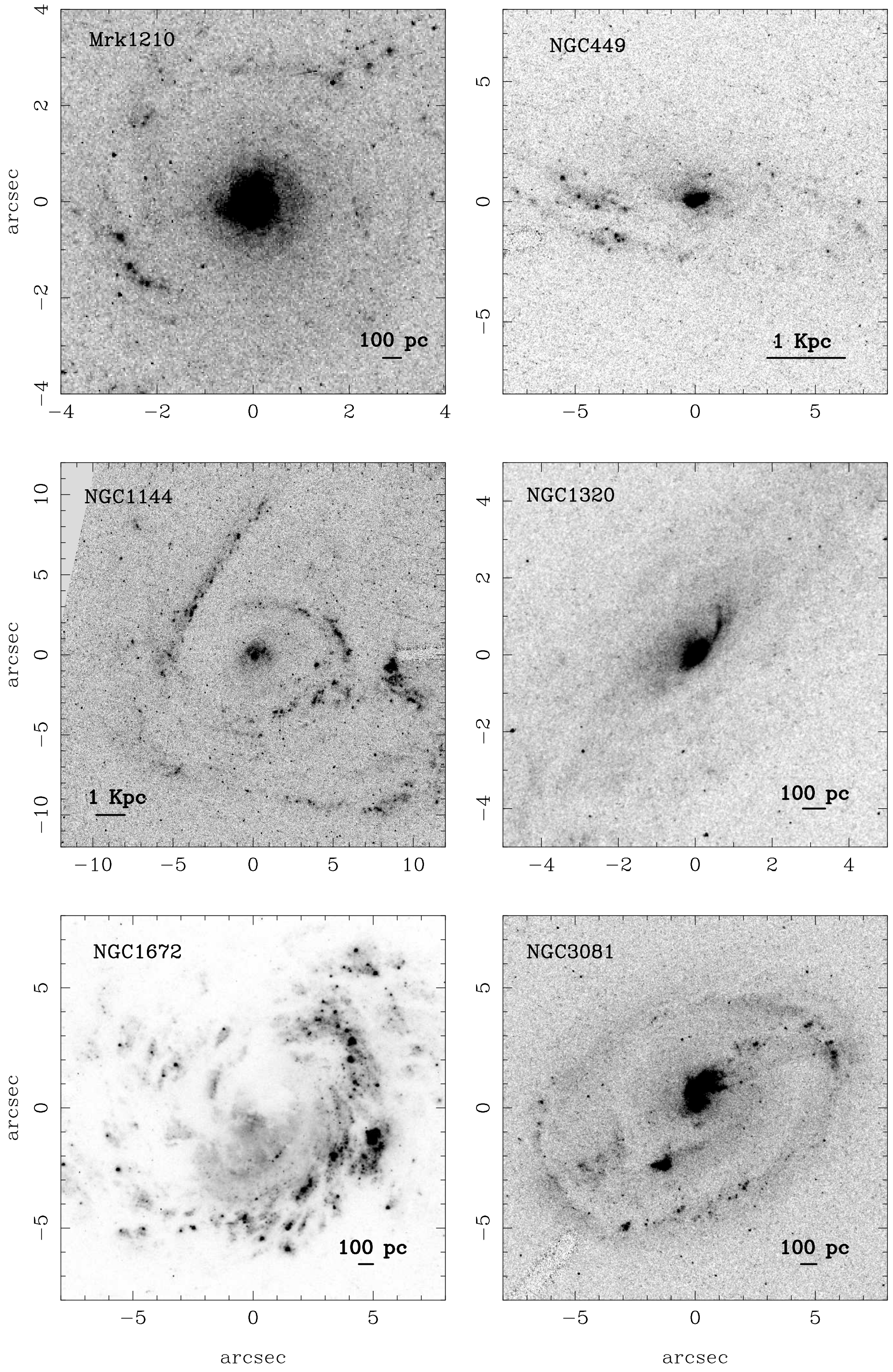

Figure 3.9: Images of the Sy2 galaxies –continued

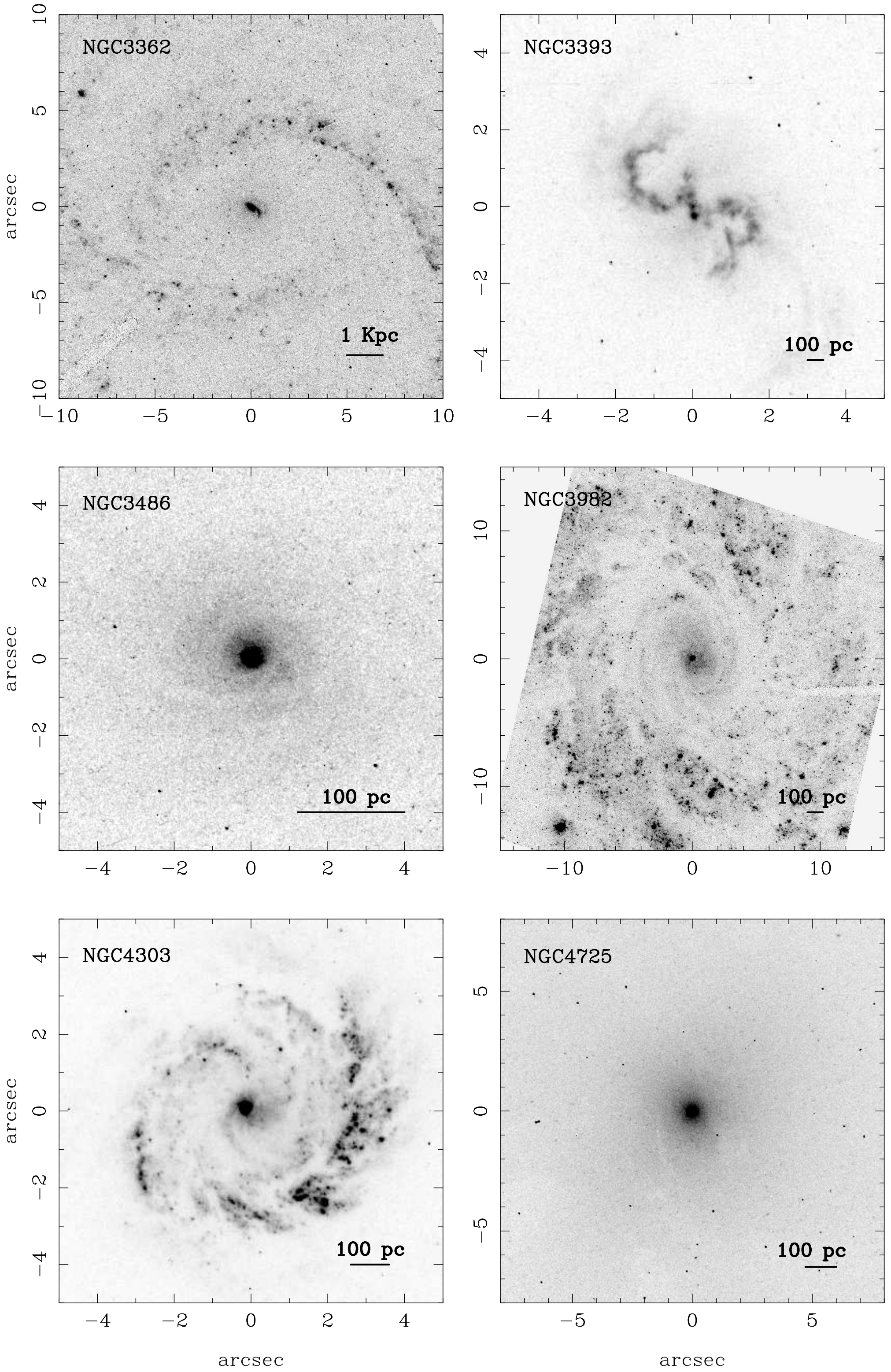

Figure 3.9: Images of the Sy2 galaxies –continued

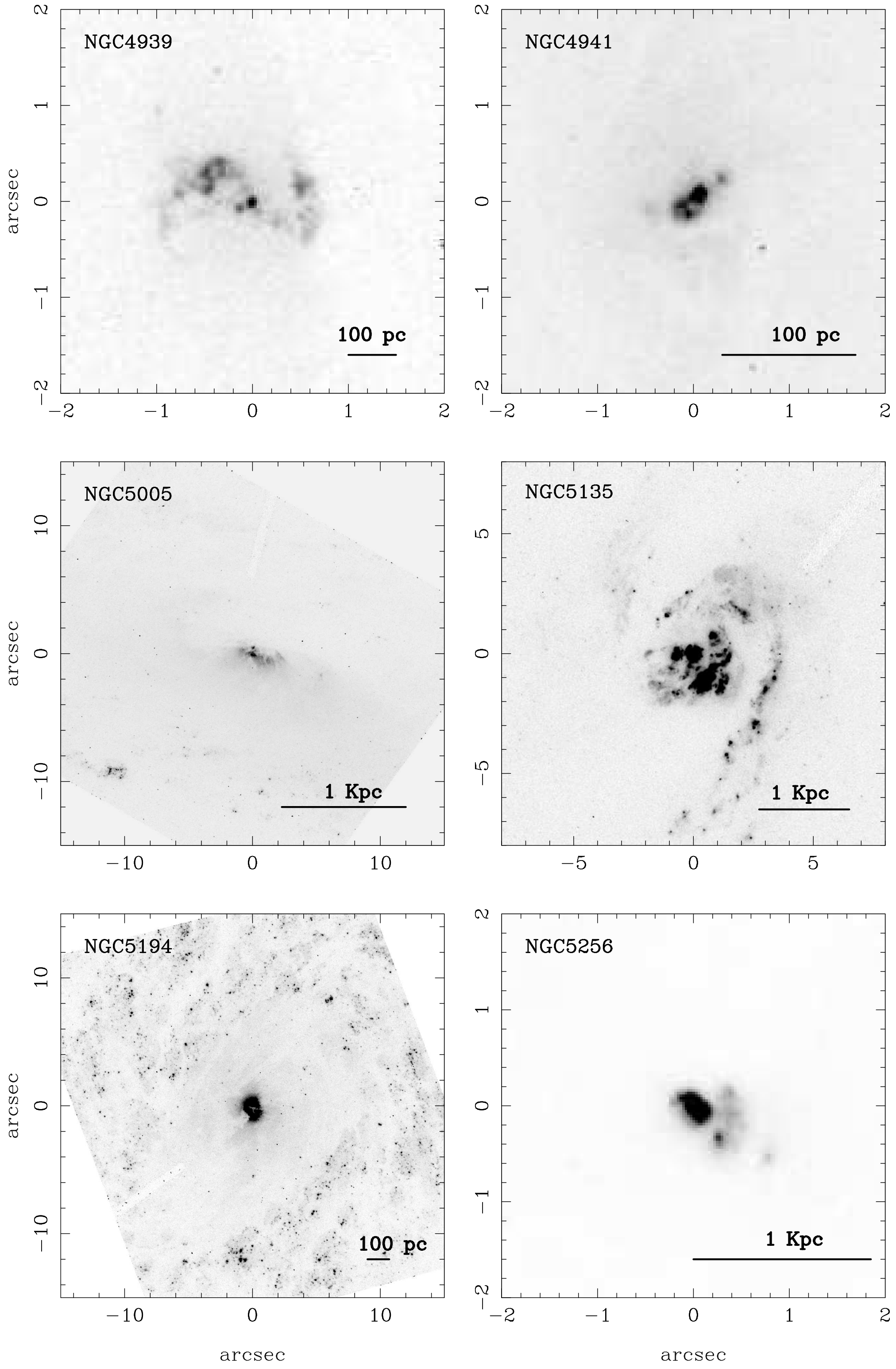

Figure 3.9: Images of the Sy2 galaxies –continued

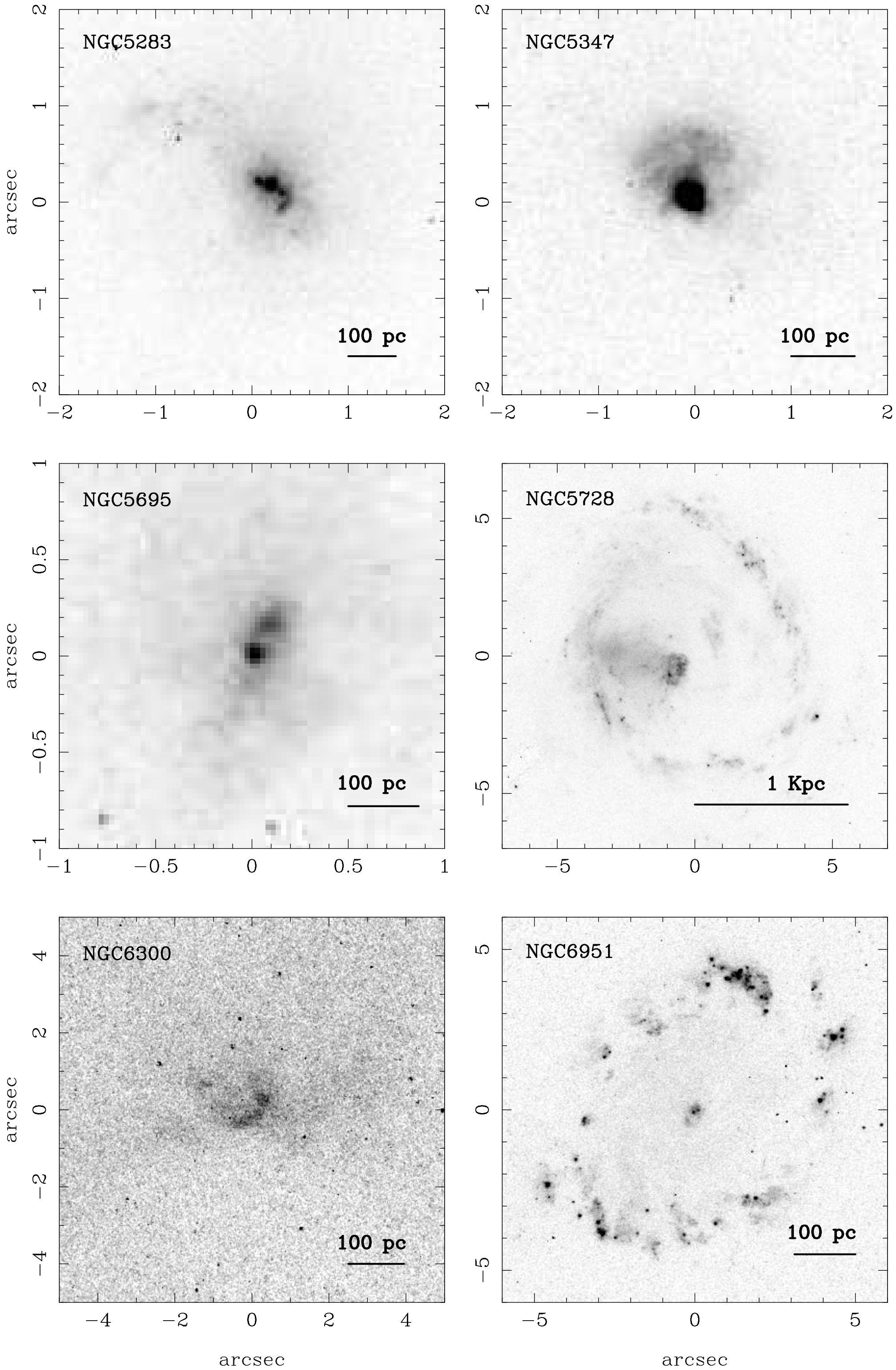

Figure 3.9: Images of the Sy2 galaxies –continued

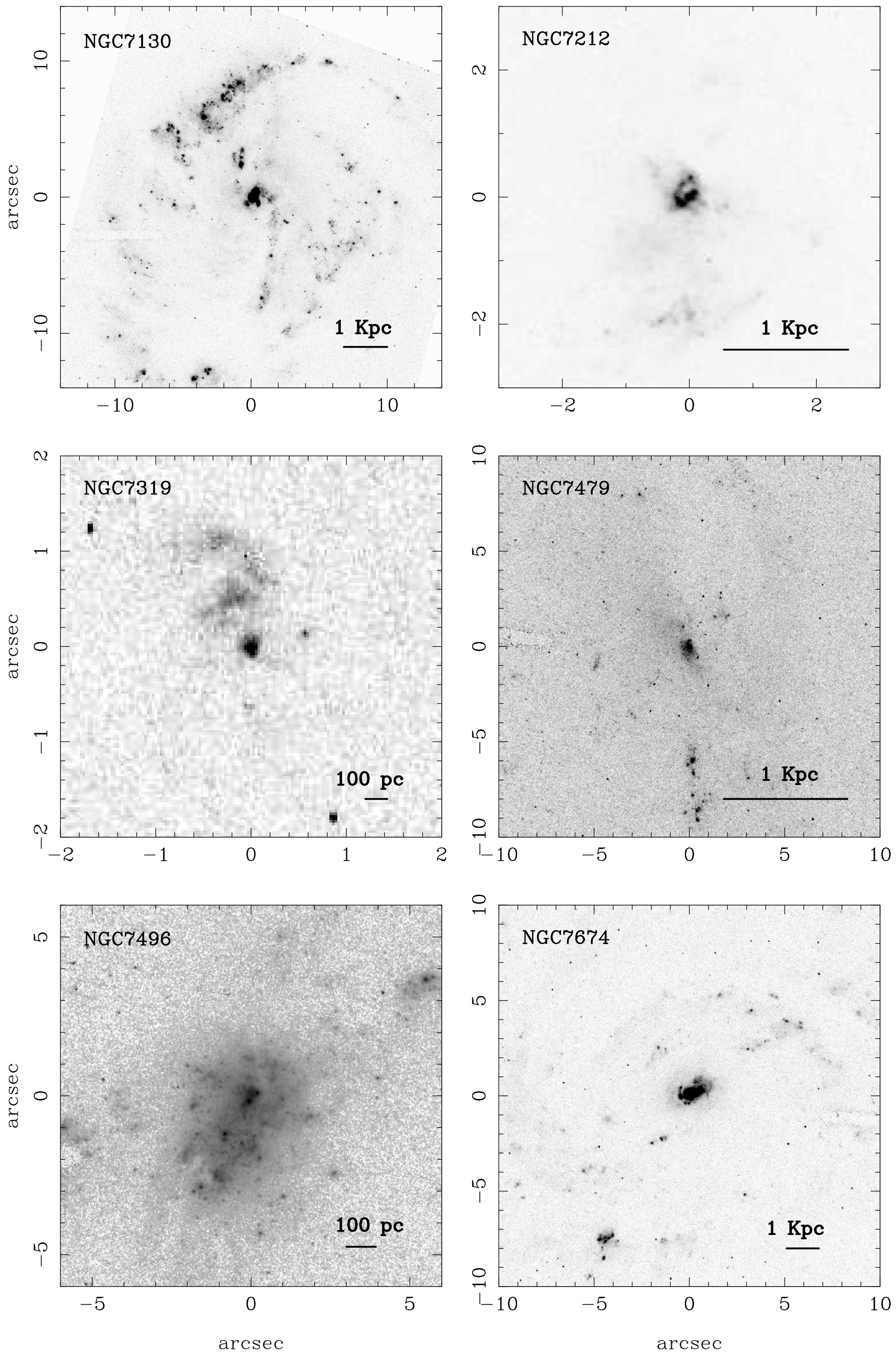

Figure 3.9: Images of the Sy2 galaxies –continued

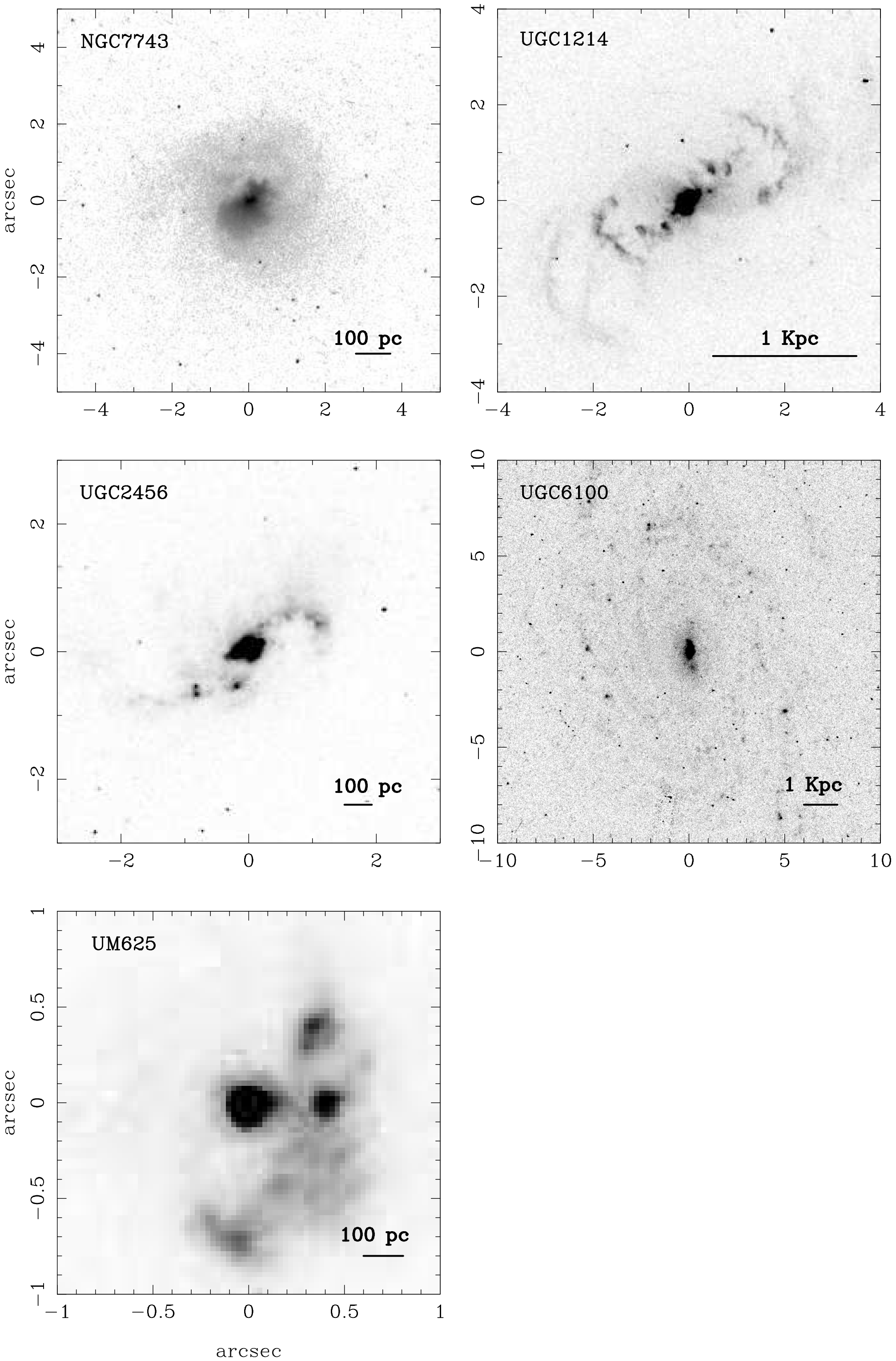

Figure 3.9: Images of the Sy2 galaxies –continued

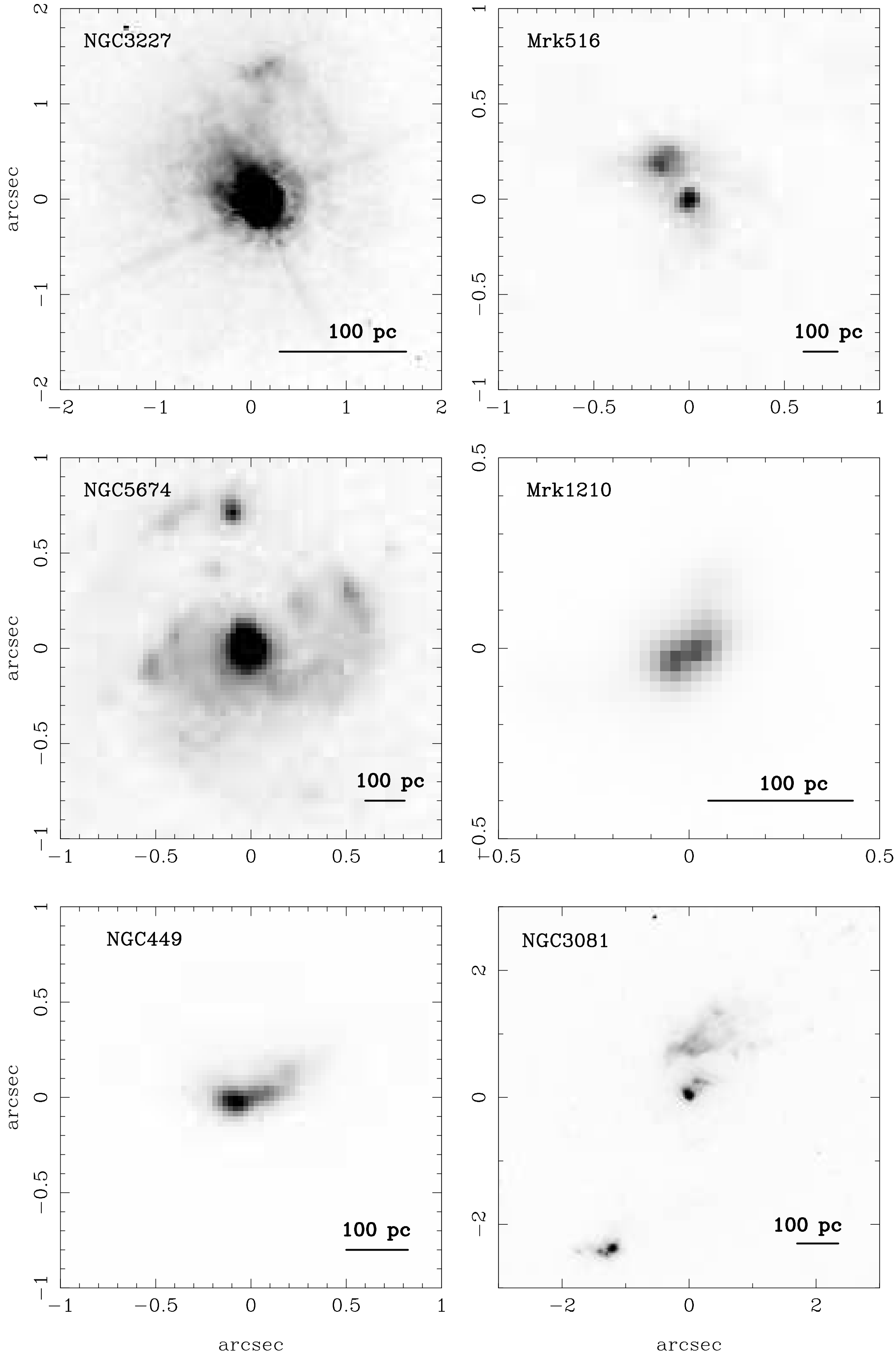

Figure 3.10: Close-up of some galaxies with interesting nuclear structure or a large luminosity range within the image

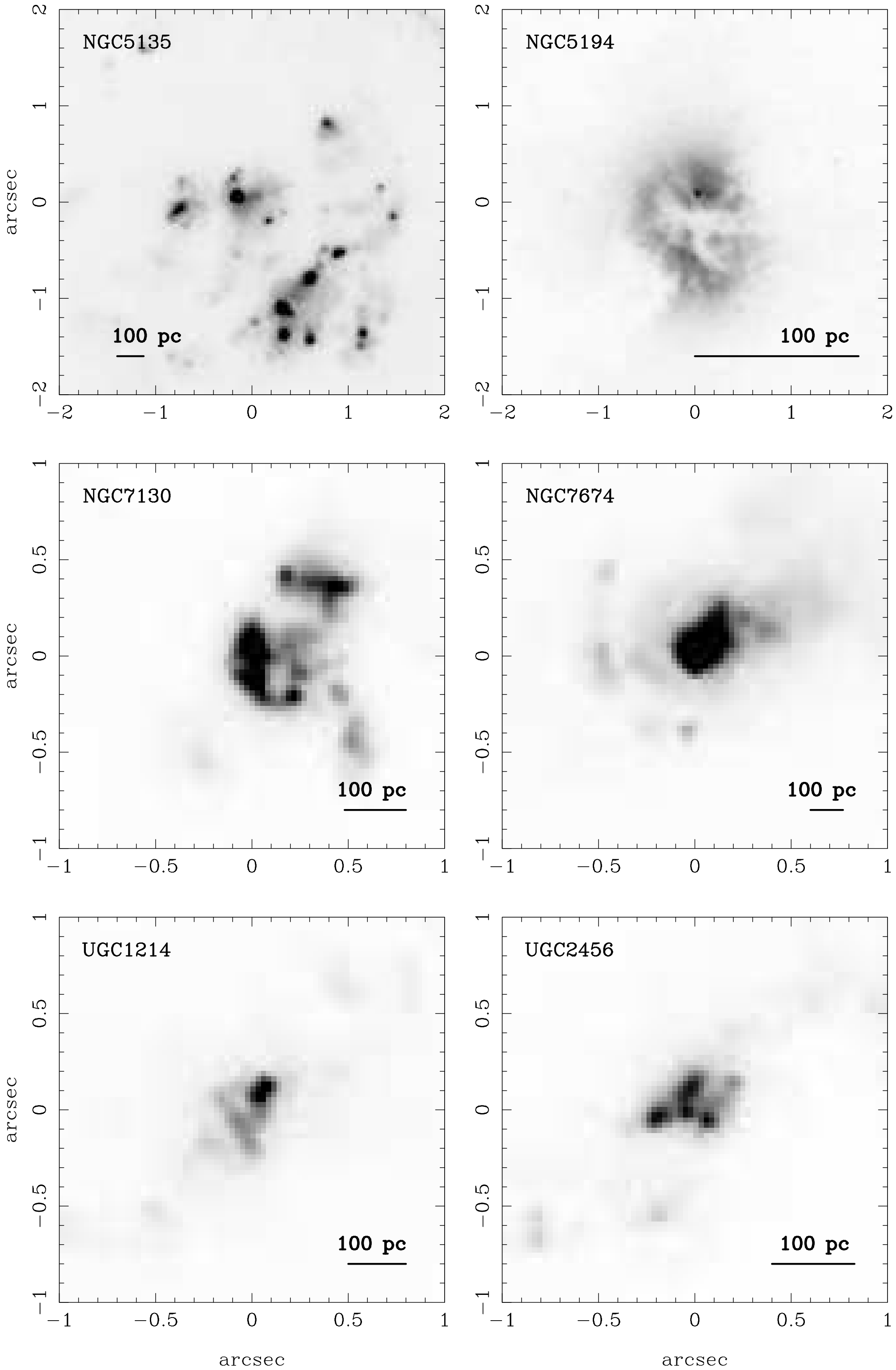

Figure 3.10: Close-up of some galaxies –continued

## 3.4 Analysis performed and its main results

### 3.4.1 Determination and classification of the surface brightness profiles. Identification of compact nuclei

Surface brightness profiles are usually constructed by means of elliptical isophotal fitting. This method works very well for early type galaxies and bands of longer wavelength. However, in the figures of former section it can be appreciated the strong irregularity of the isophotes, and therefore the usual method of isophotal fitting was ruled out. Instead, we performed a photometric analysis using circular apertures.

Aperture photometry was carried out with IRAF task ‘phot’ in order to determine the surface brightness profile and the luminosity and magnitude curves of growth. The surface brightness profile was computed by measuring the mean number of counts in circular annuli. First of all, an accurate position of the nucleus was computed when a compact source was clearly detected in the images. All the apertures were centered in the position determined by the centroid of the compact nuclear source. In the cases in which the nucleus was too obscured an approximate position was estimated by taking as a reference the nuclear position in the WFPC2 optical images (F606W and F814W), as these wavelengths are less affected by dust extinction, and using the galaxy features visible in both bands to align them. For these objects (Circinus, ESO 137-G34, ESO 362-G8, NGC 1672, NGC 2639, NGC 5194, NGC 5256, NGC 5728, NGC 6300 and NGC 6951) a precision of a few ACS pixels was achieved and that was enough for the rest of the analysis, so the inner regions are qualitatively described by the profiles.

The Point Spread Function (PSF) of the instrumental configuration was computed with the software TinyTim. The resulting PSF was compared with the radial profiles of several isolated stars in some images, showing a very good agreement. We then compared the PSF with the surface brightness profiles in order to determine whether or not the galaxies show a compact resolved nucleus. The PSF of the ACS-HRC at this wavelength has 1.8 pixels full-width at half maximum (FWHM), so a compact source with a FWHM larger than $0.05''$ should be seen slightly extended. The occurrence of a nuclear point source was determined by eye inspection of the radial profiles over-plotted, in a logarithmic scale, to the PSF profile and normalized to the same peak value. The results are summarized in Table 3.3. This table shows the number of objects of each Sy type for which the ACS-HRC shows a compact and unresolved nucleus. We have not found resolved nuclei in any galaxy from Sy1 to Sy1.5 type. On the other hand, most Sy2 nuclei appear resolved or absent (heavily obscured). For the intermediate types 1.8–1.9 the situation is something in between, with approximately one third of the nuclei resolved, one third remaining point-like, and the rest being difficult to discern. The objects with nucleus at the limit of resolution are Mrk 516, Mrk 334, NGC 4565, UGC 1395, and the Sy2 CGCG 164-019. This result is similar to that obtained at other wavelengths; for example, Nelson et al. (1996) show that in the red, Sy2 in general lack a compact nucleus while Sy1-1.5 are dominated by a bright unresolved nuclear source.

Table 3.3: Frequency of observed point-like nuclei in different Seyfert types

| Sy type | No nucleus or resolved | Unresolved | At resolution limit | Total |
|---|---|---|---|---|
| **Sy 2** | 43 (91.5%) | 3 (6.4%) | 1 (2.1%) | 47 |
| **Sy 1.8–1.9** | 5 (35.7%) | 5 (35.7%) | 4 (28.6%) | 14 |
| **Sy 1–1.5** | 0 | 14 (100%) | 0 | 14 |
| **Total** | 48 | 22 | 5 | 75 |

The table shows the number of objects of each type for which we resolve the nucleus. The numbers in brackets are the equivalent percentages relative to the total number of objects of each type. Note that no Sy1 nucleus is resolved

The computed profiles are shown in Figs. 3.11–3.13. By inspection of these plots we have classified the surface brightness profiles in one of these three categories:

- **Exponential:** The differential flux has an exponential dependence with the radius, so the dependence of the surface brightness ($\mu$) is linear with r. This is the classical model to fit well the surface brightness profile of some dwarf ellipticals and disks of spiral galaxies (Freeman, 1970).
- **de Vaucouleurs profile:** It is an $r^{1/4}$ profile. This is a good approximation to the large scale profiles of bright ellipticals and bulge of spirals.
- **Nuker law:** This is a five parameter model proposed by Lauer et al. (1995) which is a blend of two power-laws. The Nuker law is used to fit the inner parts of the galactic profiles.

Some of the galaxies are a clear example of a particular profile: e.g. NGC 5283, follows a perfect de Vaucouleurs law; ESO 362-G8 matches a Nuker law; and NGC 4725 shows a Nuker law within the inner $2''$ and a clear exponential in the outer regions. However, less than half of the objects show a correspondence with these profiles. More complex profiles are due to the effects of dust obscuration, occurrence of star-forming regions, or the presence of a bright nucleus, which can dominate the profile up to $2''$. NGC 5194 is an example of central dust obscuration, while NGC 5135 shows an irregular profile due to its nuclear starburst. The profiles can show as well the presence of a ring-like structure, as in NGC 4303 or NGC 7496. The objects whose nucleus is obscured in the UV images show a very irregular profile. The classification of the profiles is shown in the last column of Table 3.4.

### 3.4.2 Photometric analysis. Characterization of the emitting region

The differential surface brightness were obtained by calculating the flux within a very narrow circular annulus, dividing it by the area of the region, and then

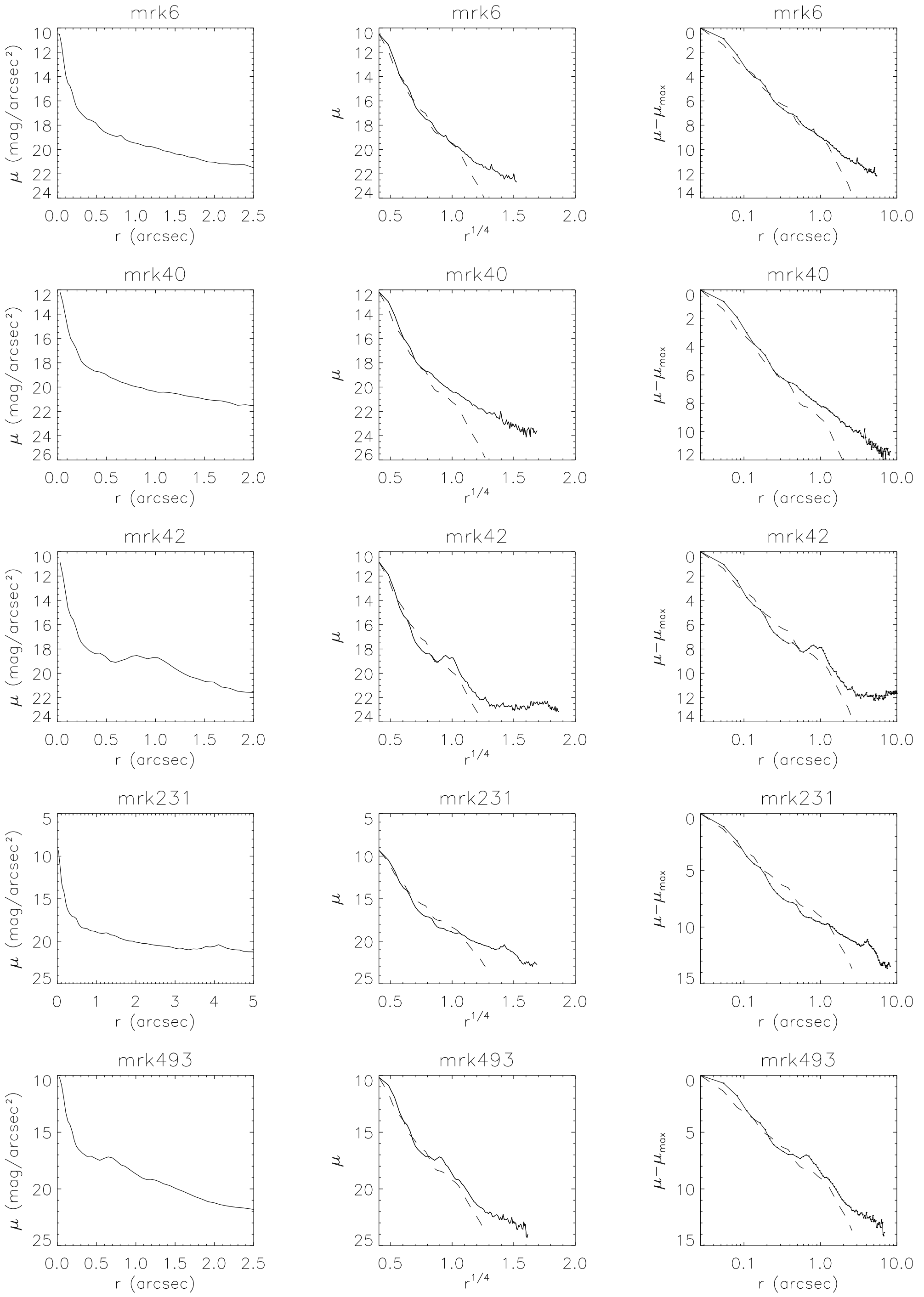

Figure 3.11: Surface brightness profiles are plotted for the Sy1 galaxies. From left to right, the abscissae are scaled linearly, with $r^{1/4}$, and logarithmic, in order to show the type of profile dominating in each galaxy (exponential, de Vaucouleurs or Nuker law). Theoretical PSF profiles are overplotted in dashed line, for comparison with each object.

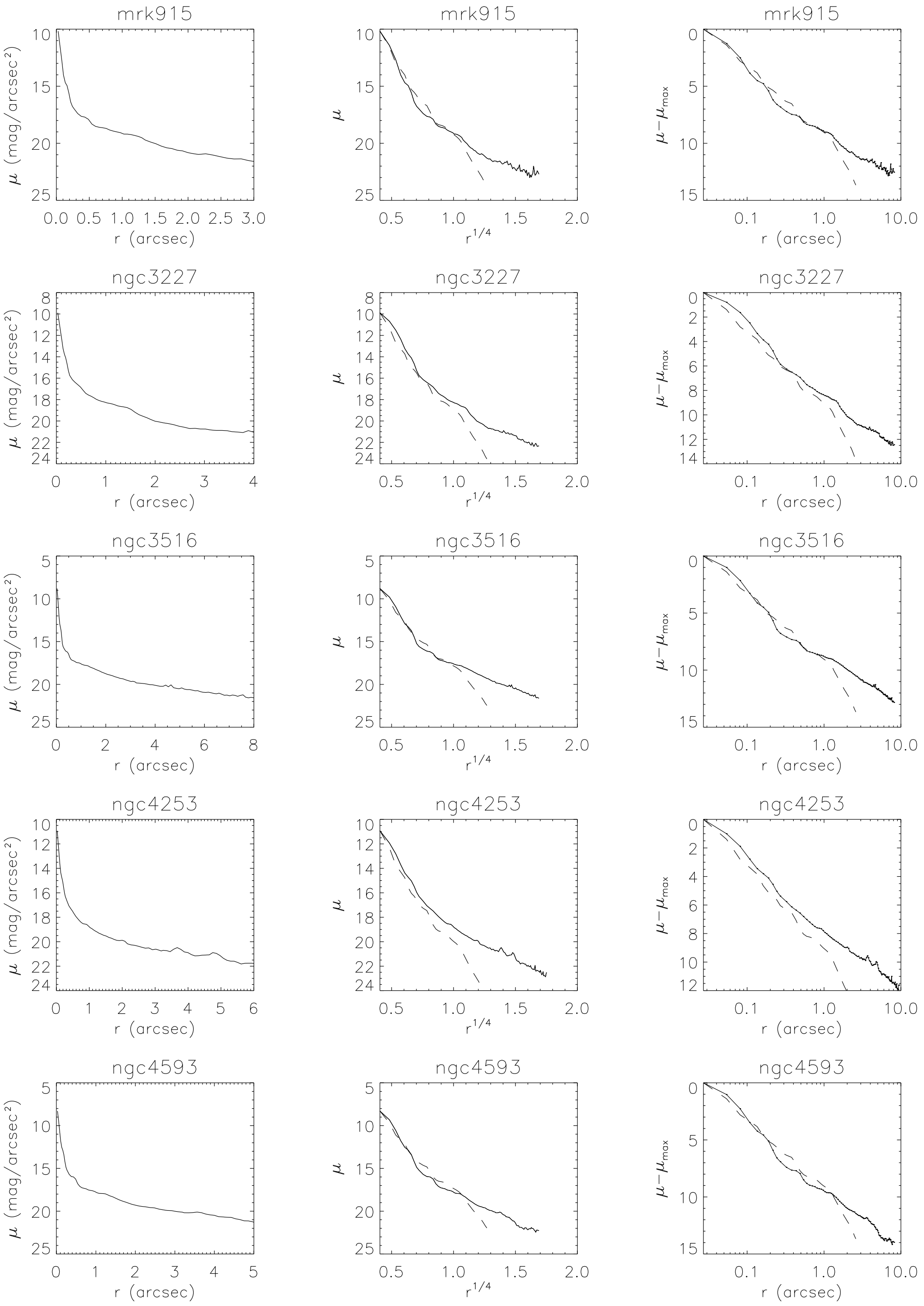

Figure 3.11: Surface brightness profiles for the Sy1 galaxies –continued

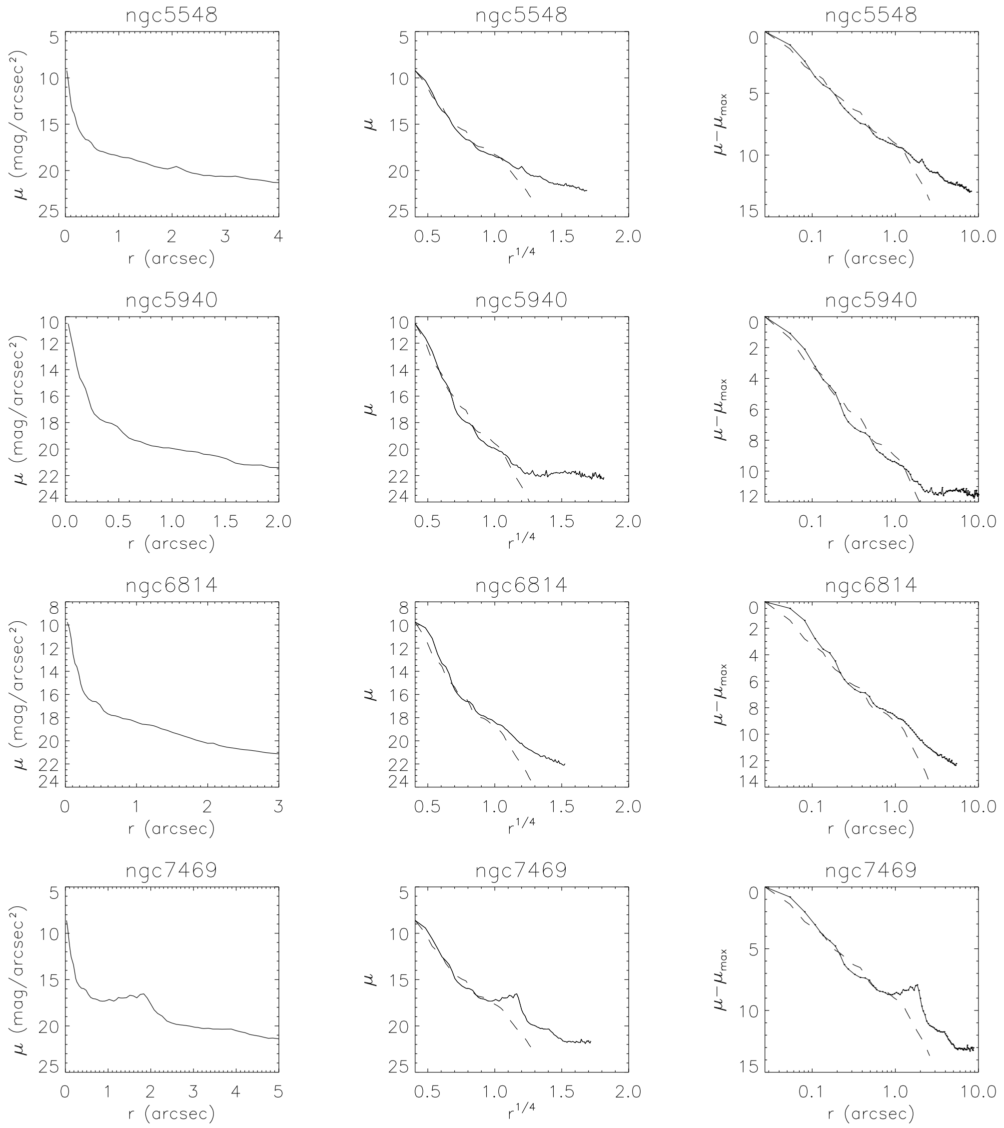

Figure 3.11: Surface brightness profiles for the Sy1 galaxies –continued

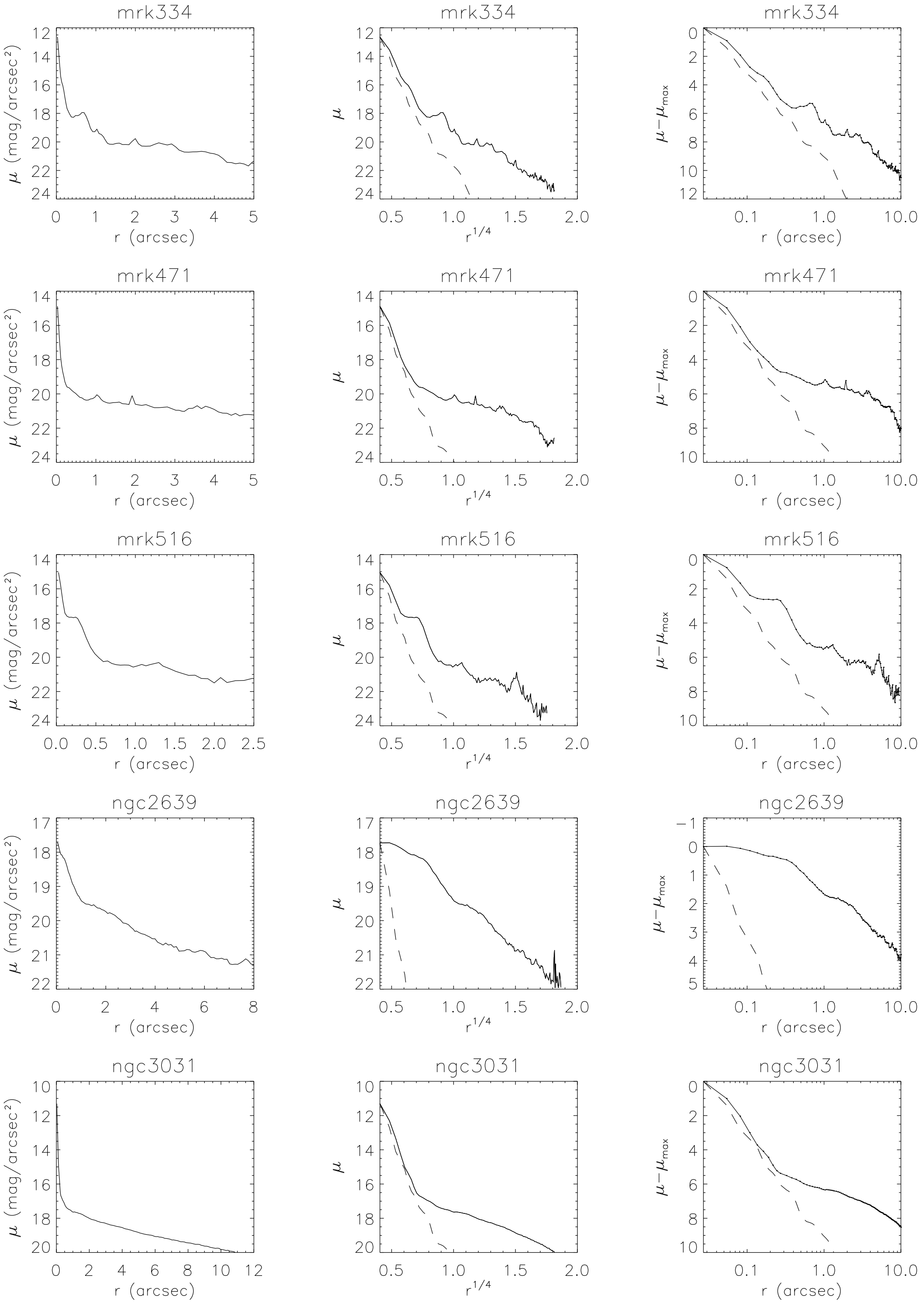

Figure 3.12: Surface brightness profiles for intermediate Sy type galaxies, with the same layout as in Figure 3.11

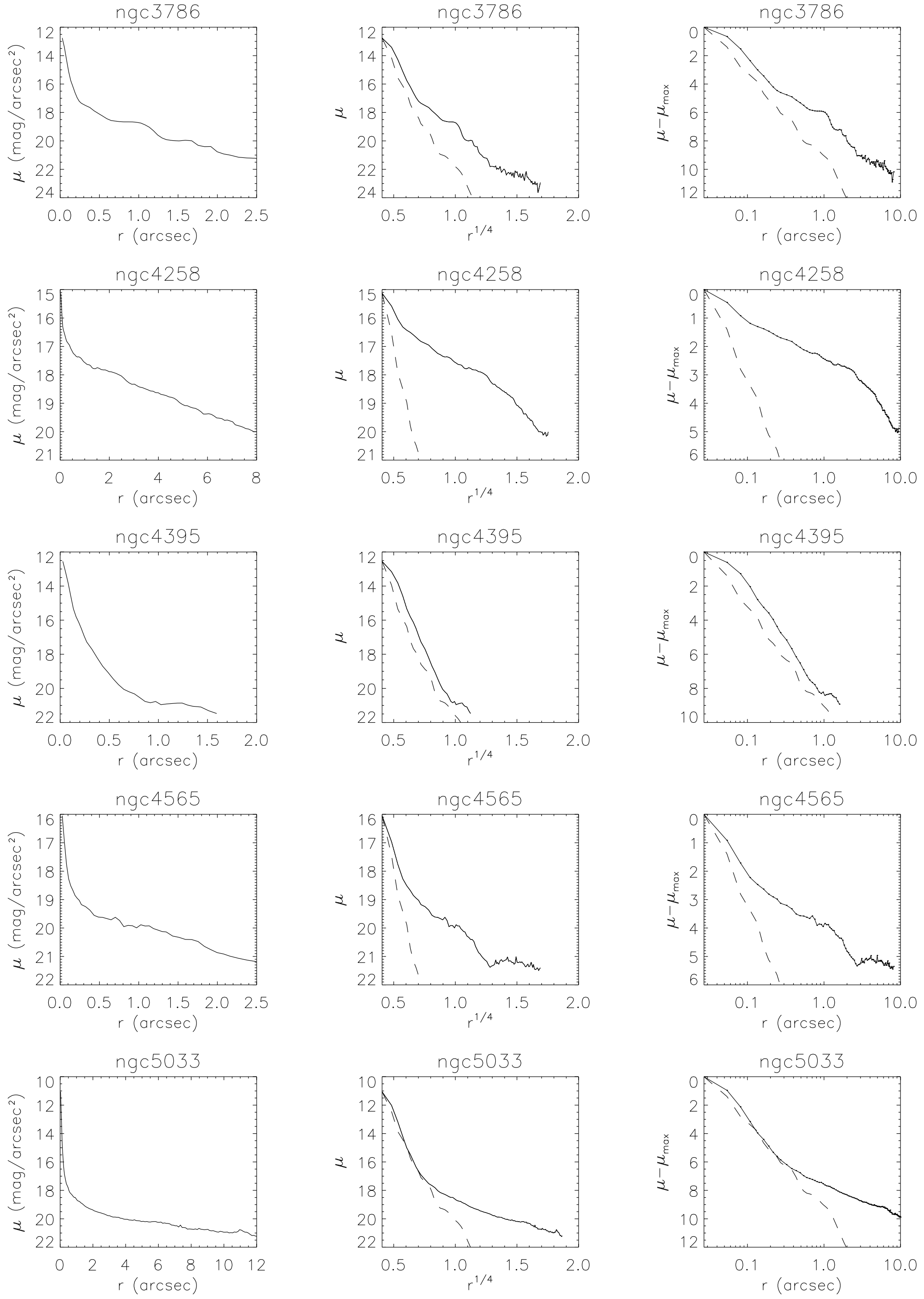

Figure 3.12: Surface brightness profiles for intermediate Sy type galaxies –continued

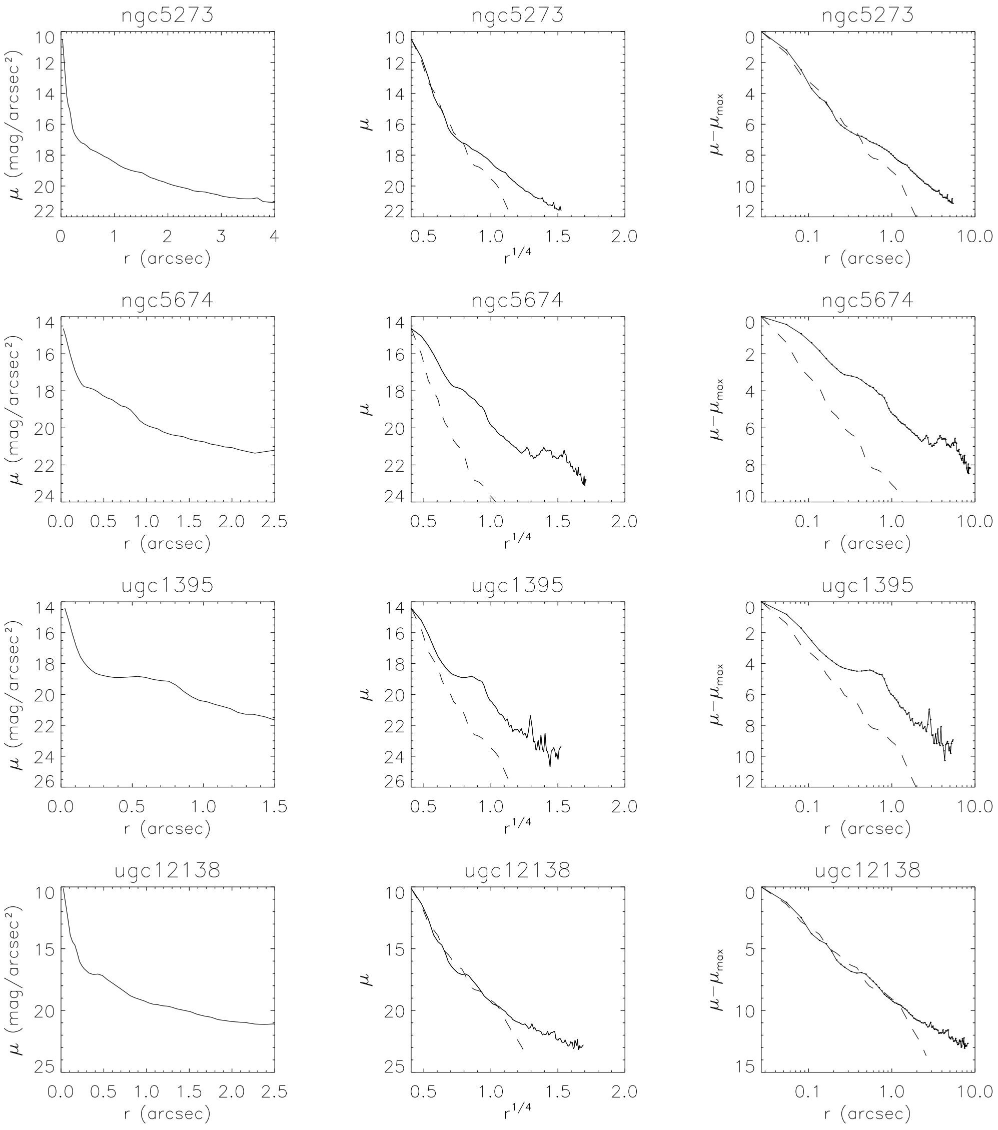

Figure 3.12: Surface brightness profiles for intermediate Sy type galaxies –continued

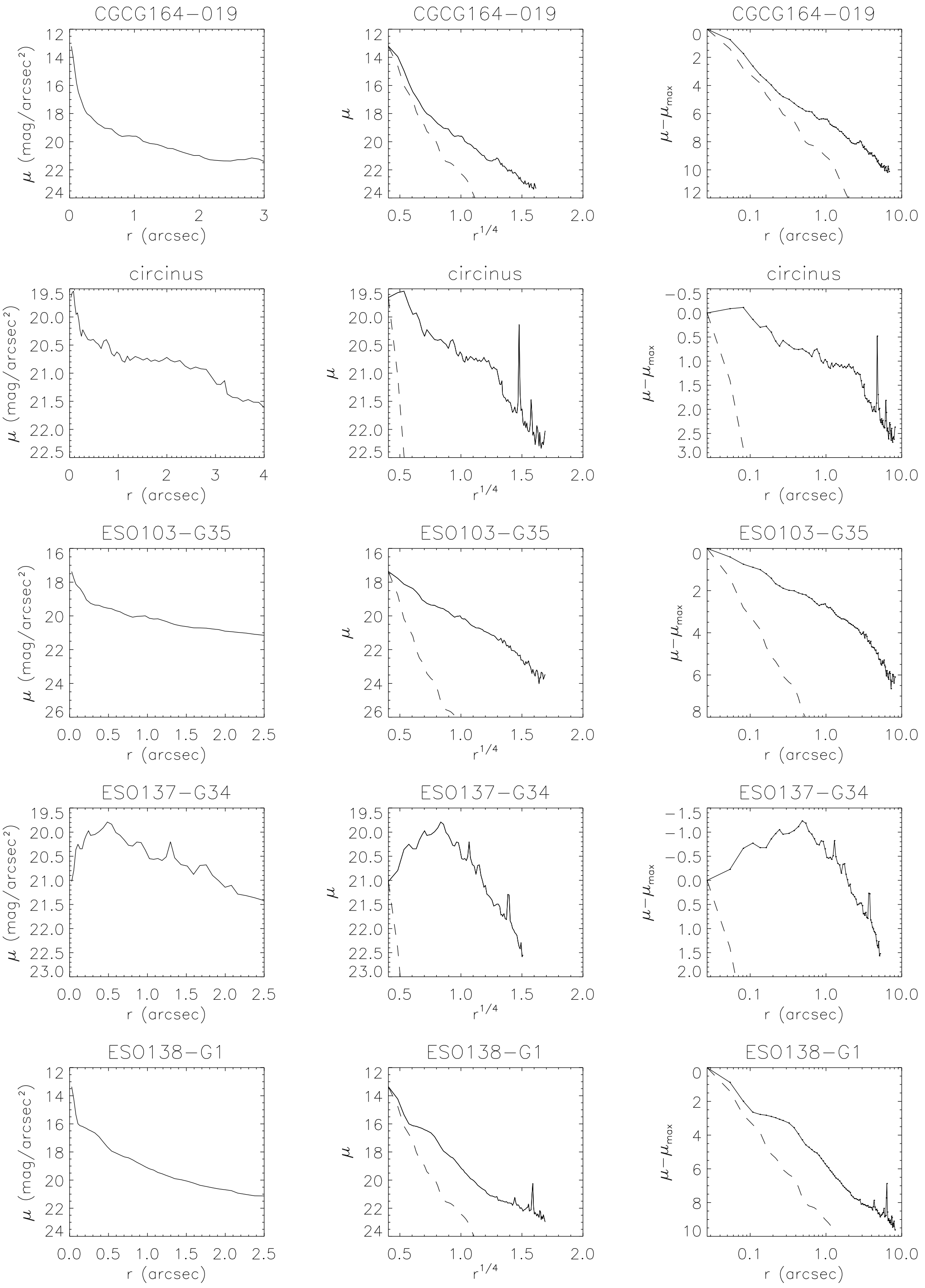

Figure 3.13: Surface brightness profiles for Sy2 galaxies, with the same layout as in Figure 3.11

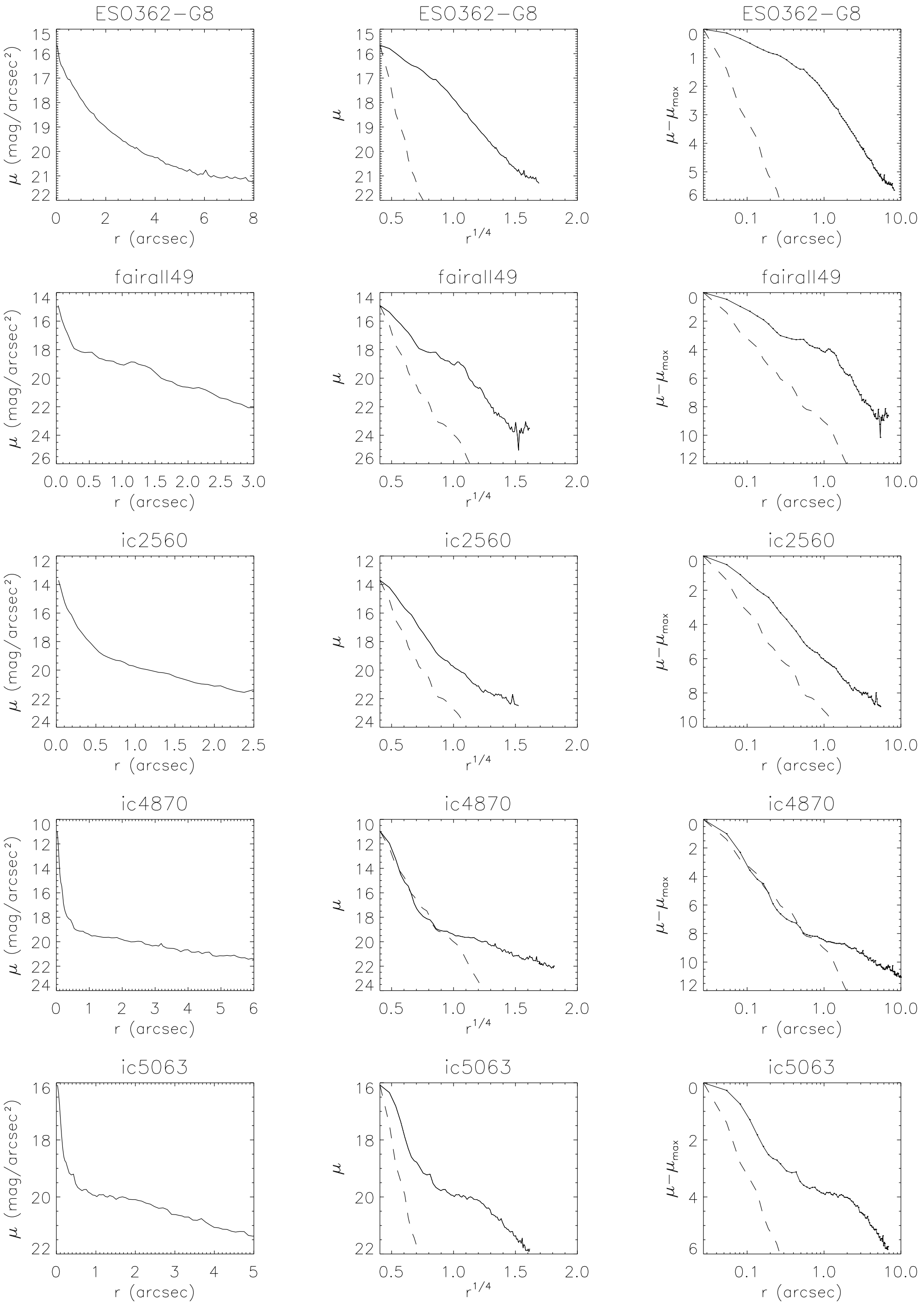

Figure 3.13: Surface brightness profiles for the Sy2 galaxies –continued.

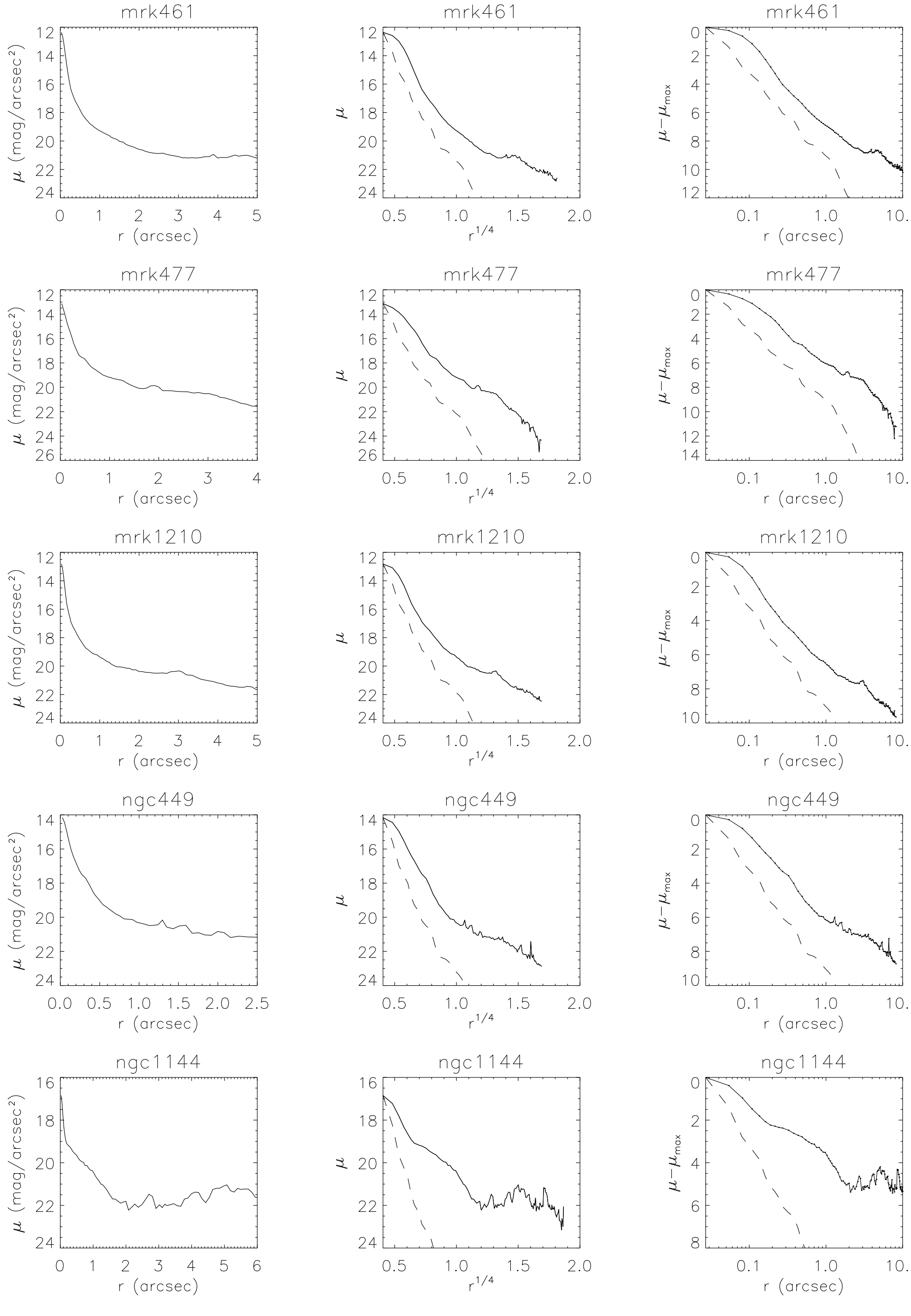

Figure 3.13: Surface brightness profiles for the Sy2 galaxies –continued.

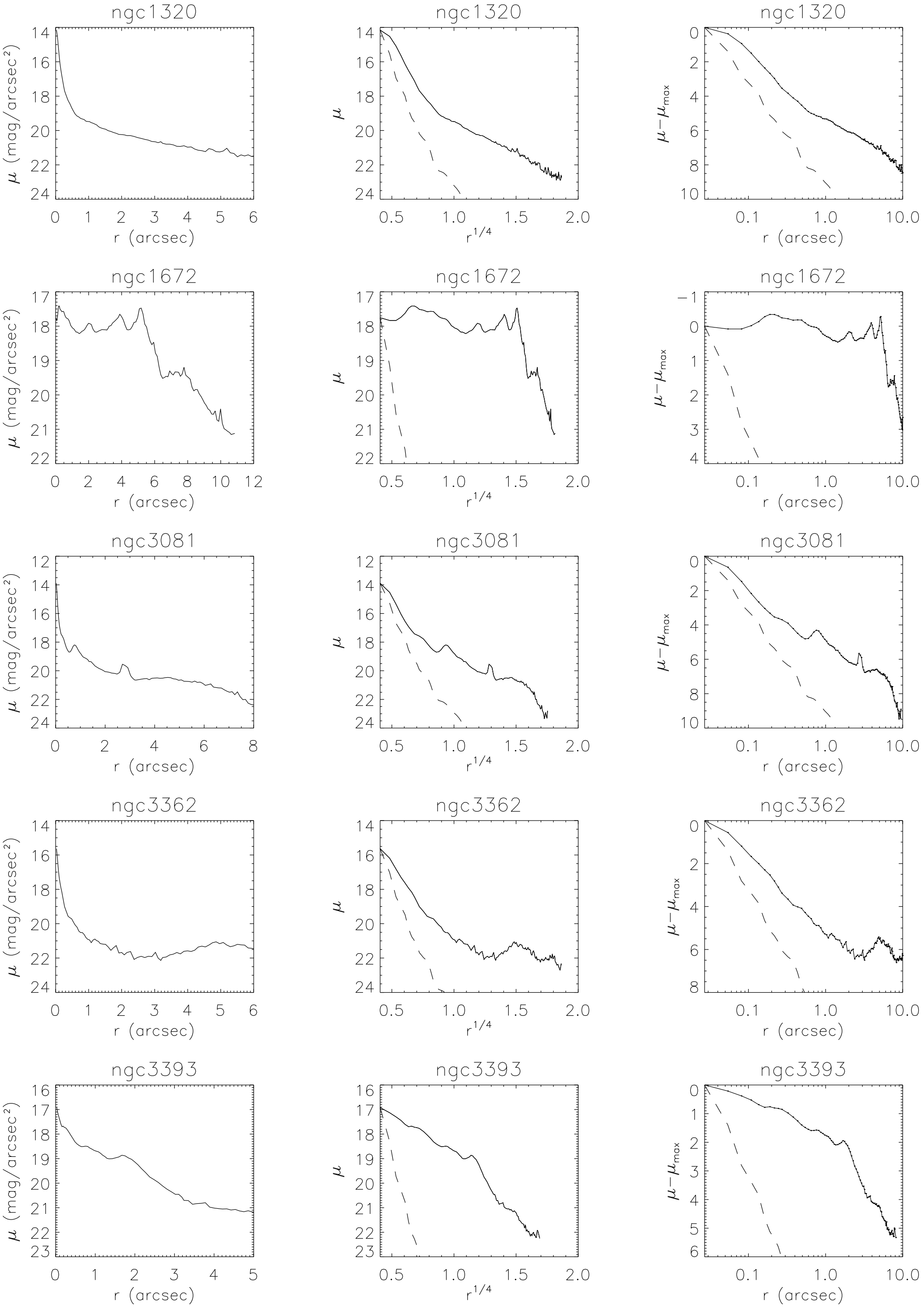

Figure 3.13: Surface brightness profiles for the Sy2 galaxies –continued.

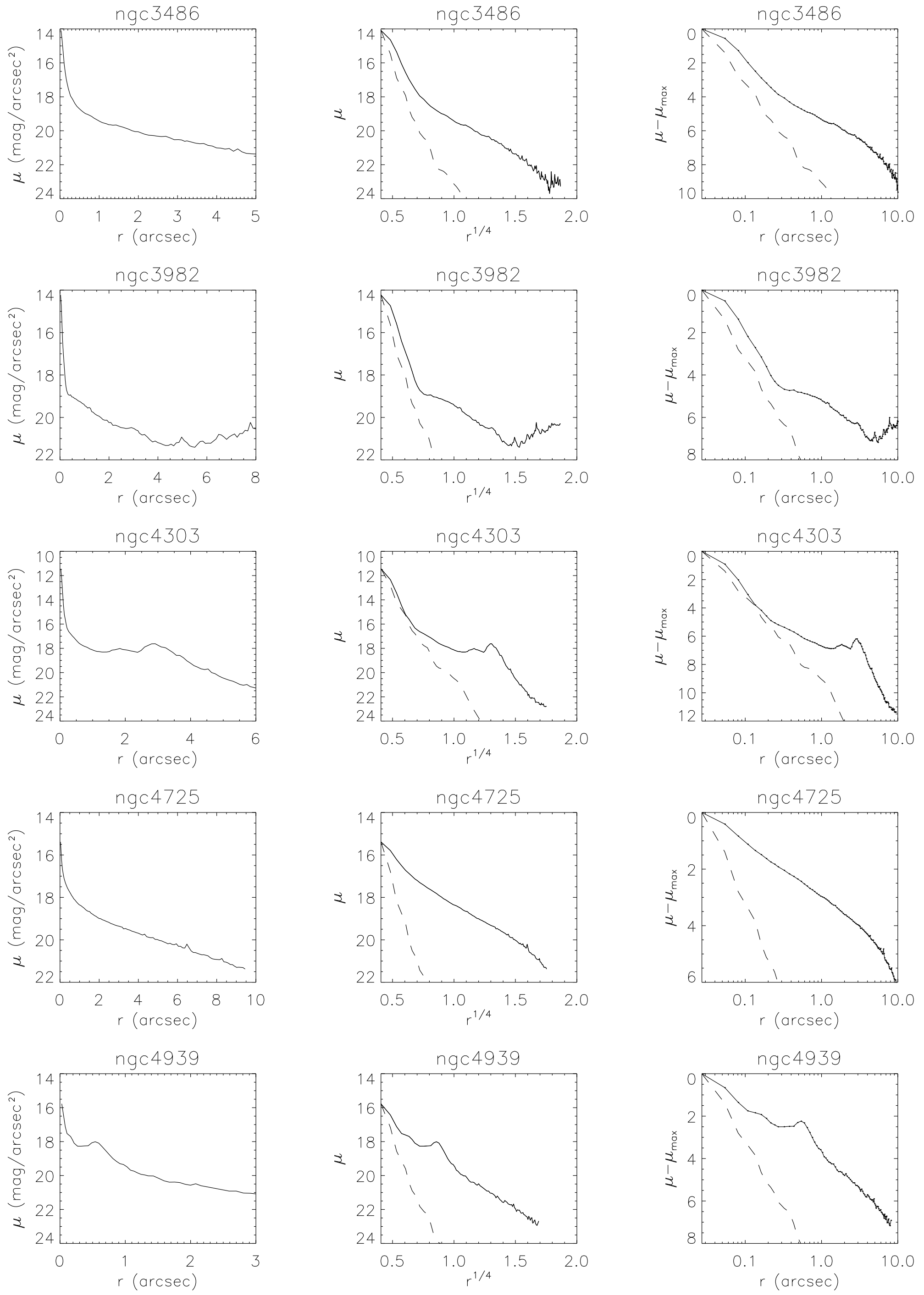

Figure 3.13: Surface brightness profiles for the Sy2 galaxies –continued.

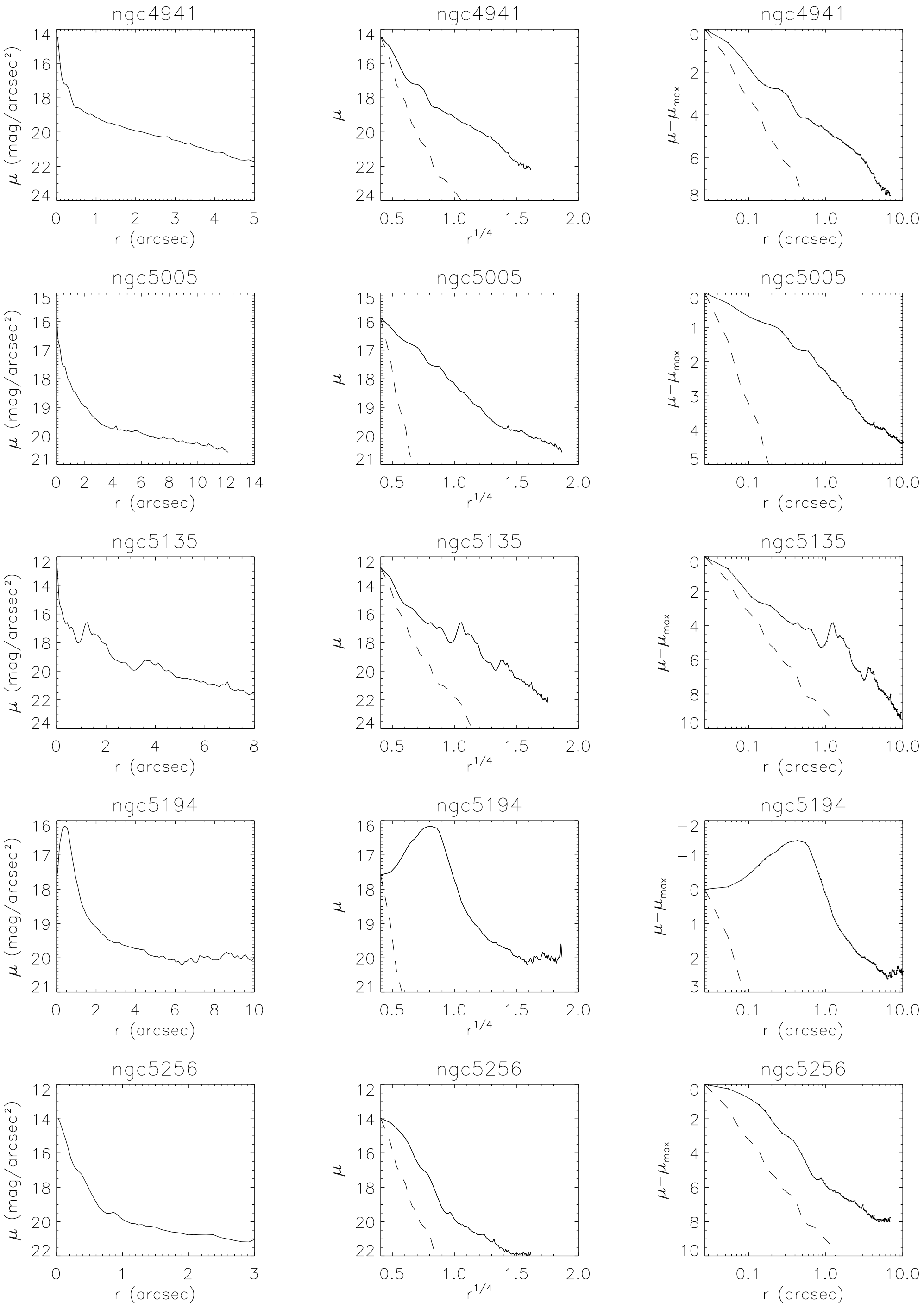

Figure 3.13: Surface brightness profiles for the Sy2 galaxies –continued.

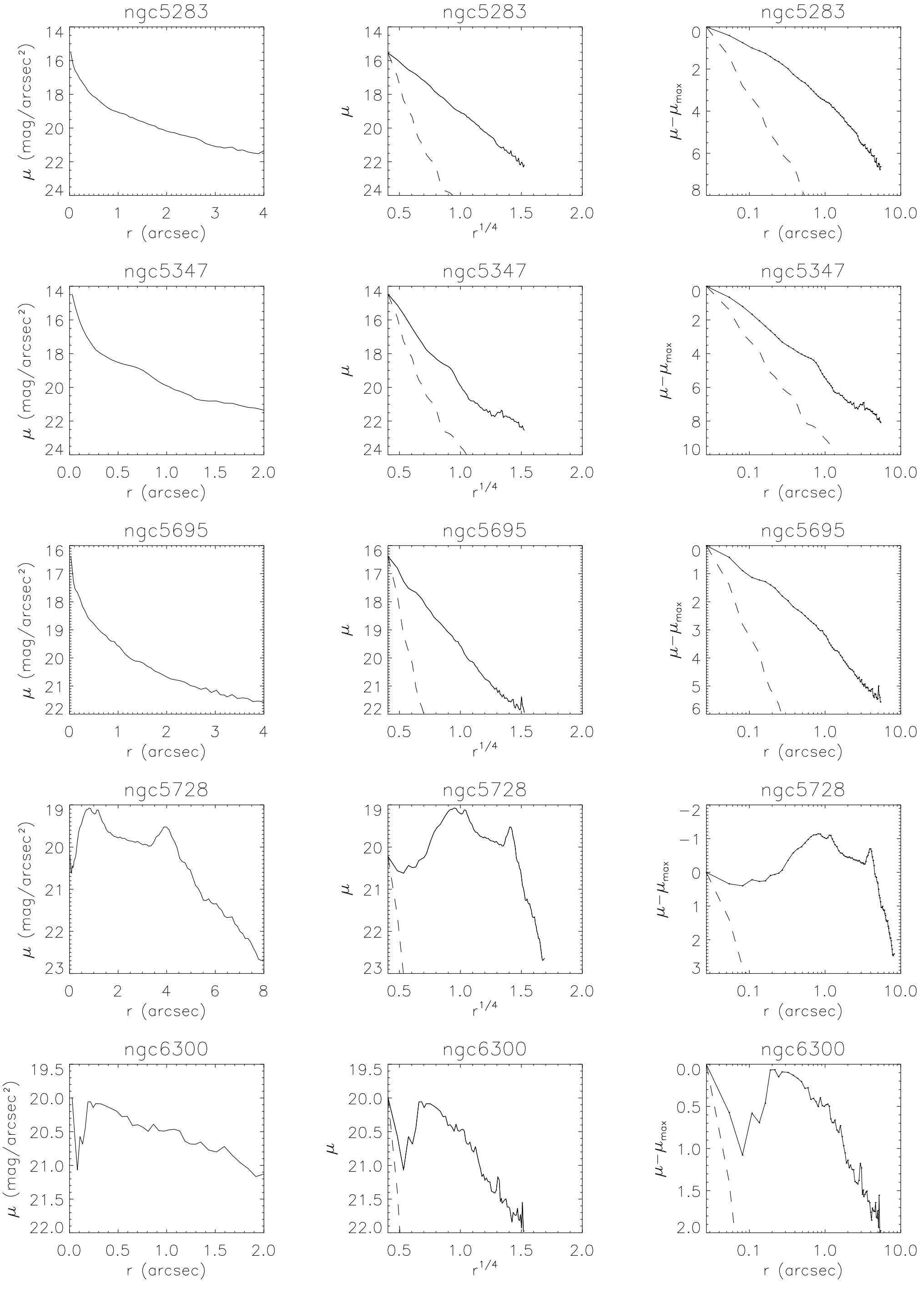

Figure 3.13: Surface brightness profiles for the Sy2 galaxies –continued.

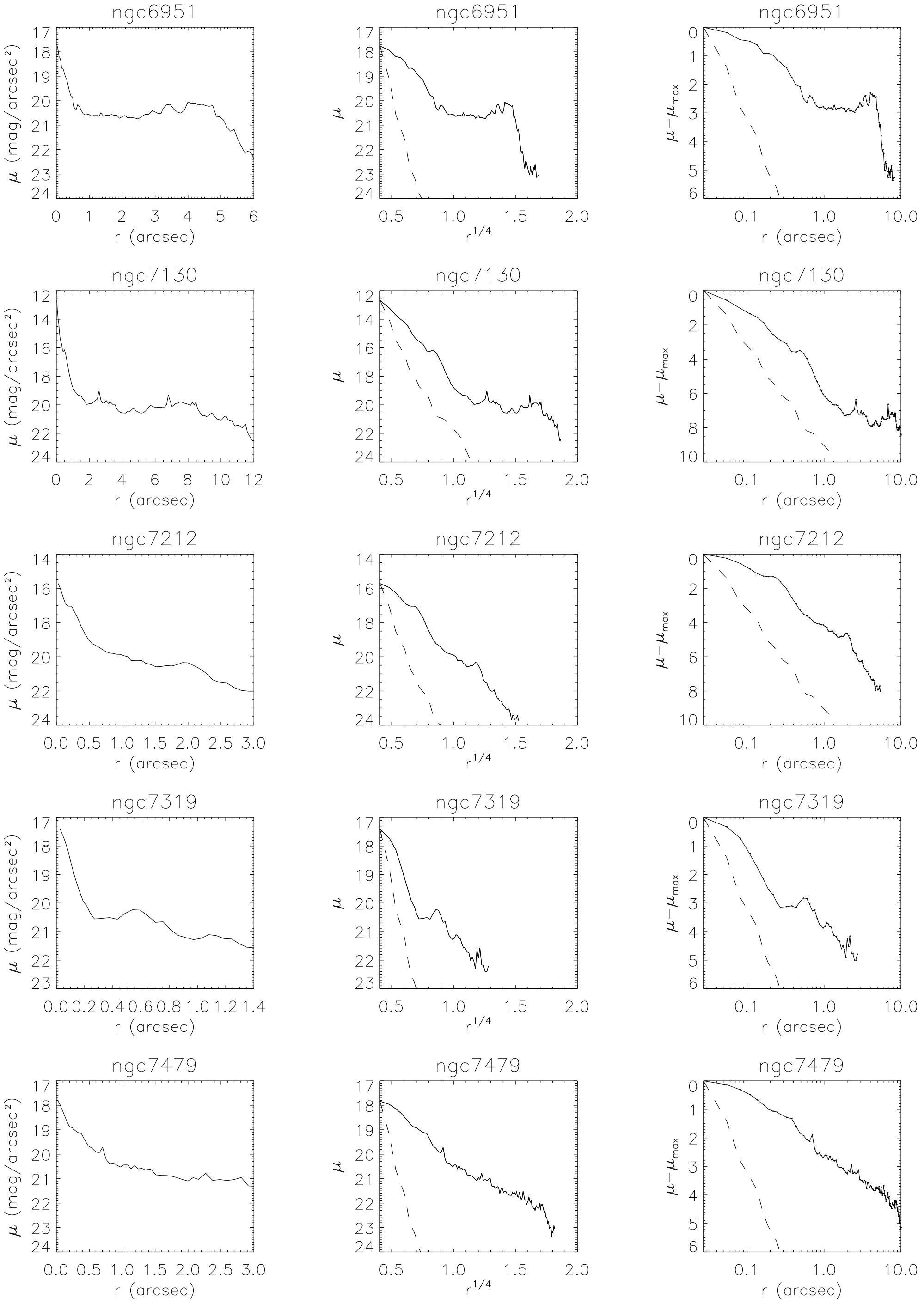

Figure 3.13: Surface brightness profiles for the Sy2 galaxies –continued.

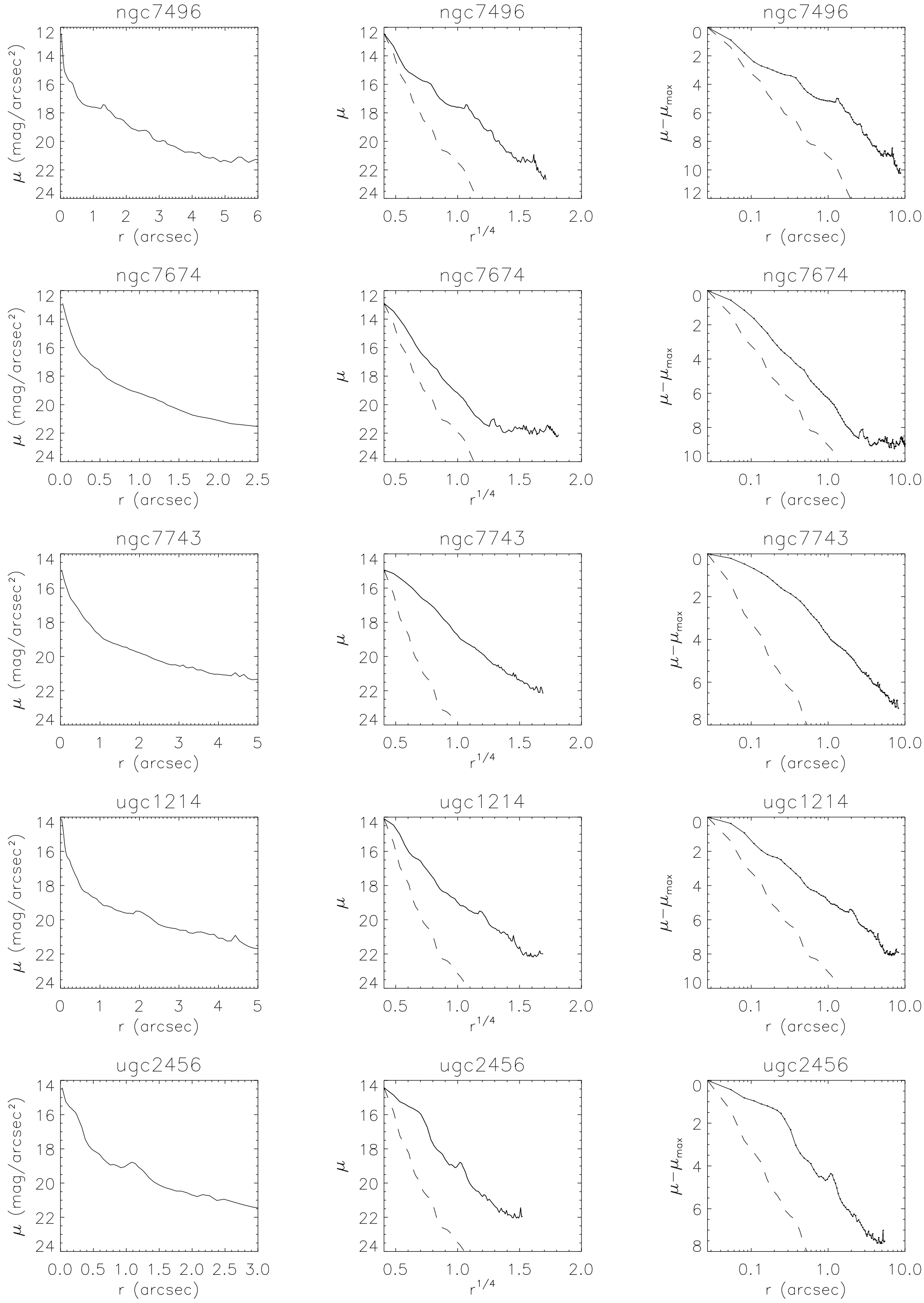

Figure 3.13: Surface brightness profiles for the Sy2 galaxies –continued.

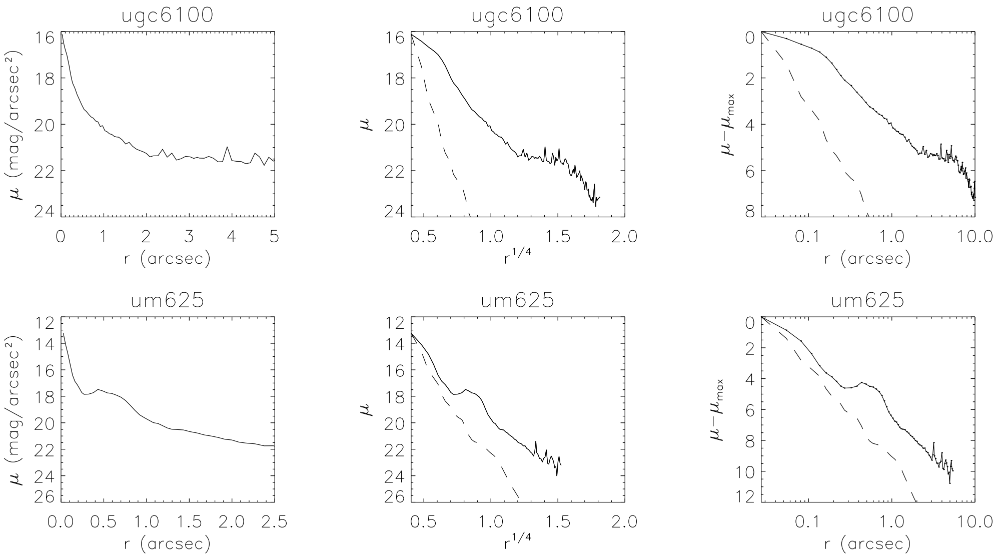

Figure 3.13: Surface brightness profiles for the Sy2 galaxies –continued.

calculating the magnitude. From the luminosity profiles and the background, we can define the maximum radius ($R_{max}$) as the distance from the centre at which the differential surface brightness equals the background value plus $1\sigma$, being $\sigma$ the standard deviation of the background. We consider that this criterion limits the region in which the flux can be calculated with enough S/N, and thus it gives an idea of the extension of the object. We have calculated the magnitude inside apertures of radii $R_{max}$, $1''$ and $0.3''$. The last two enclose respectively 94% and 86% of the total flux for a point-like source. Also, we have calculated the absolute magnitudes inside appertures of projected radii of 100 and 300 pc. All the magnitudes are calculated in the STMAG system, with the formula

$$m = -2.5 \cdot log(counts/s \cdot PHOTFLAM) - 21.1,$$

where PHOTFLAM is the inverse sensitivity.

For some objects that are too extended, $R_{max}$ is larger than the distance from the nucleus to the border of the image, and thus it could not be calculated with the standard procedure. We then take an alternative maximum radius that fitted inside the field of view but did not include the borders of the image, where the data do not have enough quality. This is the case of NGC 3031, NGC 5941 and NGC 5005, in which $R_{max}$ becomes a lower limit and thus it affects too, the other measurements of size and magnitude. Note also, that as $R_{max}$ is calculated doing an azimuthal average some emitting features or isolated star forming regions may fall outside the region we are studying.

We also calculate the differential surface brightness at $0.3''$ and $1''$ ($\mu_{0.3}$, $\mu_1$), as well as at the half-light radius (radius enclosing half of the total flux, or $\mu_{50}$) , and the radii enclosing 80%, 50%, and 20% of the total flux ($R_{80}$, $R_{50}$, and $R_{20}$). We have obtained that for several objects half or more of the flux is enclosed within a radius of one pixel. For these objects (all the Sy1 and some intermediate type Sy), which exhibit a bright point-like nucleus, we only can set an upper limit for $R_{50}$ and $R_{20}$. All the magnitudes are then corrected for galactic reddening using the extintion coefficients given in Sirianni et al. (2005), which are calculated using the extintion law of Cardelli et al. (1989). The correction for a particular filter depends on the shape of the continuum. We have used A(F330W)/E(B–V)=5.054, that is an average of the values given for Sc and elliptical galaxies in Sirianni et al. (2005). The photometry results are given in Table 3.4.

Table 3.4: Measurements and results of the general photometrical analysis

| Galaxy Name (1) | m(0.3$''$) (2) | m(1$''$) (3) | m(R$_{max}$) (4) | M(100 pc) (5) | M(300 pc) (6) | $\mu$(0.3$''$) (7) | $\mu$(1$''$) (8) | $\mu_{50}$ (9) | R$_{max}$ [pc ($''$)] (10) | R$_{80}$ [pc ($''$)] (11) | R$_{50}$ [pc ($''$)] (12) | R$_{20}$ [pc ($''$)] (13) | Profile (14) |
|---|---|---|---|---|---|---|---|---|---|---|---|---|---|
| CGCG 164-019 | 17.66 | 17.05 | 16.47 | -17.50 | -17.96 | 17.98 | 19.48 | 19.39 | 1586 (2.74) | 1013 (1.75) | 439 (0.76) | 52 (0.09) | v |
| Circinus | 14.12 | 11.88 | 9.71 | – | – | 12.93 | 13.29 | 13.43 | 62 (3.23) | 53 (2.77) | 40 (2.12) | 24 (1.27) | 0 |
| ESO 103-G35 | 19.79 | 18.06 | 17.01 | -14.20 | -15.79 | 18.93 | 19.69 | 19.92 | 578 (2.25) | 475 (1.85) | 315 (1.23) | 157 (0.61) | n |
| ESO 137-G34 | 19.83 | 17.21 | 16.11 | -14.55 | -16.47 | 18.36 | 18.77 | 18.82 | 354 (1.99) | 299 (1.68) | 221 (1.24) | 123 (0.69) | 0 |
| ESO 138-G1 | 16.4 | 15.43 | 15.09 | -17.00 | -17.62 | 15.56 | 18.11 | 16.92 | 390 (2.20) | 216 (1.22) | 95 (0.54) | 37 (0.21) | np |
| ESO 362-G8 | 17.66 | 15.85 | 14.34 | -16.50 | -18.13 | 16.51 | 17.70 | 18.97 | 1906 (6.17) | 1307 (4.23) | 659 (2.13) | 256 (0.83) | n |
| fairall49 | 18.03 | 16.75 | 15.98 | -16.38 | -17.49 | 17.66 | 18.73 | 18.74 | 930 (2.37) | 604 (1.54) | 398 (1.01) | 165 (0.42) | er |
| IC 2560 | 16.91 | 16.36 | 16.02 | -16.33 | -16.81 | 16.75 | 19.28 | 17.32 | 409 (2.16) | 231 (1.22) | 72 (0.38) | 21 (0.11) | 0 |
| IC 4870 | 15.54 | 15.34 | 14.48 | -15.23 | – | 17.2 | 18.84 | 19.05 | 283 (4.96) | 192 (3.37) | 78 (1.37) | <3 (0.05) | enp |
| IC 5063 | 19.23 | 17.9 | 15.81 | -14.47 | -15.85 | 18.74 | 19.66 | 19.92 | 876 (3.98) | 722 (3.28) | 507 (2.30) | 277 (1.26) | e |
| Mrk 6 | 14.85 | 14.67 | 14.57 | -19.53 | -19.68 | 16.31 | 18.79 | 11.32 | 732 (2.00) | 139 (0.38) | <24 (0.07) | <11 (0.03) | np |
| Mrk 40 | 16.99 | 16.72 | 16.58 | -17.61 | -17.83 | 18.22 | 20.30 | 14.52 | 691 (1.69) | 274 (0.67) | 38 (0.09) | <12 (0.03) | np |
| Mrk 42 | 15.92 | 15.67 | 15.55 | -19.01 | -19.14 | 17.8 | 18.57 | 12.35 | 796 (1.67) | 348 (0.73) | <32 (0.07) | <14 (0.03) | 0pr |
| Mrk 231 | 14.54 | 14.43 | 14.18 | -21.44 | -21.61 | 16.57 | 18.88 | 11.02 | 3749 (4.59) | 931 (1.14) | <55 (0.07) | <25 (0.03) | vp |
| Mrk 334 | 17.05 | 16.31 | 15.32 | -17.59 | -18.19 | 17.61 | 18.96 | 19.91 | 1760 (4.14) | 1309 (3.08) | 700 (1.65) | 119 (0.28) | 0 |
| Mrk 461 | 15.88 | 15.58 | 15.13 | -18.24 | -18.51 | 16.5 | 19.16 | 16.47 | 1133 (4.32) | 590 (2.25) | 77 (0.30) | 21 (0.08) | 0r |
| Mrk 471 | 19.58 | 18.49 | 16.28 | -15.76 | -16.39 | 19.57 | 20.07 | 20.75 | 2758 (4.16) | 2400 (3.62) | 1741 (2.63) | 922 (1.39) | 0p |
| Mrk 477 | 16.5 | 16.03 | 15.44 | -19.42 | -19.84 | 16.61 | 19.13 | 18.32 | 1080 (3.44) | 703 (2.24) | 203 (0.64) | 41 (0.13) | 0 |
| Mrk 493 | 14.71 | 14.5 | 14.43 | -20.50 | -20.66 | 16.58 | 18.55 | 11.49 | 1153 (1.90) | 261 (0.43) | <44 (0.07) | <18 (0.03) | 0pr |
| Mrk 516 | 18.54 | 17.83 | 17.14 | -16.07 | -17.11 | 17.7 | 20.23 | 20.17 | 1185 (2.15) | 865 (1.57) | 509 (0.92) | 127 (0.23) | 0 |
| Mrk 915 | 15.11 | 14.94 | 14.79 | -19.71 | -19.85 | 16.89 | 18.81 | 11.57 | 1137 (2.43) | 262 (0.56) | <30 (0.06) | <14 (0.03) | 0p |
| Mrk 1210 | 16.54 | 16.11 | 15.4 | -16.76 | -17.24 | 16.94 | 19.20 | 19.04 | 2866 (3.92) | 2047 (2.80) | 667 (0.91) | 73 (0.10) | 0r |
| NGC 449 | 17.45 | 16.95 | 16.51 | -16.63 | -17.06 | 17.31 | 20.02 | 18.33 | 699 (2.26) | 467 (1.51) | 133 (0.43) | 34 (0.11) | 0 |
| NGC 1144 | 19.81 | 18.22 | 16.26 | -14.87 | -16.29 | 18.91 | 20.07 | 21.67 | 2851 (5.10) | 2622 (4.69) | 2029 (3.63) | 688 (1.23) | 0 |
| NGC 1320 | 17.64 | 16.92 | 15.39 | -15.48 | -16.30 | 17.61 | 19.24 | 20.14 | 893 (5.19) | 702 (4.08) | 419 (2.43) | 127 (0.74) | v |
| NGC 1672 | 18.78 | 16.42 | 12.39 | -15.08 | -17.28 | 17.41 | 17.92 | 17.69 | 875 (10.18) | 587 (6.83) | 423 (4.92) | 280 (3.25) | 0 |
| NGC 2639 | 19.32 | 17.47 | 15.04 | -14.70 | -16.21 | 18.06 | 19.28 | 20.19 | 1326 (6.14) | 1084 (5.02) | 705 (3.26) | 352 (1.63) | n |
| NGC 3031$^{a,b}$ | 15.79 | 15.07 | 17.48 | -14.90 | – | 16.34 | 17.23 | 18.54 | >185 (10.85) | 145 (8.52) | 93 (5.45) | 43 (2.52) | ep |
| NGC 3081 | 17.76 | 16.58 | 14.71 | -15.33 | -16.54 | 17.41 | 18.50 | 20.34 | 979 (6.36) | 788 (5.12) | 489 (3.17) | 174 (1.13) | 0 |
| NGC 3227 | 14.46 | 14.27 | 14.05 | -16.74 | – | 15.85 | 18.16 | 12.11 | 283 (3.79) | 65 (0.87) | 8 (0.10) | <2 (0.03) | 0p |
| NGC 3362 | 19.22 | 18.35 | 16.52 | -15.64 | -16.45 | 19.01 | 20.77 | 21.79 | 2615 (4.88) | 2385 (4.45) | 1781 (3.32) | 600 (1.12) | nr |
| NGC 3393 | 18.67 | 16.75 | 14.95 | -15.35 | -17.08 | 17.46 | 18.30 | 18.66 | 1135 (4.69) | 784 (3.24) | 466 (1.93) | 249 (1.03) | n |
| NGC 3486 | 18.05 | 17.14 | 15.7 | -13.25 | – | 17.95 | 19.31 | 19.95 | 148 (4.12) | 116 (3.23) | 72 (1.99) | 26 (0.71) | e |
| NGC 3516 | 13.67 | 13.51 | 13.11 | -19.15 | -19.35 | 15.54 | 17.39 | 12.04 | 1014 (5.93) | 347 (2.03) | 20 (0.11) | <5 (0.03) | np |
| NGC 3786 | 17.07 | 16.37 | 15.96 | -16.03 | -16.70 | 17.32 | 18.60 | 18.33 | 381 (2.20) | 220 (1.27) | 104 (0.60) | 14 (0.08) | 0 |
| NGC 3982 | 18.44 | 17.44 | 15.38 | -13.94 | -15.14 | 18.75 | 19.35 | 20.61 | 524 (6.39) | 436 (5.32) | 263 (3.21) | 107 (1.30) | 0 |
| NGC 4253 | 15.61 | 15.3 | 14.75 | -17.98 | -18.27 | 16.41 | 18.69 | 17.31 | 1199 (4.89) | 684 (2.79) | 115 (0.47) | 15 (0.06) | np |
| NGC 4258 | 17.86 | 15.92 | 13.2 | -15.02 | – | 16.78 | 17.49 | 18.38 | 205 (6.20) | 163 (4.93) | 112 (3.39) | 59 (1.79) | en |
| NGC 4303 | 16.19 | 15.56 | 13.54 | -16.03 | -17.50 | 16.61 | 18.02 | 17.60 | 558 (5.52) | 361 (3.57) | 277 (2.74) | 141 (1.40) | 0pr |
| NGC 4395 | 16.77 | 16.57 | 16.5 | – | – | 17.43 | 20.78 | 14.40 | 22 (1.43) | 5 (0.32) | 2 (0.10) | <1 (0.04) | 0 |
| NGC 4565 | 19.91 | 18.27 | 17.16 | -13.18 | – | 19.14 | 19.86 | 20.00 | 181 (2.26) | 144 (1.80) | 100 (1.25) | 52 (0.65) | 0 |
| NGC 4593 | 13.33 | 13.22 | 13.03 | -19.51 | -19.63 | 15.35 | 17.64 | 9.64 | 813 (4.67) | 87 (0.50) | <11 (0.06) | <5 (0.03) | 0p |
| NGC 4725 | 18.26 | 16.58 | 14 | -14.80 | -16.23 | 17.31 | 18.29 | 19.64 | 651 (8.35) | 496 (6.36) | 313 (4.02) | 144 (1.84) | e |
| NGC 4939 | 18.98 | 17.08 | 16.27 | -14.99 | -16.33 | 18.06 | 19.21 | 19.44 | 553 (2.75) | 410 (2.04) | 215 (1.07) | 103 (0.51) | v |
| NGC 4941 | 18.02 | 16.93 | 15.58 | -14.26 | – | 17.26 | 18.95 | 19.60 | 279 (3.87) | 211 (2.93) | 128 (1.78) | 48 (0.67) | e |
| NGC 5005$^{a}$ | 18.15 | 16.38 | 22.32 | -15.22 | -16.54 | 17.06 | 18.11 | 20.00 | >1252 (12.15) | 1049 (10.18) | 730 (7.09) | 333 (3.23) | ev |

Continued on Next Page...

Table 3.4 – Continued

| Galaxy Name (1) | m(0.3″) (2) | m(1″) (3) | m(R$_{max}$) (4) | M(100 pc) (5) | M(300 pc) (6) | $\mu$(0.3″) (7) | $\mu$(1″) (8) | $\mu_{50}$ (9) | R$_{max}$ [pc (″)] (10) | R$_{80}$ [pc (″)] (11) | R$_{50}$ [pc (″)] (12) | R$_{20}$ [pc (″)] (13) | Profile (14) |
|---|---|---|---|---|---|---|---|---|---|---|---|---|---|
| NGC 5033 | 16 | 15.64 | 13.65 | -15.77 | -16.45 | 17.04 | 18.58 | 20.14 | 1060 (11.64) | 844 (9.27) | 520 (5.72) | 148 (1.63) | np |
| NGC 5135 | 16.49 | 15.4 | 13.59 | -17.39 | -18.52 | 16.08 | 17.47 | 17.44 | 1721 (6.47) | 1064 (4.00) | 470 (1.77) | 277 (1.04) | 0 |
| NGC 5194$^{a,b}$ | 17.73 | 15.34 | 13.44 | -14.74 | -15.83 | 16.09 | 17.56 | 19.73 | >340 (9.18) | 277 (7.48) | 173 (4.67) | 38 (1.03) | 0 |
| NGC 5256 | 17.07 | 16.54 | 16.11 | -17.81 | -18.51 | 16.86 | 19.79 | 17.42 | 1468 (2.72) | 896 (1.66) | 223 (0.41) | 70 (0.13) | 0 |
| NGC 5273 | 15.29 | 15.02 | 14.65 | -16.32 | -16.71 | 16.83 | 18.41 | 17.19 | 388 (3.76) | 162 (1.57) | 43 (0.41) | <3 (0.03) | np |
| NGC 5283 | 18.24 | 16.92 | 16 | -15.45 | -16.57 | 17.34 | 18.96 | 19.13 | 582 (2.88) | 418 (2.07) | 237 (1.18) | 91 (0.45) | v |
| NGC 5347 | 18.13 | 17.15 | 16.88 | -15.00 | – | 17.79 | 19.80 | 18.51 | 267 (1.76) | 159 (1.05) | 83 (0.55) | 24 (0.16) | 0 |
| NGC 5548 | 14.31 | 14.17 | 13.98 | -19.87 | -20.00 | 15.93 | 18.35 | 10.84 | 1213 (3.65) | 216 (0.65) | <22 (0.07) | <10 (0.03) | 0p |
| NGC 5674 | 18.05 | 16.97 | 16.61 | -16.65 | -17.65 | 17.63 | 19.67 | 18.32 | 966 (2.00) | 599 (1.24) | 292 (0.60) | 97 (0.20) | 0 |
| NGC 5695 | 19.11 | 17.6 | 16.6 | -14.90 | -16.26 | 18.18 | 19.48 | 19.94 | 767 (2.81) | 584 (2.14) | 344 (1.26) | 147 (0.54) | v |
| NGC 5728 | 21.1 | 17.52 | 14.42 | -13.67 | -16.35 | 19.48 | 18.69 | 19.22 | 1148 (6.38) | 846 (4.70) | 656 (3.64) | 369 (2.05) | 0r |
| NGC 5940 | 15.43 | 15.31 | 15.26 | -20.12 | -20.28 | 17.36 | 19.74 | 11.63 | 1042 (1.59) | 118 (0.18) | <40 (0.06) | <20 (0.03) | 0p |
| NGC 6300 | 21.1 | 18.62 | 17.62 | -12.81 | – | 19.6 | 19.99 | 20.00 | 123 (1.77) | 106 (1.53) | 78 (1.13) | 46 (0.67) | 0 |
| NGC 6814 | 13.25 | 13.13 | 13.02 | -18.27 | – | 15.26 | 17.47 | 9.93 | 279 (2.79) | 25 (0.25) | <7 (0.07) | <3 (0.03) | 0p |
| NGC 6951 | 18.23 | 16.9 | 13.74 | -14.60 | -16.55 | 17.25 | 18.73 | 18.64 | 474 (5.15) | 417 (4.53) | 344 (3.74) | 222 (2.41) | 0r |
| NGC 7130 | 15.98 | 15.17 | 13.47 | -18.13 | -18.87 | 15.53 | 18.64 | 20.04 | 3333 (10.65) | 2601 (8.31) | 1908 (6.09) | 266 (0.85) | 0 |
| NGC 7212 | 18.03 | 17.19 | 16.43 | -16.47 | -17.59 | 17.2 | 19.53 | 19.54 | 1310 (2.54) | 980 (1.90) | 518 (1.00) | 134 (0.26) | 0 |
| NGC 7319 | 20.51 | 18.91 | 18.91 | -14.05 | -15.41 | 20.15 | 20.86 | 19.84 | 441 (1.01) | 349 (0.80) | 247 (0.57) | 109 (0.25) | 0 |
| NGC 7469 | 13.22 | 13.08 | 12.65 | -20.85 | -20.98 | 15.14 | 16.85 | 11.83 | 1376 (4.35) | 506 (1.60) | 39 (0.12) | <9 (0.03) | 0pr |
| NGC 7479 | 19.56 | 18 | 16.89 | -14.01 | -15.34 | 18.49 | 19.91 | 20.05 | 367 (2.38) | 310 (2.01) | 205 (1.33) | 89 (0.58) | 0 |
| NGC 7496 | 16.48 | 15.43 | 14.35 | -16.23 | -17.18 | 15.75 | 17.55 | 17.40 | 538 (5.02) | 272 (2.54) | 143 (1.33) | 45 (0.42) | 0 |
| NGC 7674 | 16.47 | 15.89 | 15.69 | -18.52 | -19.16 | 16.4 | 18.89 | 16.48 | 1082 (1.93) | 510 (0.91) | 177 (0.32) | 50 (0.09) | n |
| NGC 7743 | 17.22 | 16.01 | 15.04 | -15.71 | -16.48 | 16.38 | 18.41 | 18.90 | 463 (4.18) | 316 (2.85) | 152 (1.37) | 48 (0.43) | n |
| UGC 1214 | 17.44 | 16.51 | 15.41 | -16.75 | -17.60 | 16.85 | 18.87 | 19.43 | 1333 (3.99) | 945 (2.83) | 522 (1.56) | 137 (0.41) | n |
| UGC 1395 | 18.52 | 17.35 | 17.26 | -15.69 | -16.79 | 18.4 | 20.06 | 18.46 | 381 (1.23) | 270 (0.80) | 177 (0.52) | 40 (0.12) | 0 |
| UGC 2456 | 16.53 | 15.85 | 15.36 | -17.11 | -17.76 | 15.84 | 18.31 | 17.75 | 598 (2.57) | 333 (1.43) | 143 (0.61) | 44 (0.19) | 0 |
| UGC 6100 | 18.84 | 17.84 | 16.63 | -15.94 | -16.99 | 18.28 | 20.11 | 21.03 | 2219 (3.88) | 1830 (3.20) | 1022 (1.79) | 297 (0.52) | n |
| UGC 12138 | 14.96 | 14.73 | 14.62 | -19.98 | -20.19 | 16.38 | 18.88 | 11.64 | 1054 (2.18) | 232 (0.48) | <34 (0.07) | <15 (0.03) | np |
| UM 625 | 17.44 | 16.35 | 16.15 | -17.39 | -18.29 | 17.53 | 19.39 | 17.37 | 887 (1.83) | 436 (0.90) | 252 (0.52) | 53 (0.11) | 0 |

Col. (1): Galaxy name; Col. (2): Magnitude within 0.3″ radius. Col. (3): Magnitude within 1″ radius. Col. (4): Magnitude within the maximum radius. Col. (5): Absolute magnitude within a projected radius of 100 pc. Col. (6): Absolute magnitude within 300 pc. Col. (7) & (8): Differential surface brightness at 0.3″ and 1″ respectively. Col. (9): Differential surface brightness at the half-light radius. Col. (10): Computed maximum radius in pc and arcsec in brackets. Col. (11), (12) & (13): Radius enclosing 80%, 50% and 20% of the flux within R$_{max}$, in pc (same in arcsec in brackets). Col. (14): Classification of the profiles from Figs. 3.11 – 3.13. The type of profile is coded with the letters: 'e' for an exponential profile, 'v' for a de Vaucouleurs law, 'n' when a Nuker law is seen, and '0' if the profile does not fall in any of the former categories. A letter 'p' is added when there is a point-like nucleus present, and an 'r' if there is a ring visible in the image.

All the magnitudes are calculated in the STMAG system and corrected for galactic extinction.

[a] In these cases R$_{max}$ is limited by the border of the field of view and not by the integration.

[b] Occulting finger of the HRC limits the radius for which the asymmetry parameter (see text) is computed (smaller than R$_{max}$).

As explained above, saturation might affect the flux in some nuclei. This effect can be corrected straightforwardly for the objects overcoming the saturation threshold which have also short exposure images. First we checked that from a radius of 0.1″ outwards, the surface brightness profiles calculated from both images were coincident. Then the inner 8 pixels of the saturated and high S/N image were replaced by the data from the unsaturated image. The final analysis was carried out on this corrected profile. For the saturated objects with just one image we performed a $\chi^2$ fit of a Tinytim-generated PSF to the wings of the nuclear PSF. The fit was done in the range of 5–12 pixels (0.13″–0.32″), range in which the pixels are not severely affected by the saturation and the S/N is still high. We considered possible focus changes by allowing the PSF to be broadened up to a 10%, choosing the best fit from the whole set of different broadenings. The inner 0.2″ of the galaxy was replaced by the fitted PSF. We checked this method with those core-saturated galaxies which have additional non-saturated exposures, obtaining a good agreement with the fluxes calculated from the combined profiles. Figure 3.14 show the fitted PSF for these four nuclei. The resulting corrections calculated range from 0.06 mag (Mrk 915) to 0.36 mag (NGC 5273). The nucleus of NGC 5940 does not reach the saturation threshold, but it is close to it. It has only a long exposure image, in which it does not seem to be affected by saturation. The correction that we expect for this object should be smaller than that for Mrk 493 or Mrk 915, which have brighter nuclei.

The magnitudes given in Table 3.4 depend on the determination of $R_{max}$, so one has to take this into account when using these fluxes. In order to illustrate this we have compared the total fluxes of some of our galaxies with the fluxes presented in Storchi-Bergmann et al. (1995) and Kinney et al. (1993). The compared subsamples are: NGC 3982, NGC 4258, NGC 5005, NGC 5256, NGC 5674 and Mrk 477, that have been studied by Kinney et al. (1993) and have published fluxes at ∼2700 Å and spectral slopes ($\beta$); and the subsample NGC 3081, NGC 3393, NGC 5135, NGC 5728, NGC 1672, NGC 7130 and NGC 7496, that have been studied as well by Storchi-Bergmann et al. (1995), giving fluxes at 2900 and 3500 Å. Figure 3.15 shows the comparison between their measurements and ours. A good general agreement is found. When comparing the fluxes several issues have to be taken into account, the different instrumental set-up being the most determining. In order to have a good S/N we have measured inside a radius $R_{max}$, while they used the aperture of the IUE slit, that is 10″×20″. This is equivalent in surface to a circular aperture of 8″, although the flux depends on the light distribution of the object and the orientation of the slit. Thus, when we use apertures of 8″ the agreement is very good, except for NGC 4258 and NGC 5005, for which we measure a flux 1.9 and 2.5 times higher respectively. In these cases the isophotes are clearly elongated, so the flux is expected to vary significantly with the slit orientation. Moreover, because the calculation of $R_{max}$ implies an azimuthal average then some bright features can lie out of this region. One example of this is NGC 5674, that has an external ring-like structure which is outside of $R_{max}$, but fits in a 8″ aperture. The fluxes at 3300 Å have been interpolated between the fluxes at 2900 Å

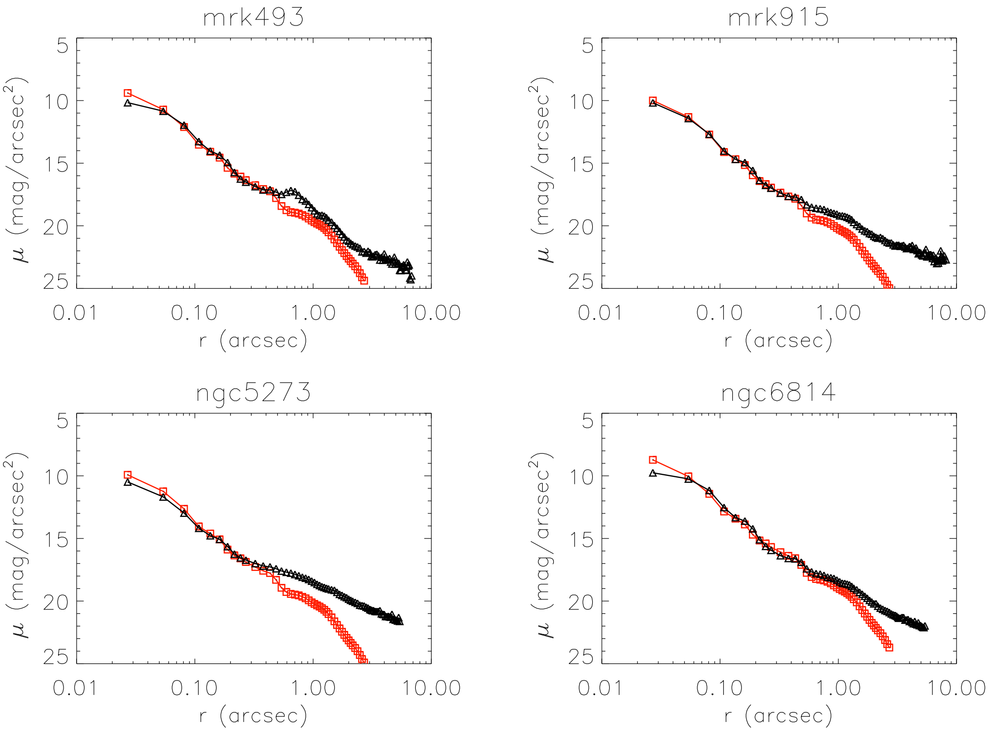

Figure 3.14: PSF fit to the nucleus for the saturated objects with two images. The fitted PSF (red line and squares) is overplotted to the surface brightness curve (black line and triangles) for each object. The most affected nucleus is NGC 6814, while Mrk 915 has barely lost flux in the saturated image.

and 3500 Å given by Storchi-Bergmann et al. (1995), or corrected from the fluxes at 2700 Å given by Kinney et al. (1993) using the value of $\beta$ that they calculate. In Table 3.5 we list the calculated photometric values for these objects.

Table 3.5: Comparison of flux measurements with literature data

| **Name** | **R**$_{max}$ ($''$) | **F**$_{3300}$ **(R**$_{max}$**)** | **F**$_{3300}$ **(8$''$)** | **F**$_{3300}$ **(10×20$''$)** |
|---|---|---|---|---|
| Mrk477$^a$ | 3.4 | 2.3 | 2.8 | 2.4 |
| NGC1672 | 10.2 | 36.2 | 32.5 | 31.0 |
| NGC3081 | 6.4 | 3.7 | 4.3 | 3.5 |
| NGC3393 | 4.7 | 2.7 | 3.6 | 3.3 |
| NGC3982$^a$ | 6.4 | 3.1 | 4.9 | 4.0 |
| NGC4258$^a$ | 6.2 | 13.0 | 21.7 | 11.2 |
| NGC5005$^a$ | 12.2 | 17.0 | 10.1 | 4.0 |
| NGC5135 | 6.5 | 10.0 | 10.8 | 10.4 |
| NGC5256$^a$ | 2.7 | 1.2 | 2.5 | 2.5 |
| NGC5674$^a$ | 2.0 | 0.7 | 2.1 | 2.1 |
| NGC5728 | 6.4 | 3.5 | 3.7 | 4.2 |
| NGC7130 | 10.7 | 13.0 | 9.8 | 8.0 |
| NGC7496 | 5.0 | 6.3 | 7.4 | 8.0 |

This table shows the comparison between our measurements and the values published by Kinney et al. (1993) and Storchi-Bergmann et al. (1995).
Col. (1): galaxy name; Col. (2): maximum radius; Col. (3): UV flux measured at maximum radius; Col. (4): UV flux measured at 8$''$ radius; Col. (5): UV flux from literature at 3300Å. Units of Col. (3) – (5) are $10^{-15}$ erg/s/cm$^2$/Å. $^a$Fluxes in Col. (5) have been calculated using the spectral slope given in Kinney et al. (1993) for these galaxies.

Figure 3.16 presents comparative histograms of the values of the magnitudes measured within 0.3$''$, 1$''$, R$_{max}$, and the magnitude in a circular ring between 0.3 and 1$''$. It is shown that Sy1 nuclei are brighter at small radii. However this trend is not observed when the contribution of the inner 0.3$''$ is subtracted, indicating that the light in Sy1 is dominated by the compact nucleus, and the difference of the subsamples in terms of magnitude is not large. The bright outlier object in the plots is Circinus galaxy, that due to its low galactic latitude has a large extinction correction that makes it even brighter than the Messier objects of the sample. In Figure 3.17 we plot the surface brightness $\mu$ at 0.3$''$ and 1$''$. The calculation of the surface brightness at 1$''$ is practically unaffected by the Sy1 nuclei, what causes the dissimilarity between the panels of Figure 3.17. This indicates no significant difference among the host of Sy1 and Sy2, in terms of surface brightness. The difference would be due just to the presence of the nuclear source in Sy1.

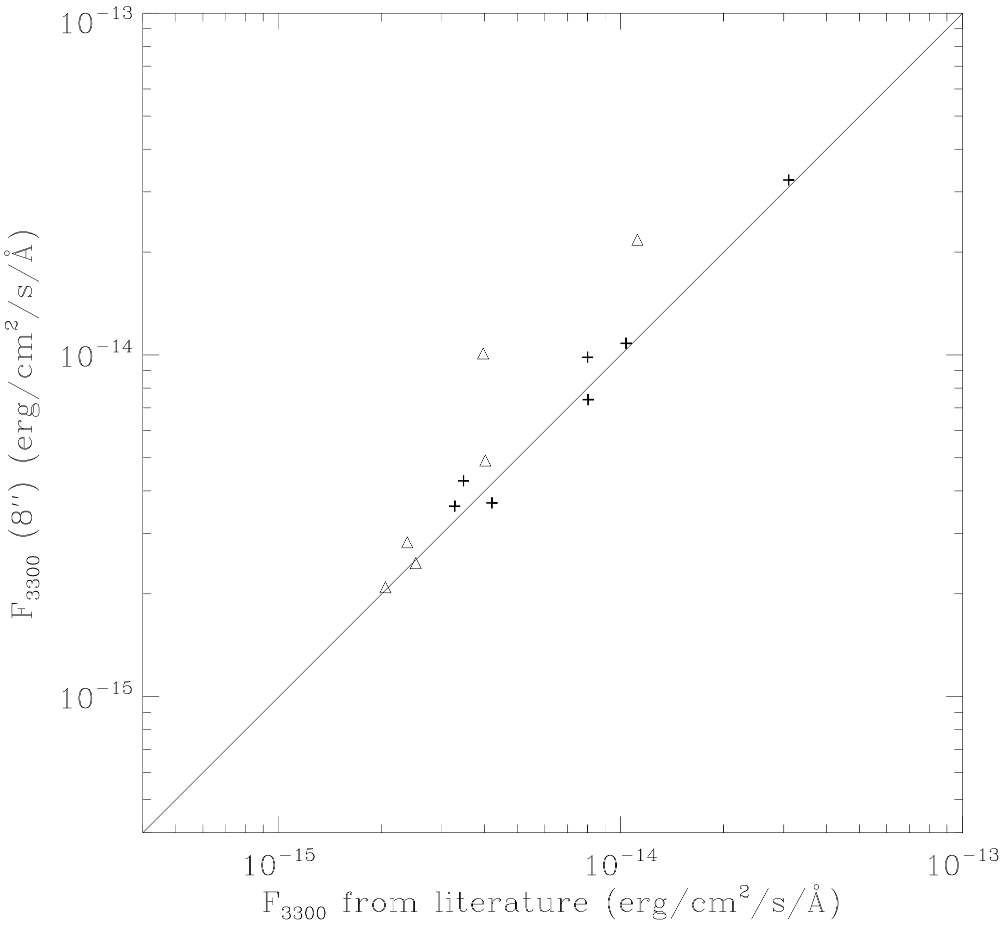

Figure 3.15: Comparison of the fluxes that we have measured with data from the literature. Triangles represent fluxes from Kinney et al. (1993), while crosses represent fluxes from Storchi-Bergmann et al. (1995). The two triangles that fall over the unity line are NGC 4258 and NGC 5005 (see discussion in text).

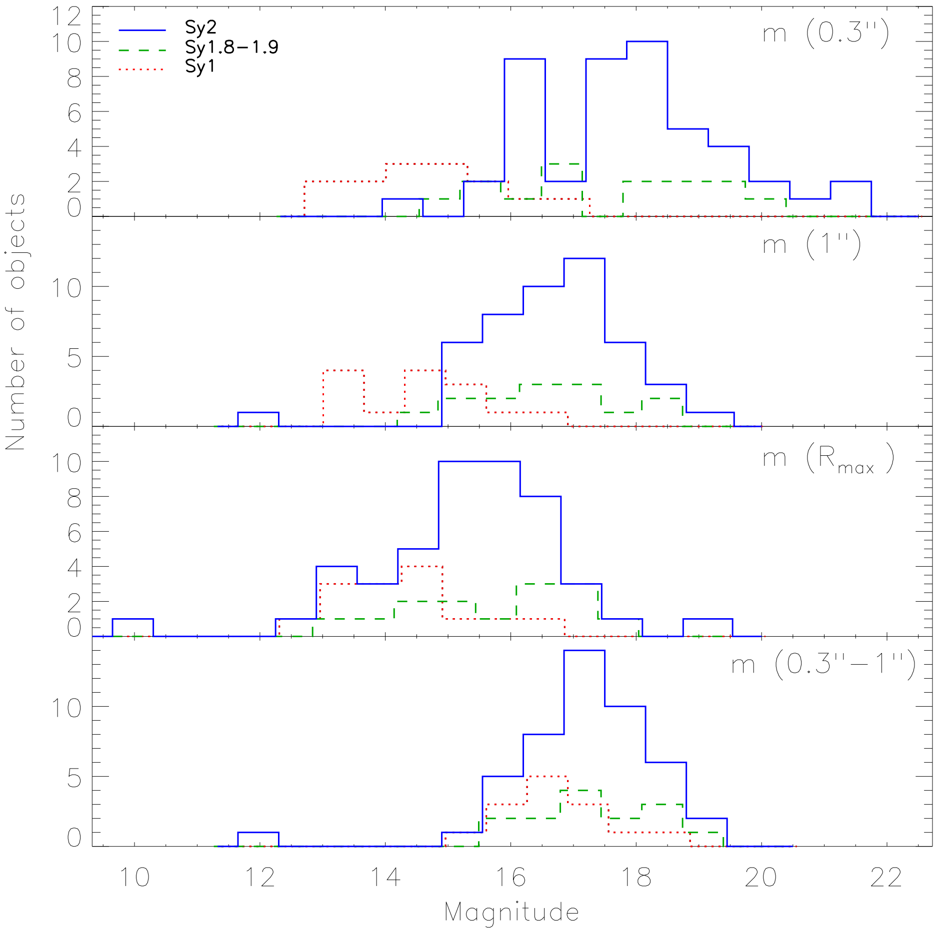

Figure 3.16: Comparative histogram of the magnitudes measured within different radii. Sy2 are plotted in full blue line; Sy1 in dotted red line; Sy1.8-1.9 in dashed green line. Sy1 nuclei tend to be brighter than the others, although this trend is softened when larger radii are considered. The lower panel shows the magnitude between 0.3 and 1″ apertures.

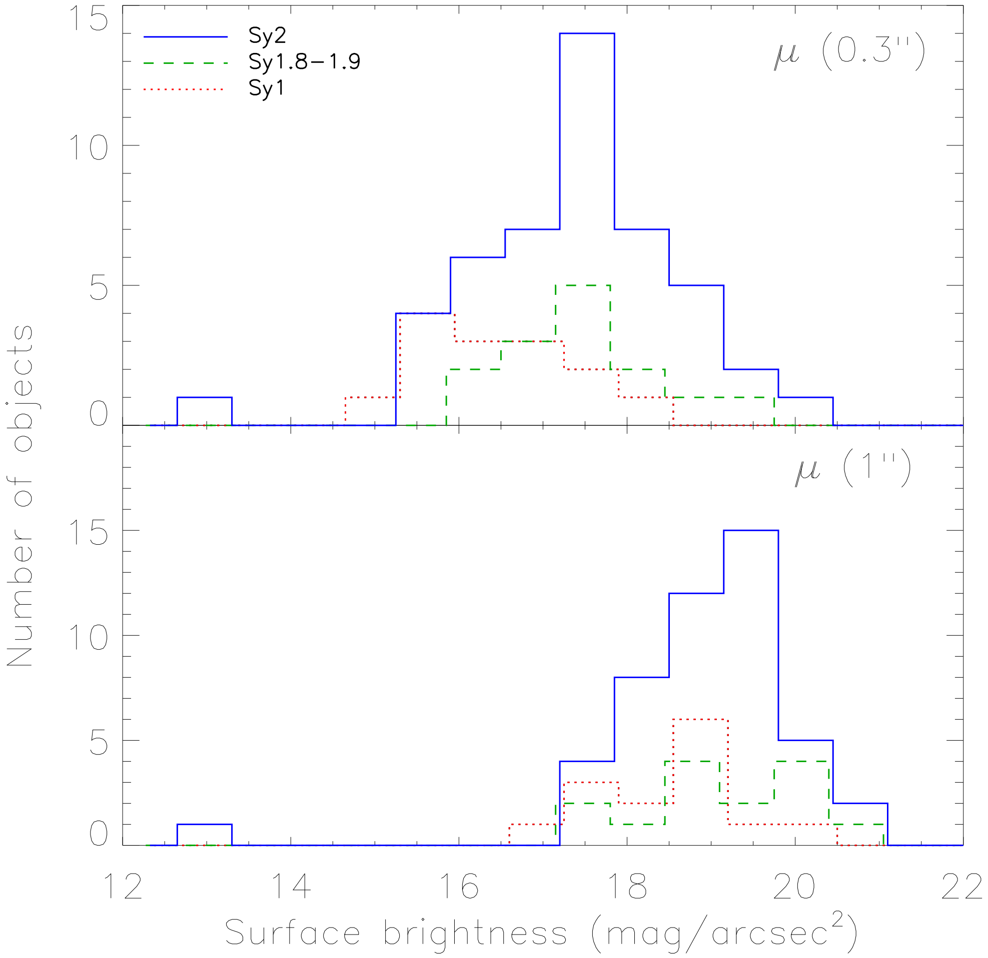

Figure 3.17: Comparative histogram of the values of the surface brightness measured at two different radii. At 0.3″ Sy1 nuclei are brighter than those from other types. At 1″, however, there is no difference in the distribution of $\mu$.

### 3.4.3 Morphological analysis: Compactness and Asymmetry parameters

The morphology of extended objects can be quantified with the concentration or compactness (C) and asymmetry (A) parameters. Due to the irregular distribution of light at $\lambda3300$, these parameters give a better description of the morphology than the classical bulge-disk decomposition. They also reflect the contribution of clumpy structure, such as star clusters and star-forming regions.

The definition of C is based in the curve of growth and depends on the ratio of two radii enclosing some fraction of the total flux. We have used the formula from Bershady et al. (2000),

$$C = 5\log(r_{80}/r_{20}),$$

where $r_{80}$ and $r_{20}$ are the radii enclosing 80% and 20% of the total flux within $R_{max}$. Figure 3.18 shows the distribution of C for the different types of Sy galaxies. The distribution of Sy2 and Sy1 are clearly different, being the Sy1 far more compact. The intermediate types show a behaviour in between the other two subsamples. We find that the values of C for Sy2 are similar to those of local normal galaxies studied in the B band by Bershady et al. (2000). However, our Sy1 have on average much higher values of C. The occurrence of a compact nucleus in the near-UV is determinant for a high value of C to be measured.

The asymmetry of a particular galaxy is calculated by subtracting a 180° rotated image from the original one. The residuals in this image are summed up and then normalized dividing by the total flux in the original image. The sum can be quadratic or in absolute value. The rotation center is the nucleus of the galaxy. The formula that summarizes the process is (Conselice, 1997)

$$A^2_{rms} = \frac{\sum (F_{ij} - F_{ji})^2}{2\sum {F_{ij}}^2},$$

where $F_{ji}$ is the rotated original image ($F_{ij}$). A is calculated only taking into account the region inside $R_{max}$, otherwise the contribution of the noise would become important. In the case of M 81 and M 51 we have measured only to a radius smaller than $R_{max}$ (5.67″ for M 81 and 6.91″ for M 51), just enough to prevent the occulting 'finger' of the ACS to enter in the region studied, which would introduce a big systematic uncertainty in the asymmetry determination (although it is uninmportant for the photometry). We decided to use this definition of $A_{rms}$ after trying out as well an absolute value sum ($A_{abs}$). In general, $A_{rms}$ weighs more the bright features, such as star forming regions, and should be less sensitive to the noise. We have checked that the choice of the exact formula does not change the general results, as well as measuring within a half-light radius does not change the general distribution of the points. Figs. 3.19 and 3.20 show the histogram of $A_{rms}$ values and a $A_{rms}$ vs C plot. The values of $A_{rms}$ for Sy2 are systematically higher, covering a wide range of values, while Sy1 show a very small scatter around $A_{rms}$=0.2. We calculated the asymmetry of some isolated point-like sources leading to a value close to 0.2, so this seems to be a lower limit for the asymmetry calculated by this

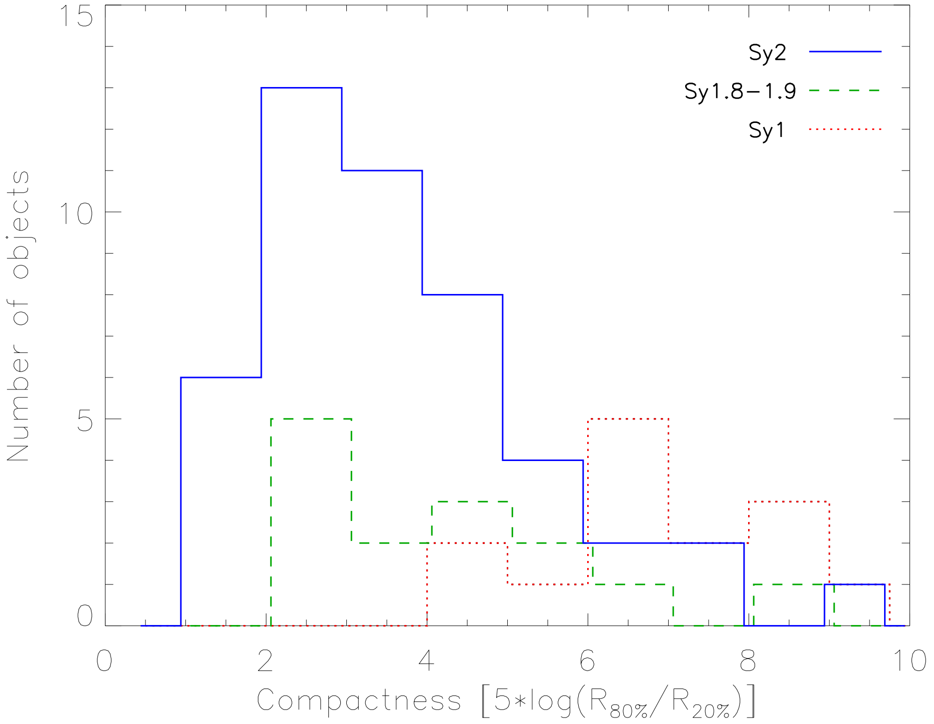

Figure 3.18: Histogram of compactness for Sy subsamples. Type of line and colors codify the Sy type in the same way as in previous figures.

method. This is a combination of the contribution of the noise and subsampling effects due to the value of the PSF FWHM. Thus, $A_{rms}$ is dominated by the nuclear PSF in Sy1, while extended emission and star-forming regions, together with a smaller nuclear contribution, determines the higher values in Sy2. In Figure 3.20 it is clearly seen how Sy1.8–1.9 reproduce characteristics of both Sy types 1 and 2. In the plot $A_{rms}$ vs C there is a clear trend that $A_{rms}$ decreases with increasing C, as had been observed before for normal galaxies (see e.g. Bershady et al., 2000). In this plot the correlation saturates when we explore high values of C, due to the limit in $A_{rms}$. Results of the calculation of C and A are summarized in Table 3.6.

Table 3.6: Results from the shape and stellar clusters general analysis

| Galaxy Name (1) | C (2) | $A_{rms}$ (3) | $f_{clus}$ (4) | $\log(F_{clus})$ $erg/cm^2/s/Å$ (5) |
|---|---|---|---|---|
| CGCG 164-019 | 6.42 | 0.17 | 0.022 | -16.69 |
| Circinus | 1.7 | 0.79 | 0.016 | -14.12 |
| ESO 103-G35 | 2.41 | 0.55 | 0 | – |
| ESO 137-G34 | 1.93 | 0.85 | 0.0058 | -17.12 |
| ESO 138-G1 | 3.84 | 0.56 | 0 | – |
| ESO 362-G8 | 3.53 | 0.44 | 0 | – |
| fairall49 | 2.84 | 0.72 | 0.033 | -16.31 |
| IC 2560 | 5.19 | 0.47 | 0 | – |
| IC 4870[a] | >9.22 | 0.21 | 0.033 | -15.71 |
| IC 5063 | 2.07 | 0.77 | 0.014 | -16.62 |
| Mrk 6[a] | >5.72 | 0.13 | 0 | – |
| Mrk 40[a] | >6.97 | 0.17 | 0 | – |
| Mrk 42[a] | >7.17 | 0.21 | 0.038 | -16.08 |
| Mrk 231[a] | >8.12 | 0.17 | 0.009 | -16.16 |
| Mrk 334 | 5.17 | 0.28 | 0.13 | -15.45 |
| Mrk 461 | 7.3 | 0.19 | 0.0081 | -16.58 |
| Mrk 471 | 2.07 | 0.71 | 0.032 | -16.45 |
| Mrk 477 | 6.24 | 0.16 | 0 | – |
| Mrk 493[a] | >6.03 | 0.30 | 0.034 | -15.68 |
| Mrk 516 | 4.18 | 0.59 | 0.033 | -16.78 |
| Mrk 915[a] | >6.58 | 0.11 | 0 | – |
| Mrk 1210 | 7.22 | 0.29 | 0.016 | -16.40 |
| NGC 449 | 5.78 | 0.47 | 0.017 | -16.81 |
| NGC 1144 | 2.91 | 0.88 | 0.032 | -16.44 |
| NGC 1320 | 3.72 | 0.36 | 0 | – |
| NGC 1672 | 1.61 | 0.94 | 0.13 | -14.28 |
| NGC 2639 | 2.44 | 0.54 | 0.0027 | -17.02 |
| NGC 3031[b,c] | 2.64 | 0.15 | 0 | – |
| NGC 3081 | 3.28 | 0.68 | 0.078 | -15.43 |
| NGC 3227[a] | >7.53 | 0.15 | 0.003 | -16.58 |
| NGC 3362 | 2.99 | 0.58 | 0.04 | -16.45 |
| NGC 3393 | 2.48 | 0.43 | 0 | – |
| NGC 3486 | 3.29 | 0.22 | 0 | – |
| NGC 3516[a] | >9.38 | 0.24 | 0 | – |
| NGC 3786 | 5.88 | 0.22 | 0.012 | -16.74 |
| NGC 3982 | 3.06 | 0.40 | 0.031 | -16.10 |
| NGC 4253 | 8.46 | 0.22 | 0.02 | -16.04 |
| NGC 4258 | 2.2 | 0.45 | 0.035 | -15.18 |
| NGC 4303 | 2.03 | 0.29 | 0.13 | -14.74 |
| NGC 4395[a] | >4.35 | 0.15 | 0.0093 | -17.07 |
| NGC 4565 | 2.21 | 0.60 | 0 | – |
| NGC 4593[a] | >6.34 | 0.50 | 0.0023 | -16.29 |

Continued on Next Page...

Table 3.6 – Continued

| Galaxy Name (1) | C (2) | $A_{rms}$ (3) | $f_{clus}$ (4) | $\log(F_{clus})$ erg/cm$^2$/s/Å (5) |
|---|---|---|---|---|
| NGC 4725 | 2.69 | 0.57 | 0 | – |
| NGC 4939 | 3 | 0.56 | 0.01 | -16.95 |
| NGC 4941 | 3.2 | 0.39 | 0.0087 | -16.73 |
| NGC 5005[b] | 2.5 | 0.85 | 0.021 | -19.05 |
| NGC 5033 | 3.78 | 0.23 | 0.007 | -16.05 |
| NGC 5135 | 2.92 | 0.80 | 0.3 | -14.40 |
| NGC 5194[b,c] | 4.31 | 0.34 | 0.145 | -14.65 |
| NGC 5256 | 5.61 | 0.52 | 0.045 | -16.23 |
| NGC 5273[a] | >8.82 | 0.18 | 0.0056 | -16.55 |
| NGC 5283 | 3.3 | 0.33 | 0.063 | -16.04 |
| NGC 5347 | 4.05 | 0.48 | 0 | – |
| NGC 5548[a] | >6.92 | 0.18 | 0.0055 | -16.29 |
| NGC 5674 | 3.95 | 0.31 | 0.11 | -16.04 |
| NGC 5695 | 2.99 | 0.44 | 0.039 | -16.49 |
| NGC 5728 | 1.8 | 0.76 | 0.04 | -15.61 |
| NGC 5940[a] | >4.11 | 0.09 | 0 | – |
| NGC 6300 | 1.78 | 0.86 | 0 | – |
| NGC 6814[a] | >4.79 | 0.13 | 0 | – |
| NGC 6951 | 1.37 | 0.88 | 0.13 | -14.82 |
| NGC 7130 | 4.96 | 0.70 | 0.25 | -14.43 |
| NGC 7212 | 4.29 | 0.51 | 0.07 | -16.17 |
| NGC 7319 | 2.53 | 0.65 | 0.023 | -17.64 |
| NGC 7469[a] | >8.86 | 0.43 | 0.115 | -14.44 |
| NGC 7479 | 2.69 | 0.77 | 0.01 | -17.20 |
| NGC 7496 | 3.9 | 0.45 | 0.38 | -14.60 |
| NGC 7674 | 5.06 | 0.47 | 0.11 | -15.67 |
| NGC 7743 | 4.13 | 0.33 | 0 | – |
| UGC 1214 | 4.18 | 0.51 | 0 | – |
| UGC 1395 | 4.1 | 0.26 | 0 | – |
| UGC 2456 | 4.34 | 0.79 | 0.3 | -15.11 |
| UGC 6100 | 3.95 | 0.77 | 0 | – |
| UGC 12138[a] | >6.26 | 0.10 | 0 | – |
| UM 625 | 4.5 | 0.33 | 0.1 | -15.90 |

Col. (1): Galaxy name; Col. (2): Compactness. Col. (3): Asymmetry. Col. (4): Fraction of light in stellar clusters. Col. (5): Logarithm of the total flux of light in clusters in erg/s/cm$^2$/Å.

[a] These objects posses a very bright compact nucleus that affects the determination of $R_{20}$ (see text). In these cases we can only set a lower limit for the compactness parameter.

[b] In these cases $R_{max}$ is limited by the border of the field of view and not by the integration. Compactness and asymmetry are computed based on this smaller $R_{max}$.

[c] Occulting finger of the HRC limits the radius for which the asymmetry parameter (see text) is computed (smaller than $R_{max}$).

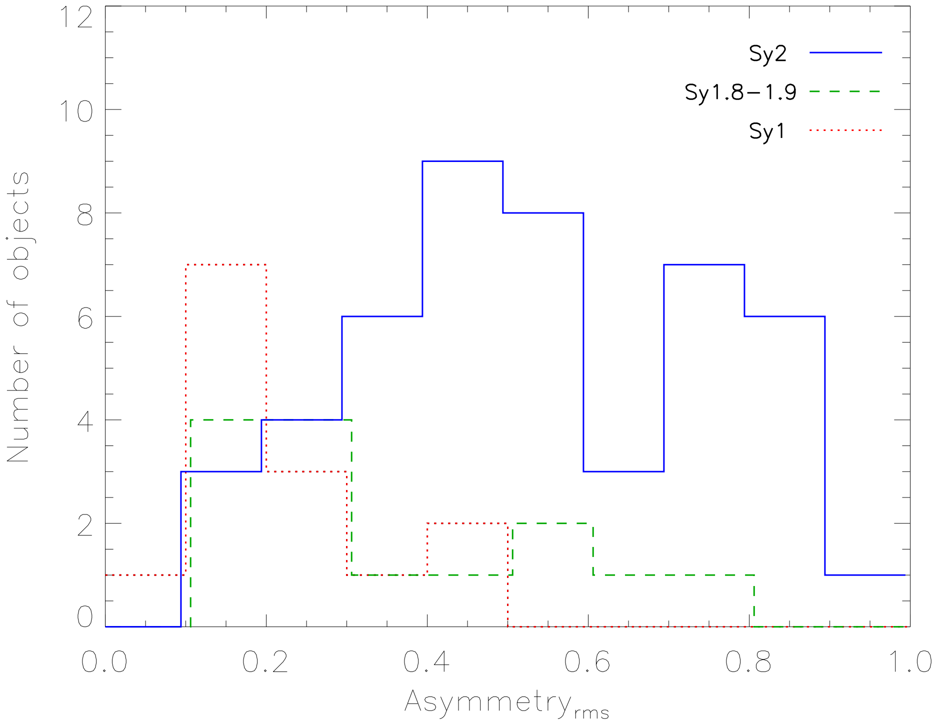

Figure 3.19: Histogram of asymmetry for Sy subsamples. The symbols are the same as in previous figures.

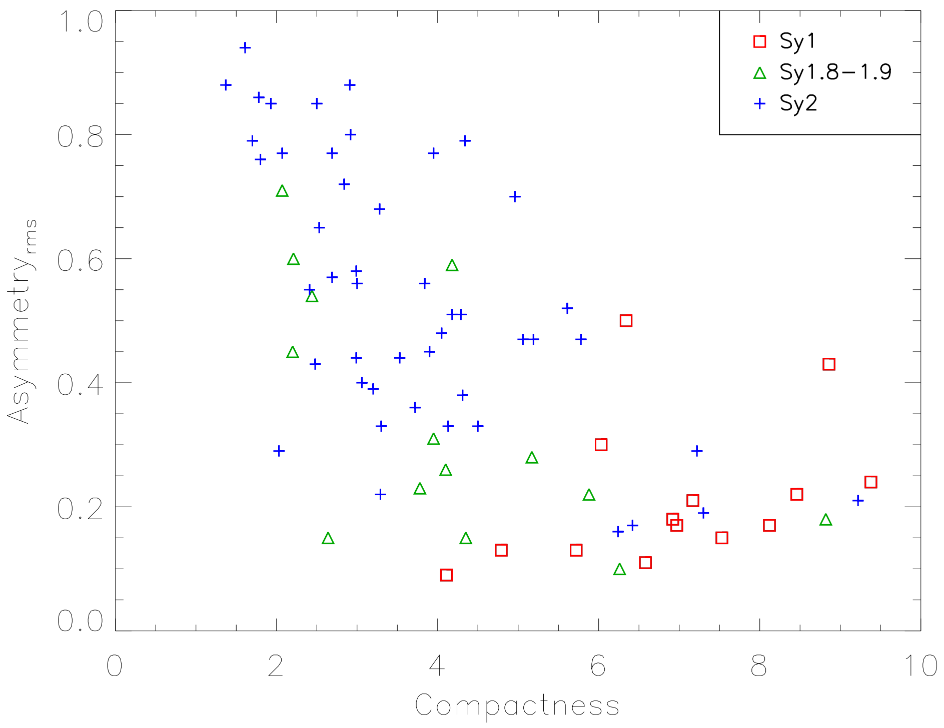

Figure 3.20: Asymmetry versus compactness plot for the galaxies in the sample. Crosses stand for Sy2 galaxies, while triangles represent intermediate types (with the same color key as in previous figures). Sy1 are plotted with squares.

### 3.4.4 Estimation of the fraction of light in clusters

In order to determine how important is the contribution of the star formation to the total UV flux we have estimated which fraction of the total flux comes from stellar clusters or very compact light emission (f$_{clus}$), not including the compact Sy1 nuclei. Several software packages were used to detect the clusters. We found that in many cases the highly varying background, and the large dynamical range in some of the images, were a problem for these algorithms to give a satisfying result. Also, the varied morphology became a problem for deciding an homogeneous and unbiased way to perform the analysis automatically. We obtained sometimes good results with IRAF task 'daofind', but it did not work well in crowded regions or with a highly varying background. Often we had to crop the resulting lists by hand and add some other objects. We thus decided to select the objects by eye inspection. To be sure that we did selections that were complete enough, we checked using linear and logarithmic displays, compared with the optical images in unclear cases, and compared with 'daofind' results. The selections were restricted to the region inside R$_{max}$, in which the total flux was measured, although sometimes there were obvious star clusters outside this region. See Figure 3.21 as an illustrative example. Note that not every clump was added, but only the ones which seemed compact enough to be considered individual clusters or tight aggregations of them. Selecting the clusters by hand proved to be effective, although the limiting magnitude cannot be determined due to the varying background. The completeness of the selection is not critical for this work. Instead, we were interested in checking how robust the estimation of the flux in clusters was with respect to different star cluster selections. Wilson et al. (2006) study the star cluster population in Arp220 with the ACS, finding the same problems. The manual cluster selection also proved to be efficient for them.

The flux determination was done with IRAF task 'phot'. We measured the flux within very small apertures, and then we applied aperture corrections from the enclosed energy curves of Sirianni et al. (2005). Using different apertures led to different results for f$_{clus}$, in part due to the use of a correction for point-like objects, when the star clusters may show a resolved structure, at least for large objects in nearby galaxies. However, in most objects, the variation of f$_{clus}$ when considering different apertures (as 3, 4, 5 or 6 pixels) was higher than the variation when using different selection methods. We therefore estimate that the main uncertainty source is the clustering of the objects and the highly varying background. Finally we decided to use an aperture of 4 pixels, as a compromise between the sampling effects of a smaller aperture and the possible aperture overlapping of a larger one, what would also introduce a larger uncertainty in the background subtraction. The background was calculated by measuring in an annulus of 6 pixel of inner radius and 2 pixel width in a median filtered image with a 15×15 pixel box. The fraction f$_{clus}$ was then determined summing up the total flux in all the objects detected inside R$_{max}$, local background subtracted and aperture corrected, and divided between the total flux within R$_{max}$. In Table 3.6 we give f$_{clus}$, as well as the logarithm of

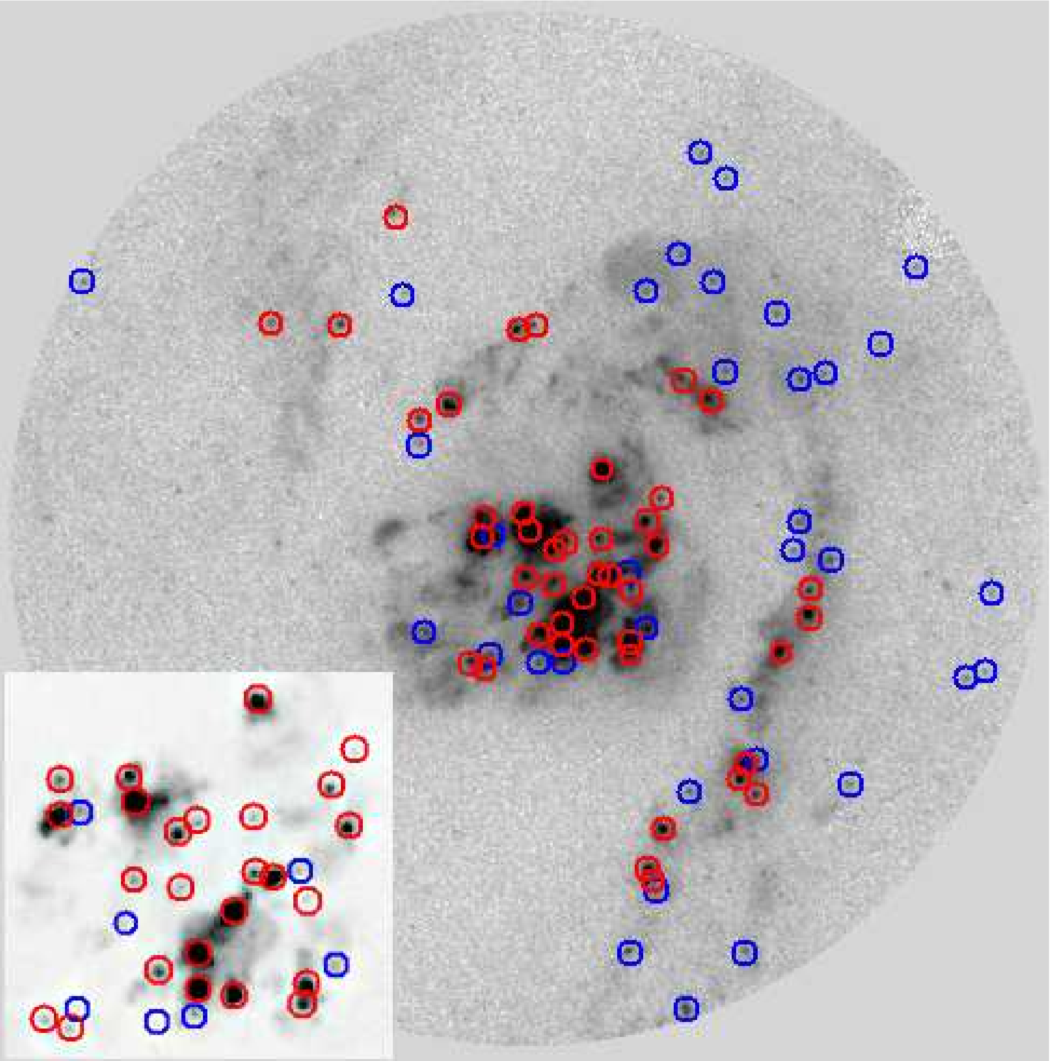

Figure 3.21: An example of the cluster selection for NGC 5135. Stellar clusters were identified combining a linear display to disentangle the brightest crowded regions (red circles), and then using a logarithmic display, in order to identify the faint population (blue circles). A close-up of the central region is shown in the lower left box.

the total flux in star clusters.

In some galaxies we could not detect any star cluster inside the $R_{max}$ aperture. This happens more often for Sy1 (6 out of 14 galaxies; or 43%) than in Sy2 (14/47; 30%) or intermediate types (5/14; 36%). Figure 3.22 shows a histogram of the distribution of $f_{clus}$ for the galaxies with detected clusters. Except for Mrk 231, no Sy1 show stellar clusters or star-forming regions contributing more than 5% to the total flux, while there are 13 ($\sim$ 28%) of the Sy2 that overcome this value. This confirms that Sy1 galaxies are core dominated objects, while clusters and star-formation account for a significant fraction of the light in Sy2. This fraction is smaller than that calculated for UV-selected starburst galaxies, in which light from clumpy structure is, on average, of the order of 20% of the total flux (Meurer et al., 1995), although these results are for a different UV filter, at 2200 Å.

In order to directly compare the flux coming from clusters among the different subsamples, we plot in Figure 3.23 a comparative histogram of the total luminosity from stellar clusters. Despite the small number of Sy1 and intermediate type galaxies involved, this Figure shows that these sources have a similar distribution of values to that of Sy2. This suggests that these sources have similar amounts of recent star formation, confirming that most of the differences seen in Figure 3.22 were due to the strong contribution from the nuclear point source in the former.

## 3.5 Conclusions

Based in a snapshot survey using the high resolution of the Advanced Camera for Surveys onboard HST, we have compiled a sample of 75 nearby Seyfert galaxies in the near-UV. These observations complete a very useful multi-wavelength database for these AGN, which have also optical and near-IR images available in the HST archive. We have carried out a general analysis of the near-UV images of this sample, consisting in the identification of unresolved compact nuclear sources, extraction of surface brightness profiles, photometry, determination of compactness and asymmetry parameters and identification of the star cluster population. The size of the sample allows us to compare the results of the analysis among different Sy types: Sy1 (including Sy1.2-1.5), Sy2 and intermediate types (Sy1.8-1.9).

The main conclusions from the photometric and morphological study are:

- In general, the morphology in the UV is very irregular, with clumpy and compact structure in most cases.
- Sy1 are completely PSF dominated objects in their inner regions, but Nuker law profiles are detected for some of the galaxies. Inspecting the surface brightness profiles we find 3/14 Sy1 galaxies, and 6/47 Sy2, which posses a star-forming ring. On the contrary, no star-forming rings are found within the intermediate Sy type subsample. Sy2 galaxies present the most varied and irregular profiles. Some profiles follow an exponential, de Vaucouleurs or Nuker law, but most of them cannot be easily classified.

- No nucleus is resolved for any of the Sy1 objects, while on the other hand, almost all Sy2 have the nucleus resolved. At least 5/14 Sy1.8-1.9 galaxies show an unresolved compact nucleus.
- In terms of surface brightness at $1''$, and also from the calculation of the integrated magnitude between $0.3''$ and $1''$, we find no significant difference between the host galaxies of Sy1 and Sy2 nuclei. The difference would arise solely due to the presence of the nuclear source in Sy1.
- Sy1 are very compact and have low values of asymmetry, while Sy2 show a very wide range of compactness and asymmetry values.

From the study of the fraction of light in clusters we conclude that:

- Bright star clusters are slightly more often seen in Sy2 (∼70%) than in Sy1 (∼57%), or in intermediate Sy types (∼64%).
- The distribution of the luminosity in star clusters does not change much among different Sy types, when considering only galaxies with detected clusters.
- The contribution of the clusters to the total flux is much more important in Sy2 (where it reaches up to 30%) than in the other Sy types, but this is at least partially due to the large contribution of the nuclear source in the Sy1 and intermediate Sy types.

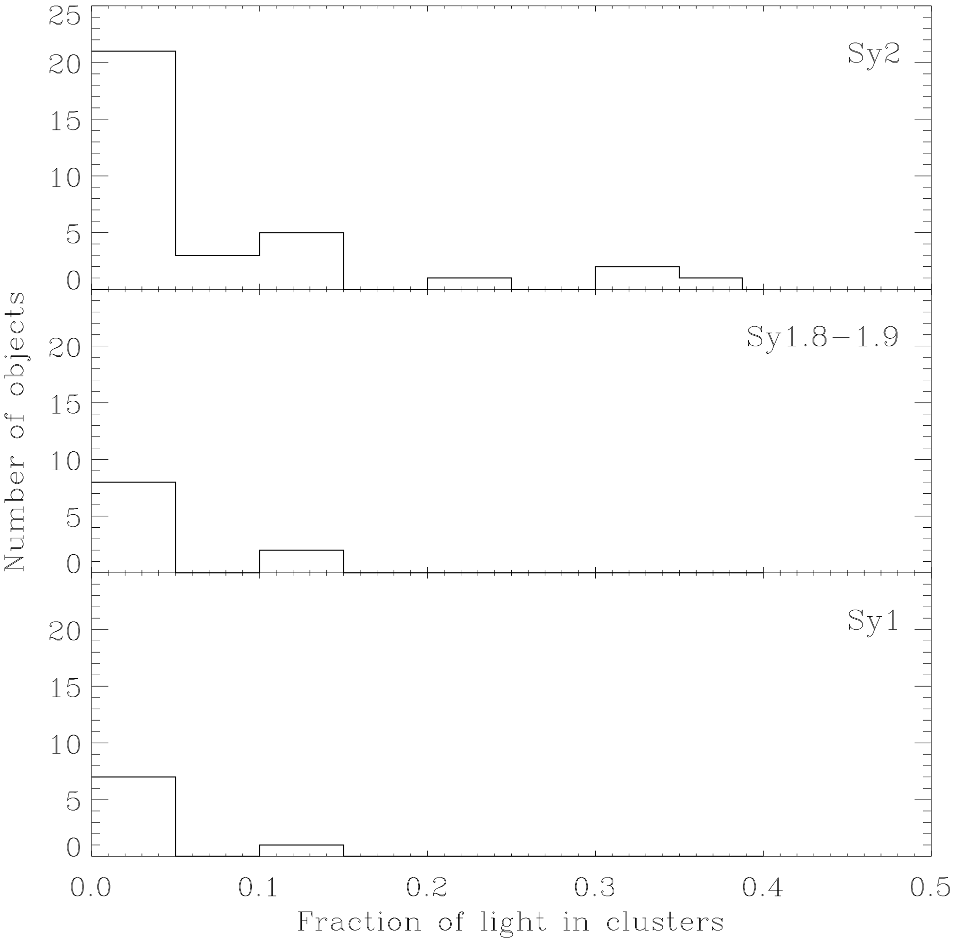

Figure 3.22: Histogram of the fraction of light in clusters ($f_{clus}$) for different Sy types. Only galaxies with detected star clusters have been included.

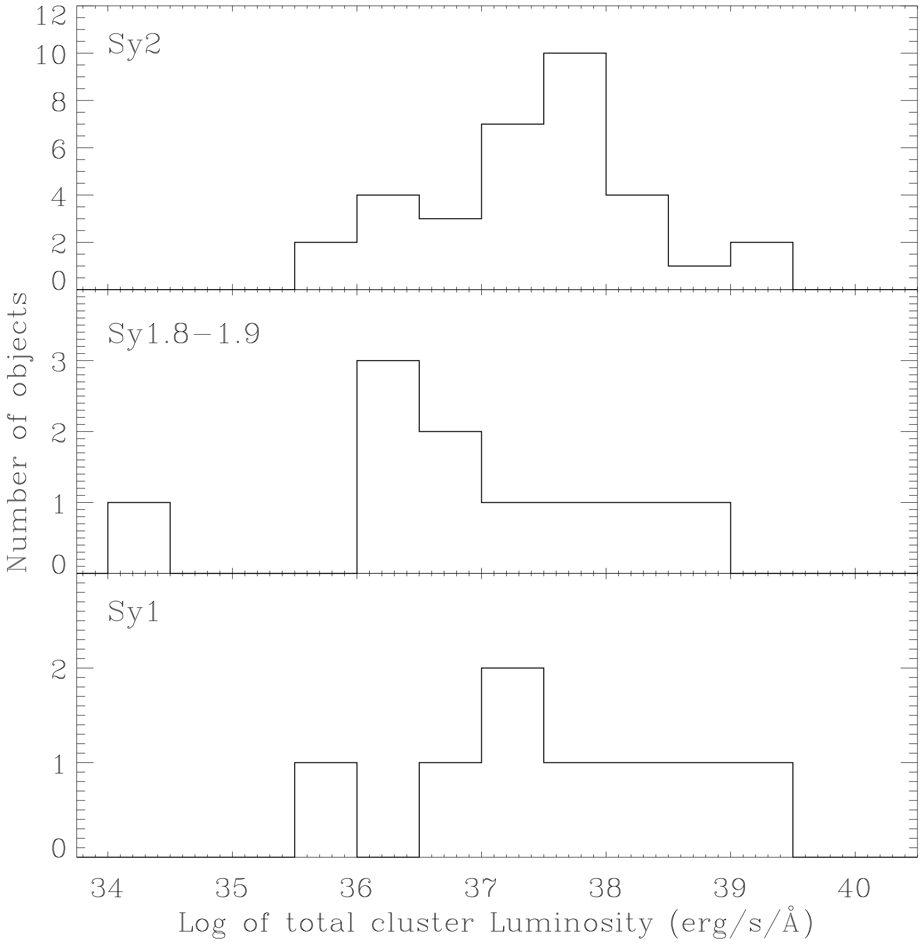

Figure 3.23: Histogram of the total Luminosity coming from star clusters for different Sy types. The three distributions look quite similar.

## Chapter 4

# Extended near-UV light in Seyfert galaxies

## Contents

## 4.1 Introduction

In the previous chapter we have constructed a useful reference atlas of 75 Sy galaxies which possess HST archival images of their nuclear region, in the near-UV, optical and near-IR, at a very high spatial resolution (∼0.05 arcsec). We have also performed a morphological and photometric analysis. We have confirmed the presence of star formation in the circumnuclear region of a fraction of the galaxies (∼60 per cent), and we have found that circumnuclear star clusters can be found equally in both Seyfert types. However we have also found extended emission, showing often a biconical structure, and/or bright filaments, which are unlikely to trace star-formation. To investigate the origin of this UV extended emission is the goal of the present chapter.

There are several processes that are expected to contribute to the extended light in the F330W filter. The most relevant ones are:

- **Stellar continuum**. If compact knots are detected, they are probably young/intermediate age massive star clusters, or clumps of them. But the extended UV emission could also be due to an unresolved population of smaller star-clusters, or generated by the disruption of ageing star clusters (Tremonti et al., 2001; Chandar et al., 2005), as well as emission from the underlying older stellar population of the galaxy.

- **Nebular continuum**. Radiation from free-free and free-bound electron transitions, as well as two photon decay of level $2\,^2S$ of H I, can be an important contribution in regions with ionised gas, and it is expected to be extended, as much of the ionised gas is.

- **Emission lines from ionised gas.** In the wavelength range covered by the F330W filter at the redshift range of the galaxies only two emission lines contribute significantly, [NeV]$\lambda\lambda$3346,3426.

- **Light from the AGN** can be scattered by free electrons or dust and contribute with extended emission.

In this chapter we aim to disentangle the contribution of the different processes that may contribute to the extended near-UV emission in Seyfert nuclei. With this purpose, and based in the Atlas presented, we focus our analysis on a subsample of galaxies in which the dominant morphology at near-UV wavelengths is extended emission that is not obviously associated to compact starbursts or star clusters, and for which both near-UV ACS data and WFPC2 [OIII] images exist. This work has been published in the journal Monthly Notices of the Royal Astronomical Society (Muñoz Marín et al., 2009).

## 4.2 Subsample construction and data used

Our sample comprises the galaxies of our Seyfert Atlas with extended emission, that are also studied by Schmitt et al. (2003). The latter work presents HST

[OIII] images of the nuclear region of 60 nearby Seyfert galaxies, the largest [OIII] imaging compilation of the Narrow Line Region (NLR) of nearby Sy's, which are imaged at a resolution comparable to ours. We end up with a final sample of 15 galaxies, from which 8 are Sy2 and 7 are Sy1. For the sake of simplicity we have included the 4 Sy1.5 and the one Sy1.8 (UGC 12138) in the Sy1 group, as they all have in common a very bright nuclear source that dominates the inner emission at near-UV wavelengths (see Chapter 3). The objects, together with some basic properties, are listed in Table 4.1. There is no significant difference between Sy1 and Sy2 subsamples, neither with respect to their mean distance (71 Mpc for Sy1, and 74 Mpc for Sy2), nor with their mean axial ratio (b/a of 0.80 for Sy1, while it is 0.74 for Sy2). This does not change when considering median values.

The F330W ACS images were reduced by the HST pipeline following the standard procedure of bias subtraction, flat-calibration and distortion correction. Then, the exposures were cleaned from cosmic rays by hand. The [OIII] images were reduced and provided by our collaborator Henrique Schmitt. They were obtained with the WFPC2, with the chip WFC in most cases, and with the PC for some objects; NGC 3393, was imaged with the WFPC before COSTAR, and had to be deconvolved. The majority of [OIII] images were taken with the linear ramp filter, whose flat-fielding is not performed by the HST pipeline, and requires a bit of extra work. For details on the reduction process of these data, see Schmitt et al. (2003) for the WFPC2 images, and Schmitt & Kinney (1996) for NGC 3393 data.

In addition to the near-UV band, we downloaded and reduced WFPC2 images of the galaxies trough the filter F547M. The use of these images has the advantage of minimising the contamination by strong emission lines, and that all the objects, except for NGC 7212 and UGC 1214, are imaged in this band (as it served in most cases for the continuum subtraction of the [OIII] image), what allows for a comparison between them. The images were used for the photometric analysis of Section 4.3.5. These images were reduced with the standard procedure using the HST pipeline. When more than one image were available, single exposures were combined and cleaned from cosmic rays with IRAF task 'crrej'. Remaining cosmic rays were eliminated by hand. Finally, the images were resampled to the ACS scale.

We completed the photometric set with NICMOS F160W images. This last filter has the advantage that there are data for all but one (NGC 7212) of the objects, and that it is so wide that we can neglect the contribution from emission lines. NICMOS single exposures were corrected for the 'pedestal effect' (produced by changes in the bias levels of the different chips during the exposure) with IRAF task 'pedsub', combined with the standard calibration pipeline, and resampled to ACS resolution.

Figure 4.1 shows a comparison between the near-UV ACS images and the narrow-band continuum subtracted [OIII]$\lambda\lambda$5007 images. This comparison shows a very similar morphology in most cases. In some cases, especially in those of clear bi-conical structure, the morphology is identical to that of the [OIII] (IC 5063, NGC 3393, and UGC 1214), implying that the near-UV emission is produced in the same region that the ionised gas, and thus nebular continuum and [NeV] emission

Table 4.1: Basic data and line ratios for the galaxies of the sample

| Object | Alternative name | Activity type | Distance (Mpc) | Scale (pc/") | $B_T$ (mag) | E(B-V) | b/a | $\frac{[OIII]}{[NeV]}$ | $\frac{[OIII]}{H\beta}$ | Ref. |
|---|---|---|---|---|---|---|---|---|---|---|
| IC 5063 | ESO 187-G23 | Sy2 | 44.8 | 217 | 12.89 | 0.061 | 0.67 | | 8.8 | dG92 |
| Mrk 6 | IC 450 | Sy1.5 | 80.8 | 392 | 15.0 | 0.136 | 0.625 | 12.0 | $2.4^a$ | mo83 |
| Mrk 915 | | Sy1 | 99.0 | 480 | 14.82 | 0.063 | 0.833 | | $7.0^a$ | dG92 |
| NGC 1320 | Mrk 607 | Sy2 | 35.3 | 171 | 13.32 | 0.047 | 0.316 | | 9.0 | dG92 |
| NGC 3393 | | Sy2 | 50.3 | 244 | 13.09 | 0.075 | 0.909 | 16 | 12.5 | sb96 |
| NGC 3516 | | Sy1.5 | 40.8 | 198 | 12.5 | 0.042 | 0.765 | 7.5 | $1.6^a$ | an70 |
| NGC 4253 | Mrk 766 | Sy1.5 | 56.2 | 273 | 13.70 | 0.020 | 0.8 | 5.7 | 13 | gp96 |
| NGC 4593 | Mrk 1330 | Sy1 | 38.8 | 188 | 11.67 | 0.025 | 0.744 | | $0.33^a$ | dG92 |
| NGC 5347 | | Sy2 | 36.6 | 178 | 13.4 | 0.021 | 0.765 | 6.2 | 10.0 | STIS |
| NGC 5548 | | Sy1.5 | 74.0 | 359 | 13.3 | 0.020 | 0.929 | 3.3 | 8.1 | cr98 |
| NGC 7212 | | Sy2 | 111.1 | 538 | 14.78 | 0.072 | | | 10.8 | wh92 |
| NGC 7674 | Mrk 533 | Sy2-H II | 119.7 | 580 | 13.92 | 0.059 | 0.909 | 6.8 | 14.3 | STIS |
| UGC 1214 | Mrk 573 | Sy2 | 70.0 | 339 | 13.68 | 0.023 | 1.0 | 5.6 | 14.6 | STIS |
| UGC 6100 | | Sy2 | 124.0 | 601 | 14.30 | 0.012 | 0.617 | | 12.0 | cg94 |
| UGC 12138 | | Sy1.8 | 103.9 | 503 | 14.24 | 0.085 | 0.875 | | $2.71^a$ | dG92 |

Col.(1,2): galaxy name; Col. (3): spectral type; Col. (4): distance corrected from a Virgo Infall model; Col. (5): physical scale of the images; Col. (6): total asymptotic magnitude in B, B_T, from RC3 catalogue; Col. (7): reddening, E(B-V); Col. (8): axial ratio (b/a); Col. (9): ratio [OIII]$\lambda\lambda$5007/[NeV]$\lambda\lambda$3346,3426; Col. (10): ratio [OIII]$\lambda\lambda$5007/H$\beta$; Col. (11): references for emission line fluxes (an70: Anderson (1970); cr98: Crenshaw et al. (1998); cg94: Cruz-González et al. (1994); dG92: de Grijp et al. (1992); gp96: González Delgado & Pérez (1996a); mo83: Malkan & Oke (1983); wh92: Whittle (1992); STIS: calculated from STIS nuclear spectra)
Quantities for columns 2 to 8 are extracted from NED.

[a] Includes H$\beta$ broad component.

will be the main contributors to the UV light emission. In the case of NGC 3516 the morphology is very dissimilar, with an extended UV emission surrounding the bright nucleus that does not match the bi-conical structure in [OIII]. This means that in this case we may be observing mostly light which seems not to be associated to the ionised gas emission. Also in NGC 5347 this kind of emission is likely responsible for the conical region extending to the north at less than 1 arcsec from the central source. There are also a few cases in which, in addition to the extended emission, the UV light comes from knots or clumps produced probably by star clusters. NGC 4253 and NGC 7212 are two examples of this.

## 4.3 Analysis of the near-UV and [OIII] images

### 4.3.1 Estimation of the [Ne V] lines contribution

The forbidden lines [NeV]$\lambda\lambda$3346,3426 are the only emission lines strong enough to contribute to the light through the F330W filter. These high ionisation lines are expected to be strongly diluted in the presence of a bright continuum and give a rather small equivalent width. Studying a sample of NLSy1 of the ROSAT Deep Survey, Hasinger et al. (2000) find that the equivalent width of [NeV] is only 4 Å, probably as a consequence of the strong continuum contribution. However [NeV] lines can also be locally strong, in the presence of a hard ionising spectrum. For

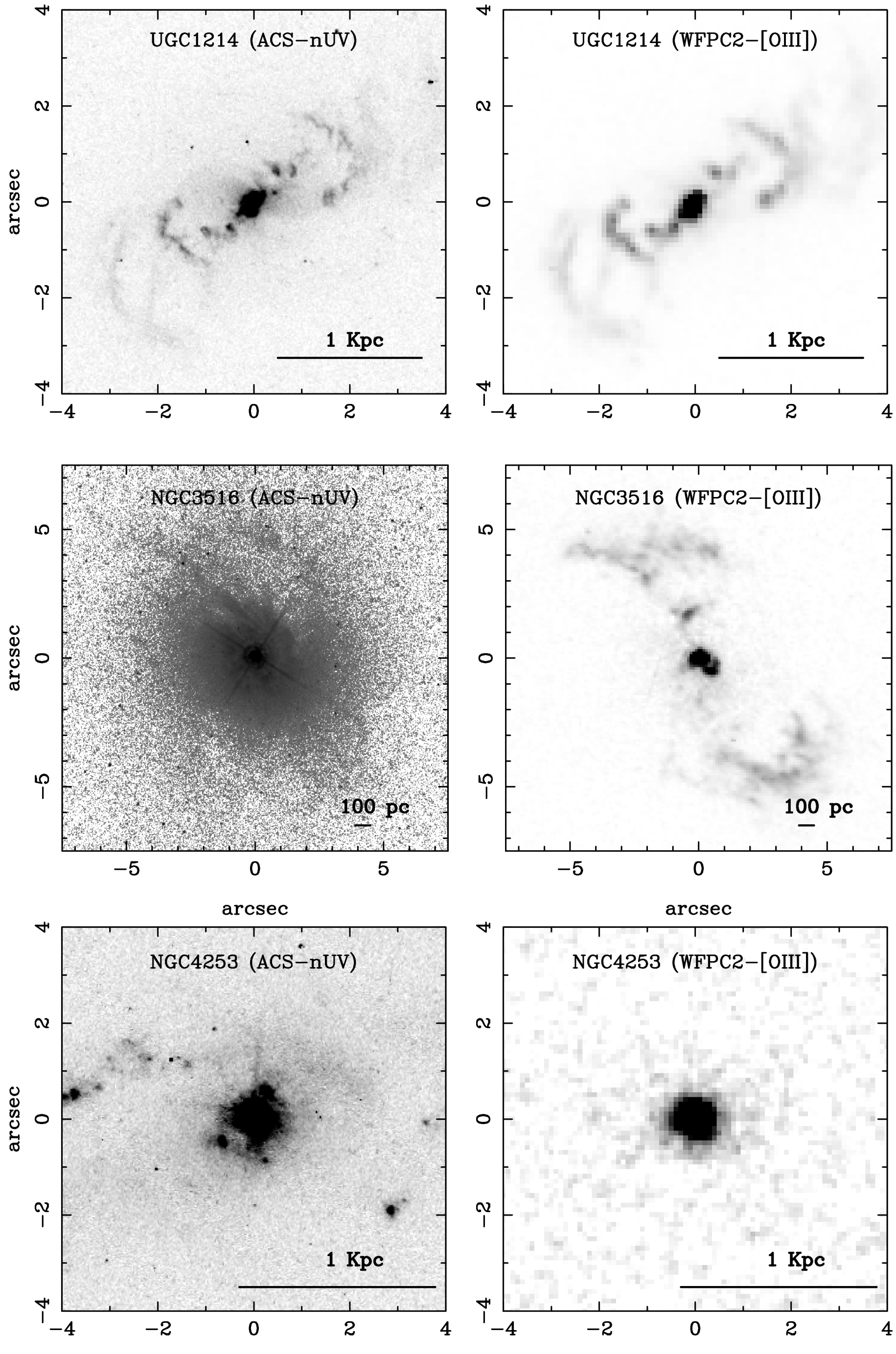

Figure 4.1: Three examples comparing the near-UV and ionised gas morphology. On the left, the images in F330W with ACS; on the right, images in [OIII]$\lambda\lambda$5007 with WFPC2. The region of interest is plotted with the same scale for each object. For UGC 1214 the morphology at near-UV is identical to that of the ionised gas, while for NGC 3516 it is very dissimilar. NGC 4253 constitutes an example of compact regions of star-formation and star-clusters that do not appear in the [OIII] image.

example, Soifer et al. (1995) find strong [NeV] lines in FSC 10214+4724, a Sy2 and ULIRG at high redshift, with a [OIII]/[NeV] ratio of 3.85. Storchi-Bergmann et al. (1996) find that this ratio can vary from 2 to 30, although most objects fall in the range [OIII]/[NeV]∼5-15. Note the caveat that most of these measurements come from the study of the NLRs, while the emission in our sample extends in many cases to several arcseconds, corresponding to the Extended Narrow Line Region (ENLR).

In Table 4.1, we list [OIII]/[NeV] and [OIII]/H$\beta$ ratios for the objects of our sample. These have been compiled from a variety of sources. We found published fluxes for [NeV] for a limited number of galaxies (Mrk 6, NGC 3393, NGC 3516, NGC 4253, NGC 5347, NGC 5548). In order to complement these data, for the objects NGC 3393, NGC 5347, NGC 7674, and UGC 1214 (Mrk 573), we have used published spectra from Spinelli et al. (2006), obtained with HST/STIS and with a spectral range covering the [NeV] wavelength. These spectra have been extracted in windows of 0.2 arcsec and cover the optical and UV. This window is the best possible angular resolution achievable with the observations, corresponding to a region of 52 pc radius for NGC 3393, 120 pc for NGC 7674, 33 pc for NGC 5347 and 72 pc for Mrk 573 centred on the nucleus. For details of the reduction process of the spectra see Spinelli et al. (2006).

The line fluxes in the STIS spectra were measured with IRAF task ‘splot’ through a gaussian fitting to the line. For the two objects with STIS spectra and published [NeV] data (NGC 3393 and NGC 5347), we find a reasonable agreement between our measurements and published data. The ratio [OIII]/H$\beta$ is around 10 in both cases, while in the ratio [OIII]/[NeV] there is a factor 2 difference, which is nevertheless within the expected uncertainty in the flux measurements of [NeV] lines. In the case of NGC 5347 we will use the STIS value, as the data in González Delgado & Pérez (1996b) is very noisy in the UV, while for NGC 3393 we will use the data of Storchi-Bergmann et al. (1996), as the STIS spectra is noisier in this case. Overall, [OIII]/[NeV] ratios vary between 3 and 20.

Due to the lack of data of [NeV] for some galaxies of the sample, we use bibliographic data of other objects in order to constrain their expected range of line ratio values. In Table 4.2 we compile some values of [OIII]/[NeV] and [OIII]/H$\beta$ for galaxies with different activity types, found in several studies (Storchi-Bergmann et al., 1995; Morris & Ward, 1988; Koski, 1978). Overall, the objects and the compiled data, are very inhomogeneous. However, this should give us an estimate of the expected value of [OIII]/[NeV] ratio. This line ratio can be used to scale the narrow-band [OIII] image, in order to obtain an approximate [NeV] image. For Sy1 (Sy1, 1.2 and 1.5) we find a mean [OIII]/[NeV] ratio of 8.4, with a dispersion of 5.8; for Sy1.9 galaxies this value is 22.2 with 9.1 dispersion; and for Sy2 galaxies we calculate a ratio of 16.9 with a dispersion of 6.7. We want to remark the wide range for the ratios, from 1 to a few tens. Also, the values from Storchi-Bergmann et al. (1995) may be upper limits to the actual NLR value, as they used very wide slits in order to match the aperture of IUE data which was used in combination with the optical data. From these results it can be concluded that any scaling between 1/2–1/30 to the [OIII] image may be a reasonable approximation to the [NeV] emission, depending very much on the nature of the object. Note, however, that these values have been obtained from spectra dominated by the NLR contribution, and we are assuming that the [OIII]/[NeV] ratio in the ENLR is similar to the value in the NLR.

### 4.3.2 Estimation of the nebular continuum emission

Due to the short mean wavelength and large width of the near-UV filter, the nebular continuum may be an important contribution at this band. The main contributions to this continuum are electron-ion recombinations. There is also a contribution of free-free transitions, by means of free electron-ion interaction followed by bremsstrahlung radiation from the electrons. The latter is more important at longer wavelengths, and is negligible in the F330W filter band. The most important role is played by hydrogen and helium recombination. Another source of nebular continuum at this wavelength is the two-photon decay of the $2^2S$ level of H I.

The emission coefficient for the mechanisms described above depend both on frequency and temperature, and can be written as:

$$j_\nu(H\,I) = \frac{1}{4\pi} N_p N_e \gamma_\nu(H^0, T) \tag{4.1}$$

$$j_\nu(He\,I) = \frac{1}{4\pi} N_{He^+} N_e \gamma_\nu(He^0, T) \tag{4.2}$$

$$j_\nu(He\,II) = \frac{1}{4\pi} N_{He^{++}} N_e \gamma_\nu(He^+, T) \tag{4.3}$$

$$j_\nu(2q) = \frac{1}{4\pi} N_p N_e \gamma_\nu(2q) \tag{4.4}$$

where $\gamma_\nu$ is a coefficient that takes into account the bound-free and free-free transitions for each ion at a given temperature. The coefficient $\gamma_\nu$ is calculated numerically. We used the tabulated data of Ercolano & Storey (2006).

In order to calculate the total intensity of radiation ($I$), $j_\nu$ has to be integrated over the solid angle, frequency range, and optical depth. In order to get rid of the geometry, it is more useful to relate the continuum intensity to the intensity of some important emission line, often Balmer H$\beta$, whose emission coefficient ($j_{H\beta}$) is defined as:

$$N_p N_e \alpha^{eff}_{H\beta} = \frac{4\pi j_{H\beta}}{h\nu_{H\beta}} \tag{4.5}$$

where $\alpha^{eff}_{H\beta}$ is the effective recombination coefficient.

So the relation between intensities is:

$$\frac{I_\nu(ion)}{I_{H\beta}} = \frac{N_{ion^+}}{N_p} \frac{\gamma_\nu(ion, T)}{h\nu_{H\beta}\alpha^{eff}_{H\beta}} \tag{4.6}$$

And taking into account the conversion between frequency and wavelength, the wavelength intensity can be written in terms of I$_{H\beta}$ as:

Table 4.2: [NeV] data for galaxies in the literature

| Name | Redshift | Type | [OIII]/[NeV] | [OIII]/H$\beta$ | Ref. |
|---|---|---|---|---|---|
| 1ES 1615 | 0.0379 | Sy1 | 20.3 | 1.4 | mw88 |
| 3C 33 | 0.0597 | NLRG/Sy2 | 24.6 | 13.3 | ko78 |
| 3C 184.1 | 0.1182 | RG/Sy1 | 16.3 | 11.1 | ko78 |
| 3C 273 | 0.1592 | QSO | 1.9 | 0.13 | mw88 |
| 3C 445 | 0.0568 | Sy1 | 13.0 | 2.0 | mw88 |
| IC 3639 | 0.0109 | Sy2 | 11.6 | 5.3 | sb95 |
| IRAS F18389-7834 | 0.0742 | Sy1 | 2.1 | 0.28 | mw88 |
| Fairall 51 | 0.0138 | Sy1 | 4.6 | 0.89 | mw88 |
| MCG -6-30-15 | 0.008 | Sy1.2 | 10.9 | 0.64 | mw88 |
| MKN 509 | 0.0329 | Sy1.2 | 0.9 | 0.35 | mw88 |
| MKN 841 | 0.0365 | Sy1.5 | 5.0 | 0.57 | mw88 |
| MKN 871 | 0.0333 | Sy1.5 | 4.6 | 0.73 | mw88 |
| MKN 896 | 0.0262 | Sy1 | 4.5 | 0.32 | mw88 |
| MRK 1393 | 0.0543 | Sy1.5 | 13.1 | 1.2 | mw88 |
| NGC 4748 | 0.0146 | Sy1 | 18.4 | 6.0 | sb95 |
| NGC 3783 | 0.0096 | Sy1 | 10.7 | 0.86 | mw88 |
| NGC 4593 | 0.0087 | Sy1 | 6.9 | 0.30 | mw88 |
| NGC 449 | 0.0159 | Sy2 | 24.0 | 11.8 | ko78 |
| NGC 1068 | 0.0038 | Sy2 | 6.7 | 13.0 | sb95 |
| NGC 3393 | 0.0125 | Sy2 | 27.6 | 11.0 | sb95 |
| NGC 3081 | 0.0080 | Sy2 | 14.4 | 14.3 | sb95 |
| NGC 5506 | 0.0059 | Sy1.9 | 35.1 | 7.2 | mw88 |
| NGC 5643 | 0.0038 | Sy2 | 12.5 | 13.1 | mw88 |
| NGC 5940 | 0.0339 | Sy1 | 1.8 | 0.36 | mw88 |
| NGC 6814 | 0.0051 | Sy1.5 | 8.6 | 0.77 | mw88 |
| NGC 7314 | 0.0054 | Sy1.9 | 16.5 | 8.6 | mw88 |
| TOL 113 | 0.0571 | Sy1.9 | 14.9 | 9.5 | mw88 |
| TOL 20 | 0.0233 | Sy1 | 7.4 | 0.86 | mw88 |
| UGC 10683b | 0.0308 | Sy1 | 1.6 | 0.59 | mw88 |

Col (1): Object name; Col (2) Redshift; Col (3) Activity type; Col (4) Measured line ratio for [OIII]$\lambda\lambda$5006.8 over [NeV]$\lambda\lambda$3425.8; Col (5) Line ratio for [OIII]$\lambda\lambda$5006.8 over H$\beta$; Col (6) References: mw88, Morris & Ward (1988); sb95, Storchi-Bergmann et al. (1995); and ko78, Koski (1978).

$$I_\lambda(ion) = \frac{N_{ion^+}}{N_p}\frac{\lambda_{H\beta}}{\lambda^2 h\alpha^{eff}_{H\beta}}\gamma_\nu(ion,T)I_{H\beta} \tag{4.7}$$

From a direct comparison of the $\gamma$ factors, in Fig 4.1 of Osterbrock (1989), we obtain that the contribution of two-photon continuum will be ~30 per cent of that of H I recombination (half a dex smaller). In order to asses the contribution to the nebular continuum from the recombination of each different ion, we need to know the ionisation fraction of each species. We obtained the mean ionisation running the CLOUDY code (Ferland et al., 1998) with typical NLR values, such as a Lexington model (Ferland, 1995), which has electron density of $10^4$ cm$^{-3}$ and temperature $10^4$ K. The models yield a similar ionisation fraction for H and He. From the ionised He, 70 per cent is singly ionised and 30 per cent twice ionised.

For He I, the factor $\gamma_\nu(He\,I,T)$ has a break at 342.2 nm, longward of which it falls approximately an order of magnitude. This is almost in the middle of the F330W filter. In order to calculate how it affects the nebular continuum contribution we integrate the filter throughput considering that, for wavelengths larger than 342.2 nm, the contribution is 10 per cent the one for smaller wavelengths and then divide by the total integrated troughput. This ratio is 0.66 at restframe, but rises to 0.75 for the objects with the highest redshift in the sample. We will use a mean correction of 0.7 for the continuum estimation. Therefore we can use the next formulae which relate the continuum fluxes with the helium abundance (Y) and the ionisation fraction (IF):

$$\frac{I_{NC}(He\,I)}{I_{NC}(H\,I)} = IF(He\,I)Y\frac{\gamma_\nu(He\,I,T)}{\gamma_\nu(H\,I,T)}0.7 \tag{4.8}$$

$$\frac{I_{NC}(He\,II)}{I_{NC}(H\,I)} = IF(He\,II)Y\frac{\gamma_\nu(He\,II,T)}{\gamma_\nu(H\,I,T)} \tag{4.9}$$

The relation between $\gamma_\nu(He\,I,T)$ and $\gamma_\nu(H\,I,T)$ at ~330 nm is approximately equal to 1.2. The ratio for He II recombination is 2.4. Assuming an abundance ratio of 1/10, and an IF of 0.7 for He$^+$ and 0.3 for He$^{++}$, the contributions of He I and He II recombination to the nebular continuum are ~6 per cent and ~7 per cent respectively of that of H I. We will assume a temperature for the ionised gas of 10,000 K. In order to calculate the contribution in flux of the nebular continuum to the F330W filter, we calculate $I_\lambda(H\,I,T)$ at the average wavelength of the filter (AVGWV) and T=10,000 K and multiply by its rectangular width (RECTW). The parameters AVGWV and RECTW of the filter F330W were calculated with IRAF SYNPHOT task 'bandpar', yielding 336.72 nm and 54.418 nm respectively. As a good approximation, the nebular continuum flux in the filter F330W can thus be estimated as follows:

$$I_{NC,F330W} \simeq 1.43 \cdot I_{AVGWV}(H^0,T) \cdot RECTW, \tag{4.10}$$

where the factor 1.43 corresponds to the sum of the contribution of the H I recombination continuum (1), the two-photon continuum (0.30), and the He I and He II recombination continuum (0.06 + 0.07).

And from Equation 4.7 and the values of the parameters AVGWV, RECTW and T, we obtain:

$$I_{NC,F330W} \simeq 3 \cdot I_{H\beta} \tag{4.11}$$

In our case it is more convenient to express the former relation in terms of the [OIII] flux. This will introduce a further uncertainty, but it is a necessary step, in order to adapt the study to the data we have. We expect that the narrow line components of both Sy1 and Sy2 have similar [OIII]/H$\beta$ line ratios, when only the narrow component of H$\beta$ is included. For the Sy2 galaxies in Table 4.2, we calculate a mean [OIII]/H$\beta$ ratio of 12.3 with a dispersion of 2.8, this being 8.61 and 0.87 respectively for Sy1.9. For the Sy1 galaxies, Morris & Ward (1988) tabulate the total H$\beta$ line flux, including the broad component. Including the broad component would yield an unrealistically high nebular continuum for the NLR. The data for the object 3C 184.1, from Koski (1978), include only the narrow component, and the ratio is 11.1. This value is consistent with those from Sy2, and also agrees with the data in Table 4.1, in which [OIII]/H$\beta$ ranges from 8 to 14. Therefore we will assume a single [OIII]/H$\beta \simeq 10$ for all the Sy galaxies.

With these considerations, and the caveats expressed above, we can make a prediction of the nebular continuum through F330W in terms of the [OIII] flux with the equation:

$$I_{NC,F330W} \sim f \cdot I_{[OIII]}, \tag{4.12}$$

with **f** $= 0.3$ and taking into account that, for the range of the line ratio cited above, **f** may vary between 0.375 and 0.2.

Dust obscuration may have an important effect in the calculated ratio between [OIII] and near-UV emission. Extinction coefficients for the ACS filters using the interstellar extinction from Cardelli et al. (1989) are tabulated in Sirianni et al. (2005), from where we take $A_{F330W}/E(B-V) = 5.054$, and A$_{F502N}/E(B-V) =$ 3.458. Thus, the difference in magnitude between filters F330W and F502N due to obscuration is

$$A_{F330W} - A_{F502N} = 1.6E(B-V) = 1.6A_V/3.1 \simeq 0.5A_V,$$

what translates into a flux ratio of $10^{-0.2A_V}$. This means that an extinction of $A_V = 1$, would reduce the near-UV contribution of the ionised gas emission to 63 per cent of its unextincted value, reducing the value of **f** in Equation 4.12 from 0.3 to 0.19. Thus,

$$F_{NC,F330W} \sim 0.3 \cdot 10^{-0.2A_V} \cdot F_{[OIII]}, \tag{4.13}$$

where we have adopted 0.3 as an average scaling for the [OIII] images, keeping in mind that the reddening effect may change its value.

The value of **f** is subject to several other effects and assumptions. From the values of $\gamma_\nu(ion, T)$ tabulated in Osterbrock (1989), we estimate that a change of 1000 K in the temperature may produce a change up to 10 per cent in the value of **f**. The ionisation parameter (U) can also affect the result. In the regions of highest U there might be a higher contribution of the nebular continuum. The ratio [OIII]/H$\beta$ is expected to vary with U, although data from Table 4.1 suggest a quite stable ratio for these objects. Anyway, a certain degree of spatial variation of the scaling factor **f** is to be expected. In addition, as noted by Luridiana et al. (2003), the NC from two-photon decay could be higher due to the reprocessing of Ly$\alpha$ photons inside the nebula. For a theoretical thick and dust free nebula, the contribution of two-photon decay could be 3 times higher than the one considered, becoming as important as hydrogen recombination, and rising the value of **f** in equation 4.11 from 3 to 5. However the latter value is an upper limit, and the actual value should lie in between. Due to all these caveats, this number has to be taken just as a reference value.

### 4.3.3 Contribution of the scattered light from the AGN

On basis of the unified model we expect this contribution in both Sy types. This emission is expected to correlate spatially with the [OIII] emission to a certain degree, although the correspondence may not be perfect. Scattered light can be identified through polarimetric studies, as it is expected to be at least partially polarised. The two processes have a different dependence on density $N_e$, and polarisation also depends on the scattering angle; line emission would roughly go with $N_e^2$ while polarised flux would go with $N_e \times P$, where the degree of polarisation (P) depends on the scattering angle. To make things more complicated, a low polarisation does not necessarily imply a low contribution from the scattered light, as the scattered light might have a low intrinsic polarisation.

Scattered nuclear emission from dust is known since long in some bona-fide hidden Sy1, as NGC 1068, in which it occurs in compact knots and extended regions far from the nucleus (Antonucci & Miller, 1985; Miller et al., 1991). In some objects, the UV emission is known to be dominated by scattered light from the AGN. Capetti et al. (1995), find that most, if not all, of the central UV emission in NGC 1068 may be due to scattered light from the obscured AGN (polarisation up to 65 per cent). Kishimoto et al. (2002b) find a polarisation of ~20 per cent for Mrk 3, which has an extended emission with biconical clumpy morphology similar to some objects in our sample (UGC 1214, NGC 3393 or IC 5063). On the other hand, Kishimoto et al. (2002a) study Mrk 477 concluding that scattered light is responsible for only as much as 10 per cent of the UV emission. Smith et al. (2002) study a sample of Sy1 galaxies, several of which are in our sample, finding a degree of polarisation bellow 2 per cent at optical wavelengths. Nevertheless, the polarisation value could be higher, if one considers that it may be diluted by the contribution of the nuclear flux. We have estimated the contribution of the nuclear flux in our Sy1 images by subtracting a PSF (point-spread function) obtained from the image of a star observed through the same filter. On average, we had to scale the PSF to 75 per cent of the peak nuclear flux in order to eliminate the nuclear point source. Then, assuming that the bulk of the polarisation comes from the extended emission, and considering that the AGN emission accounts for 3/4 of the total nuclear emission, the degree of polarisation would be around 8 per cent. That could imply an important contribution of the scattered light, in case that the intrinsic polarisation of this component were around 10 per cent.

Inglis et al. (1993) studied IC 5063, measuring a polarisation of 1-2 per cent in the optical continuum. They argue that scattered light cannot account for most of the emission. NGC 7212 and NGC 7674 are traditionally considered highly polarised objects (Miller & Goodrich, 1990; Kay, 1994), so they are likely to have a strong contribution of scattered light. By fitting a galactic template to some spectral features, Tran (1995) calculated a contribution of the stellar continuum of 73 per cent and 56 per cent, respectively. However, as they discuss, this determination is very uncertain, and it depends of the determination method (see, for example, Kay, 1994).

As a summary, we could say that the contribution of scattered light in the circumnuclear region may be important for some objects, although it is not trivial to correct for it. A detailed study of this component would need polarimetric imaging, that is beyond the scope of this work.

### 4.3.4 Analysis: contribution of the ionised gas to the near-UV light

In the previous sections we have shown that the contribution of [NeV]$\lambda\lambda$3346,3426 emission line fluxes and the nebular continuum to the light in the filter F330W, is expected to be of the order of 30 per cent of the [OIII]$\lambda\lambda$5007 flux for Sy galaxies. However, this contribution may vary from less than 20 per cent, up to 70 per cent in extreme cases, depending on the factors explained above. Both components originate in the same region, most probably the photoionised NLR and ENLR, therefore their effect is reinforced in the image. Our aim in this section is to check whether the contribution of the [NeV] lines and the nebular continuum are enough to explain the similarities of the morphology of the objects in the near-UV F330W and in the [OIII] narrow band images. We do this by creating a synthetic ionised gas ([NeV] emission + nebular continuum) image, by direct scaling of the [OIII] image.

The [OIII] images were obtained with WFPC2, and have a lower resolution, so first we had to resample these images to the ACS resolution with the IRAF task ‘geotran’. For every pair of near-UV and [OIII] images, we convolved each image with the PSF of the other instrument configuration, which we created using the software TinyTim. For the [OIII] images taken with the WFPC2 linear ramp filter, a monochromatic wavelength of 500.7 nm was used when creating the PSF. We calibrated the ACS images into integrated flux, by multiplying by the inverse sensitivity (header keyword PHOTFLAM) and the filter width (RECTW parameter) calculated by the task ‘bandpar’ of the SYNPHOT package. Finally, we aligned and trimmed the images using some sharp features in the image. The result of this process are flux calibrated [OIII] and near-UV images that can be directly compared.

All the Sy1-1.8 galaxies in the sample show a very bright compact nuclear source. This source is unresolved in the ACS frames (Chapter 3), showing the features of a pure PSF in the images, such as diffraction spikes and Airy rings. Before comparing the [OIII] and the ACS images, this point-like source has to be removed. This was performed by our collaborator Patricia Spinelli, who provided us with the nucleus-free images after the following procedure. They performed a subtraction of the compact nuclear source from the ACS frames using a bright star, with a colour similar to that of the galaxies, and observed with the same instrumental configuration, as PSF template[1]. For each galaxy with an obvious diffraction pattern, the star image was scaled to match the intensity of the central source of the galaxy, in such way that each galaxy had its own reference PSF. This was done by shifting the position of the peak flux in the PSF image to that of the compact nucleus of each galaxy and scaling it to the same flux value. Then the reference PSF was scaled by a factor of 5 per cent and a series of images were created by subtracting from the galaxy image this scaled reference PSF in steps of 5 per cent. Finally, for each galaxy, we ended up with several images, each one corresponding to the subtraction of the scaled PSF by increasing factors of 5 per cent, 10 per cent, 15 per cent... The best subtraction was chosen by visual inspection, choosing the image where the diffraction spikes had completely disappeared and the nuclear residuals near the centre, which inevitably appear, were minimised. These residuals are mostly due to the undersampling of the images, breathing effects (slightly change of focus) of the telescope optics and due to alignment errors of about 0.05 pixels. The whole process is performed in the _FLT images (before correcting from geometric distorsion) and then the resulting images were distorsion-corrected. This proved to leave smaller residuals than working directly in the final _DRZ images (after multidrizzle task correction). After this procedure we were left with near-UV images free from the nuclear contribution, which can now be compared with the [OIII] images, after the matching procedure described in the previous paragraph.

For each object, we have next scaled the [OIII] image in order to create a synthetic nebular continuum plus [NeV] image. We expect there might be variations of the ratio [OIII]/[NeV] over the field of view, but as a first approximation we neglect this position dependence. As described in the previous section, **f** is the scale factor we use to multiply the [OIII] image previous to its subtraction from the flux-calibrated near UV image (F330W image in flux density times RECTW). We have tried different **f** values, looking for the one that best removes the extended emission. During this process we have also refined the alignment of the images by minimising the residuals. In previous sections, we have discussed the range of reasonable **f** values (0.2–0.7, but most frequently expected ∼0.3). Based on that we can deduce for each object individually, whether the ionised gas can explain the morphology observed in the near-UV exposure. Using this procedure we have created the synthetic [NeV]+NC images, and estimated the **f** factor for each object. This is illustrated in Figure 4.2, in which we show the synthetic images with the most likely value of **f**. In some cases we use a very high **f** in order to show that the ionised gas cannot account for most of the emission. The result is commented in

---

[1] ACS PSF Characterisation HST Proposal 9667

detail for each object in the next section, including the photometric analysis of the residuals, which we discuss bellow.

### 4.3.5 Analysis: photometry of the residuals and other emitting mechanisms

After the subtraction of the ionised gas component (using the synthetic [NeV] + NC images), the objects showed still residual near-UV emission. In this section, we use some of these images in order to investigate the nature of the residual light.

F330W images were degraded to the resolution of WFPC2, after removing the gas contribution with the factor **f** estimated in Section 4.3.4. The addition of WFPC2 F547M and NICMOS F160W images, allowed us to study two colours. However, many of the objects show a bright compact nucleus, which may affect the study of the extended emission in the very inner regions of the galaxy. In addition, at the F160W band there could be a contribution of the torus emission, difficult to account for. Therefore, we will avoid studying the central region when the image is dominated by a strong nuclear point-like source contribution.

Aperture photometry was performed with the IRAF task 'phot'. Depending on the morphology of each object in particular, we calculated the colour radial structure, or integrated the light in certain apertures or rings. Comparing the results with synthetic photometry (see bellow) we can derive conclusions about the emitting mechanisms for some objects. We present the results for each galaxy in the next section.

#### 4.3.5.1 Synthetic photometry

In order to compare our photometric measurements with the expected colours of a certain stellar population, we have obtained the synthetic colours (F547M–F330W and F160W–F547M) using the Spectral Energy Distribution (SED) of several sets of Single Stellar Population (SSP) models. Synthetic photometry was computed by multiplying each SED by the filter transmission curve plus detector response, and then comparing that to the result of doing the same with a reference spectrum, what defines the magnitude scale used. We tested the accuracy of our measurements with our own software using the SYNPHOT IRAF package. We chose the STMAG magnitude system, which uses a reference spectrum that has a constant flux density per wavelength interval. Colour indexes were then calculated from the magnitudes at F330W, F547M and F160W ($\sim U$, $V$ and $H$) bands.

We have used model SED obtained using two different codes for spectral synthesis modelling: Starburst99 code (hereafter SB99; Leitherer et al. 1999, or Vázquez & Leitherer 2005) and the models of Bruzual & Charlot (2003, hereafter BC03). The SSP models were obtained using:

**a)** SB99 with the Padova 1994 and Geneva 1994 tracks, assuming a Salpeter IMF with mass limits between 0.1 and 100 $M_\odot$. We used the Lejeune stellar atmospheres with solar metallicity. We covered a range of ages from 1 Ma to 10 Ga, with a non-

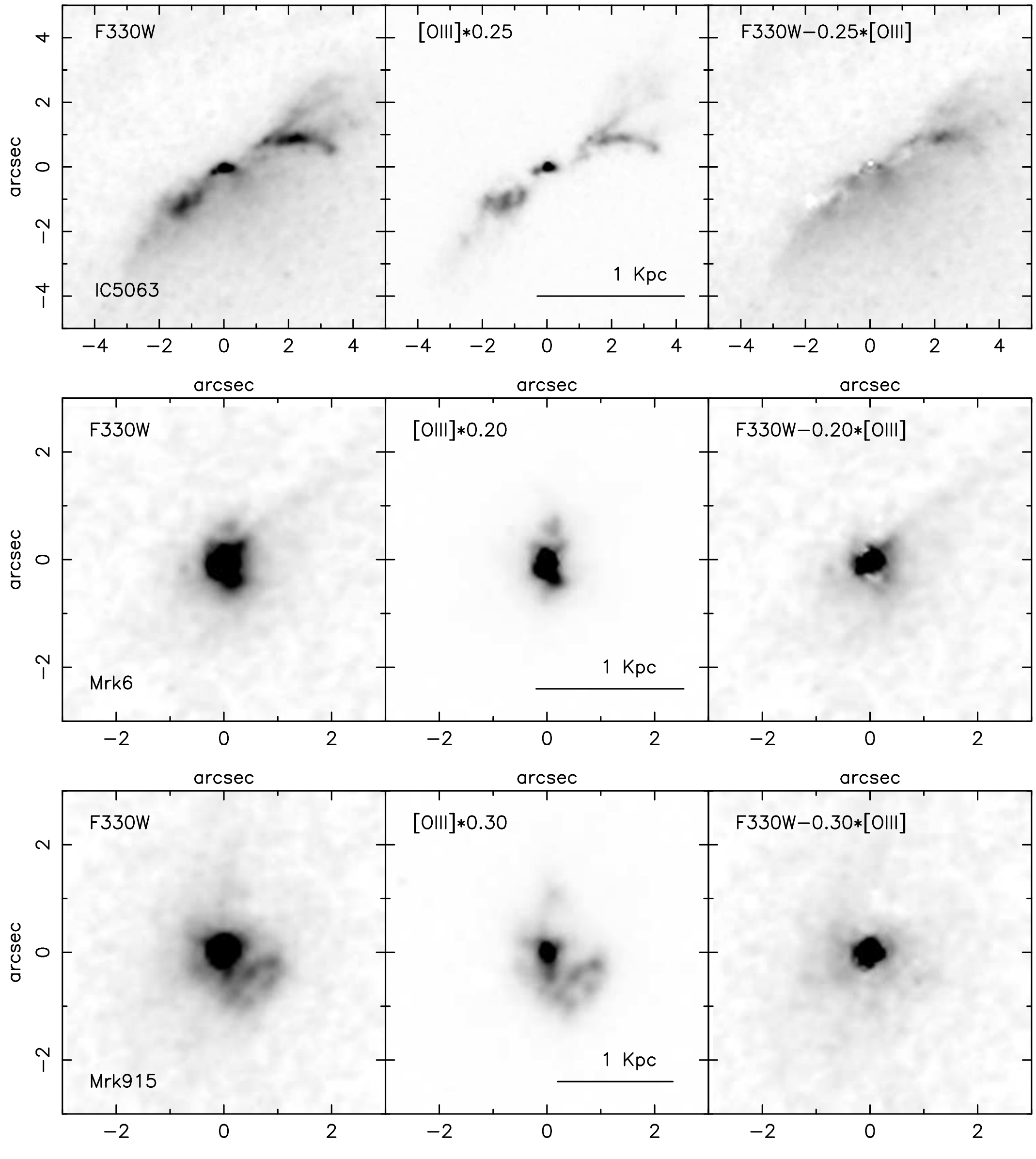

Figure 4.2: The panels show sets of three images showing the same field of view, and plotted with the same intensity scaling. Left panel: F330W ACS image convolved with WF3 PSF; middle panel: [OIII] image scaled by the indicated factor (see discussion in text); right panel: residuals from the subtraction of the images in the middle panel from those in the left panel. North is to the top; East is to the left.

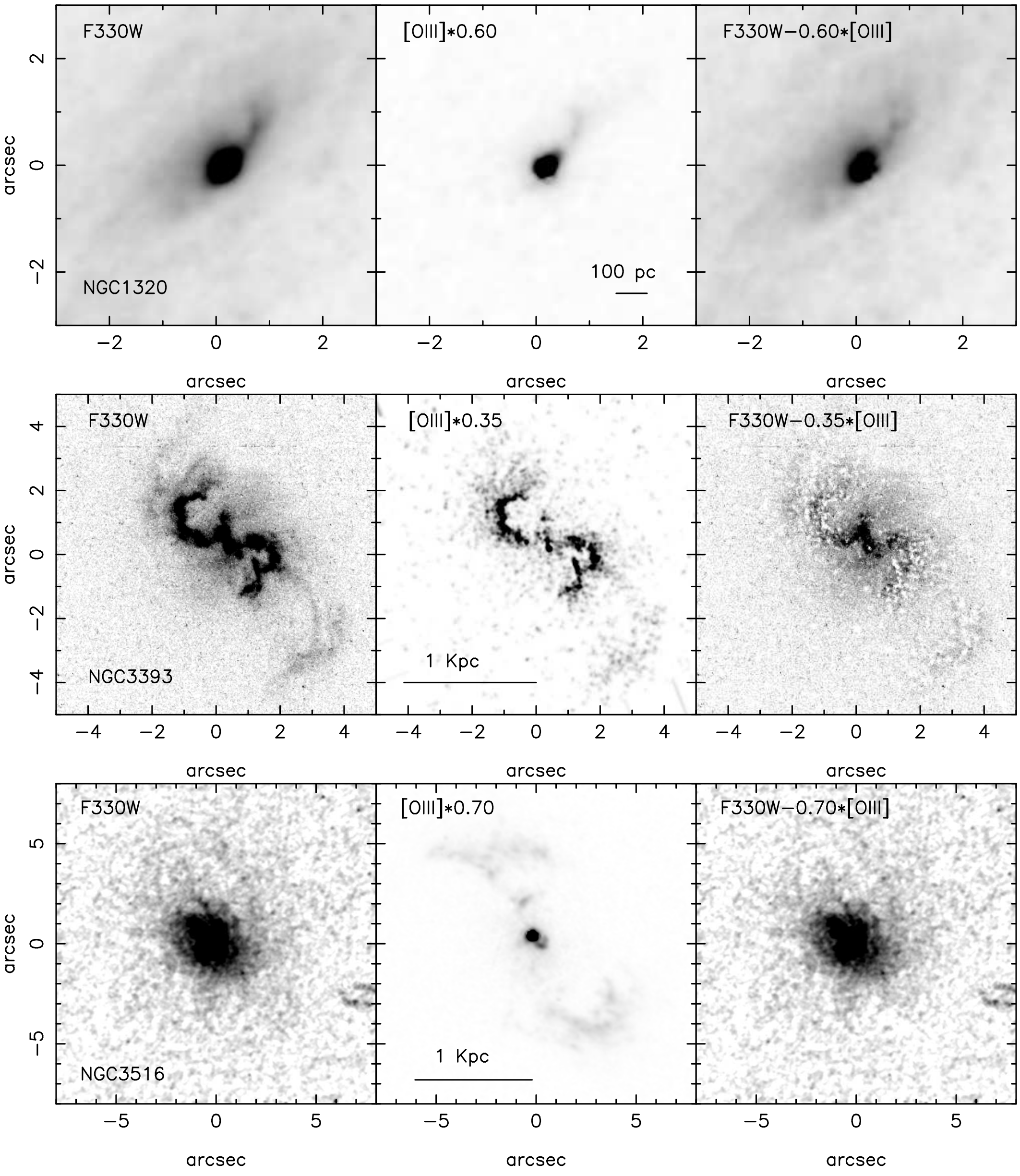

Figure 4.2: Ionized gas scaling and subtraction –continued

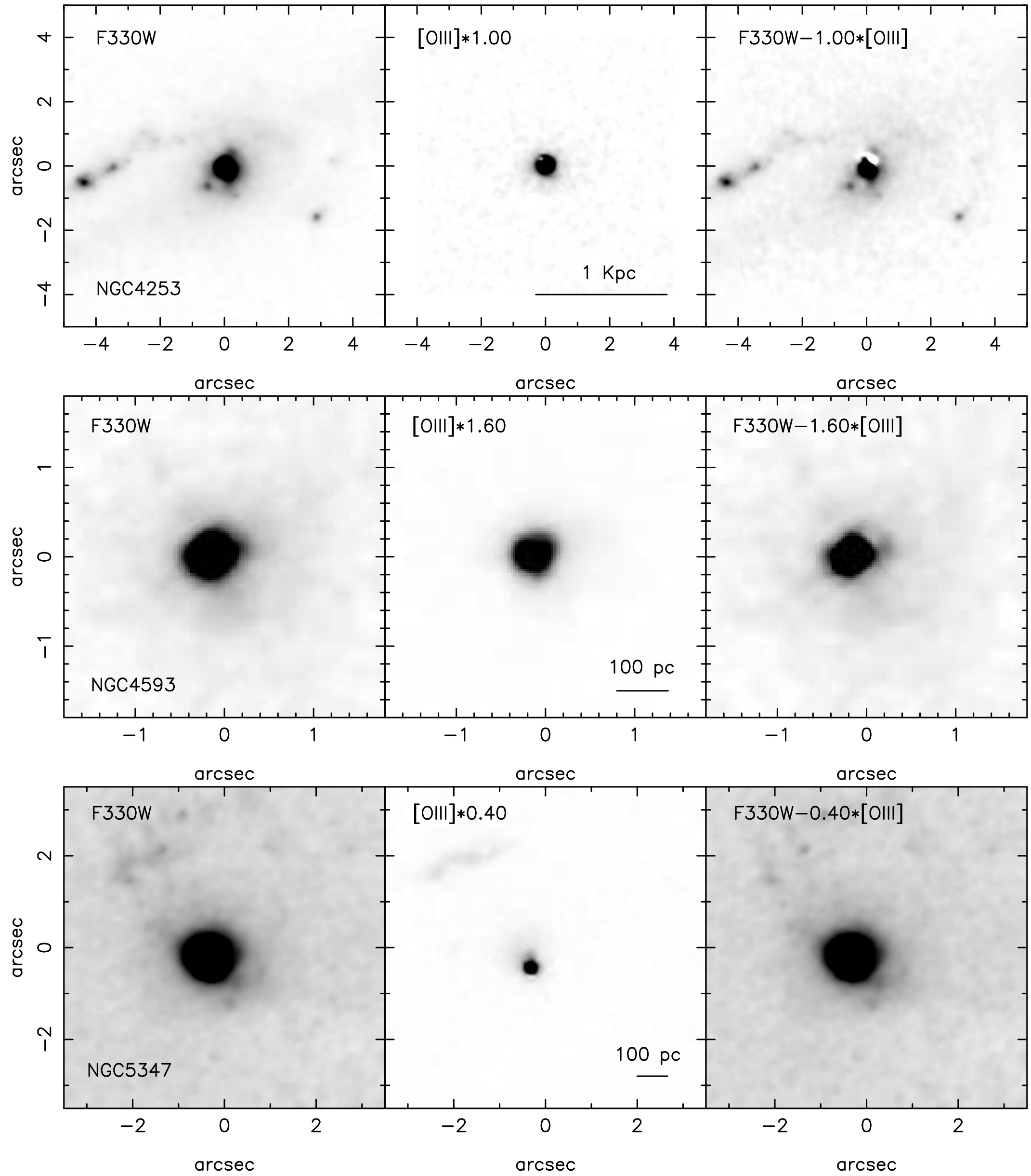

Figure 4.2: Ionized gas scaling and subtraction –continued

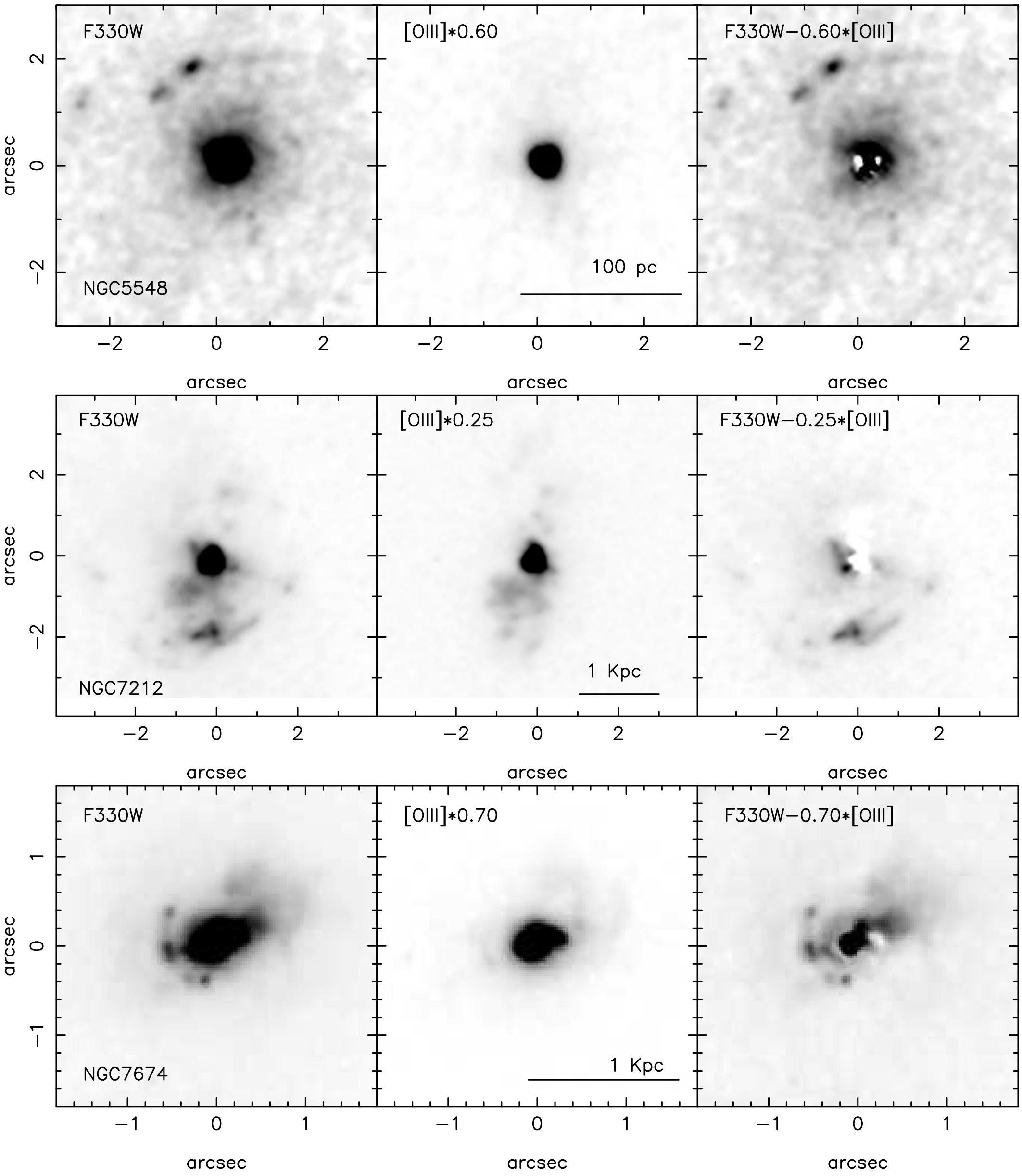

Figure 4.2: Ionized gas scaling and subtraction –continued

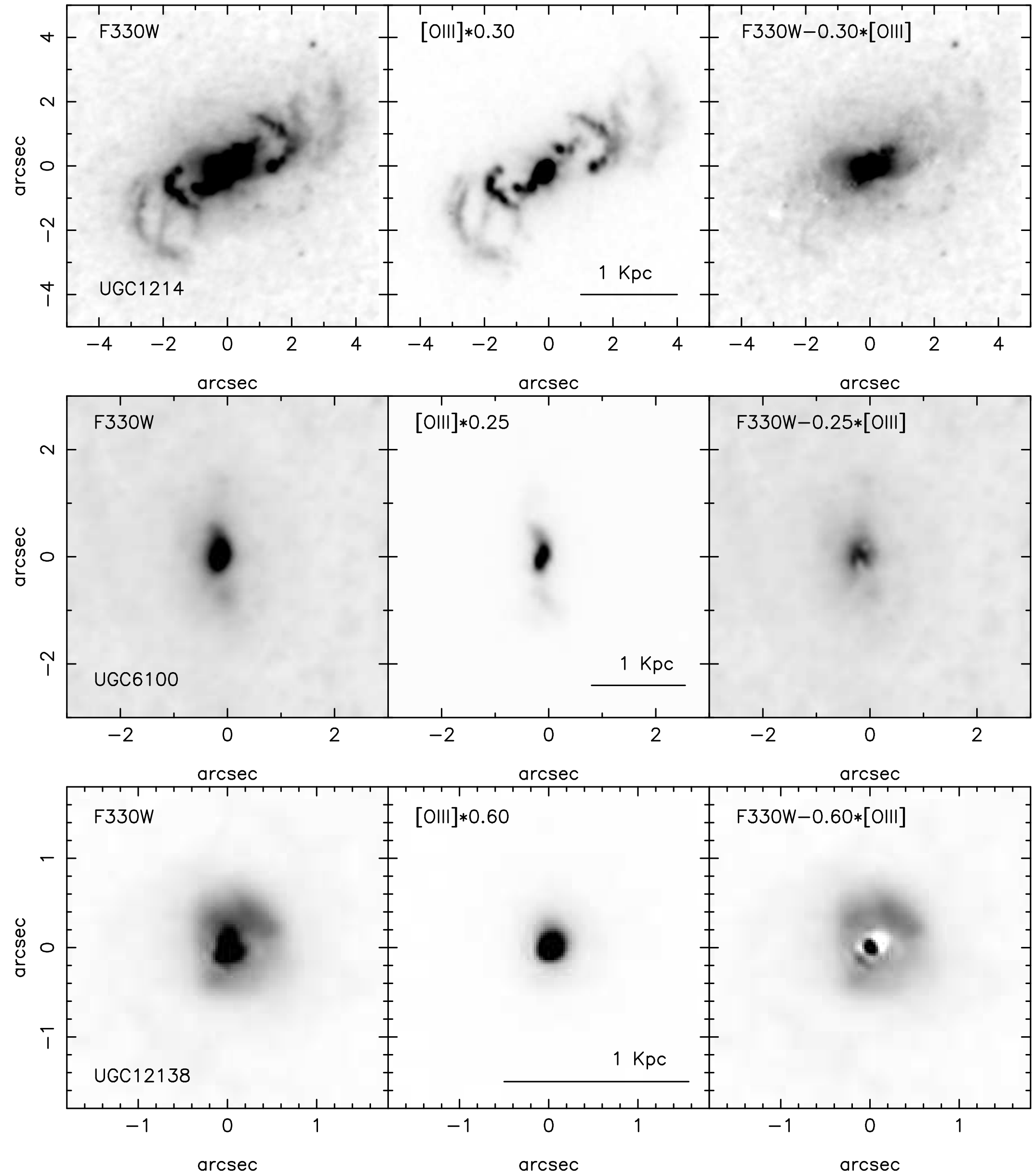

Figure 4.2: Ionized gas scaling and subtraction –continued

uniform age interval.

**b)** BC03 also with the Padova and Geneva 1994 tracks, Salpeter IMF and solar metallicity (see Bruzual & Charlot, 2003, for more details), with the same age range than above.

We have chosen these two codes because they are well recognised and frequently used throughout the literature. Both models allow for the use of two different well-known stellar evolutionary tracks: Padova and Geneva tracks. Stellar tracks are critical in order to determine the result of the models. Synthesis models have many additional ingredients affecting the output spectra, such as the Initial Mass Function (IMF) or the stellar atmospheres used for different evolutionary faces. Even using the same ingredients, different synthesis codes may output different results, due to the numerical implementation, as for example, different methods of interpolation within the evolutionary tracks. Thus, it is not surprising to find discrepancies in the photometry using output spectra from different codes. This can be noted in Figure 4.3, where we plot the time evolution of F330W–F547M and F547M–F160W colours of SSP models from SB99 and BC03. Both sets of models use a standard Salpeter IMF with mass limits between 0.1 and 100 $M_\odot$. The discrepancies are due to the effects commented above. As explained in Vázquez & Leitherer (2005), Geneva tracks fit better the young stellar populations, while Padova tracks are optimised for older stellar populations.

We have also calculated the expected location of AGN light in the (F330W–F547M) vs (F547M–F160W) diagram. We performed synthetic photometry through the given filters of power-law spectra with indexes (in flux density per unit frequency, defined as $f_\nu \propto \nu^{-a}$) 1, 1.5, and 2. This is the expected range for the index of the spectrum of an AGN nucleus at optical-near-UV wavelength (Osterbrock, 1989), being more common the smaller values. The results are redder colours than those of the youngest stellar populations. The presence of scattering by dust might make the colours bluer, although not necessarily if dust is distributed in a clumpy medium (see Vernet et al. 2001; note that free electrons produce also a grey scatter, wavelength independent). However, the scattered light, as well as any young stellar population, is most likely found diluted in an old bulge population, what would shift the colours to redder values. Different mixture fractions with the red population may lead to confusion between the contribution of a diffuse young stellar population and the scattered AGN light. Reddening processes may affect the colours according to the same trend. In Figure 4.4 we illustrate this degeneracy, by comparing the synthetic photometry of the power-laws with that obtained from a sequence of SSP BC03 models. We also include in this figure the photometry of two series of spectra: (1) the combination of a young 3 Ma old stellar population to a 10 Ga old one and (2) the combination of a power-law with exponents 1, 1.5, and 2, to the same 10 Ga old stellar population. The normalisation is such that, at the average wavelength of the blue filter (336.72 nm, calculated with SYNPHOT package), the contribution of the bluer spectrum to the total flux is a factor $q$. We used q values in the range 0–0.9 with increments of 0.1 (10 per cent of the total contribution), plus 0.95, 0.975, 0.99, and 0.9975. In Figure 4.4 it is appreciated how a small contribution (note: small in flux, not in mass) of an old stellar population shifts the colours of the blue spectra to positions where it can be confused with reddened older stellar populations. In addition, the 3 Ma and the power-law sequences follow a similar path in the diagram. We can conclude that, in general, it will be very difficult to disentangle the two mechanisms with the available filters. However, the colour analysis can give us important clues for particular objects.

## 4.4 Result of the analysis for each individual object

In this section we give details of the analysis procedure followed for each object. The particular morphology of each nucleus, and the availability and quality of the data, put some constrains on the kind of analysis we can perform in each case. For example, in some cases it is convenient to perform a radial colour profile, as illustrated in Figure 4.5, while other times we just carry out aperture photometry in one or more regions. We have attempted to extract the most from the images of each galaxy. The measurements discussed below, and plotted in Figure 4.6, are corrected for galactic extinction only, using the law of Cardelli et al. (1989), and the E(B-V) values from NED. The results are also summarised in a tabular form in Table 4.3, in which we include the relative contribution of each component when possible, as well as a summary of the photometry of the objects after removing the Sy nucleus and the contribution of the ionised gas. Note that the contribution of ionised gas is given respect to the F330W flux once the point-like nucleus is subtracted. In this way it is possible to do a direct comparison between objects with and without nucleus. In order to present the results in a more homogeneous way, we have chosen to give the fluxes and fractions in a physical region of 1 kpc radius around the centre of each object. Along this section we commonly write $U$–$V$ and $V$–$H$ when referring to F330W–F547M and F547M–F160W colours.

### 4.4.1 IC 5063 (Sy2)

Most of the emission to the southeast is removed with $\mathbf{f}$=0.20, but in order to get rid of the northern filamentary structure, the scaling factor has to be increased to 0.25-0.30. Some negative residuals appear in the subtracted image (top right panel of Figure 4.2). Rather than a change in the ionisation parameter, we suspect that these residuals may be due to dust obscuration, affecting much more the near-UV image than the [OIII] one. This object is heavily obscured by dust, which can explain the axial asymmetry of the emission. This is better appreciated in the F330W filter, as the bulk of the emission is concentrated to the southwest of the line northwest–southeast. The largest negative residuals after the subtraction process are found in the northern border of this axis, where we expect the obscuration to be larger. After the subtraction there is much extended emission to the southwest and a couple of clumps left. We have performed aperture photometry in three regions of radius 0.75 arcsec next to the nucleus (1–2 arcsec distance to the southwest of the peak of the near-UV emission). The photometry yields the colours $U$–$V\sim$1.7, $V$–

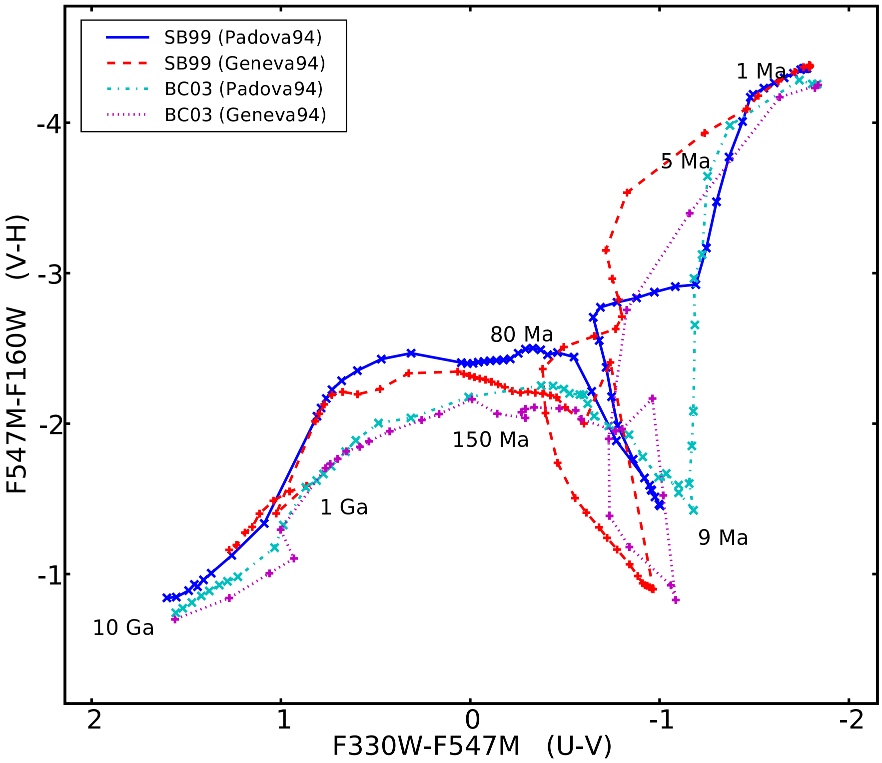

Figure 4.3: Evolution of the studied colours with age of a Single Stellar Population model in a (F330W–F547M) vs (F547M–F160W) diagram. The graph shows the comparison of Starburst99 (SB99) and Bruzual & Charlot (2003, BC03) models for both, Padova 1994 and Geneva 1994 tracks. All the models have a standard Salpeter IMF function. In blue full line, SB99 models with Padova tracks; in cyan dotted-dashed line, BC03 with Padova tracks; in red dashed line, SB99 with Geneva tracks; magenta dotted line stands for BC03 models with Geneva tracks.

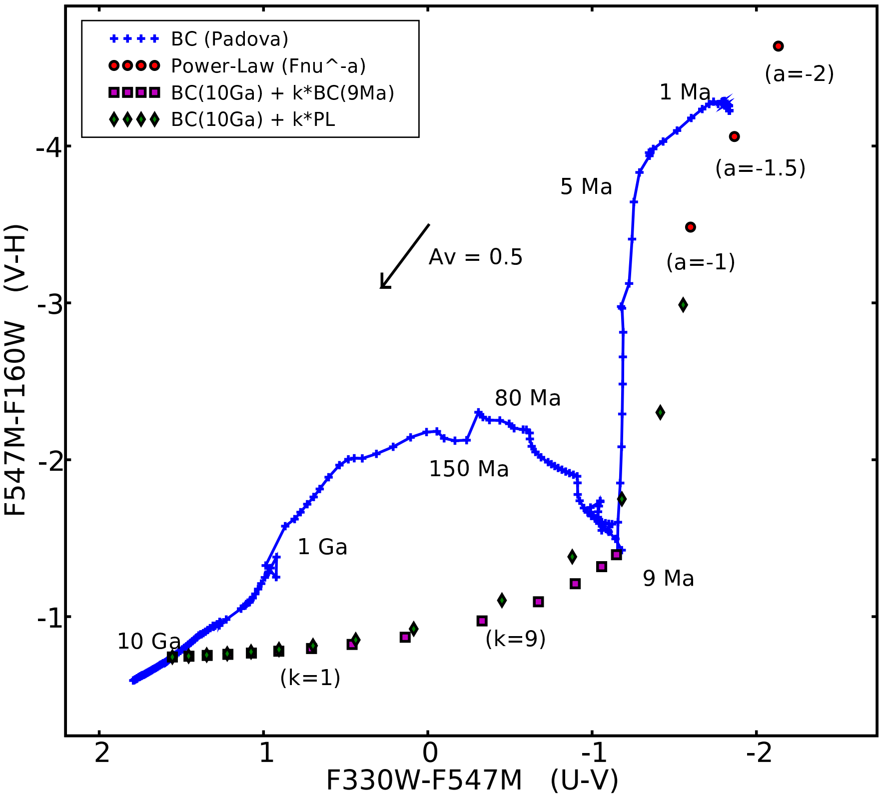

Figure 4.4: Same colour-colour diagram than Figure 4.3, showing the location of some power-law spectra, and two sequences of a 10 Ga old stellar population added to: (1) a young population of 3 Ma (magenta squares), and (2) a power-law $f_\nu \propto \nu^{-a}$ with $a$=1, 1.5, 2 (green diamonds). For reference, we have also plotted the reddening vector, and the evolution of a SSP model of Bruzual & Charlot (2003), with Padova tracks and Salpeter IMF. The scaling factors k and k' are related to the fraction q, described in text, as $q = k/(1 + k)$.

$H$~-0.6. These are compatible either with a very old stellar population (older than 10 Ga), or with an old obscured population. The bright clump which lies ~3 arcsec to the northwest shows a somewhat bluer $U$–$V$ colour (1.07). This may indicate the contribution of localised star formation, or scattered light from the AGN in a denser region of the ionisation cone. From the literature data and the estimated **f** value we infer that the nebular continuum alone can account for the light coming from the filamentary structure (23 per cent of the near-UV emission in the inner kpc), while most of the remaining light is stellar continuum from the bulge (~77 per cent of the total emission in the inner kpc).

### 4.4.2 Mrk 6 (Sy1.5)

This is a Sy1 galaxy with a bright nucleus. After the best nuclear subtraction some positive residuals are left, which are seen as a compact, though slightly extended, source in the convolved image. The factor **f** is relatively small for this object. A value of 0.2 accounts for the brightest regions and blobs to the north and south of the nucleus. At the same time it does not leave strong negative residuals, as **f**=0.3 does. Once the bright Seyfert nucleus is removed, the ionised gas emission account for an important part of the remaining extended emission (~60 per cent). Some nuclear emission remains, as well as an extended component. In addition, there seems to be a narrow diffuse filament extending towards northeast, and perpendicular to it, two small arcs in a symmetric structure both sides of the nucleus. This structure may be related to the radio emission. Kharb et al. (2006) report a double-bubble structure in 6 cm VLA radio-maps, and one of the directions with strongest emission matches the orientation of the near-UV filament (see Figure 1 of their work). In NICMOS F160W, and WFPC2 F547M images, the galaxy appears completely dominated by the bright nucleus, so we will not perform a further photometric analysis of the residuals.

### 4.4.3 Mrk 915 (Sy1)

The best value of **f** is around 0.30, with which most of the flattened-O shaped emission to the southwest is subtracted. There remains however a strong extended emission, that is unlikely to be due to ionised gas. This galaxy is a Sy 1 with a strong nuclear component. As in the case of Mrk 6, the best nuclear subtraction still leaves some positive residuals in the centre which, after convolving with the PSF of WFPC2, resemble a compact nuclear source. One could argue that a too conservative PSF subtraction may mimic that effect, although this is unlikely, as the subtraction was stopped when negative residuals began to appear. In order to check how much of the extended emission would be due to light from the extended wings of the PSF in case of a poor PSF subtraction, we subtract to the near-UV image a PSF (convolution of F330W PSF with one of the WF3 at 500.7 nm) of flux 3e-13 erg/cm$^2$/s. This subtracts most of the light in the inner 0.6 arcsec. From aperture photometry of this image and the scaled [OIII] subtracted one, we can set a very conservative upper limit, estimating that at 0.75 arcsec from the nucleus, no more than 30 per cent of the light can be due to a bad subtraction of the central source. Therefore, there is another mechanism beyond ionised gas emission and contamination by a poor PSF subtraction, that is producing the extended UV halo and compact emission. WFPC2 and, to a greater extent, NICMOS images, are dominated by a strong nuclear emission, so any further analysis would be dominated by the nuclear subtraction uncertainties.

### 4.4.4 NGC 1320 (Sy2)

This galaxy is an interesting case. In order to try to remove the filament to north-west, we have used f = 0.6, which is twice the average value obtained for other cases. Some structure is still seen, but applying a higher factor will introduce strong negative residuals next to the nucleus which are difficult to justify. The value of **f** as high as 0.6 might be justified as possibly due to a smaller [OIII]/H$\beta$ ratio in this galaxy, but still it does not explain all the emission. Most likely, it has a regular **f** ($\sim$0.3) and a further contribution in the central region. Considering that **f** $\lesssim$0.6, photometry in the inner 500 pc sets an upper limit of 15 per cent for the contribution of the nebular emission to the total near-UV light. We have carried out a circular aperture photometric study in the residual image. The profile shows a nearly constant U–V colour gradient of $\sim$ –0.12 mag/100 pc at radii larger than 100 pc (compare with UGC 6100), and a central blue drop, whose depth depends on the adopted **f** factor. However, even with values as high as f=0.6, the inner drop is evident in the inner 100 pc (see Figure 4.5). This indicates that there is a contribution either from a young population in a circumnuclear disc, or from scattered AGN light. This result is confirmed measuring the colours in a 0.4 arcsec radius aperture around the nucleus. The colours ($U$–$V$=1.06, $V$–$H$=-0.25) point to the existence of an old bulge population with a significant bluer component. This conclusion does not change using neither slightly wider or narrower apertures, nor applying previously a different scaling factor to the ionised gas image (between 0.2 and 0.35). Cid Fernandes et al. (2001) found that $\sim$10 per cent of light at 486.1 nm is due to young/intermediate age stars and/or a power law component. However, spectropolarimetry observations did not find any polarised broad emission in this galaxy (Tran, 2001), so the likelihood of the blue light being scattered light is very small, this emission is most likely due to star formation. It is interesting that we obtain such a red $V$–$H$ colour for this nucleus. Further than 200 pc the colours are closer to the ones we obtain for other objects, but with a significant blue component. In the inner region the nuclear torus emission contributes to the light through the F160W filter. However, this emission is visible as a point-like source (Quillen et al., 2001). Between 100 and 200 pc from the nucleus we have to invoke either a high reddening or another contribution to F160W, apart from stellar emission, that we are not taking into account.

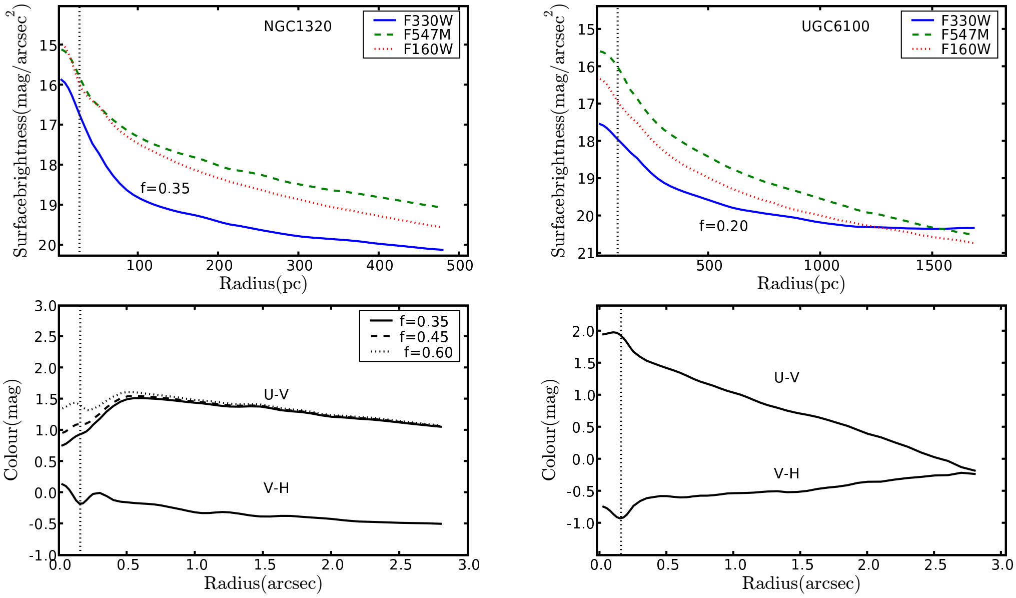

Figure 4.5: A photometric comparison of two Sy2 with a strong central near-UV emission, which cannot be accounted for by emission from ionised gas. In the upper panels we plot the surface brightness profiles for the filters F330W (blue full line), F547M (green dashed line), and F160W (red dotted line), which were obtained with circular apertures. Bellow we show the radial dependence of the colours F330W–F547M and F547M–F160W. The FWHM of the PSF is marked with a vertical dotted line. A central component of different nature for each object is found in the inner 100 pc (see discussion in text).

### 4.4.5 NGC 3393 (Sy2)

The [OIII] image of this galaxy was obtained with WF/PC before COSTAR, so it had to be deconvolved. The resulting image is quite clumpy, an artifact of the deconvolution process. The artifact structures remain after convolving with the ACS PSF. So a detailed analysis, as we do with the other objects, will not be possible for this galaxy. In this case we compare the images directly, without convolving first with the PSF of the other band, taking into account that the resolution for the two images is quite similar.

An scaling factor of 0.20 removes the brightest part of the filaments. With a factor of 0.50, most of the structure is gone, although strong negative residuals are left. The best result is achieved with **f** $\sim$ 0.30–0.35. This fits with the expected value of 0.35, calculated from the data in Table 4.1. The range of **f** values necessary to remove the different parts of the filaments might be due to the clumps mentioned above, as well as to a change in the ionisation parameter along the filaments. Most of the central structure in the F330W image does not seem to be due to ionised gas (remains after subtraction with **f**=0.50). Through photometry in the inner kpc we estimate a contribution of the ionised gas of $\sim$33 per cent to the total near-UV light, with a higher uncertainty than for other objects, due to the artifacts of the reduction process. Because of this uncertainty we have not attempted a further photometric analysis, although the estimated value of **f** supports the results from similar objects such as UGC 1214 (see below).

### 4.4.6 NGC 3516 (Sy1.5)

After removing the Seyfert nucleus, there remains a diffuse emission around it, which shows no clumps or star clusters. For this object the morphology in the near-UV and [OIII] is very dissimilar. This is probably the best example in the whole sample in which [NeV] and NC contribute very little to the near-UV light. Simple aperture photometry shows that in the inner kiloparsec, the contribution of the ionised gas accounts for less than 10 per cent (considering a scaling factor of **f**=0.6) of the diffuse near-UV light. Smith et al. (2002) find no intrinsic polarisation in this galaxy, which makes the scattered light explanation unlikely, in spite of earlier works showing a high polarisation for the same object (Martel, 1996). In order to understand the origin of this light we perform an aperture photometry analysis of the three bands. Curiously, the F547M image does not show a very bright nucleus, as the others, so the usual data reduction and resolution-matching process is enough for this band. On the contrary, the NICMOS image shows a bright point-like source, although in this case it doesn't preclude the study of the also bright bulge surrounding it. After the standard calibration process, we remove the near-IR nucleus using the same procedure explained for F330W images, with a PSF created with the TinyTim software. We avoid using the inner 0.4 arcsec of the image, as the central pixels are affected by the residuals of the subtraction of the PSF. The analysis yields fairly constant colours ($U$–$V$$\sim$1.4, $V$–$H$$\sim$-0.6) in the whole studied range (from 0.4 arcsec up to 5 arcsec), which are the expected colours for an old stellar population. We thus conclude that the bright underlying bulge is responsible in this case for most, if not all, the extended emission in the UV.

### 4.4.7 NGC 4253 (Sy1.5)

After the subtraction of the PSF from the near-UV image of this Sy1.5 galaxy, there still remains a central bright compact source and several compact knots resembling massive star clusters or star-forming regions. The [OIII] emission in this galaxy is very compact. A literature based estimate for **f** (from Table 4.1) yields 0.41. However, applying a scaling factor as high as **f**=1 still leaves most of the nuclear emission, but negative asymmetric residuals begin to appear near it. Therefore, gas emission cannot account for most of the light in the near-UV. An scaling factor of 0.6 yields an upper limit of 16 per cent for the contribution of nebular emission to the inner kpc near-UV light. In the filter F547M, the total exposure time is 20 seconds, so only the bright nucleus can be seen with enough signal to noise, and no further analysis was attempted.

### 4.4.8 NGC 4593 (Sy1)

This is a Sy1 with a very bright nucleus. After the best nuclear subtraction there remain some residuals at the nucleus and a diffuse light component, but the emission is quite compact overall. The [OIII] emission is also very compact and mainly limited to the inner 1 arcsec (less than 200 pc). Considering a scaling factor of 0.6 we can set an upper limit to the nebular continuum and [NeV] contribution of less than 8 per cent of the total flux inside the inner 350 pc, limited to the region in which there is enough signal-to-noise for the [OIII] emission. As [OIII] emission appears to be more compact than the near-UV, this probably constitutes a strong upper limit. In order to study the compact light emission we would have to remove the PSF from the three bands, which yields too many uncertainties to conclude anything further about the inner region.

### 4.4.9 NGC 5347 (Sy2)

This galaxy has two components in the [OIII] image: a compact central emission, plus a narrow arc ∼3 arcsec to the north-east. The near-UV image is somewhat similar, although the compact component is much brighter than the arc, relative to the [OIII] image. Although a literature based estimate of **f** yields a value of 0.58, the arc is subtracted with **f**=0.4, while the central emission persists even with very high **f** values. We have integrated the flux within the inner 620 pc, finding that the contribution of the ionised gas is probably less than 4 per cent of the flux in F([F330W]). This implies that neither the nebular continuum nor the [NeV] can account for the extended emission near the centre. In the two bluer bands (F330W and F547M) this emission is asymmetric, with the shape of a cone, opening towards the north-northeast. On the contrary, in the F160W filter (dominated by the bulge emission and the central AGN) the emission is quite symmetric. To avoid an azimuthal averaging, in this kind of object we prefer to perform aperture photometry in certain regions. We chose two small apertures of 0.25 arcsec radius to the north and northeast, including the extended emission but avoiding the nucleus. For the U band we used the F330W image minus the [OIII] contribution scaled with a factor **f**=0.4. Using a literature based **f**=0.6 yields a difference of only 0.04 magnitudes in the regions studied. In the NICMOS image we had to perform the subtraction of a PSF in order to eliminate the contribution of the nuclear source, as the apertures were only ∼0.5 arcsec far from the centre. The U–V colours obtained ($U$–$V$∼0.9, $V$–$H$∼-0.9) are around 0.5 magnitudes bluer than the Padova tracks (recommended for old stellar populations) for a population of 3 Ga. This implies that there is a contribution of a bluer component that may represent 10–30 per cent of the near-UV light (deduced from Figure 4.4). Due to this low percentage, we think that the asymmetry of the emission in the bluer bands might be caused by dust obscuration, what seems obvious to the south of the nucleus also in the F547M image. Scattered light from the AGN could produce this cone shape naturally, but the contribution of the blue component to the total light seems too low to explain the morphology by this mechanism only.

### 4.4.10 NGC 5548 (Sy1.5)

As in the other Sy1 described above, this galaxy shows a compact near-UV emission, once the nuclear contribution is subtracted. Data in Table 4.1 suggest a high **f** value for this object (0.67), although using such high scaling leaves strong negative residuals and still does not explain the bulk of the emission. From this we estimate that less than 25 per cent of the flux can be attributed to the ionised gas. Apart from the central light excess there is an extended surrounding emission, and a star-forming arc at ∼2 arcsec to the north-east. These features are not visible in the F547M image, due to its short exposure time (only 24 seconds). With only one colour, and the extremely bright nucleus dominating the near-IR, there is not much room for a further analysis of the residuals.

### 4.4.11 NGC 7212 (Sy2)

The diffuse emission region to the south of the nucleus is removed with **f**=0.25. However this leaves negative residuals in the nuclear region and next to it to the north. It is expected that those regions suffer from a heavy absorption, as the usual bi-conical structure is shown here as a single cone towards the south. The scale factor needed to remove the small northern emitting zones is just 0.15. As explained in Section 4.3.2, this can be accounted for with an internal extinction of $A_V$= 1. The subtraction of the ionised gas emission by this method, allows us to identify the bright clumps to the south as star-forming regions, although some contribution by scattered light from the AGN might be expected near the nucleus (see Section 4.3.3). Unfortunately, this interesting object lacks an F547M image, as well as any NICMOS exposure.

### 4.4.12 NGC 7674 (Sy2)

This galaxy is imaged with the PC, so the [OIII] image has a better resolution than for the other objects. The galaxy is a very blue object, classified as Sy2/H II, and with a bright nucleus. However, it is shown to be resolved (Chapter 3), so no PSF subtraction was attempted. It has a clumpy arc, at 0.5 arcsec southeast of the nucleus, which is very likely a string of star-formation regions. A bright area of diffuse emission is also remarkable, visible in the F330W image up to 1.25 arcsec from the nucleus, in the opposite direction. Although the morphology in the [OIII] band slightly resembles that of F330W image, the ionised gas emission can explain only a small amount of the near-UV flux. With factors as high as 0.9, the bulk of the nuclear and extended emission remains unsubtracted, as well as the star-forming arc. Athough the literature data suggest a scaling factor of 0.36, we find more likely a higher value of about 0.4-0.6. Using **f**=0.5 yields a contribution of the ionised gas of ~28 per cent over the total. This galaxy is relatively far, with a radial velocity of 8671 km/s (from NED), which shifts the bright [OIII] lines into the F547M wavelength range. Thus we expect some degree of contamination of the F547M exposure by the cited emission lines. The NICMOS image is dominated by a bright nucleus. As in other cases we perform a PSF subtraction until removing the diffraction patterns and not leaving strong residuals. However, any analysis in the inner ~0.5 arcsec would have strong uncertainties. Due to these two factors, we avoid the nucleus and we focus in studying the extended emission to the northwest. We have performed aperture photometry in two circular apertures of radius 0.25 arcsec at ~0.8 arcsec (~500 pc) from the nucleus. The analysis yields very blue colours ($U$–$V$~-0.18, $V$–$H$=-0.93; see Figure 4.6) compatible with the light being dominated by a blue component (up to 90 per cent of the near-UV flux, once subtracted the ionised gas contribution). For the measurements we used the F330W after subtracting the [OIII] image with an scaling **f**=0.50. We have checked that a change of 0.1 in **f** leads to a change of 0.05 magnitudes in the U–V colour, so the result is quite robust against the assumed **f**, while it constitutes a lower limit of the importance of the blue component due to the possible contamination of the F547M image discussed above. There is obvious star-formation around this Seyfert nucleus, as evidenced by the clumpy arc to the southeast and its spectroscopic classification. Previous studies have shown an important contribution of young stellar population in the inner 2 arcsec of this object (Cid Fernandes et al., 2001; González Delgado et al., 2001). However, taking into account the polarimetry data in the bibliography for this object (Section 4.3.3), and the lack of features in the extended emission to the northwest, we speculate that this last emission is scattered light from the AGN, which explains its very blue U–V colour. Actually, the colours are those of an almost pure power-law with index a=1 (see Figure 4.4). Another possibility would be the existence of a very young stellar population, although there is no sign of clumps, knots or point-like sources, as it is common in star-forming environments.

The young stellar population may come from disrupted star clusters in the nuclear environment, although the presence of knots in the southeast arc indicates that young star-clusters do not necessarily get disrupted at that distance (∼100–150 pc) from the nucleus. We do not discard that the contribution of young stars is larger in the inner 200 pc, which would increase the relative contribution of star formation in studies at lower resolution.

### 4.4.13 UGC 1214 (Sy2)

We used the procedure explained above, with **f**=0.30, and end up with a residual image free from the filamentary structure observed in both [OIII] and F330W images. This is the best example in which a reasonable scaling of the [OIII] image can account for all the filamentary structure. From this we deduce that ∼40 per cent of the near-UV light comes from nebular continuum and [NeV] emission. The resulting image shows a central oval structure (see Figure 4.2) of diffuse light. Although this object has no F547M exposure, it does have a NICMOS image which is dominated by the bulge. As in other cases, we reduced the NICMOS image and subtracted the central point-like source, ending up with a smooth bulge. Although we cannot have both $U$–$V$ and $V$–$H$ colours for this object, we verified, using SSP models, that the colour F330W–F160W ($U$–$H$) behave monotonically with age. We performed aperture photometry and were able to trace a colour profile up to 2.5 arcsec (∼1200 pc). From 0.5 to 2.5 arcsec the profile stays fairly flat around $U$–$H$=0.9, and in the inner 0.5 arcsec there is a blue drop of 1.5 magnitudes. This implies that the extended emission can be attributed to the underlying bulge, and that there exists a compact blue region in the very centre of the galaxy. A simple proof with synthetic photometry similar to the one used in Figure 4.4, but only with one colour, shows that, in order to have a drop of 1.5 magnitudes in the centre, it is necessary a contribution of ∼70 per cent from a young population or a power-law. On the other hand, Cid Fernandes et al. (2001) studied the stellar population in the inner 2 arcsec, reporting a contribution of young/intermediate age stellar population and featureless continuum of 10 per cent of the light at 486.1 nm. Therefore, the previously reported young stellar population in this object may be located in the inner 0.5 arcsec.

### 4.4.14 UGC 6100 (Sy2)

A range of **f** between 0.2 and 0.3 removes what seems to be the ionised gas emission. A higher fraction starts to leave patchy negative residuals near the nucleus. There is an important nuclear contribution which can be attributed to a mechanism different from the NC or [NeV] line emission, unless there is a strong variation in the value of **f** in these small scales, due to a varying ionisation parameter and/or thick obscuring patches. The photometric analysis suggests that the remaining light may probably be explained by stellar emission. As can be appreciated in the colour profiles of Figure 4.5, there is a constant $U$–$V$ colour gradient of ∼ -0.12 mag/100 pc extending out more than 1.5 kpc from the nucleus. However, in the inner 100 pc we find a small red cusp, that is wider than the PSF FWHM. In *V–H* colour the behaviour is the opposite, with a slight positive gradient ($\sim 0.03\,\mathrm{mag}/100\,\mathrm{pc}$), and a central blue dip. This galaxy is listed in NED as of possible Sa type, so the *U–V* gradient is to be expected. It is unlikely that the colours of the inner 100 pc are caused by an excessive subtraction of the UV emission, due to the small **f** used (0.25). Moreover, the [OIII] image is smoother in the centre, and the feature remains when using a smaller **f**. Instead, we suspect that the central colours may be due to contamination of the F547M image by emission lines. This is because the redshift is high enough to make the strong [OIII]$\lambda\lambda$5007 fall in the blue wing of the filter, in a position where it has almost 70 per cent of its peak transmission. However, the results beyond 100 pc from the nucleus are quite robust, and there is no need for other mechanism to be invoked, apart from the stellar emission of bulge and disc components.

### 4.4.15 UGC 12138 (Sy1.8)

The emission is quite compact, concentrated in less than 1 arcsec. The reasonable values of **f** are too small to eliminate the nuclear emission in this case. Forcing a high value of **f** ($> 0.8$) the nuclear emission is subtracted, although the extended emission around it remains, and also negative residuals start to appear with $\mathbf{f}\geq 0.5$. Using a scaling factor of 0.35 yields that the contribution of the ionised gas is $\sim$18 per cent of the total near-UV light (once the Sy nucleus is subtracted). So most of the emission is not due to ionised gas in this object. This remaining light constitutes a compact halo around the nucleus, which is visible in the two bluer bands (F330W and F547M). For this object it is worthwhile to perform a PSF subtraction in all the three bands, in order to study the halo close to the nucleus. Then, we performed circular aperture photometry in an annulus around the nucleus, with inner and outer radii of 0.35 arcsec and 0.75 arcsec, that correspond to 175 pc and 375 pc, respectively. The inner radius is large enough to avoid uncertainties due to the subtraction of the nuclear contribution in the bluer bands. The major uncertainties will come by the adopted scaling value for the [OIII] image. Altough in this object the estimate of the ionised gas contribution has a big uncertainty, we will use a factor $\mathbf{f}$=0.35, that seems to work well for the objects with ionisation cones. The colours of the extended emission (*U–V*=1, *V–H*=-0.98) are similar to those in NGC 5347, which has also a similar morphology. With the caveat discussed above, we interpret the colour as due to an old bulge with a contribution of scattered nuclear light.

Table 4.3: Summary of the results of the extended light analysis

| Object name | Seyfert type | Scale ("/kpc) | E(B-V) | Nucleus | Nuclear contrib. | m(1kpc) (mag) | likely f | Δf | Fneb/Ftot | ΔFn/Ft | Polarimetric studies | Photometry of the residuals |
|---|---|---|---|---|---|---|---|---|---|---|---|---|
| IC 5063 | Sy2 | 4.61 | 0.061 | No | | 15.66 | 0.25 | 0.05 | 0.23 | 0.05 | P∼1-2% in the optical[d] | Remaining light compatible with bulge population |
| Mrk 6 | Sy1.5 | 2.55 | 0.136 | Yes | 0.72 | 15.94 | 0.20 | 0.05 | 0.62 | 0.16 | P∼1% at red wavelengths[e] | |
| Mrk 915 | Sy1 | 2.08 | 0.063 | Yes | 0.72 | 16.22 | 0.30 | 0.05 | 0.30 | 0.05 | | |
| NGC 1320 | Sy2 | 5.85 | 0.047 | No | | 14.80 | | | $< 0.15^c$ | | | Old bulge population with a significant bluer component, likely star-formation. |
| NGC 3393 | Sy2 | 4.10 | 0.075 | No | | 15.00 | 0.35 | 0.05 | 0.33 | 0.10 | | |
| NGC 3516 | Sy1.5 | 5.05 | 0.042 | Yes | 0.60 | 14.46 | | | $< 0.11^c$ | | | Compact diffuse emission with bulge colours. |
| NGC 4253 | Sy1.5 | 3.66 | 0.020 | Yes | 0.32 | 15.24 | $0.41^a$ | | $< 0.16^c$ | | | |
| NGC 4593 | Sy1 | 5.32 | 0.025 | Yes | 0.71 | 14.53 | | | $< 0.08^c$ | | P<1% at red wavelengths[e] | |
| NGC 5347 | Sy2 | 5.62 | 0.021 | No | | 16.26 | $0.40^b$ | 0.05 | $< 0.08^c$ | | | Old population plus a 10-30% contribution of bluer component. Indicates reddening effects or scattered AGN light. |
| NGC 5548 | Sy1.5 | 2.79 | 0.020 | Yes | 0.74 | 15.70 | | | $< 0.25^c$ | | P<1% at red wavelengths[e] | |
| NGC 7212 | Sy2 | 1.86 | 0.072 | No | | 16.61 | 0.20 | 0.05 | 0.53 | 0.13 | P∼10%. Scattered light may contribute $\lesssim 30\%$ [f] | Clear star-formation. Scattered light may be present. |
| NGC 7674 | Sy2 | 1.72 | 0.059 | No | | 15.58 | 0.50 | 0.15 | 0.28 | 0.08 | P$\gtrsim$10%. Scattered light may contribute $\lesssim 40\%$ [f] | Very blue residuals. Both, star-formation and scattered light, are present. |
| UGC 1214 | Sy2 | 2.95 | 0.023 | No | | 15.59 | 0.30 | 0.05 | 0.39 | 0.07 | | Old bulge plus a blue contribution in the inner 0.5". |
| UGC 6100 | Sy2 | 1.66 | 0.012 | No | | 17.04 | 0.25 | 0.05 | 0.18 | 0.04 | | Mostly stellar emission. |
| UGC 12138 | Sy1.8 | 1.99 | 0.085 | Yes | 0.72 | 16.13 | 0.35 | 0.10 | 0.18 | 0.05 | | Mostly bulge emission with a small bluer contribution. |

Col.(1) : galaxy name; Col. (2): nuclear activity type; Col. (3): inverse scale, as angular size of the studied region, calculated from Table 4.1; Col. (4): galactic reddening, E(B-V), from NED; Col. (5): occurrence of a point-like nucleus in the near-UV; Col. (6): contribution of the nucleus to the total near-UV light inside 1 kpc; Col. (7): F330W magnitude of the inner 1 kpc (after nuclear subtraction), corrected from galactic extinction; Col. (8): estimated value for the scaling factor **f**; Col. (9): estimated uncertainty of scaling factor **f**; Col. (10): calculated contribution of nebular emission to the total emission (after nuclear subtraction) in the inner 1 kpc; Col. (11): uncertainty of (10), calculated from (9) and considering an uncertainty of 5 per cent of the peak value when scaling the PSF for the nuclear subtraction.; Col. (12): polarimetric studies for some objects of the sample; Col. (13): summary of the results from the photometry of the images after subtraction of the ionised gas component.

[a] Literature based value.

[b] Calculated for the arc of emission to the north-east.

[c] Upper limits are normally calculated for f=0.6, either in the inner kpc or in the region in which we have enough [OIII] signal-to-noise.

[d] Reference: Inglis et al. (1993)

[e] Reference: Smith et al. (2002)

[f] Reference: Tran (1995)

## 4.5 Summary and discussion

The near-ultraviolet morphology of the 15 objects studied in this work has been described in Chapter 3. In this chapter we intend to gain insight into the light emitting processes that generate the particular morphology of each object. In the nuclei of Seyfert type 1 to 1.5, the dominant component is the AGN emission, visible as a bright point-like source. In these objects the nucleus has to be removed prior to any further analysis.

In order to understand the diffuse light emission we start by focussing on the ionised gas emission. We have used the narrow band [OIII] images from Schmitt et al. (2003) to remove this component. The [OIII] images were scaled in order to model and subtract the predicted contribution from the [NeV] lines and nebular continuum from the F330W image. An estimation of a reasonable range of scaling factors was presented in Section 4.3.2. A comparison of the narrow band images (tracing the ionised gas), with the near-UV broad band images, show a strong similarity in many cases. We have demonstrated, by scaling accordingly the [OIII] images, that the emission of the ionised gas can explain the extended emission visible in several objects. This is the case of the filamentary structure in IC 5063, NGC 3393 or UGC 1214 (Mrk 573), as well as parts of the more diffuse emission in Mrk 6, Mrk 915, NGC 5347 and NGC 7212. These regions of ionised gas are large, extending from 100 pc to 1 kpc from the nucleus, and in general can be accounted for with a scaling factor for the [OIII] image (in the range f∼0.2–0.4), consistent with the expected level of line emission and nebular continuum contamination.

When possible, we have performed a photometric study in three bands: near-UV (ACS F330W), optical (WFPC2 F547M), and near-IR (NICMOS F160W). The results are summarised in a colour-colour diagram, in Figure 4.6. We have measured colours around F160W–F547M∼-1 and F547M–F330W∼0.8–1.8, in STMAG, for several objects. These colours are consistent with a several Ga old stellar population. We interpret this as an indication that the diffuse emission remaining after estimating and subtracting the ionised gas contribution, can be attributed to the underlying stellar population of the bulge. This is the case of objects such as IC 5063, NGC 1320, NGC 3516, UGC 1214, UGC 6100, and UGC 12138.

In a number of objects we also find a strong near-UV emission extending less than 100 pc from the nucleus (see for example NGC 4593). These are mostly Sy1 in which even after the best nuclear-PSF subtraction, there remains a compact but resolved emission. We have already argued that we do not think this is an artifact of the PSF subtraction of the nucleus, but a real feature. However, it is true that the nuclear subtraction generates uncertainties that preclude any accurate analysis of the very inner region. In these cases, we cannot say much about the origin of this light. We have made some calculations to set an upper limit to the contribution of the ionised gas emission, as indication for a different mechanism. A strong change in the ionisation parameter (higher towards the centre) has not been ruled out, though.

The physical regions studied in this work are located between 100 pc and 1 kpc from the Seyfert nuclei. At these scales, the scattered light from the AGN does not seem to contribute in a significant fraction to the total light, in the majority of the cases. We demonstrated that, in general, an ionised gas contribution is very difficult to distinguish from a young stellar population with a photometric analysis and the filters used. However, we suspect that in the case of NGC 7674, the scattered light from the AGN is responsible for the near-UV emission to the northwest of the nucleus. This is the only evidence for scattered AGN light that we find among the objects studied, although absence of evidence is different from evidence of absence, and scattered light could play an important role in other objects with an unidentified blue component, as for example NGC 7212. This result differs from those in radio galaxies studies. For example, Tadhunter et al. (2002) find that the objects with largest UV polarisation tend to have the largest emission line luminosities. In Cygnus A, Ogle et al. (1997), find reflection nebulae in polarised light that have a similar scale and general morphology to the ionisation cone seen in emission lines. There is a possible way out of this. Dust is expected to correlate with the gas distribution, and therefore some scattered emission might have been subtracted with the ionised gas. That would explain high values of the scaling factor for the [OIII] image, as in the case of NGC 1320, and at least in part, the positive residuals of some of the objects. However, as discussed above, ionised gas emission alone can explain the cases in which the near-UV morphology matches the [OIII] emission.

Regarding a possible starburst component, we have not found, in general, unequivocal evidence of extended unresolved young stellar populations. However there are several objects, such as IC 5063, NGC 1320, NGC 3393, NGC 5347, and UGC 1214, which show spectroscopic evidence for young or intermediate age stellar population (Cid Fernandes et al., 2001, 2004a; González Delgado & Pérez, 1996b) but do not show obvious star clusters in the near-UV images. That would be the case of a population of small star clusters appearing unresolved in our images, or a very high rate of cluster disruption in the nuclear region. Star-forming regions and massive star clusters stand out as compact knots in the near-UV image. They make a significant contribution in a fraction of objects (4/15, or ∼27 per cent); namely, NGC 4253, NGC 5548, NGC 7212, and NGC 7674. In addition there are 2 objects (NGC 4593 and UGC 6100) in which star clusters are identified but lay at kpc distance from the centre of the galaxy, far away of the region studied and thus they do not contribute to the near-UV emission in the nuclear region. This is why we leave out these two objects in the general conclusions. Therefore ∼40 per cent of the sample (6/15 objects, including the two objects with clusters further than 1 Kpc) show circumnuclear star clusters, while in the original sample we find star clusters in around 70 per cent of the sample. This difference can be attributed to a bias due to the fact that the sample analysed here is only a small subsample of the larger sample, selected on the basis of availability of [OIII] data.

There exists the possibility that a young stellar population is completely diluted in the bulge light and we cannot detect it. Emission from the ionised gas, as well as the underlying bulge stellar population are enough to explain the diffuse light in most cases. On the contrary, the clumps and compact emission are likely due to star-formation or AGN light.

The results in Table 4.3 show no apparent trend between the Seyfert type and the magnitudes calculated, such as estimated scaling factor for the [OIII] image, the ionised gas contribution to the total near-UV light, or the flux in the inner kpc. However, we have to take into account the small size of the sample and the difficulties to study some Sy1 for which we could set only upper limits to the ionised gas contribution.

## 4.6 Conclusions

Our main conclusions are:

- For ~50 per cent of the galaxies of the sample (8/15), emission of ionised gas from the NLR dominates the near-UV extended emission reaching up to 1 kpc from the nucleus.
- For 7 galaxies, we could obtain broad-band photometry of the UV images after the subtraction of the ionised gas emission; for 6 of them, colours of the extended emission left after the subtraction of the gas emission are consistent with those of an old stellar population; among these galaxies there are also 5 objects for which we find evidence of an additional contribution of either scattered nuclear light or a diffuse young stellar population.
- Only for 1 galaxy we have found that scattered light dominates the extended emission, although this kind of emission might be present at a lower level in a large fraction of the objects.
- For 4/15 galaxies of the sample, star forming regions appear as compact knots surrounding the nucleus and contribute significantly to the near-UV light in the inner kpc.

In summary, there is not a unique and dominating mechanism responsible for the near-UV emission. Each object deserves a particular study and a close inspection, as we find the most varied morphologies. A deeper study would require the use of spectroscopy, and optimally, the use of IFU data with enough resolution and polarisation observations.

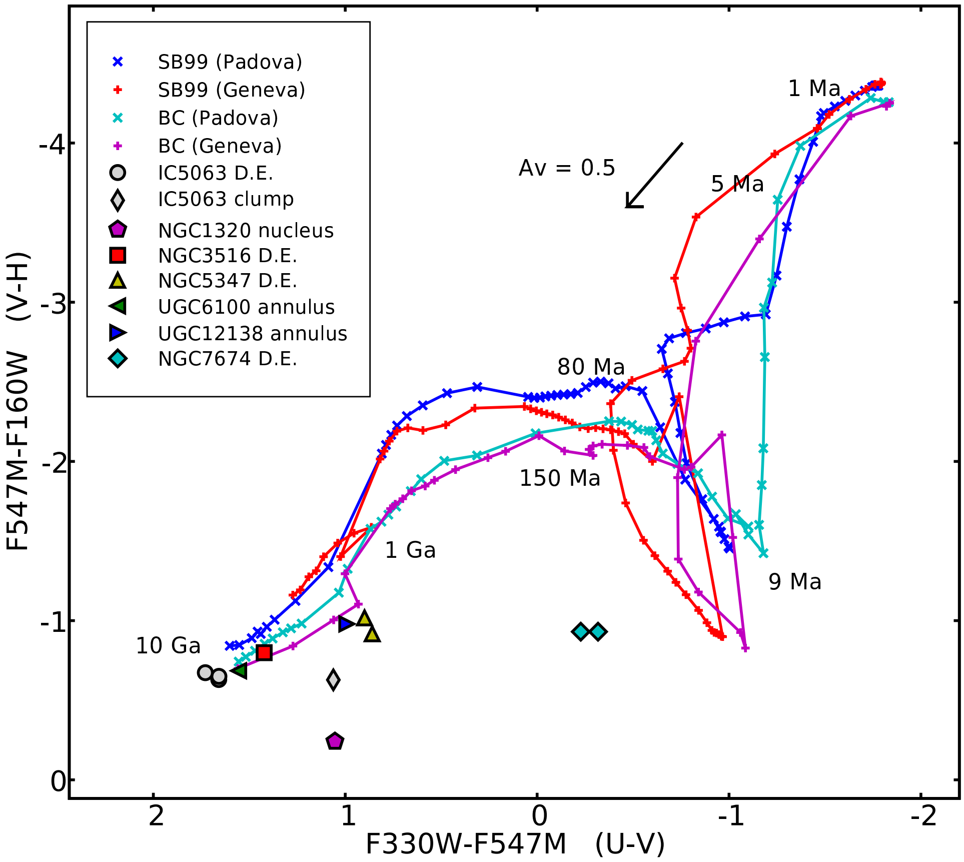

Figure 4.6: Same colour-colour diagram as Figure 4.3, but adding the photometric results for several objects. Different colours and symbols stand for different objects and regions, which are labelled in the plot legend, in which 'D.E.' stands for diffuse emission. The photometric points are corrected for galactic extinction with the law of Cardelli et al. (1989). The reddening vector corresponding to $A_V$=0.5 is also plotted for reference.

# Chapter 5

# A methodology to study the star cluster population, and its application to NGC 5135

---

Contents

## 5.1 Introduction

The determination of the properties of the nuclear and circumnuclear star cluster population is critical in order to understand the past and present evolution of the bulge and SMBH environment. The main methods used to study unresolved extragalactic clusters are basically two: either obtaining deep and high-quality spectroscopy (Whitmore et al., 1999; Bastian et al., 2009), or by means of high-resolution broad-band photometry and comparison with predictions of population synthesis models (e.g. Chandar et al., 2010). The first method is costly in terms of observing time, and is mostly limited to small samples of bright clusters. Beyond the Local Group of Galaxies only broad-band photometry of large samples would yield statistically significant results. With the use of this method, the multi-wavelength data presented in previous chapters will allow us to determine the frequency of circumnuclear starbursts, down to levels that cannot be observed from the ground; characterize the properties of these clusters, such as flux, color, size, mass, age, etc.; to study the luminosity function of star clusters and their survival rate close to the AGN. Moreover, the extension of this study to a large sample of Seyfert galaxies would let us address questions about the relation between AGNs and starbursts, like the possible connections between the masses of black holes and luminosities of starbursts, and the implications for the evolution of the black holes and their host galaxy bulges.

The goal of this chapter is to optimize a procedure to study the star cluster population with this kind of data. This method could be later extended and applied to a larger sample of galaxies in order to draw statistically significant conclusions. However, one should keep in mind that the peculiar morphology of each object, combined with the effect of the distance on the final resolution, pose a limit on how an automatized algorithm can be applied to a large sample, and a fine tuning of the method would be required in order to adapt it to each galaxy.

Our approach has been to focus in a particular object to perform the analysis, and identifying the caveats and necessary steps in order to carry out the study. We have chosen the Seyfert 2 / LIRG galaxy NGC 5135, as it clearly shows the main components that we have noted studying the Atlas of the whole sample. This object possesses a rich population of clusters and star-forming areas in its nuclear region. Two sharp dust lanes produce strong light absorption in the shorter wavelength bands in a spiral pattern. A cone-shaped structure of extended emission (best identified in the F606W and F330W filters) is also observed, opening to the south of the bright red nucleus. Figure 5.1 shows a color image of the circumnuclear region of NGC 5135. We have assumed a distance of 55 Mpc (from NED), which yields a physical scale of 6.7 pc/pixel.

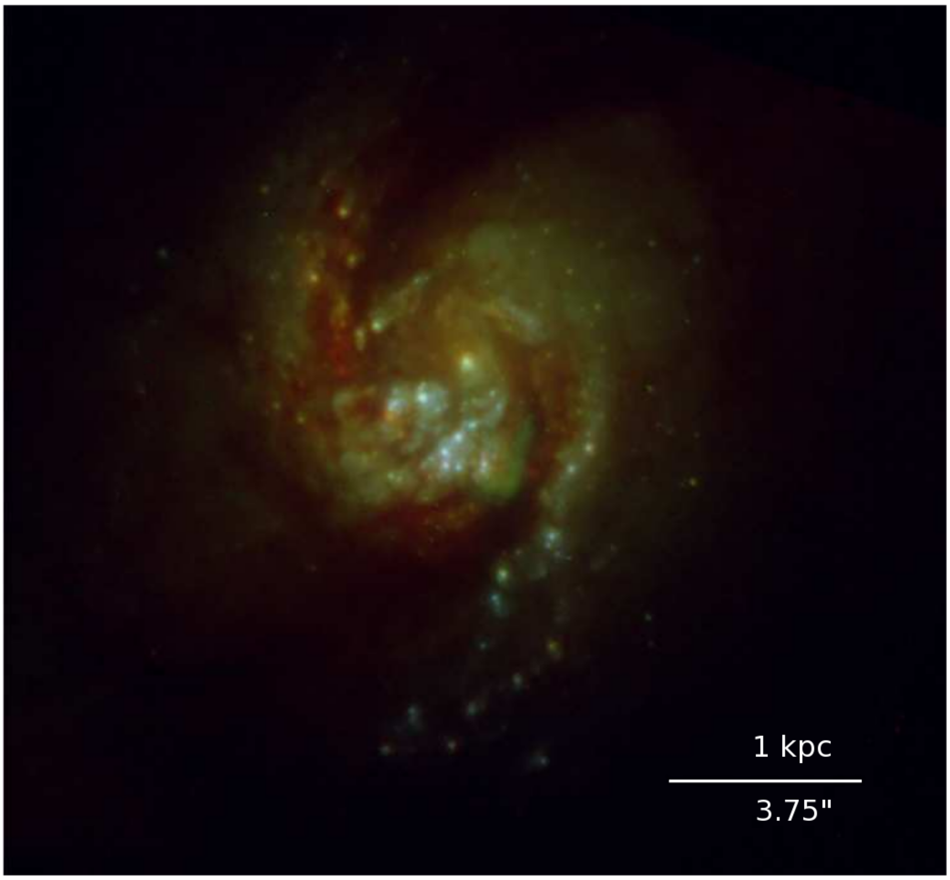

Figure 5.1: False color image of the circumnuclear region of NGC 5135 composed from broad band HST images. In the blue channel the F330W ACS exposure (∼U), in the green channel the F606W WFPC2 image (∼R), and in the red channel the F110W NICMOS exposure (∼J). North is up, east to the left.

Table 5.1: Basic data of the HST images used for this study

| Filter name | Wavelength (Å) | Instrument | Scale (″/pixel) | Exposure Time (s) | Orientation angle (°) |
|---|---|---|---|---|---|
| F210M | 2187.8 | FOC, F/96 | 0.014 | 1962.5 | 77.13 |
| F330W | 3367.2 | ACS, HRC | 0.025 | 1200 | 0 |
| F606W | 6035.2 | WFPC2, PC | 0.046 | 500 | 346.83 |
| F110W | 11353 | NICMOS, NIC2 | 0.076 | 80 | 70.41 |
| F160W | 16074 | NICMOS, NIC2 | 0.076 | 320 | 223.44 |

In column (1) the observation band; in column (2) the average wavelength of the filter, calculated with IRAF package 'synphot'; in column (3) the instrument and detector used for the observation; in column (4) the scale plate calculated from the image header; in column (5) the total exposure time; in column (6) the orientation angle with respect to the north.

## 5.2 Data

### 5.2.1 Available data

Data from the archive of the Hubble Space Telescope provide the high spatial resolution at a large wavelength coverage that we need for our analysis. Images in five bands are available for the nuclear region of this object, ranging from the ultraviolet to the near-infrared: F210M, F330W, F606W, F110W and F160W. The F210M data (UV) are images from the Faint Object Camera (after COSTAR), which is a first generation instrument, and thus the sensitivity and photometric accuracy is lower. The F330W (near-UV or ∼ U) observations are Advanced Camera for Surveys (ACS) data, in its High Resolution Configuration. The F606W (∼ V+R) image is taken with the PC chip of the Wide Field Planetary Camera 2 (WFPC2-PC). The F110W (∼ J) and F160W (∼ H) are NICMOS-NIC2 images. The data were reduced with the HST pipeline on-the-fly calibration, and further removed of cosmetic defects, cosmic-rays, pedestal effect (for NICMOS data), etc., as described in previous chapters. In Table 5.1 we summarize the basic data of the images used.

### 5.2.2 Image alignment

In order to better identify the stellar clusters, and to do a homogeneous analysis in the different bands, we aligned the available images, matching them to the ACS data. The orientation and pixel scale of the images were extracted from the image header (see Table 5.1). Then, with a first run of the IRAF task 'geotran', we applied a rotation and rescaling of the images to match the orientation (north up) and pixel scale of the ACS frames (0.025 arcsec per pixel). The chosen reference image, the

F330W ACS exposure, was cropped to the area of interest, in which all the clusters that were visible in every band laid. Next step was to determine the shift between each image and the reference one. In order to do that, we calculated the centroid position of several clusters visible in both images of every pair, and used the task 'geomap' to determine the correct transformation. With the results from 'geomap' we run once more 'geotran' task, obtaining images in which the clusters are in the same positions than their counterparts in the reference image, ready for further analysis.

## 5.3 Analysis

In this section we present the procedure used to characterize the cluster population. First, we used IRAF task 'daofind' in order to find and select the stellar clusters visible in every band. After creating object lists for each band, we performed aperture photometry of the cluster population. This step yields which is the luminosity range we are working with. Finally, we performed some simulations, adding to the images artificial clusters in this luminosity range, and repeating the finding and selection process. This provides an estimate of the fraction of objects that we can recover and with what precision we can measure their fluxes, or in other words, the completeness of the cluster population and the uncertainty of the calculated magnitudes.

### 5.3.1 Cluster identification

The star clusters were identified using 'daofind' task from the IRAF package 'daophot', which has been developed for finding point-like objects. The configuration parameters of the task, used in the search algorithm, depended on the image we worked with. It is thus not possible to give a set of parameters which work in every occasion and data set. Our approach was to try several parameter sets, until we found an optimizing set for each band, which identified most of the clusters obvious by eye-inspection of the data, while not introducing image artifacts as false detections. The cluster lists were further cropped with an extra criterium of sharpness and roundness, both following the internal definitions of 'daophot', which together give an estimation of how point-like and object is, thus preventing us from identifying whole compact star-forming regions as star clusters. In some bands, a few clusters which were visible by eye-inspection were missed by 'daofind', probably due to strong background variation. In these cases the clusters were added manually to the output lists.

We identified 101 clusters in the F330W band, 72 clusters at F606W, and 78 at F110W. In the F160W band the objects were harder to identify, as this wavelength offers the worse resolution, due to a wider PSF, and a higher background. We decided to relax the criteria for finding clusters, thus obtaining a larger list of 131 candidate objects, and letting the previous bands to limit our final set of clusters. Dealing with the F210M FOC data resulted quite tricky. Despite having the longest exposure time, the lower sensitivity of this configuration made these data of poorer quality than the rest of the bands. A relaxed set of sharpness and roundness parameters yielded 27 objects, but a close inspection of the image showed that most of them were obviously spoiled by cosmic-rays, cosmetic defects and similar, and they did not show the usual PSF aspect. Therefore, we ended up selecting 9 objects with clear point-like appearance, rejecting the others, as we expected large errors in their fluxes.

Finally we cross-correlated the lists of the different filters, considering objects in different images to be the same object if the separation between them was smaller than 3 pixel. This is equivalent to a 1.5 pixel uncertainty in the cluster position, which we considered appropriate taking into account the wider NICMOS PSF. After this, we ended up with 9 clusters unambiguously identified in all 5 bands, and 21 more in all but the FOC data. Therefore, 30 objects were left to do fitting of Single Stellar Populations to derive some physical parameters of them. These are few respect to the number of clusters found in the individual bands, but one has to take into account that ultraviolet and near-infrared bands trace different stellar populations, and the objects which are bright in UV are not necessary the same which are brighter in the near-IR. This effect is enhanced in our data because we find mainly the brightest clusters at each band. Probably, with deeper data we would have had a larger overlap between the lists. All the clusters found lay in the central region of 350 pixel radius, which correspond to 2.5 kpc to the distance of NGC 5135.

### 5.3.2 Cluster photometry

We performed aperture photometry with the IRAF task ‘phot’, in a similar way for the five different bands. Circular apertures of 5 pixels radius were used, and the background level was calculated as the mode in a circular annulus of 5 pixels of inner radius and 2 pixels width. This seems enough to get most of the light in (∼80% of the total for the near-UV band and ∼60% in the near-IR), and avoid severe contamination by other clusters in the crowdiest regions. We tried first with larger apertures, of 7 pixels radius with background between 7 and 9 pixels, in order to get more light into the aperture. However, the artificial cluster simulations explained bellow, yielded a larger dispersion for the measured fluxes, probably due to the background determination. The fluxes measured in the aperture, with the background subtracted (DN), were transformed to magnitudes in the STMAG system with the usual formula:

$$m = -2.5 \cdot \log \left( \frac{DN \cdot PHOTFLAM}{EXPTIME} \right) - 21.1$$

### 5.3.3 Corrections to measured magnitudes

#### 5.3.3.1 Aperture corrections

When working with aperture photometry of point-like objects in crowded fields, it is usual to measure the flux in a small aperture. The goal of this is to avoid very high uncertainties due mainly to the background determination. As a drawback, an important part of the flux of the object may fall outside the selected aperture, and therefore the flux has to be aperture-corrected. This correction is usually calculated by performing the same measurement in an isolated object that allows the use of a large aperture for comparison. Another way is to use the theoretical PSF of the instrument and generate an artificial object of known flux. The ratio between the measured flux and the total flux gives the correction to be used. As there are no isolated point-like objects in our images we have adopted the second method of analysis.

One thing to be taken into account is that the physical scale of the ACS image, at the assumed distance of 55 Mpc, for NGC 5135 is around 6.7 pc per pixel. That means that some of the brightest clusters should appear at least slightly resolved. For comparison, Scheepmaker et al. (2007) find cluster sizes in M 51 between 0.5 and 10 pc, with a mean of 2.5 pc (corresponding to near 1/3 of a pixel, on average). This effect should be negligible for the bands with a PSF much wider that the expected FWHM of the objects, as well as for F210M, in which the aperture is much larger than the PSF and the correction very small. For these reasons, and in order to asses whether this is an important effect for our data, we carried out the next analysis in the F330W.

An artificial PSF for this filter was created with TinyTim software, with a flux of 1e-16 erg/s/cm$^2$. The FWHM (as measured with IRAF task ‘imexam’) of this pure PSF was 1.4 pixel, while most of the point-like objects in the image exhibited a FWHM between 2 and 3.5 pixels. This difference could be due also to the data reducing, and image stacking, as well as changes in the telescope focus, but the effect in our measurements is the same to the clusters being resolved. Then, we used the IRAF task ‘gauss’ to change the FWHM of the artificial PSF by convolving the former with several gaussians of different width. Aperture corrections were then calculated for 7 pixels apertures and background determined in an annulus of 7-9 pixels. This yielded an aperture correction of 1/0.823 for a pure PSF, 1/0.8176 for a simulated cluster of FWHM of 2.5 pixel, and 1/0.8145 for a cluster of FWHM of 3 pixel (see Table 5.2). This suggests that for each band we can use a unique aperture correction for all the objects, with an error bellow 1% in most of the cases.

#### 5.3.3.2 Reddening correction

The extinction due to the interstellar medium in the Milky Way must be corrected prior to any further analysis. We have assumed a value for the color excess E(B-V) of 0.060 as listed in NED. We have used also the law of Cardelli et al. (1989), which gives the dependence with wavelength $\lambda$ of the total extinction A. Extinction in a

Table 5.2: Dependence of the aperture correction with the size of the cluster

| $\sigma$ of gaussian convolution kernel | resulting FWHM | enclosed flux (%) |
|---|---|---|
| 0 | 1.38 | 82.30 |
| 0.5 | 1.60 | 82.14 |
| 0.6 | 1.89 | 81.95 |
| 0.7 | 2.19 | 81.84 |
| 0.8 | 2.5 | 81.76 |
| 0.9 | 2.74 | 81.60 |
| 1.0 | 3.0 | 81.45 |
| 1.1 | 3.23 | 81.22 |
| 1.18 | 3.38 | 81.02 |

Fraction of the total flux of a simulated cluster (in %) measured in a 7 pixel aperture subtracting the sky in a circular annulus between 7 and 9 pixel radius. When plotted, these data show a polynomial dependence on FWHM.

band depends both, on the filter shape, and on the shape of the spectrum at the wavelength range. As we do not know a priori how is the spectrum of the objects, we have used a whole set of Bruzual & Charlot (2003) models. Each model was reddened with Cardelli's law and the assumed color excess. The photometry in every band was then performed with the original spectrum and the reddened one. The extinction correction is the difference in magnitude before and after reddening is applied. The dependence with age was found to be very small for all the bands, except for the F210M filter. An average value of the correction was used for each band as a unique correction for all the photometric measurements in that band. The age of the model set used was sampled logarithmically, so the calculated value of the reddening correction represents better the value expected for young clusters than that for old clusters. However, those clusters detected in F210M (the only band with a strong dependence on age) are expected to be young clusters, with a strong UV emission. The use of a single value for the reddening correction is thus justified.

#### 5.3.3.3 Charge Transfer Efficiency correction:

When reading the CCD some charge is lost in the process of transferring the charge along the CCD columns. The amount of charge lost depends on the number of charge transfers from the original pixel to the amplifier, and hence it depends on the position on the chip. The effect in the photometry depends also on the amount of charge which is transfered, the lower charge needing the larger corrections. Therefore, two important parameters are: local background (the higher the background subtracted, the less charge is lost), and object flux (larger fluxes, smaller corrections). The charge transfer inefficiency increments with time, as the detector deteriorates with the environmental radiation. In order to do fine photometry a correction for the Charge Transfer Efficiency (CTE) is usually needed.

For the chip HRC of the ACS, the charge transfer correction is calibrated in ISR ACS2009-01 (Chiaberge et al., 2009) with the next equation:

$$\Delta(mag) = 10^{\gamma} \times SKY^{b} \times FLUX^{c} \times (Y_{tran}/1000) \times (MJD - 52333)/365 \tag{5.1}$$

where $\Delta(mag)$ is the magnitude correction to the photometry of the object, $SKY$ is the local background subtracted (in units of counts), $FLUX$ is the brightness of the object (in counts), $Y_{tran}$ is the number of vertical transfers (from the original pixel to the border of the chip), and $MJD$ is the Julian date of the observation. The value of the parameters are: $\gamma = -0.44$, $b = -0.15$, and $c = -0.36$. Usually, only the column charge transfer is considered, as charge transfer inefficiency due to serial transfer (in X direction) is negligible (Riess & Mack, 2004).

We have checked how important this effect is for our objects by plotting the correction calculated with the formula above, against the visual magnitude for the clusters found in the F330W filter (Figure 5.2). We have calculated a superior limit by using $Y_{tran} = 1024$, this is the position on the border of the chip. In the figure we appreciate that, in general, for a cluster of magnitude 25 in the border of the chip the correction is at most 0.01 magnitudes. Therefore, we can neglect this effect for our objects, as our expected uncertainty is much higher.

For the WFPC2 camera the CTE correction is calibrated by Dolphin (2000). A preliminary estimation of this effect for our F606W data yielded a correction for a typical cluster of m = 23.5 between 0.01 and 0.04 magnitudes. We therefore decided to perform the complete CTE correction for this band. Following Dolphin (2000) we correct for CTE with the next set of equations:

$$\begin{aligned}
yr &= epoch - 1996.3 \\
lct &= \ln(counts) - 7 \\
lbg &= \ln(background) - 1 \\
YCTE &= \frac{Y}{800} \times [\, y0 + (y1 + y2\, yr) \times (y3 + \exp(-y4\, lct)\,) \times \exp(-y5\, lbg - y6\, lbg)\,] \\
XCTE &= \frac{X}{800} \times [\,(x1 + x2\, yr) \times \exp(-x4\, lct - x5\, lbg)\,] \\
\Delta_{mag} &= \frac{Y}{800} \times YCTE + \frac{X}{800} \times XCTE
\end{aligned} \tag{5.2}$$

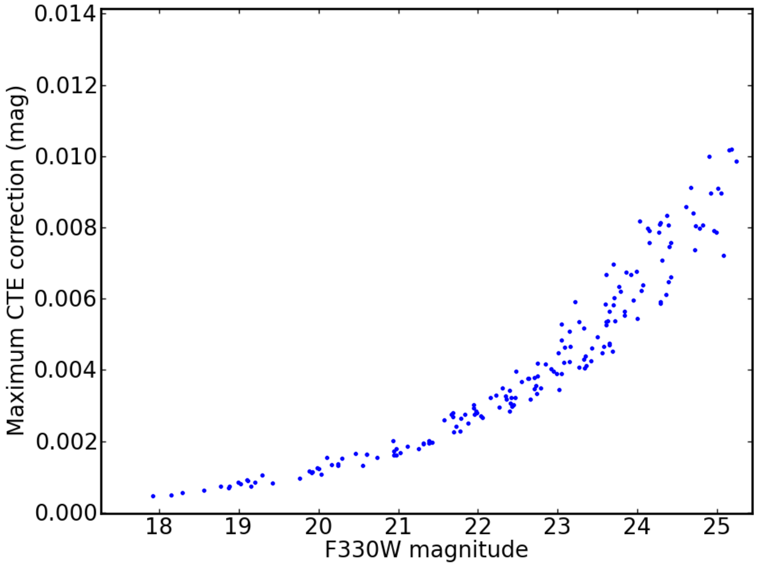

Figure 5.2: Charge transfer efficiency (CTE) correction versus magnitude for the clusters found in the F330W exposure. CTE correction is calculated with Equation 5.1, asuming a position in the border of the chip, so it is an upper limit for the correction of a typical cluster of our sample.

where *epoch* is the date of the observation (year with fraction), and *counts* and *background* are given in counts, as in the case of ACS discussed above. The parameters *xi* and *yi* are tabulated in Dolphin (2000). X and Y are the pixel coordinates in the original image, so we had to transform the coordinates of the clusters found in the transformed image to the ACS scale to the original one by a sort of inverse transformation with the next equations:

$$\begin{aligned} X &= q\,(X_t\,cos\phi + Y_t\,sin\phi) + s_x \\ Y &= q\,(-X_t\,sin\phi + Y_t\,cos\phi) + s_y \end{aligned} \tag{5.3}$$

with $X_t, Y_t$ the coordinates in the transformed image, $\phi$ the orientation angle of the original F606W image (346.83°), $q$ the scale factor (ACS plate scale divided by WFPC2 plate scale, which is 0.54888 in this case), and $\{s_x, s_y\}$ a zero point shift in each coordinate, calculated from several clusters visually identified in the original and transformed images. Figure 5.3 shows the correction for the clusters at F606W and its dependence with the cluster magnitude.

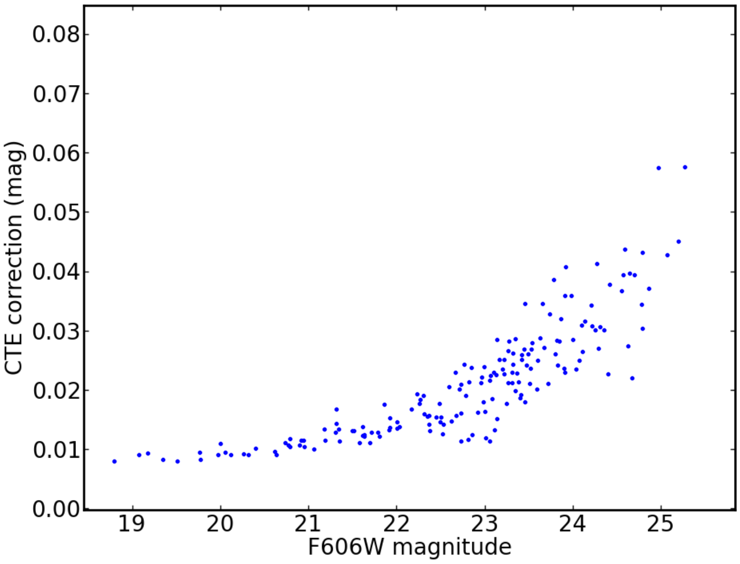

Figure 5.3: Charge transfer efficiency (CTE) correction versus magnitude for the clusters found in the F606W exposure. CTE correction is calculated with Equation set 5.2.

For the NICMOS bands this kind of correction is not needed, as NICMOS detector is a HgCdTe chip, which is read without the need of charge transfer unlike a CCD. The F210M image is a Faint Object Camera exposure. FOC is a first generation Hubble instrument and the uncertainty in the absolute photometric calibration is quite high (around 10–15 %, as explained in the FOC Data Handbook of STScI). Therefore we neglect this effect against other uncertainties.

### 5.3.4 Simulations of artificial clusters

In order to asses the validity of the search and selection process, we added several set of artificial clusters to the original images in each filter. In each run, we generated 100 randomly positioned point-like objects of a certain magnitude from an artificial Tinytim PSF. The same software and methods used to find the clusters were applied to the resultant image. In this way, we could calculate the fraction of objects that we were able to recover, and with what precision we could calculate their magnitude. We repeated this process with clusters of magnitude from 18 to 25, at 0.5 magnitude interval. We computed 10 runs for each magnitude value, what improved significantly the overall statistics, while we kept a small number of clusters in every individual run (100) to match better the apparent cluster density in our data. See Figure 5.4 for an example of this.

The clusters were separated for their study in two groups. These groups consisted in clusters that fell in and out of a circle of 150 pixel radius (1 kpc) centered in the nuclear region. The clusters in the inner region suffered from a high and strong variable background, and a higher crowding (due to the occurrence of star-clusters and star-forming regions), while the clusters laying in the outer region had on average lower background and constituted a more disperse cluster population. The background variance and the object crowding could make a difference for the finding algorithm and the precision with what we can measure the magnitudes. We have observed in the simulations that the clusters in the outer region, with lower and smoother background are on average easier to detect. However this effect is only important for clusters weaker than magnitude 22 (see Figure 5.5 for an example with the F330W image). In order to asses the effect of crowding we repeated the simulations with 200 objects by run. In Figure 5.6 we plot the dependence of the number of clusters found with the total number of clusters which fell in the studied region. It can be noted that the results of the simulations tend to fall bellow the 1-1 line, with a stronger effect for those of 200 clusters. The effect of the number of clusters, in the range studied, seemed to be less important than the effect of the background. However, it is important in every case to run the simulations with a number of artificial clusters which gives a cluster density reasonably similar to our data, and take our results from the region in which the clusters are more numerous. We therefore decided to use the results for the simulations of 100 clusters, selecting only those in the inner kiloparsec. Figure 5.7 shows also that the finding method is 90% complete up to magnitude 22.5 for the filters F330W, F110W and F160W, and to magnitude 21.5 for F210M and F606W bands.

Aperture photometry was then performed on the artificial objects. The objects simulated had a constant and known magnitude, while the recovered magnitudes were higher on average, and had a certain dispersion around this value. The dispersion of the measured magnitudes gave an estimation of the uncertainty measuring

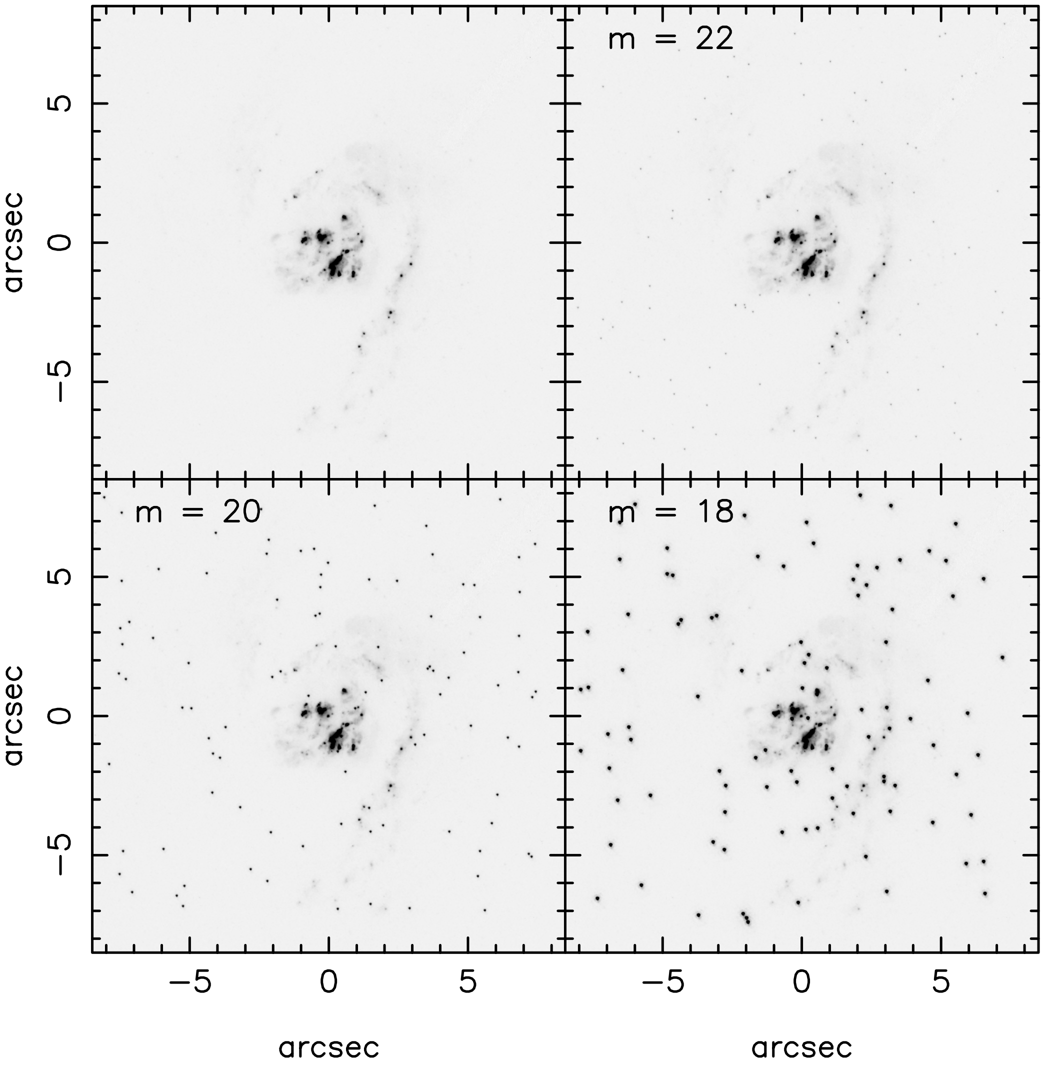

Figure 5.4: Example of randomly generated artificial clusters in the F330W image of NGC 5135. The clusters generated have magnitudes 18, 20, and 22, and are compared to the original image (in the upper left panel). North is up, east to the left.

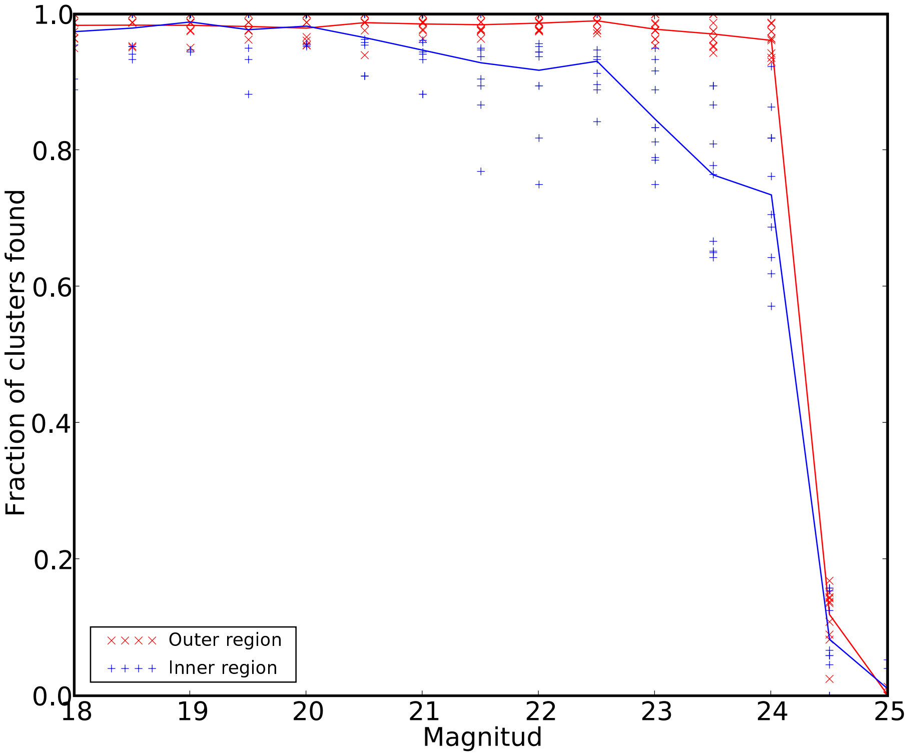

Figure 5.5: Example of completeness function for the filter F330W, determined from 10 runs of 100 artificial clusters for each magnitude. The points represent the individual runs, and the lines give the average of each set of 10. The finding method is 90% complete to magnitude 22.5.

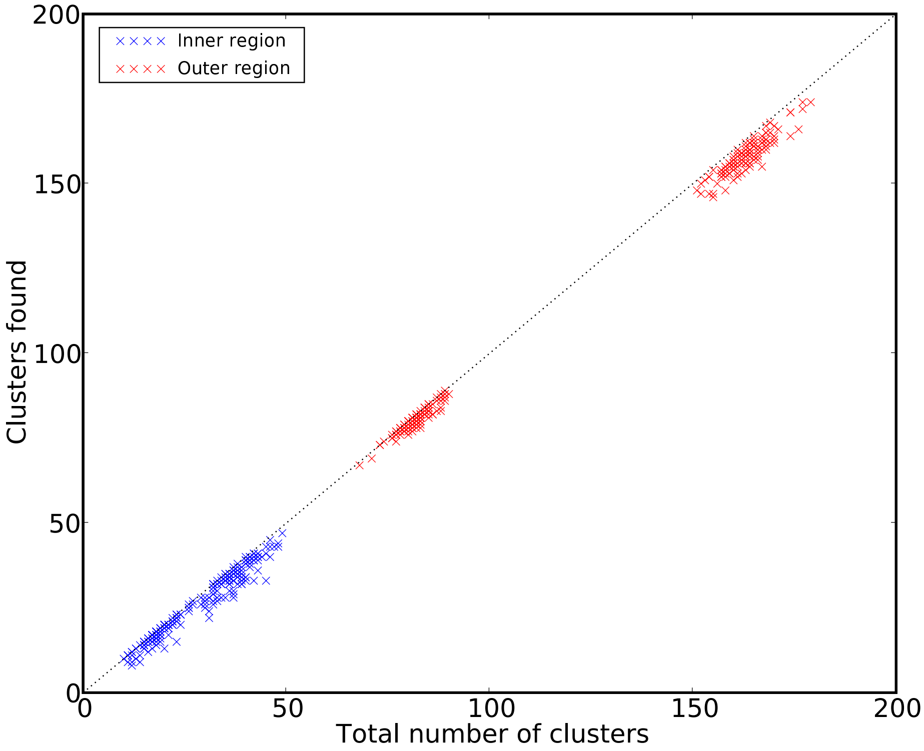

Figure 5.6: Test of the effect of crowding. The number of clusters found in a certain region is plotted versus the number of clusters generated in that region. The data have been taken from 80 runs of 100 random clusters and 80 runs of 200 random clusters. The magnitude range covered in these proofs was from 18 to 21.5. A slight trend with crowding is noted in both regions.

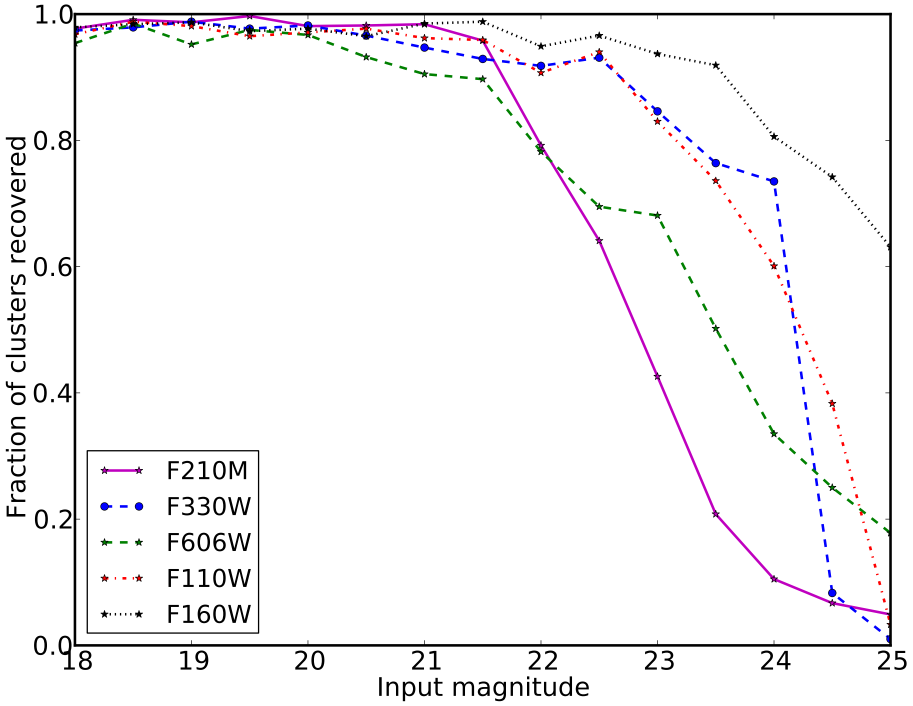

Figure 5.7: Completeness of the recovered cluster population in the inner kiloparsec and its dependence on the magnitude of the synthetic object, as calculated from the simulations of artificial clusters. Different line styles stand for the different bands.

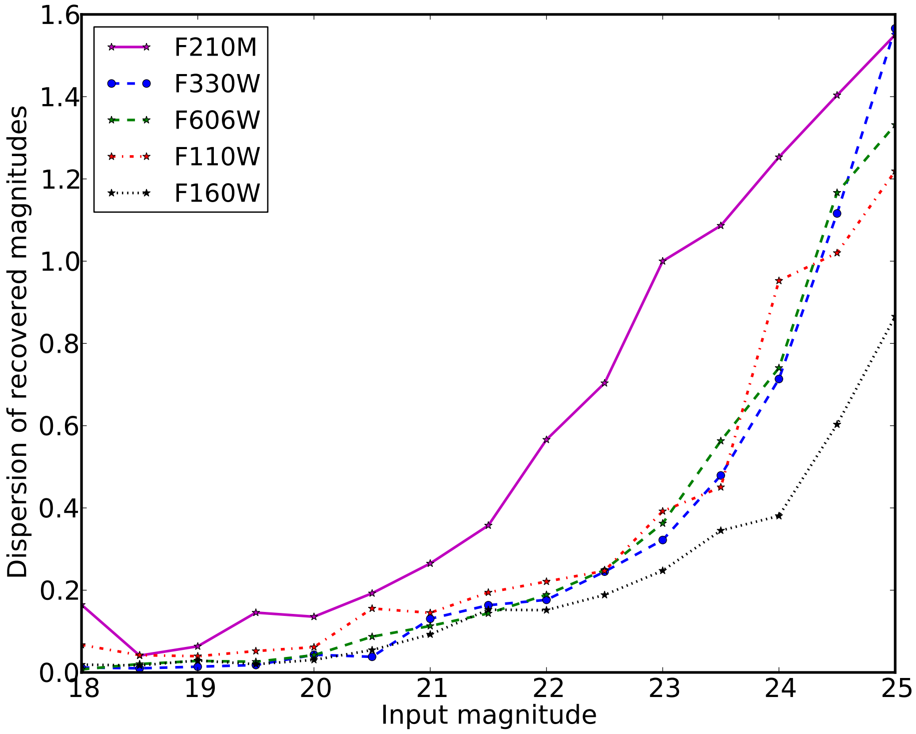

Figure 5.8: Uncertainty on the measured cluster magnitudes and its dependence on the magnitude of the synthetic object, as calculated from the simulations of artificial clusters. Different line styles stand for the different bands.

the star clusters. In addition, comparing the mean of the measured magnitudes with the real magnitude of the synthetic clusters we were able to calculate an aperture correction for a given instrumental configuration. This offset had a value which did not depend on the input magnitude of the clusters, as corresponds to an aperture correction. We found that the dispersion of the measured magnitudes is larger when we used wider apertures. This was probably due to flux contamination inside the photometric aperture by nearby clusters or compact star-forming regions. So we improved the precision by using a radius for the apertures of 5 instead of 7 pixel, as initially guessed. We also found that a certain part of the objects yielded a magnitude well apart from the average. For this reason we rejected those objects that deviated more than 3 times the standard deviation of the magnitude distribution. The result is an uncertainty that includes several error sources, and depends strongly on the magnitude of the object (Figure 5.8). The error sources which are not accounted for were added quadratically to this one (see Section 5.3.5).

### 5.3.5 Uncertainties of measured magnitudes

There are several sources of uncertainty in the magnitudes calculated for the clusters, some of them depending strongly on the instrumental configuration used to obtain the particular image.

- The relative error in the calibration of the absolute photometry with the Faint Object Camera is, following the FOC manual, about 15%. This source of uncertainty dominates for this band, while is unimportant for the other instruments.

- Another source of error is the read-out noise (RN), which is an uncertainty when determining the exact charge accumulated in every pixel of the detector during the exposure. This is zero for the FOC, as this is a photon-counting detector, while it can be an important contribution for other bands. The value of RN is usually given in electrons/pixel, and can be extracted from the image FITS header or in each instrument Handbook. The total error scales with the square root of the total number of pixels within the aperture ($n_{pix}$), and it is enlarged when transforming the electrons to digital numbers by the detector's amplifier, so it has to be multiplied as well by the GAIN factor. The RN and GAIN values used are: 6.1 e$^-$/s and 5.4 for NICMOS, 5 e$^-$/s and 7 for WFPC2, and 4.71 e$^-$/s and 2.216 for ACS. This way, if we call $\sigma_{RN}$ to the uncertainty associated to the read-out noise, then we can calculate it with the next formula:

$$\sigma_{RN} = \sqrt{n_{pix}} \cdot GAIN \cdot RN$$

- The Poisson uncertainty is other error source to be considered. The photons are detected with a certain probability, so for a low number of counts they follow a Poisson distribution, with an associated uncertainty of the square root of the number of counts. The flux of the object is an indirect measurement, so the total poissonian uncertainty is the quadratic sum of the poissonian uncertainties of the flux within the aperture (DN$_{ap}$) and that of the background determination scaled with the ratio between the areas of the aperture and the background annulus. Thus, taking into account that

$$DN_{obj} = DN_{ap} - A_{ap} \cdot DN_{bkg}/A_{bkg},$$

then

$$\sigma_{poi} = \sqrt{\sigma_{poi}(DN_{ap})^2 + \sigma_{poi}(DN_{bkg})^2 \cdot \left(\frac{A_{ap}}{A_{bkg}}\right)^2} = \sqrt{DN_{ap} + DN_{bkg} \cdot \left(\frac{A_{ap}}{A_{bkg}}\right)^2}$$

- Uncertainties coming from the aperture correction due to the structure of the clusters. In our analysis we have considered that NGC 5135 is far enough so that we can treat the clusters as point-like objects. However, at the assumed distance to the galaxy the corresponding scale is a bit less of 7 pc per pixel of 0.025 arcsec. This means that the biggest clusters should appear slightly extended in the short wavelength images, which possess a narrower PSF. In spite of that, we have shown in Section 5.3.3.1 that for a reasonable range of cluster size the aperture correction does not change much. Anyway, any residual effect should be accounted for with the simulation of artificial clusters and considering the measurement dispersion.

- Geometric effects due to a highly variable background, effects of differences in the crowding of objects, etc. could be important, although they are also accounted for with the cluster simulations performed (see Section 5.3.4).

Next, the overall uncertainty is estimated summing quadratically the uncertainties estimated from the simulations to the ones explained in this section, taking into account that the propagation of the the calculated uncertainties from the value of the flux of the object to the cluster magnitude follows the next equation:

$$\sigma(m) = \frac{\partial m}{\partial DN} \cdot \sigma(DN) = \frac{-2.5}{\ln 10} \cdot \frac{\sigma(DN)}{DN}$$

## 5.4 Determination of cluster parameters

From the aperture photometry, and once the necessary corrections were applied, we obtained a coarse spectral energy distribution (SED) from the UV to the near-IR for each cluster. These photometric points were compared to synthetic SEDs of single stellar populations (SSP) in order to derive basic cluster parameters. Only the 30 clusters unambiguously detected in at least 4 out of the 5 bands were considered for this porpoise.

We chose the GALAXEV models of Bruzual & Charlot (2003) (hereafter BC03), using the Padova 1994 evolutionary tracks and a Salpeter IMF of mass cutoffs 0.1 and 100 solar masses. As a first order approximation we have assumed solar metallicity, considering only age and reddening as free parameters. Two different methods have been used in order to estimate the most probable values of these parameters: a color-color diagram, and a direct SED fitting using a $\chi^2$ minimization algorithm.

It is well known that the uncertainties in the theoretical models might be larger than other systematic uncertainties (e.g. Anders et al., 2004). Although in the tables we give the results for the Padova models, we have considered useful to perform a consistency check, repeating all the calculations with the Geneva tracks and comparing the results. Thess comparisons are presented in their respective subsections.

### 5.4.1 Color-color diagrams

With this method not all the photometric bands are used. Therefore, some information is lost and it is less accurate overall. It is used as a complement for the $\chi^2$ minimization method. The same color-color diagram was used for all the clusters. This forced us to leave apart the F210M photometry, as it was only available for 9 clusters. On the other hand, a quick inspection of the SSP photometry shows that the F110W–F160W has very small dependence on age, so any photometric error in those bands would be severely amplified if this color was used. We noted also that the magnitude span of F606W–F160W color is wider than that of F606W–F110W. We thus decided to use a F330W–F606W vs F606W–F160W ($\sim$ U–V vs V–H) diagram.

Photometry of the SSP SEDs was performed with IRAF 'synphot' package in the bands studied. This was repeated with a reddening of $A_V=1$ with the reddening law of Cardelli et al. (1989). A mean reddening was calculated for a logarithmic-like sampling of the age parameter, although the dependence on the SSP age of $A_V$ is not strong, except for the F210M band. With this, a reddening vector $\mathbf{A_V}$, of components ($A_{V1}$,$A_{V2}$) in the space (U–V,V–H), was derived. For each cluster, the photometry in the three considered bands determines its position in the color-color diagram, (c1,c2). This point and the reddening vector define a line whose intersection with the SSP track gives the most probable values for the age, and the length of the line to this point defines the reddening suffered by the cluster. This is illustrated in Figure 5.9. Being (c1,c2)≡C' the coordinates of the cluster in the color-color space, $C_i$ the series of coordinates for the age sequence considered, and $r$ the line defined by $\mathbf{A_V}$ and C', then we can express this mathematically as:

$$\widehat{\mathbf{A_V}}_\perp = \frac{1}{|\mathbf{A_V}|}(-A_{V2}, A_{V1})$$

$$\text{age} = \min\left(d[C_i, r]\right) = \min\left(\overrightarrow{C'C_i} \cdot \widehat{\mathbf{A_V}}_\perp\right)$$

$$\text{extinction} = \frac{1}{|\mathbf{A_V}|^2}\,\overrightarrow{C'C_{age}} \cdot \mathbf{A_V}$$

In Figure 5.10 we have plotted the measured colors of the 30 clusters considered. Taking into account the reddening vector calculated, 5 of the clusters fall in a forbidden region of the diagram, which cannot be reached by reddening a point from the SSP tracks. These clusters have been excluded from this part of the analysis. There are also 3 points which have a bluer U–V color than the models. This can be accounted for assuming a higher metallicity than solar for these points, with a very small change in the calculated value for the age.

This procedure was repeated for the GALAXEV models with Geneva1994 tracks. A comparison between the calculated values of age and reddening is shown in Figure 5.11. As can be appreciated in the plot, the determination of the age is fairly robust. Depending on the age, the Geneva models may yield a smaller value for the reddening.

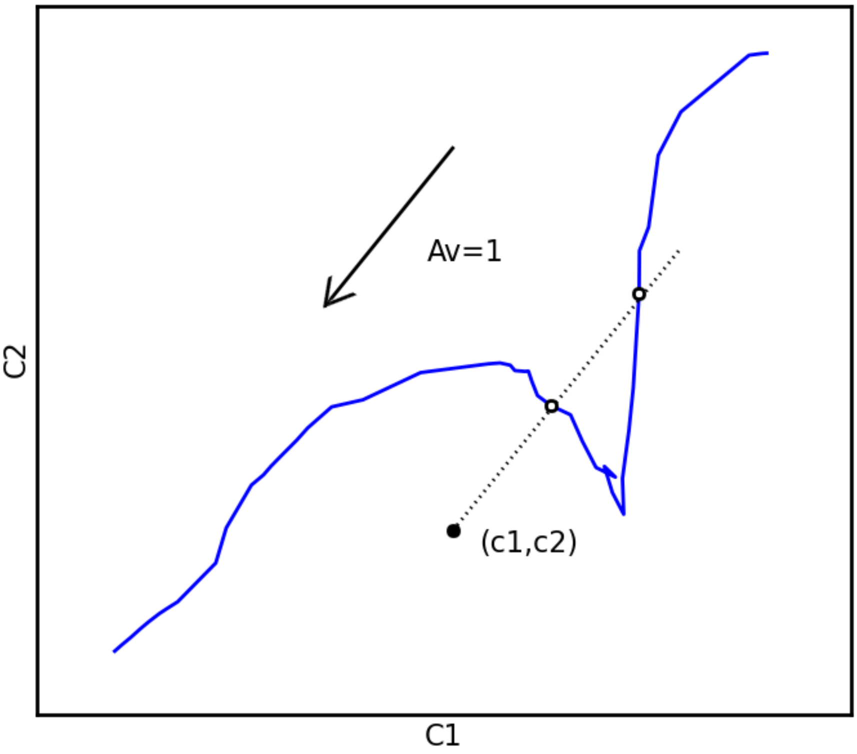

Figure 5.9: Sketch of the method followed to derive the most probable age and reddening pair for every cluster, using a single color-color diagram. This may yield two or only one pair of values. Not both solutions are necessarily possible, as a negative reddening has no physical sense.

### 5.4.2 Direct fitting to Single Stellar Populations

Broad band photometry in the studied bands was performed for a grid of BC03 models with 'synphot'. Age was sampled every Ma from 1 to 10 Ma, every 5 Ma from 10 to 100 Ma, every 100 Ma from 100 Ma to 1 Ga, and every 1 Ga from 1 to 10 Ga. Reddening was linearly sampled with 100 values of $A_V$ between 0 and 3, for the clusters with F210M photometry, and from 0 to 5 for the rest. For the photometric measurements of each cluster, we performed a least squares fitting algorithm, weighted with the uncertainty of each individual object, which was calculated as explained in Section 5.3.5. Every model in the grid is fitted to

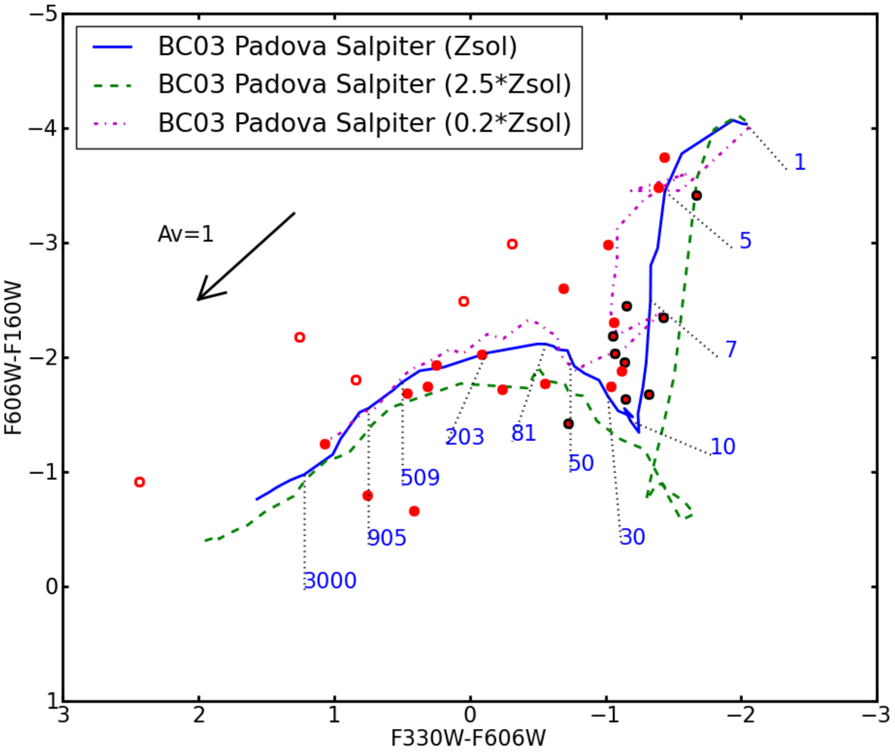

Figure 5.10: Color-color diagram for the clusters with at least 4 bands available. The circles with a black edge are those clusters unambiguously detected in the 5 bands. The empty circles are clusters that were not considered in this method, as they lie out of the region allowed by the models. The Bruzual & Charlot (2003) SSP models are plotted as a blue full line. The location along the tracks of several selected models is marked for reference (ages in Ma). For comparison, tracks for the models of 2.5 solar metallicity, and 1/5 solar metallicity, are also plotted as green dashed line and magenta dot-dashed line respectively.

the photometric set of a certain cluster by scaling the model spectrum by a certain factor, or shifting the model photometry a value of $K$ magnitudes. The value of $K$ which minimizes the error-weighted residuals is the one which satisfies the next equation:

$$\frac{\partial}{\partial K}\chi^2 = \frac{\partial}{\partial K}\sum_i \frac{(m_{o,i} - m_{m,i} - K)^2}{{\varepsilon_i}^2} = 0, \tag{5.4}$$

where $m_{o,i}$ is the observed magnitude at band $i$, $m_{m,i}$ is the magnitude of the model

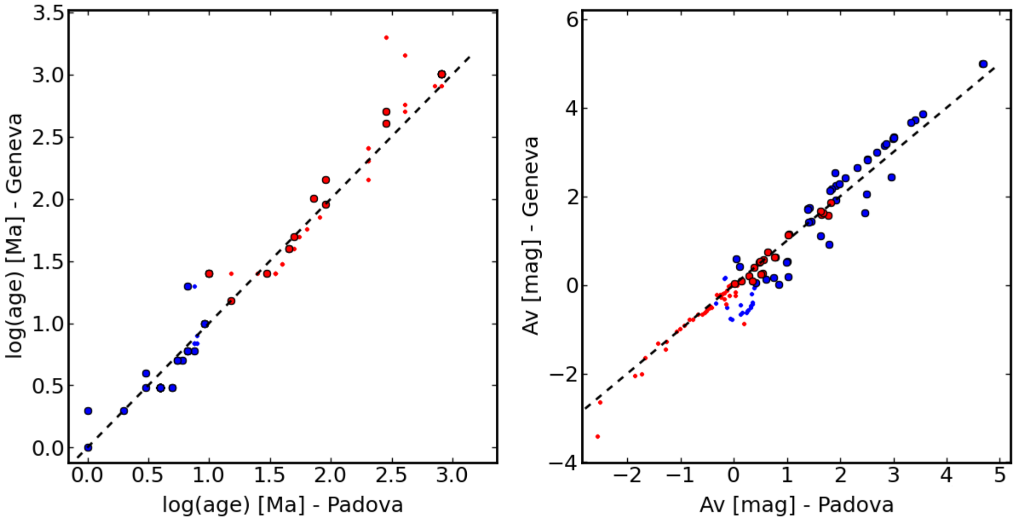

Figure 5.11: Consistency test for the cluster parameter determination using the color-color diagram, for Padova and Geneva tracks. Two solutions are depicted for every single cluster for a full comparison. The little dots correspond to the solutions without a physical sense (reddening less than zero). Blue circles represent the clusters detected in the 5 bands, and red circles represent the clusters not detected in the F210M image.

at that band, and $\varepsilon_i$ is the error calculated for the cluster photometry in the filter. The value of $K$ can thus be calculated as:

$$K = \frac{\sum_i \frac{(m_{o,i}-m_{m,i})^2}{{\varepsilon_i}^2}}{\sum_i \frac{1}{{\varepsilon_i}^2}} \tag{5.5}$$

In this way we obtained a grid of best-fitting models, with its associated $\chi^2$ as defined by Equation 5.4, and each one corresponding to a pair of parameters age and reddening. From this grid we can plot a bidimensional graph with contours of equal $\chi^2$ in the space of parameters, which are $A_V$ and log(age), in our case. An example is shown in Figure 5.12.

In order to derive the set of parameters that best fit our data, two different approaches may be followed. The first is to consider just the values of the parameters which yield the minimum $\chi^2$. The second is to associate to each parameter set a probability density of the kind $p \sim e^{-\frac{1}{2}\chi^2}$, which is a function of $A_V$ and age. The most probable value of a certain parameter is obtained by marginalization of this function in the next way:

$$P(t_1) = \int p(t_1, t_2)\mathrm{d}t_2$$

In our case, we have to integrate the function $p$ in all the possible values of $A_V$, for each value of age in the grid. The most probable age would be the mean calculated from P(age), and the same procedure has to be followed for $A_V$. This second method is more robust than the simple minimization and allows us to estimate a confidence interval for the result. As a drawback, the probability function might have two maxima, so the mean could correspond to a value between both, and it actually may have far smaller probability than any of the maxima. In these cases, the probability density was divided in two parts, each one around one maximum, and two pairs of solutions were derived independently (see Figure 5.13 for an example of this). The values of the parameters ($t_i$) and the uncertainty ($\sigma_i$) are calculated as follows:

$$\bar{t_i} = \frac{\int t_i p(t_i) \mathrm{d}t_i}{\int p(t_i) \mathrm{d}t_i}$$

$$\sigma_i^2 = \frac{\int (t_i - \bar{t_i})^2 p(t_i) \mathrm{d}t_i}{\int p(t_i) \mathrm{d}t_i}$$

As with the previous method, all the calculations were repeated changing the evolutionary tracks of the comparison theoretical models. In Figure 5.14 we show the plots for the calculated cluster parameters (age, reddening and mass) and the $\chi^2$ of the best fitting model. We have found no biasing trend in the results for using the Padova 1994 or Geneva 1994 evolutionary tracks. The median value of the $\chi^2$ of the best fit for all the clusters is the same for both set of models. However, the mean $\chi^2$ value is slightly smaller for the Padova 1994 tracks (10 versus 23), and the visual aspect of the fit for some clusters is better for those tracks. For this reason, we list the results for the Padova 1994 models in the summary tables.

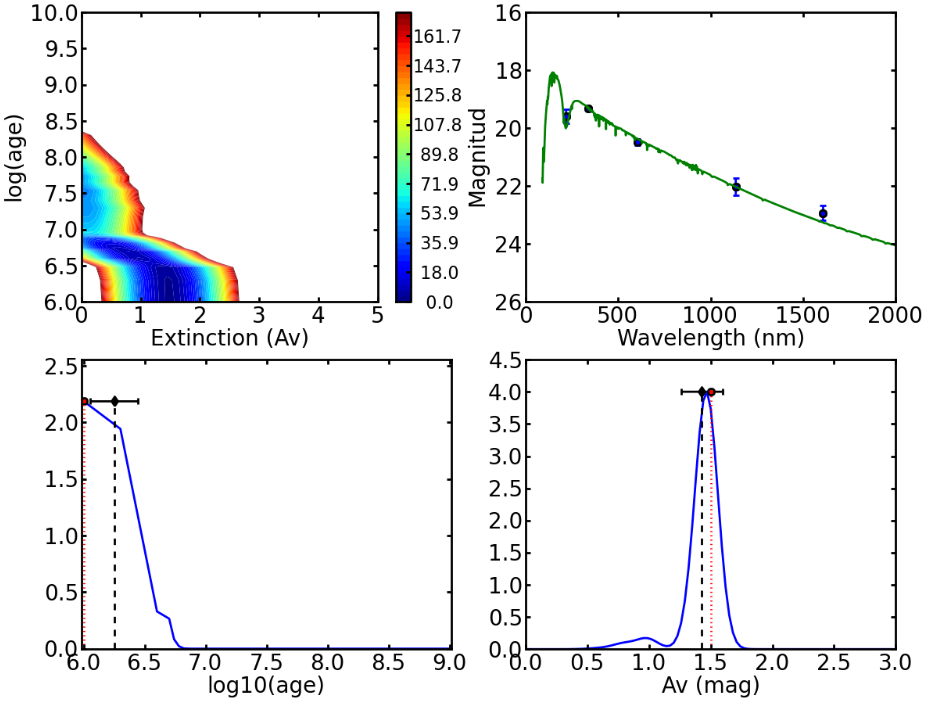

Figure 5.12: Example of a $\chi^2$ fit for a cluster with 5 photometric bands. On the upper-left panel: a contour plot of the $\chi^2$ for the computed grid of parameters; some degeneration in age and reddening is observed. On the upper-right panel: the best model fit (that of the lowest $\chi^2$ value) is overplotted to the cluster photometry. Lower panels: the marginalization of the probability density, normalized so that the integral in log(age) and $A_V$ equals 1. The parameter with the lowest $\chi^2$ are plotted with a red circle and dotted line, while the mean value of the probability density is plotted with a black diamond and dashed line. An uncertainty estimation is also given as a horizontal error bar.

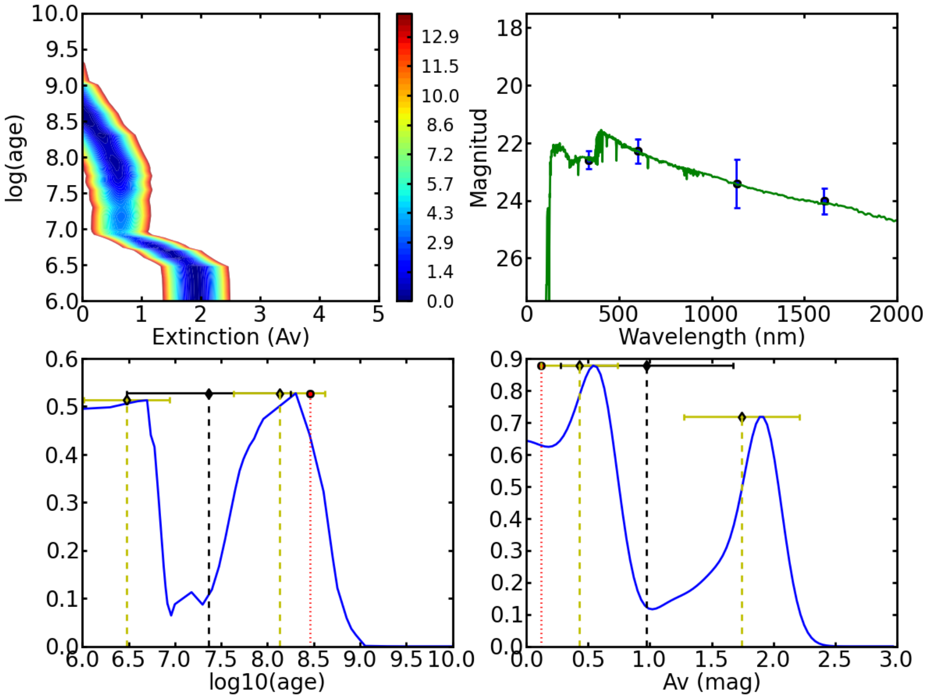

Figure 5.13: Example of a $\chi^2$ fit for a cluster with 4 photometric bands and a clearly bimodal probability density. Panels are organized as in Figure 5.12. In the cases like this, the two maxima were considered separately and two possible pair of values were calculated. The mean and standard deviation of each pair are marked in the lower panels with yellow dashed lines and diamonds. For the rest, the legend is similar to Figure 5.12.

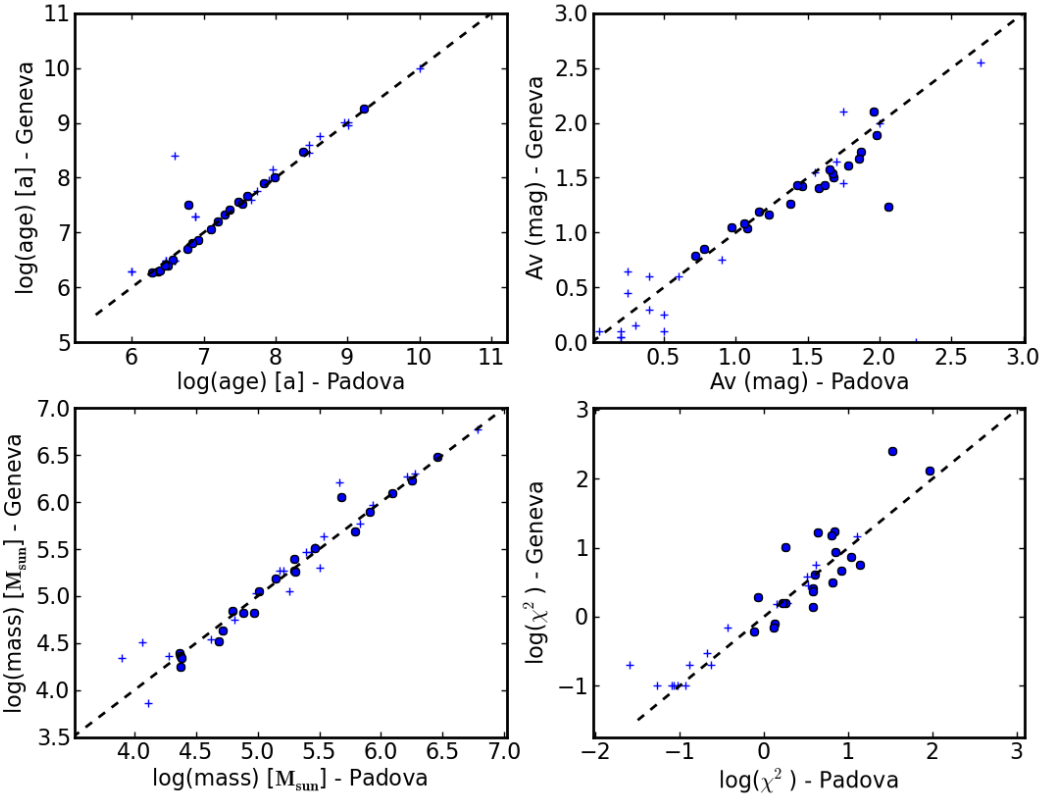

Figure 5.14: Consistency test for the cluster parameter determination (age, reddening, mass and the associated $\chi^2$) using the SED fit and a $\chi^2$ minimization algorithm (Section 5.4.2), for theoretical models with different evolutionary tracks. Every panel shows the comparison between the results using the Padova 1994 and Geneva 1994 tracks. The circles represent the results from the model with the minimum $\chi^2$, and the plus symbol the results from marginalization of the probability density (see text). The 1–1 line is plotted for reference as a dashed line.

### 5.4.3 Comparison of the different methods

In Table 5.3 we show the results of the determination of age and reddening of the 30 clusters identified in at least 4 bands. The 3 methods explained above are considered. The color-color diagram method, as well as the marginalization of the probability density, can yield two possible pair of values for the parameters. The clusters number 15, 17, 24, 25 and 28, were excluded from the analysis of the color-color diagram, as these are points which lie in a forbidden region of the diagram. This method has the drawback that an error in any of the bands would displace the point in the diagram, changing noticeably the results. On the contrary, in the direct fit of the SSP photometry this would tend to be diluted, as the method tries to fit all the data simultaneously. However, the weight of all the points is not the same, but depends on the estimated uncertainty. Therefore, an error in the photometry would affect the result in a different way, depending on the band. The marginalization method is the most robust overall, and besides, it provides an estimation of the uncertainty of the result. It has the problem that depending on the exact shape of the dependency of $\chi^2$ with the parameters, the calculated value could actually be close to a local minimum of the probability (as shown in Figure 5.13. We have overcome this problem by dividing the probability density function in two for the clusters whose $\chi^2$ showed a clear bimodality, although this effect could still have some effect at a smaller scale.

Some other caveats affect similarly to the different methods. Solar metallicity was assumed along the study, which is a reasonable assumption for the nuclear region of these galaxies. As it was shown in Figure 5.10, considering a higher metallicity would not change much the age results, and only slightly the reddening determination. The uncertainty in the SSP models would be the main caveat of these results. Apart from this, the results for the different methods agree very well, in general, within the estimated uncertainty range.

From the set of different values, a most likely value for the age and the reddening was chosen. The overall fit to the data and the shape of the probability density was taken into account. We considered that the most robust determination of these parameters were those derived from the marginalization of the probability density ($p$), the overall mean in the cases of a well behaved $p$, and the peak that yielded the better fit in a case of a bimodal $p$. These are the values listed in Table 5.4, with their associated uncertainty.

### 5.4.4 Estimation of the mass of the clusters

The mass of every cluster has been calculated from the scaling of the best-fitting SED to the cluster photometry. For each cluster, the best-fitting model was calculated with the methodology explained above. In order to fit the photometric data, the model SED has to be scaled by a certain factor depending on cluster luminosity, what in the end can be related to the cluster mass.

The GALAXEV tracks come normalized to a total mass of $1\,\mathcal{M}_\odot$ at zero age,

Table 5.3: Comparison of the results of cluster parameters for the different methods

| Cluster | Offset ($''$) | | C-C Diagram | | Minimum $\chi^2$ | | Marginalization | |
|---|---|---|---|---|---|---|---|---|
| ID | West | North | log(age) | Av | log(age) | Av | log(age) | Av |
| 1 | 1.63 | -3.65 | 6.96 | 1.0 | 6.74 | 0.87 | 6.5 ± 0.3 | 1.3 ± 0.4 |
| 2 | 1.70 | -3.48 | 6.88 | 0.1 | 6.00 | 1.50 | 6.2 ± 0.2 | 1.4 ± 0.2 |
| 3 | 2.08 | -2.16 | 6.88 | 0.3 | 6.74 | 0.75 | 6.5 ± 0.3 | 1.2 ± 0.4 |
| 4 | -0.39 | -2.08 | 6.90 | -0.06 | 6.88 | 0.15 | 6.885 ± 0.014 | 0.13 ± 0.05 |
| 5 | 0.37 | -2.06 | 6.96 | 1.0 | 6.88 | 0.39 | 6.88 ± 0.03 | 0.38 ± 0.06 |
| 6 | -0.41 | -1.82 | 6.88 | -0.3 | 6.82 | 0.03 | 6.81 ± 0.02 | 0.06 ± 0.04 |
| 7 | 2.42 | -1.74 | 6.82 | 0.8 | 6.82 | 1.14 | 6.84 ± 0.12 | 1.1 ± 0.2 |
| (7) | | | 7.65 | 0.06 | | | | |
| 8 | -0.14 | -1.53 | 6.82 | 0.3 | 6.82 | 0.45 | 6.821 ± 0.008 | 0.45 ± 0.04 |
| 9 | 0.65 | -0.94 | 6.96 | 0.6 | 6.00 | 0.66 | 6.3 ± 0.2 | 0.61 ± 0.12 |
| 10 | -0.29 | -7.60 | 6.82 | 1.0 | 7.74 | 0.18 | 7.1 ± 0.7 | 0.6 ± 0.6 |
| (10) | | | 7.70 | 0.01 | | | | |
| 11 | -1.07 | -6.92 | 6.88 | 0.2 | 6.88 | 0.12 | 6.8 ± 0.5 | 0.6 ± 0.5 |
| 12 | 1.01 | -6.30 | 6.82 | 0.3 | 6.78 | 0.30 | 6.6 ± 0.4 | 0.7 ± 0.4 |
| 13 | 1.70 | -5.64 | 6.60 | 2.8 | 8.61 | 0.12 | 6.4 ± 0.4 | 1.9 ± 0.4 |
| (13) | | | 8.46 | 0.3 | | | 8.3 ± 0.4 | 0.4 ± 0.3 |
| 14 | 0.57 | -4.70 | 6.60 | 0.1 | 6.60 | 0.15 | 6.4 ± 0.2 | 0.4 ± 0.2 |
| 15 | 0.74 | -4.23 | – | – | 6.60 | 1.05 | 6.5 ± 0.2 | 1.2 ± 0.2 |
| 16 | 1.51 | -4.20 | 6.88 | 0.3 | 6.88 | 0.24 | 6.9 ± 0.6 | 0.6 ± 0.5 |
| (16) | | | 7.54 | 0.2 | | | | |
| 17 | 4.47 | -2.41 | – | – | 8.96 | 0.00 | 8.4 ± 0.5 | 0.5 ± 0.4 |
| (17) | | | | | | | 6.5 ± 0.5 | 2.0 ± 0.5 |
| 18 | -1.47 | -2.29 | 6.70 | 1.9 | 6.48 | 1.62 | 6.8 ± 0.8 | 1.2 ± 0.6 |
| (18) | | | 8.3 | 0.03 | | | | |
| 19 | -1.30 | -1.47 | 6.74 | 3.0 | 7.96 | 1.05 | 8.0 ± 0.7 | 1.0 ± 0.5 |
| (19) | | | 7.96 | 1.8 | | | | |
| 20 | 0.12 | -1.29 | 6.48 | 0.8 | 6.48 | 0.54 | 6.4 ± 0.2 | 0.5 ± 0.2 |
| 21 | 2.25 | -1.01 | 6.6 | 2.5 | 8.46 | 0.03 | 6.5 ± 0.5 | 1.7 ± 0.5 |
| (21) | | | 8.46 | 0.02 | | | 8.0 ± 0.5 | 0.4 ± 0.3 |
| 22 | -0.85 | -0.75 | 6.3 | 1.4 | 6.00 | 0.93 | 6.3 ± 0.2 | 0.88 ± 0.12 |
| 23 | 0.53 | -0.66 | 6.0 | 1.9 | 6.00 | 1.20 | 6.5 ± 0.4 | 1.0 ± 0.3 |
| 24 | -1.75 | 0.66 | – | – | 6.60 | 1.35 | 6.8 ± 0.6 | 1.2 ± 0.4 |
| 25 | 2.60 | 1.04 | – | – | 9.01 | 0.15 | 6.5 ±0.5 | 2.1 ± 0.7 |
| (25) | | | | | | | 8.7 ±0.5 | 0.5 ± 0.4 |
| 26 | -2.99 | 1.61 | 6.82 | 2.5 | 7.65 | 1.02 | 7.5 ±0.5 | 1.1 ± 0.3 |
| (26) | | | 7.65 | 1.7 | | | | |
| 27 | 2.06 | 1.74 | 6.60 | 2.7 | 8.46 | 0.12 | 6.5 ±0.5 | 1.7 ± 0.5 |
| (27) | | | 8.46 | 0.2 | | | 8.1 ±0.4 | 0.97 ± 0.3 |
| 28 | -2.25 | 1.98 | – | – | 10.0 | 0.36 | 9.2 ±0.6 | 0.9 ± 0.4 |
| 29 | 0.96 | 2.42 | 6.74 | 1.6 | 7.91 | 0.30 | 7.2 ±0.8 | 0.8 ± 0.6 |
| (29) | | | 7.86 | 0.5 | 7.91 | 0.30 | 7.2 ±0.8 | 0.8 ± 0.6 |
| 30 | -2.40 | 2.91 | 6.60 | 3.5 | 9.01 | 0.24 | 8.4 ±1.0 | 0.7 ± 0.8 |
| (30) | | | 8.91 | 0.5 | | | | |

Comparison of the derived values for age and reddening from the different methods considered, for the 30 clusters identified in at least 4 out of the 5 bands. Col.(1): cluster identifier; Col.(2,3): cluster offset with respect to the galactic nucleus in arcseconds (north and west offsets are considered positive); Col.(4,5): logarithm of age and reddening, from the method of the color-color diagram; Col.(6,7): the same, for the least square fitting and the model with the lowest $\chi^2$; Col.(8,9): idem, for the method of marginalization of the probability density p$\sim$exp($-\chi^2/2$), with its associated uncertainty. All the ages are given in years and the reddening in magnitudes. Methods 1 and 3 may yield two different pairs of values for the parameters.

in units of solar luminosities per Angstrom ($\mathcal{L}_\odot = 3.826 \cdot 10^{33}$ erg/s). In order to transform the model flux per unit wavelength into the measured flux density per unit wavelength, we have to multiply the first by a factor $\mathrm{M}\times\mathcal{L}_\odot/d^2$, with M the total mass of the cluster (at age zero), and $d$ the distance in cm to NGC 5135 (from NED, $57.7 \pm 4$ Mpc, equivalent to $1.78 \pm 0.12 \cdot 10^{26}$ cm). This relation can be better visualized in the next scheme:

| | | | | | | | |
|---|---|---|---|---|---|---|---|
| | (Models) | | | | | | (Measured flux) |
| Units: | $\mathcal{L}_\odot$ / Å | → | $\mathcal{L}_\odot$ / Å | → | erg/s/Å | → | erg/cm$^2$/s/Å |
| Mass: | $1\,\mathcal{M}_\odot$ | (×M) | $\mathrm{M}\,\mathcal{M}_\odot$ | ($\times\mathcal{L}_\odot$) | $\mathrm{M}\,\mathcal{M}_\odot$ | ($/\mathrm{d}^2$) | $\mathrm{M}\,\mathcal{M}_\odot$ |

Therefore, the photometry applied directly to the models is shifted a certain value from the experimental data, that can be expressed as follows:

$$\Delta m = -2.5 \cdot \log(\mathrm{M}\mathcal{L}_\odot/d^2) = -2.5 \cdot \log(\mathrm{M}) + 47.296$$

From this expression it is possible to calculate the mass of the clusters, given a fit to the photometric points. This magnitude shift happens to be the factor $K$, as defined in Section 5.4.2. The mass for every cluster was calculated using the model with the most likely values for the age and reddening parameters, as listed in Table 5.4.

The accuracy in the mass determination depends directly on the accuracy of the age and reddening fit. The uncertainty on the calculated mass was estimated by calculating the value of the mass in the limits of the confidence box, defined by the uncertainties in the logarithm of age and the reddening $\mathrm{A}_V$. The larger deviations (high and low) from the assumed mass were assigned to the upper and lower confidence limits of the cluster mass.

When comparing our results with other works one has to take into account that the cluster masses have been determined fitting SSPs with a Salpeter IMF, but sometimes a Kroupa IMF is used, and the later has the effect of underestimating the calculated masses respect to the former (Goddard et al., 2010).

## 5.5 Results and discussion

### 5.5.1 Fraction of light in clusters

We have calculated the fraction of light in clusters by summing up the aperture corrected photometry of the clusters found in each band. We have done so with two sets of clusters: firstly we have used only the objects which are unambiguously identified with ‘daofind’ in each band, and secondly we have merged the lists of objects found in every band to get a complete cluster list. We measured in each band with both lists, applying the proper aperture correction of the individual objects to the summed flux. We have compared this to the total flux encircled in a 2 kpc radius aperture, centered in a region among the brightest clusters, in a way that most of the clusters fell within the aperture. This was performed in the same way for all the bands, except for the F210M image, in which we were limited by the border of the image, so we chose a 1.2 kpc aperture. However, in this band virtually all the emission is concentrated in the inner kpc, so it does not change the results. Figure 5.15 shows the results of this analysis. We obtained that in the UV bands the emission of the clusters account for around the 30% of the total flux in the central 2 kpc, while for the optical-infrared bands this ratio is about three times less (10%), falling to just a 5% in 1.6 $\mu$m.

Comparing this detailed analysis with the coarser estimation of the fraction of light in clusters that we have presented in Chapter 3, yields a consistent result ($f_{clus}$ was 0.3 for this object). This indicates that the visual identification of clusters should be quite robust. The result also fits well with previous published works in extreme environments. For example, Meurer et al. (1995) estimated that 20–50 % of UV light in starburst galaxies come from star clusters, and Zepf et al. (1999) calculate that 15–20 % of the light in the B band come from clusters in the galaxy merger NGC 3256. Moreover, in a comprehensive study of 31 nearby galaxies, Larsen & Richtler (2000) find a fraction of total luminosity coming from clusters in the U band between 0 to 15 %, correlating very well with the star-formation rate. This would confirm the strong starburst character of the nuclear region of this local LIRG.

### 5.5.2 Cluster population by filter

In Figure 5.16 we show the histogram of the calculated magnitudes for the cluster population found at each band. These magnitudes have been corrected for galactic extinction, and the applied aperture correction was determined from the cluster simulations. As explained in Section 5.3.1, these populations, as observed in different bands, are not coincident. The histograms thus compare the magnitudes of the brightest and sharpest clusters of every band, not the same group of objects. It is worth to be noted, that the F330W image, possessing an optimal combination of signal-to-noise and resolution, offers the greatest range in cluster magnitude and the largest population to be studied. The agreement between the observed upper cut in magnitude (around magnitude 24-25) and the completeness functions determined by the simulations is quite good, except for the F210M filter, in which it seems that we may be overestimating the completeness of the cluster sample. As already noted in previous sections, the F210M image has resulted to be a complicated band to work with, and the calculated magnitudes suffer a high uncertainty, so the results for this filter have to be taken with caution. It is worth noting the apparent lack of clusters brighter than magnitude 20 in the near-IR bands. The brightest clusters are observed in the UV. With the filter F330W we are sampling a larger magnitude interval, what makes the cluster population found in this band the largest of the five. This result confirms our initial assumption that the configuration chosen for

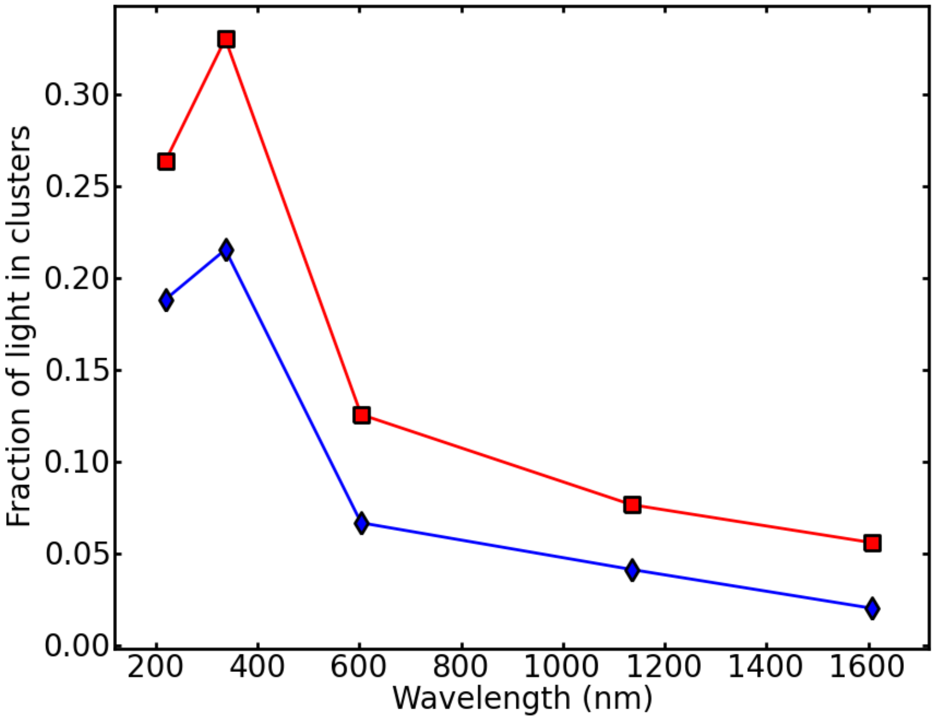

Figure 5.15: Fraction of the total emission in the inner 2 kpc, which is coming from star clusters. In blue diamonds we plot the fraction of light considering only the clusters unambiguously identified in that band, and in red squares considering all the cluster positions that are unambiguously identified in at least one of the five bands.

the construction of the Atlas is the optimal to detect massive star clusters in this kind of objects, provided that the dust obscuration is not too severe.

### 5.5.3 Table of results

Table 5.4 summarizes the photometric results for the clusters unambiguously identified in at least 4 out of the 5 bands available. The most probable values for the cluster age and interstellar reddening, and the calculated mass of each cluster are also listed, together with their associated uncertainty, determined as explained in Section 5.4

The typical mass of the clusters we are studying is $1.6 \cdot 10^5$ M$_\odot$ (logarithm of mass is 5.2), without any difference between those clusters identified in F210M and those that are not. On the other hand, the typical age in these two groups is different, with a median of 6 Ma for the ones detected in F210M, and 32 Ma for the rest. They are overall quite young, as expected for being detected in the near-UV, with only 17% of the clusters (5/30) older than 200Ma. In Figure 5.17 we show a scatter plot of the calculated mass versus the age of the cluster. Despite the plot is scarcely populated it can be guessed a low-mass cutoff about $10^4\,\mathrm{M}_\odot$, and a magnitude limit as a diagonal cutoff to the right of the diagram. There is also an apparent lack of objects with age between 10 and 100 Ma, what points to a star formation history in bursts, rather than continued.

Our results for the age of the clusters support those of previous studies. For example, González Delgado et al. (1998) study optical and UV spectra of the circumnuclear region of this object, finding a starburst age of ∼3-5 Ma, based on fits of wind lines by O and B stars, and ∼4-8 Ma based on the continuum slope. Besides, Bedregal et al. (2009) find signatures in the infrared of star formation ∼6-8 Ma old, with hints of an older stellar population.

### 5.5.4 Central morphology of the galaxy

The clear view to the central part of this object is allowed by its almost face-on alignment. A couple of thick dust lanes with a spiral pattern are conspicuous in the HST images. These arise from the inner part of a large scale bar with orientation southeast-northwest, which is not visible in our images. This is probably the feeding mechanism for the central starburst. In Figure 5.18 we show a color map created with the filters F606W and F110W. This color traces the dust distribution, and at the same time enhances other features, as for example ionized gas (F606W includes H$\alpha$ emission). This map clearly shows a cone-shape emission opening to the south-southwest. Another remarkable feature that we have observed when inspecting the images is that the strongest nuclear emission is not coincident in all the bands. It shows a displacement to the southwest when moving to shorter wavelengths. In addition, the nuclear emission is point-like at H band, and becomes comet-shaped at shorter wavelengths. This is illustrated in Figure 5.19.

Taking all these clues together we hypothesize that the conical structure may be an ionization cone. Nevertheless, we have to take into account possible projection effects, and this shape might also be serendipitously created by the complicated dust distribution. Unfortunately there are no archival HST images in H$\alpha$ or [OIII] to directly test this. Literature studies are not conclusive about the matter. Levenson et al. (2004) present Chandra data which show an emitting extended source of soft X-rays in the region of the apparent cone. They associate that to star-formation, likely an outflowing starburst super-wind. Díaz-Santos et al. (2008) report also at the southwest of the nucleus P$\alpha$ emission, which is commonly associated to star-formation. In addition, Bedregal et al. (2009) using infrared data report at the same location $H_2$ (1-0 S(1) transition at 2.12 $\mu$m), sign of molecular gas, and [FeII]$\lambda\lambda$1.64$\mu$m, which is usually regarded as a supernova-remnant tracer. On the other hand, Bedregal et al. (2009) in the same study find emission of [SiVI]$\lambda\lambda$1.46$\mu$m. This coronal line needs a very hard ionizing continuum, as that from the Seyfert nucleus. The emission appears to be stronger in the same axis that

Table 5.4: Summary table with photometry and calculated properties of the clusters

| Clus. ID | W-offset (arcsec) | N-offset (arcsec) | U (mag) | fUV–U (mag) | U–V (mag) | V–J (mag) | J–H (mag) | log(age) (a) | $A_V$ (mag) | log(mass) ($M_\odot$) |
|---|---|---|---|---|---|---|---|---|---|---|
| 1 | 1.63 | -3.65 | 20.02 | 0.35 | -1.07 | -1.21 | -0.82 | 6.71 ± 0.12 | 0.9 ± 0.3 | $4.7^{+0.3}_{-0.3}$ |
| 2 | 1.70 | -3.48 | 19.33 | 0.26 | -1.15 | -1.53 | -0.92 | 6.2 ± 0.2 | 1.43 ± 0.17 | $5.42^{+0.08}_{-0.4}$ |
| 3 | 2.08 | -2.16 | 19.43 | 0.22 | -1.05 | -1.41 | -0.77 | 6.72 ± 0.09 | 0.8 ± 0.2 | $4.9^{+0.2}_{-0.2}$ |
| 4 | -0.39 | -2.08 | 17.99 | -0.39 | -1.32 | -1.01 | -0.66 | 6.89 ± 0.02 | 0.13 ± 0.05 | $5.23^{+0.08}_{-0.03}$ |
| 5 | 0.37 | -2.06 | 18.42 | -0.07 | -1.14 | -1.00 | -0.63 | 6.88 ± 0.03 | 0.38 ± 0.06 | $5.22^{+0.14}_{-0.14}$ |
| 6 | -0.41 | -1.82 | 17.59 | -0.38 | -1.43 | -1.56 | -0.78 | 6.81 ± 0.02 | 0.06 ± 0.04 | $5.23^{+0.03}_{-0.09}$ |
| 7 | 2.42 | -1.74 | 19.61 | 0.93 | -0.72 | -0.80 | -0.61 | 6.84 ± 0.12 | 1.13 ± 0.17 | $5.13^{+0.4}_{-0.19}$ |
| 8 | -0.14 | -1.53 | 17.74 | -0.23 | -1.14 | -1.18 | -0.78 | 6.82 ± 0.01 | 0.45 ± 0.04 | $5.43^{+0.03}_{-0.03}$ |
| 9 | 0.65 | -0.94 | 19.36 | -0.69 | -1.67 | -2.26 | -1.15 | 6.27 ± 0.19 | 0.61 ± 0.12 | $4.87^{+0.05}_{-0.4}$ |
| 10 | -0.29 | -7.60 | 21.75 | — | -0.55 | -1.39 | -0.38 | 7.1 ± 0.7 | 0.7 ± 0.6 | $4.5^{+0.9}_{-0.9}$ |
| 11 | -1.07 | -6.92 | 21.01 | — | -1.12 | -1.39 | -0.49 | 6.8 ± 0.5 | 0.6 ± 0.5 | $4.15^{+0.9}_{-0.12}$ |
| 12 | 1.01 | -6.30 | 20.97 | — | -1.06 | -1.44 | -0.86 | 6.6 ± 0.4 | 0.7 ± 0.4 | $4.10^{+0.7}_{-0.02}$ |
| 13 | 1.70 | -5.64 | 22.32 | — | 0.46 | -1.06 | -0.62 | 8.3 ± 0.4 | 0.4 ± 0.3 | $5.3^{+0.5}_{-0.5}$ |
| 14 | 0.57 | -4.70 | 19.74 | — | -1.43 | -2.52 | -1.22 | 6.4 ± 0.2 | 0.4 ± 0.2 | $4.61^{+0.10}_{-0.3}$ |
| 15 | 0.74 | -4.23 | 19.86 | — | -0.31 | -1.67 | -1.32 | 6.6 ± 0.3 | 1.0 ± 0.2 | $4.8^{+0.4}_{-0.4}$ |
| 16 | 1.51 | -4.20 | 21.76 | — | -1.04 | -0.79 | -0.95 | 6.9 ± 0.6 | 0.6 ± 0.5 | $4.1^{+1.0}_{-0.4}$ |
| 17 | 4.47 | -2.41 | 23.19 | — | 0.84 | -1.03 | -0.77 | 8.4 ± 0.5 | 0.5 ± 0.4 | $5.2^{+0.5}_{-0.5}$ |
| 18 | -1.47 | -2.29 | 20.50 | — | -0.09 | -0.97 | -1.05 | 8.1 ± 0.4 | 0.4 ± 0.6 | $5.6^{+1.0}_{-0.4}$ |
| 19 | -1.30 | -1.47 | 21.82 | — | 0.76 | -0.72 | -0.07 | 8.0 ± 0.7 | 1.0 ± 0.5 | $5.7^{+0.7}_{-0.7}$ |
| 20 | 0.12 | -1.29 | 18.18 | — | -1.39 | -1.96 | -1.52 | 6.4 ± 0.2 | 0.47 ± 0.19 | $5.26^{+0.12}_{-0.3}$ |
| 21 | 2.25 | -1.01 | 22.83 | — | 0.25 | -1.64 | -0.29 | 8.0 ± 0.5 | 0.4 ± 0.3 | $4.75^{+0.7}_{-0.6}$ |
| 22 | -0.85 | -0.75 | 17.31 | — | -1.02 | -1.53 | -1.45 | 6.3 ± 0.2 | 0.88 ± 0.12 | $5.92^{+0.05}_{-0.4}$ |
| 23 | 0.53 | -0.66 | 20.15 | — | -0.69 | -1.33 | -1.27 | 6.8 ± 0.6 | 0.6 ± 0.5 | $4.5^{+1.0}_{-0.2}$ |
| 24 | -1.75 | 0.66 | 19.55 | — | 0.05 | -1.52 | -0.97 | 6.8 ± 0.6 | 1.2 ± 0.4 | $5.22^{+0.9}_{-0.09}$ |
| 25 | 2.60 | 1.04 | 23.44 | — | 1.26 | -0.77 | -1.40 | 8.7 ± 0.5 | 0.5 ± 0.4 | $5.4^{+0.3}_{-0.4}$ |
| 26 | -2.99 | 1.61 | 21.26 | — | 0.41 | -0.24 | -0.42 | 7.5 ± 0.5 | 1.1 ± 0.3 | $5.6^{+0.4}_{-0.6}$ |
| 27 | 2.06 | 1.74 | 22.59 | — | 0.31 | -1.13 | -0.61 | 8.1 ± 0.5 | 0.4 ± 0.3 | $4.9^{+0.7}_{-0.4}$ |
| 28 | -2.25 | 1.98 | 23.80 | — | 2.44 | -0.43 | -0.48 | 9.2 ± 0.6 | 0.9 ± 0.4 | $6.3^{+0.5}_{-0.5}$ |
| 29 | 0.96 | 2.42 | 22.98 | — | -0.24 | -1.19 | -0.53 | 7.9 ± 0.6 | 0.4 ± 0.3 | $4.5^{+0.7}_{-0.8}$ |
| 30 | -2.40 | 2.91 | 21.90 | — | 1.07 | -0.64 | -0.60 | 8.9 ± 0.3 | 0.3 ± 0.3 | $6.1^{+0.4}_{-0.3}$ |

Photometric results of the 30 clusters identified in at least 4 out of the 5 bands. Col.(1): cluster identifier; Col.(2,3): cluster offset with respect to the galactic nucleus, as identified in the near-IR bands, in arcseconds (north and west offsets are considered positive); Col.(4): magnitude at F330W filter (U); Col.(5): color F210M–F330W (fUV–U); Col.(6): color F330W–F606W (U–V); Col.(7): color F606W–F110W (V–H); Col.(8): color F110W–F160W (H–J); Col.(9): logarithm of the most probable age in years; Col.(10): most probable reddening; Col.(11): estimated cluster mass, in solar masses.

our proposed cone, but just in the opposite side of the nucleus (toward the north-east). However, they also clearly identify [SiVI] 2″ to the southwest of the nucleus, but fainter. They argue that this may be due to different extinction and projection effects. Prieto et al. (2005) showed that coronal-line emission tends to align in the same direction than the lower ionization extended narrow-line region, so the result from Bedregal et al. (2009) supports our hypothesis. Yet it remains unexplained why the lower ionization cone would be better noticed in the side of the nucleus of fainter coronal-line emission. Another thing to be determined is whether the bright diffuse emission bar visible in the shorter wavelength bands, but which lies in front of a dust lane thick enough to affect the near-IR band, is actually associated to this possible cone, or on the contrary, to the obscured star-formation in that area revealed by the other studies.

### 5.5.5 Cluster spatial distribution

The nearness of the active nucleus and the center of the potential well of the galaxy may provide a dynamical and disturbing environment for the circumnuclear star clusters. In order to investigate possible trends of this kind we have plotted in Figure 5.20 the dependence of the calculated mass and age of the studied clusters with the distance to the nucleus. The position of the nucleus is easily derived from the near-IR images. The plots show a high scatter and strong conclusions cannot be inferred. It seems however that the clusters in the inner 2 arcsec (∼530 pc) tend to be younger than 10 Ma.

A further analysis is presented in Figure 5.21, in which we plot the spatial distribution of the clusters detected in at least 4 bands. The objects have been divided in three age intervals: clusters younger than 15 Ma, in blue color; clusters with ages between 15 and 200 Ma, in yellow; clusters older than 200 Ma, in red. We also plot the location of the near-IR nucleus and the apparent ionization cone. This last is inferred by visual comparison of the V and U band images (which present some contamination by ionized gas), with the J band (which shows almost purely stellar light), as explained above. As a complement, the spatial distribution of the cluster mass is shown in Figure 5.22. Clusters are divided in three mass intervals: lighter than $10^5\,M_\odot$, with masses between $10^5$ and $10^6\,M_\odot$, and heavier than $10^6\,M_\odot$.

In the plots it is observed that the older and intermediate-age clusters are evenly positioned around the nucleus, while the distribution of younger clusters is strongly biased towards the south half of the circumnuclear region. In fact almost all the young clusters fall in the opening angle of the cited cone, or very close to it. Most of these clusters are in fact lighter than $10^5\,M_\odot$. The apparent gap dividing these clusters in two groups about half a kiloparsec from the nucleus is probably due to a thick dust lane which is well observed in the image of Figure 5.1. We could be observing a projection effect, in which either the AGN or the starburst itself might have cleansed of dust the interstellar medium of NGC 5135 just above the galactic plane in that direction, making those young and not very massive clusters easier to be detected there. In fact González Delgado et al. (1998) find outflowing gas (through absorption of Ly$\alpha$ line) in nuclear spectra of this object. They also find a blue-shifted component in H$\beta$, [OIII], and HeII$\lambda\lambda$4686. The interpretation of Levenson et al. (2004) of their X-ray results points also in the same direction.

## 5.6 Conclusions

In this chapter we have optimized a methodology to study the star cluster population with multi-wavelength Hubble data. We have chosen the nuclei of NGC 5135, that belongs to our Atlas of Seyfert galaxies. This object possesses a rich population of clusters and stands as a good example to learn the technics that may be extended later to a larger sample, and yet give interesting results. Star cluster studies in the literature are usually focussed in closer objects and larger portions of the disk. However, with the distance to our object and the instrumental configuration we are very limited in the number of clusters that we can measure.

We have used automatic search software to find a population of 101 well-defined clusters at the F330W band (∼ U), 72 clusters at F606W (∼ V+R), and 78 at F110W (∼ J). Another 27 objects in F210M (UV), not all with good photometry, and 131 candidates in F160W (∼ H). Applying restrictive criteria we ended up with 30 objects clearly detected in at least 4 bands (9 of which were detected in all 5 bands), which yielded reliable photometry. Our magnitude detection limit is around 24 in U, V and J, and 25 in H. Photometry with a careful uncertainty calculation has been tabulated. Several methods have been explored and compared to derive cluster parameters, such as age, reddening and mass. The errors calculated and listed in the tables do not account for the effect of different model ingredients and uncertainties. However, we have performed some tentative tests with different models and realized that, despite differences in particular clusters, there is no bias in the overall results.

Some conclusions may be derived from our study:

- The calculated cluster parameters are not strongly dependent on the theoretical models chosen for comparison.

- We have confirmed that the F330W filter constituted the best choice to study the young massive cluster population, providing the largest sample with the lowest uncertainty in the results.

- We have also confirmed the strong starburst character of the nuclear region of NGC 5135 through the analysis of the fraction of light in clusters, which in the U band is 30% of the total flux in the inner 2 kpc.

- Indications of a discontinuous star formation history has been found, with possible bursts 100 Ma ago and less than 10 Ma.

- From the distribution of cluster parameters we have found a mass segregation in the clusters, with a central grouping of young massive clusters, and an alignment of less massive clusters in the south of the nucleus. The cluster distribution is very asymmetrical, with much less objects in the northern half.

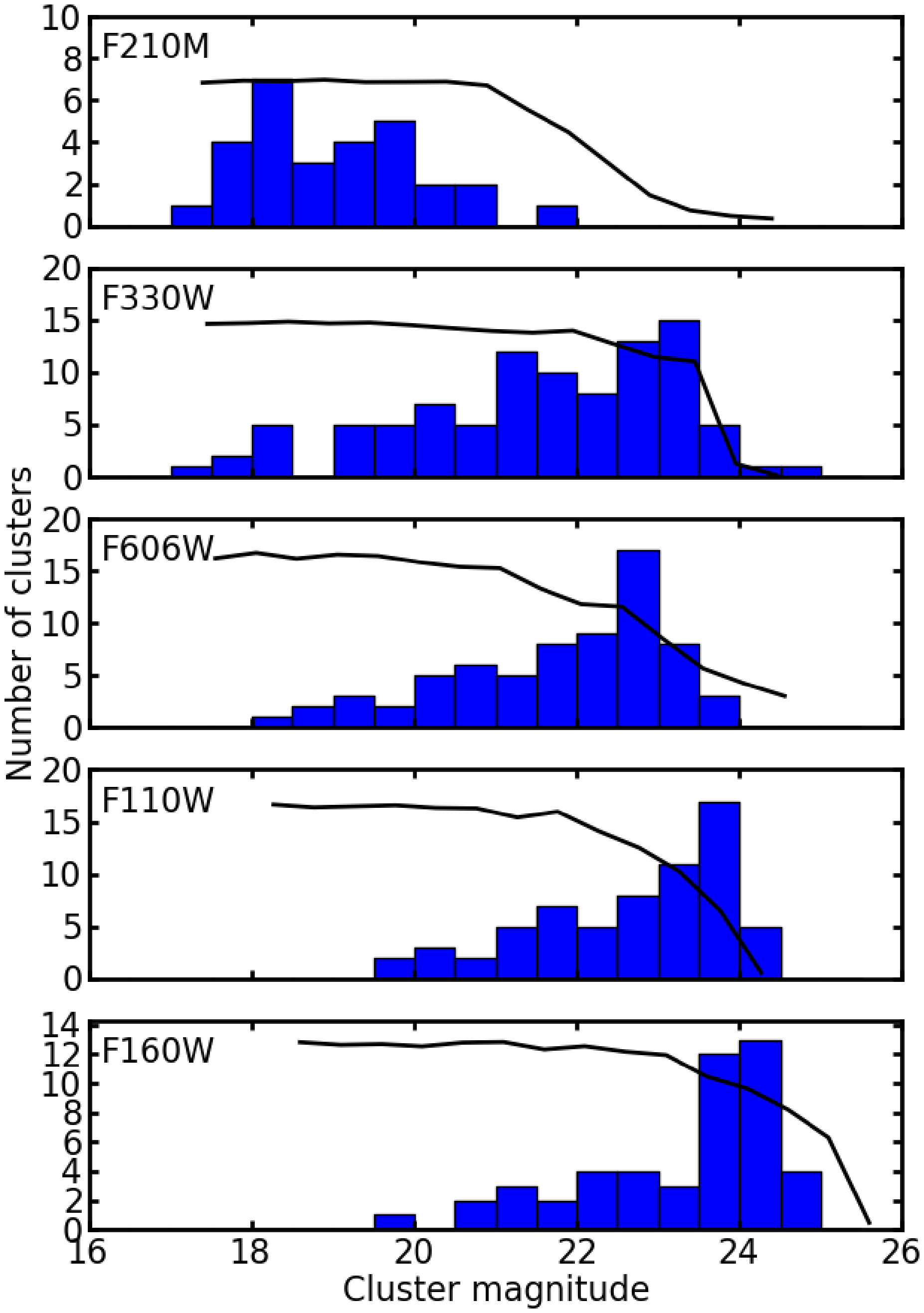

Figure 5.16: Histograms of the measured magnitudes of the clusters detected in each particular band. The completeness function, as calculated from the simulations, are over-plotted as a full line for reference. These are normalized to the maximum value of the histogram in each band.

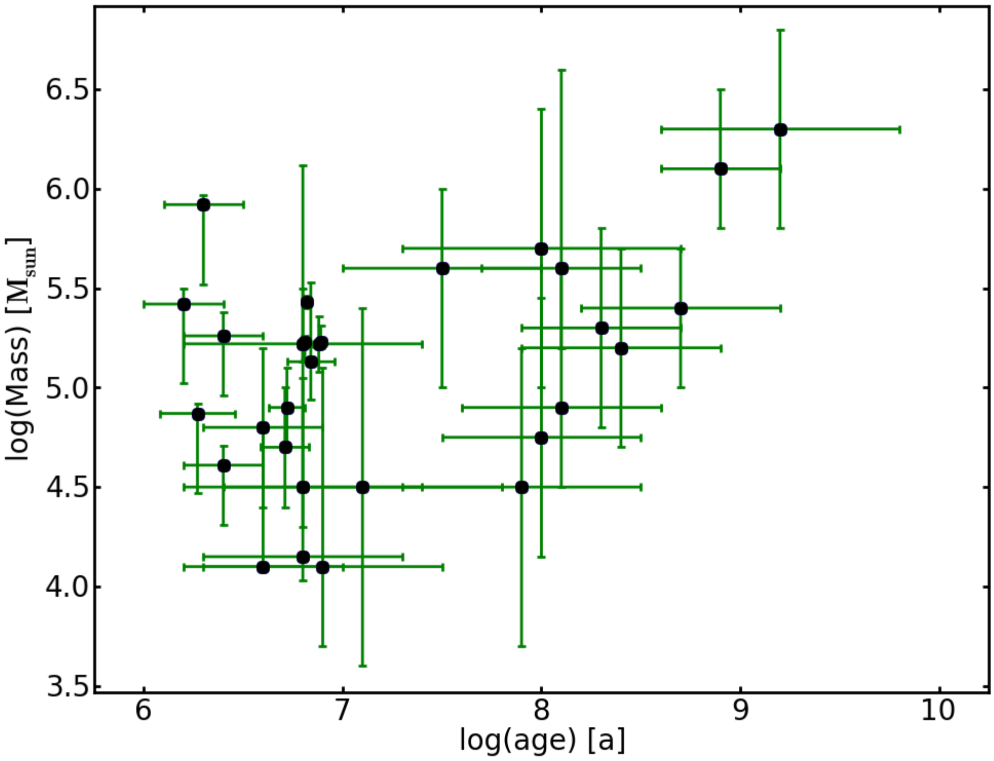

Figure 5.17: A scatter plot of the calculated cluster mass versus the age of each cluster.

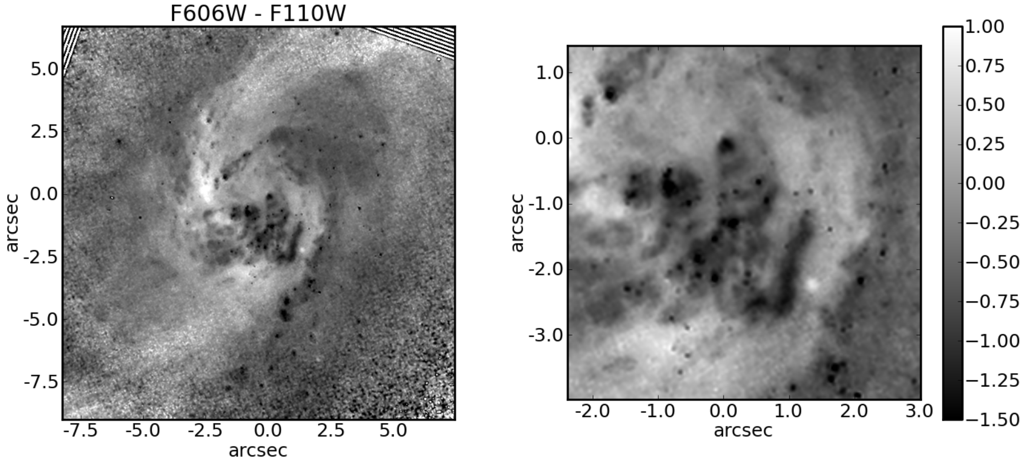

Figure 5.18: A color map of the central region of NGC 5135 with filters F606W (WFPC2) and F110W (NICMOS). It shows the dust distribution as white patches and the features bright at F606W as dark clumps or extended emission. A close up of about 1.4 kpc side is also shown. It can be observed a cone-shaped emitting feature opening from the nucleus (at the origin) to the southwest. North is up, east to the left.

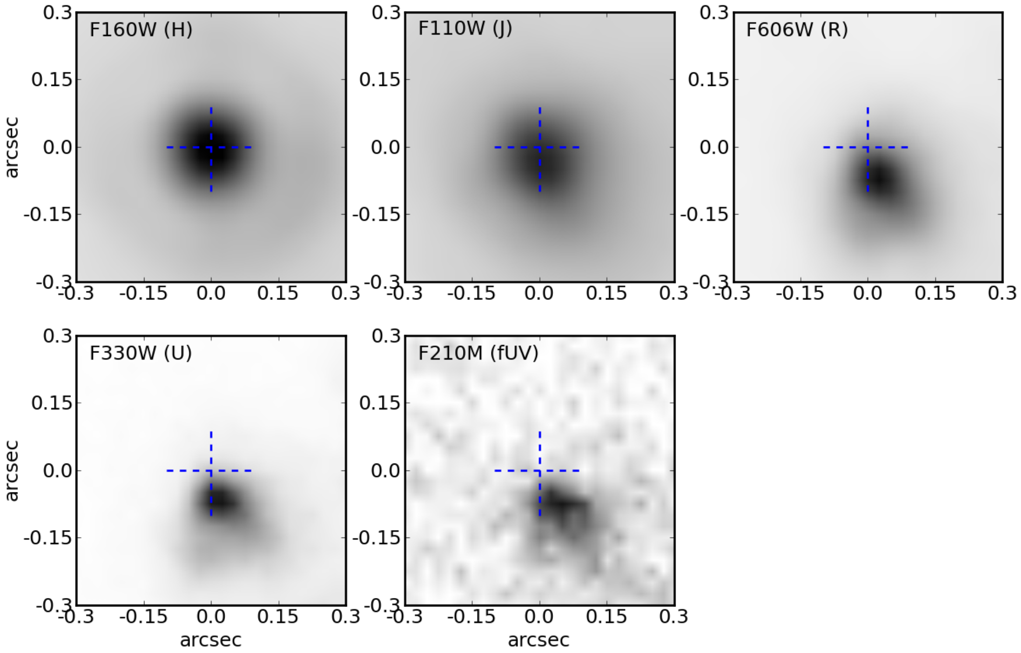

Figure 5.19: Each panel shows the precise position of the nuclear peak emission at a different band, for all the studied images. The images have been aligned using several star clusters, as explained in the text, and the origin has been chosen as the centroid of the nucleus at F160W. Both, comet-shape and offset from (0,0), increase toward shorter wavelengths. North is up, east to the left in all of them.

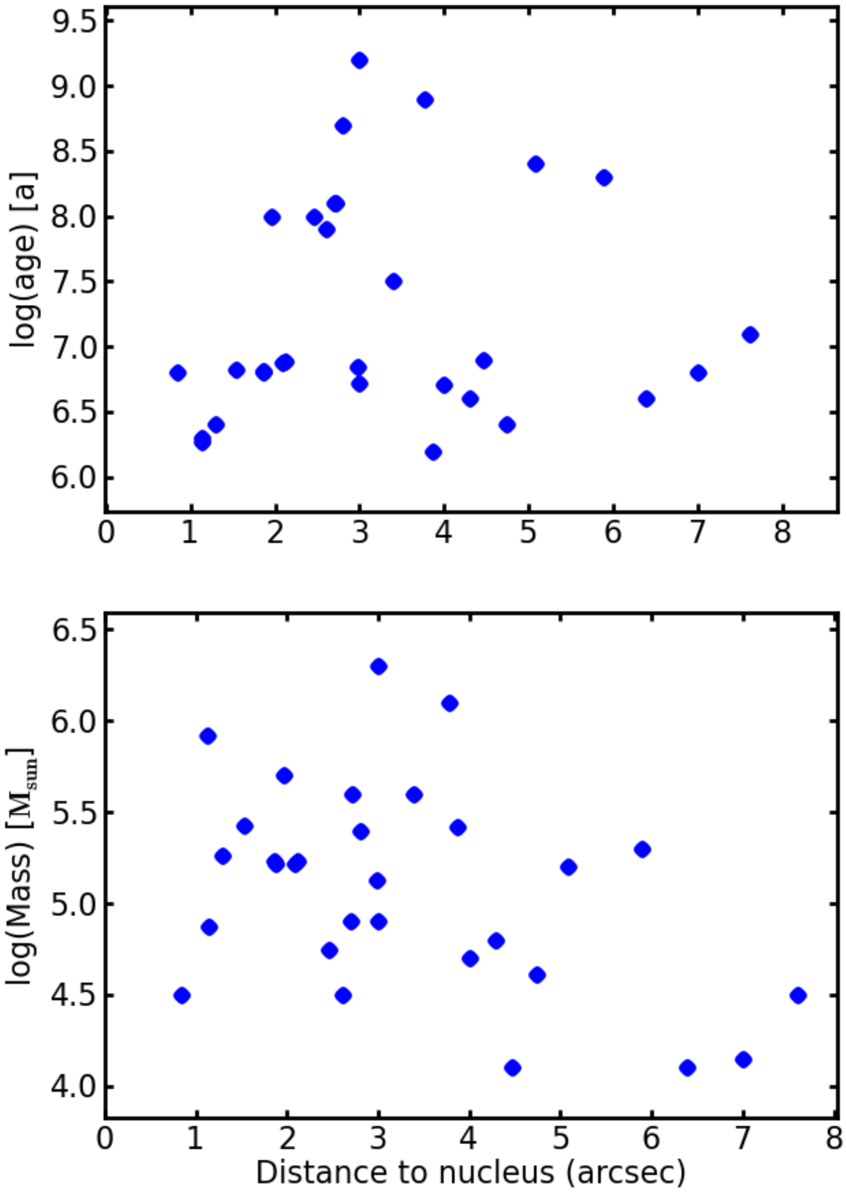

Figure 5.20: The upper panel shows the dependence of the most probable age calculated for each cluster with the distance to the nucleus of the galaxy in arcseconds (3.75″ equals 1 kpc). The lower panel shows the same dependencecy, but for the calculated cluster mass.

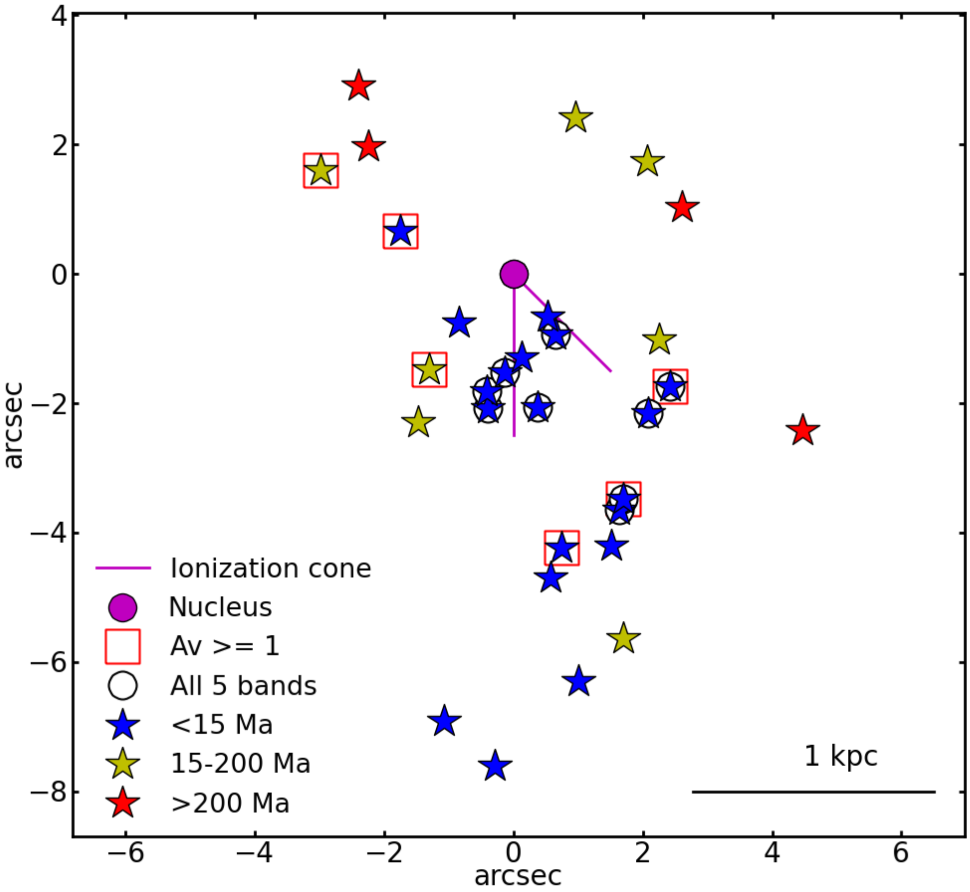

Figure 5.21: Sketch of the central region in NGC 5135 showing the star clusters with photometry in at least 4 bands, and their location respect to the nucleus and the possible ionization cone (in magenta). The clusters are separated in three age intervals: clusters younger than 15 Ma, in blue color; clusters with ages between 15 and 200 Ma, in yellow; clusters older than 200 Ma, in red. We have marked the clusters with a large reddening and those detected also in the F210M filter (see figure legend). North is up, East to the left.

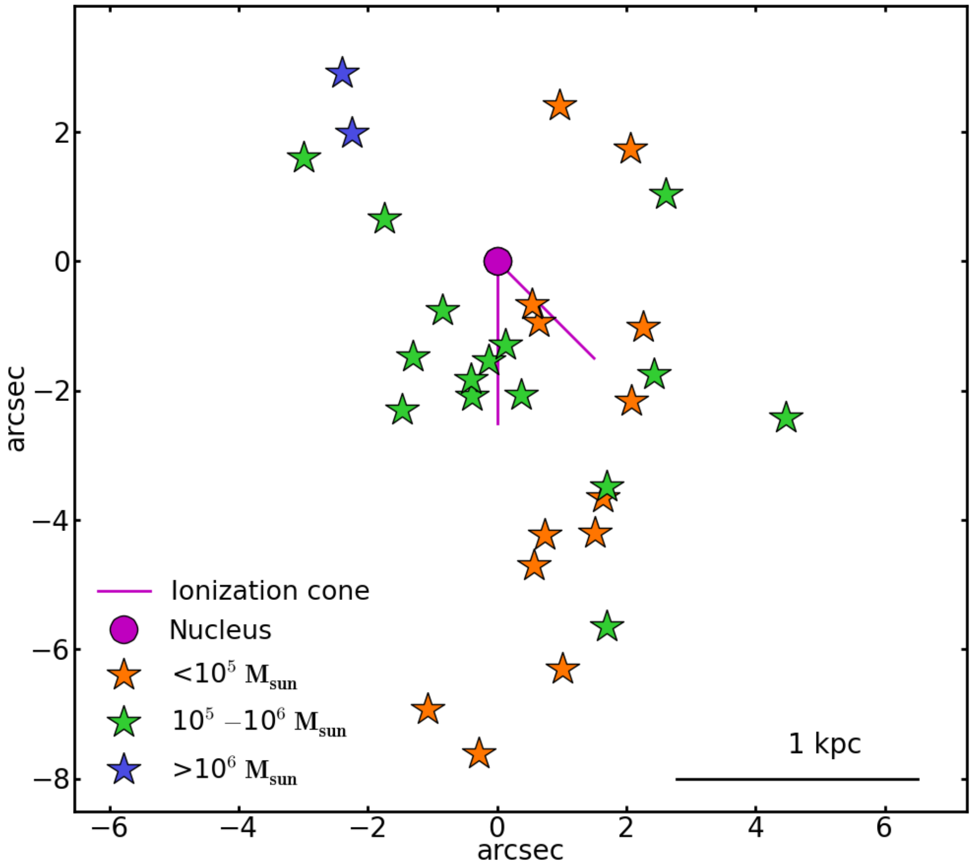

Figure 5.22: Sketch of the central region in NGC 5135 showing the star clusters with photometry in at least 4 bands, and their location respect to the nucleus and the possible ionization cone (in magenta). The clusters are separated in three mass intervals: less than $10^5$ $M_\odot$ in orange, with masses between $10^5$ and $10^6$ $M_\odot$ in green, and heavier than $10^6$ $M_\odot$ in blue. North is up, East to the left.

## Chapter 6

# Final remarks

Based in a snapshot survey using the high resolution of the Advanced Camera for Surveys onboard HST, we have compiled a sample of 75 nearby Seyfert galaxies in the near-UV. These observations complete a reference multi-wavelength database for these AGN, which have also optical and near-IR images available in the HST archive. In this work we have studied the characteristics of the near-UV emission, first in a general way, then focussing on the extended emission, and finally studying the concentrated light component: the star cluster population.

In our analysis we have found that in the near-UV Seyfert 1 galaxies are objects completely dominated by their central source, a point-like nucleus. In contrast, Seyfert 2 galaxies lack in general an unresolved nucleus. This would account for most of the differences that we have observed within types, favoring the unified model. However, our data indicate that bright stellar clusters are slightly more often seen in Seyfert 2 than in the other types, and they also contribute more to the total near-UV emission. This could point to a possible intrinsic difference between types.

The morphology that we find within the sample is varied and very irregular, with clumps and compact structure, as well as extended emission. While the clumps are mostly produced by star-forming regions, there is not a unique mechanism for the extended emission. We have shown how the different contributions can be disentangled by means of aperture photometry and analysis of emission line images. We have found that the emission by ionized gas dominates the near-UV light in ∼50% of the objects with extended emission.

We have also optimized a methodology to study the star cluster population with multi-wavelength Hubble data. This poses a powerful complement to spectroscopic data, and with it we can derive cluster parameters, infer the star-formation history, observe spatial correlations, and determine their possible relation to different processes and components of the nuclear environment. Applying this method to an interesting example, as NGC 5135, yields robust cluster parameters and results compatible with, and supporting other works in the literature.

# Conclusiones

Basándonos en un sondeo usando la alta resolución de la Cámara ACS (del inglés, Advanced Camera for Surveys) del Telescopio Espacial Hubble en el ultravioleta cercano, hemos construído una muestra de 75 galaxias Seyfert cercanas. Estas observaciones constituyen una base de datos multi-frecuencia de referencia para estos AGN, que poseen también imágenes en el óptico y el infrarrojo cercano en el archivo del Telescopio Espacial. Este trabajo está estructurado en tres partes, en las que estudiamos las características de la emisión ultravioleta cercano, primero desde un punto de vista general, luego centrándonos en la emisión extendida, y finalmente estudiando la población de cúmulos estelares.

En la primera parte de este trabajo hemos llevado a cabo un análisis general de las imágenes en luz ultravioleta cercano de esta muestra, consistente en la identificación de fuentes nucleares no resueltas, fotometría y extracción de perfiles de brillo superficial, determinación de los parámetros morfológicos Asimetría y Compacidad, y la identificación de la población de cúmulos estelares para cada objeto. El tamaño de esta muestra nos permite comparar los resultados de este análisis entre diferentes clases de actividad: Seyfert 1 (incluyendo Seyfert 1.2-1.5), Seyfert 2, y Seyfert de tipos intermedios (Seyfert 1.8-1.9).

Las conclusiones principales del estudio morfológico y fotométrico mencionado son las siguientes:

- En general, la morfología en el ultravioleta es muy irregular, con estructura grumosa y compacta, en la mayor parte de los casos.
- Las galaxias Seyfert 1 son objetos totalmente dominados por la PSF en sus regiones más internas, pero se detectan perfiles tipo Ley de Nuker para algunas galaxias. Inspeccionando los perfiles de brillo superficial encontramos 3/14 Seyfert 1 y 6/47 Seyfert 2 que poseen un anillo de formación estelar. Por el contrario, no hemos encontrado ningún anillo de formación estelar en la submuestra de Seyfert de tipos intermedios. Las galaxias Seyfert 2 presentan los perfiles más irregulares. Algunos perfiles siguen una ley exponencial, de de Vaucouleurs o ley de Nuker, pero la mayoría no se pueden clasificar fácilmente.
- No resolvemos el núcleo para ninguna Seyfert 1, mientras que casi todas las Seyfert 2 muestran el núcleo resuelto. Al menos 5/14 Seyfert 1.8-1.9 muestran un núcleo puntual, no resuelto.
- En términos de brillo superficial a $1''$, y a partir del cálculo de la magnitud integrada entre $0.3''$ y $1''$, no encontramos ninguna diferencia significativa entre las galaxias que albergan núcleos Seyfert 1 o Seyfert 2. La diferencia se

debería solamente a la presencia de la fuente puntual nuclear en objetos de tipo 1.

- Las galaxias Seyfert 1 son muy compactas y muestran valores bajos de asimetría, mientras que las Seyfert 2 muestran un amplio rango de valores de asimetría y compacidad.

Del estudio de la fracción de luz en cúmulos podemos concluir que::

- Se detectan cúmulos estelares brillantes ligeramente con más frecuencia en Seyfert 2 (∼70%) que en Seyfert 1 (∼57%), o Seyfert de tipos intermedios (∼64%).
- Cuando se consideran sólo galaxias con cúmulos detectados, la distribución de luminosidad de los cúmulos no cambia mucho entre distintos tipos de Seyfert.
- Finalmente, la contribución de los cúmulos estelares al flujo total es mucho más importante en Seyfert 2 (donde alcanza hasta un 30%) que en otros tipos de actividad, pero esto es debido en parte al menos a la gran contribución de la fuente nuclear en Seyfert 1 y tipos intermedios.

Seguidamente, hemos construído una submuestra de galaxias que también poseen imágenes de banda estrecha en la línea [OIII]$\lambda\lambda$5007. Para estos objetos hemos intentado separar la contribución de los distintos componentes a la emisión en el ultravioleta cercano. Las imágenes de emisión en [OIII] han sido escaladas para sustraer la contribución del continuo nebular y las líneas de emisión de [NeV] en el filtro F330W. Usando datos disponibles en otras longitudes de onda, hemos realizado fotometría de banda ancha para constreñir la naturaleza de la emisión restante. En resumen podemos decir que no existe un único mecanismo responsable para la emisión en ultravioleta cercano. Cada objeto merece un cuidadoso estudio particular, debido a lo variado de las morfologías observadas. Un estudio más profundo requeriría además el uso de espectroscopía, idealmente el uso de espectroscopía 3D con suficiente resolución, y observaciones polarimétricas.

Nuestras principales conclusiones del estudio de la emisión extendida en el ultravioleta cercano son:

- Para ∼50% de las galaxias de la submuestra (8/15), la emisión de gas ionizado de la región de líneas estrechas (Narrow-Line Region) domina la emisión extendida en ultravioleta cercano, llegando a 1 kpc del núcleo.
- Para 7 galaxias hemos podido obtener fotometría de banda ancha en las imágenes en ultravioleta, después de sustraer la emisión del gas ionizado; para 6 de ellas los colores de la emisión extendida residual son consistentes con los de una población estelar vieja; entre estas galaxias hay 5 objetos para los que no encontramos evidencias de ninguna contribución adicional por luz nuclear dispersada o una población estelar joven difusa.

- Solamente para 1 galaxia (NGC 7674) hemos encontrado que la luz dispersa del núcleo domina la emisión extendida, si bien este tipo de emisión puede estar presente a un nivel más bajo en gran parte de los objetos.

- Para 4/15 de las galaxias de la muestra observamos regiones de formación estelar, que aparecen como grumos compactos alrededor del núcleo, y estas contribuyen significativamente a la luz ultravioleta cercano en el kiloparsec central.

En la última parte de esta tesis hemos optimizado una metodología para estudiar la población de cúmulos estelares con datos multifrecuencia del Telescopio Espacial Hubble. Hemos elegido el núcleo de NGC 5135, que pertenece a nuestro atlas de galaxias Seyfert. Este objeto posee una rica población de cúmulos y constituye un buen ejemplo para aprender las técnicas que podrían ser posteriormente extendidas a una muestra mayor, y al mismo tiempo dar resultados interesantes. Los estudios de cúmulos estelares en la literatura se centran normalmente en objetos más cercanos y cubren una parte mayor del disco galáctico. Sin embargo, con la distancia a nuestro objeto y la instrumentación utilizada estamos limitados en la cantidad de cúmulos que podemos medir.

Hemos usado programas de búsqueda automática para detectar una población de 101 cúmulos bien definidos en el filtro F330W ($\sim$U), 72 cúmulos en F606W ($\sim$V+R), y 78 en F110W ($\sim$J). Además hemos identificado otros 27 objetos en F210M (UV), no todos con buena fotometría, y 131 candidatos en F160W ($\sim$H). Nuestro límite de detección en magnitud está en torno a 24 en U, V, y J, y 25 en H. Aplicando criterios restrictivos sobre la calidad de las medidas acabamos con 30 objetos que se detectan claramente en al menos 4 bandas (9 de ellos detectados en los 5 filtros), y que producen una fotometría fiable. Hemos tabulado la fotometría de estos objetos con una determinación cuidadosa de sus incertidumbres. Se han explorado y comparado varios métodos para determinar los parámetros fundamentales de los cúmulos, como su edad, masa y enrojecimiento. Además hemos llevado a cabo varios tests con diferentes modelos para determinar estos parámetros y hemos encontrado que, pese a diferencias en los valores particulares de algunos objetos, no se encuentra un sesgo general en los resultados.

De este estudio podemos derivar algunas conclusiones:

- Los parámetros calculados no dependen fuertemente del modelo teórico utilizado de comparción.

- Hemos confirmado que el filtro F330W constituye la mejor opción para estudiar la población de cúmulos jóvenes y masivos de las configuraciones instrumentales consideradas, dando la mayor muestra con las menores incertidumbres en las medidas.

- Hemos confirmado el fuerte carácter de starburst de la región nuclear de NGC 5135 a través del análisis de la fracción de luz en cúmulos, que en la banda U alcanza un 30% del flujo total en los 2 kpc centrales.
- Se han encontrado indicios de una historia de formación estelar discontinua, con posibles estallidos hace 100 Ma por un lado y menos de 10 Ma por otro.
- La distribución de los parámetros de los cúmulos parece mostrar cierta asociación con un posible cono de ionización del AGN

Chapter 7

# Ongoing and Future Work.

Contents

We present in this chapter how and in which fields we intend to extend our work. We also comment on some of the analysis that we have already started, in parallel to our thesis work.

## 7.1 Star cluster population in different types of AGN

The aim of Chapter 5 was to develop and to optimize a method to study the circumnuclear star cluster population with this kind of data. Now we are in the position of confronting a detailed study in a sample of galaxies of moderate size, that should allow us to draw some general conclusions.

We plan to characterize the sizes, colors, luminosities and masses of these clusters. We also intent to derive the luminosity function of the clusters and determine their evaporation over time in the vicinity of the AGN. We expect to be able to compare the results for galaxies with a different type of active nucleus, pointing to possible differences or common trends among types. In this way we may be able to address the question of whether there exist an evolution from Seyferts to Transition Objects and LINER.

Ideally we would have just to apply the same method to a large and varied sample of galaxies, however, we have learned from our experience working with these data that this process can hardly be automated. Each galaxy will pose a different resolution, a different morphology, background and clumping of the clusters, and a varied dataset. This will imply that the analysis will have to be slightly adapted to every object, in order to optimize the scientific output. We are confident in our capacity of doing this task, coming from our acquired experience along this work.

In order to assess the difficulties and possibilities of this study we have preselected some objects that show an interesting and rich cluster population and posses the needed data coverage in the HST archive:

- **NGC 5135** This galaxy has already been studied in Chapter 5 and will serve as a reference

- **NGC 4303** It is classified as a Seyfert 2, although it seems that it posesses a super massive ionizing cluster in its center. There are ACS archival images in several bands: F330W, F435W, F555W, F625W, F814W; and NICMOS F160W.

- **NGC 1672** Another Seyfert 2. With an obvious asymmetrical obscuration may serve as a test to explore possible ways to calibrate the difference of the effect of the reddening from the effect of age in the fits. There is a complete ACS archival dataset: F330W, F435W, F550M, F814W; NICMOS F160W; and completed with some WFPC2 exposures.

- **NGC 4321** This object is a LINER with also a rich dataset: ACS images in F330W, F555W, and F814W; and WFPC2 in the filters F439W, F555W, and F702W.

- **NGC 7742** This is also an interesting Low Luminosity AGN, although it has only data on WFPC2 (WF3): F336W, F555W, F675W, F814W; and also NICMOS F160W.

## 7.2 Extension of the work to Low Luminosity AGN

### 7.2.1 Motivation

Low Luminosity AGN (LLAGN) are the most common type of AGN[1]. They are present in ∼30% of the local bright galaxies (Ho et al., 1997). These comprise LINER galaxies and Transition Object (TO, also called weak-[OI] LINER), whose properties are in between classical LINER and HII nuclei. The physical processes operating in the central regions of Low Luminosity AGN are still nowadays a matter of debate. Its ionizing source could either be a low efficiently accreting supermassive black hole, as well as a massive star cluster. It is thought now that a large fraction of LINER (which are the most common LLAGN) host actually a true active

---

[1] Here the term implies possessing an AGN-like spectrum, but not necessarily sharing its nature.

nucleus with a low radiative efficiency accretion flow (Quataert, 2001; Kewley et al., 2006). On the other hand there are examples of galaxies with a central ionizing massive star cluster. At least in TO, there is also evidence for the existence of circumnuclear starbursts (González Delgado et al., 2004; Colina et al., 2002), and signs of intermediate age stellar populations (Cid Fernandes et al., 2004b; González Delgado et al., 2004). In a number of objects both processes may coexist and play a similarly important role in the galactic nuclei evolution. Moreover, LINER themselves appear to be a very heterogeneous set of galaxies (e.g. Stasińska et al., 2008).

In order to disentangle both possible contributions we have constructed a sample of 41 LLAGN imaged at the near-UV with HST. The very high spatial resolution of ACS-HRC and WFPC2 will allow us to estimate the presence of unresolved nuclear point-like sources that could be attributed to an AGN, as well as to determine the frequency of nuclear and circumnuclear stellar clusters in LLAGN. We also plan to complement these observations with optical and near-IR archival HST data, in order to carry on a more detailed study of the stellar cluster population in the most interesting objects and to compare our results with the studies presented in this thesis for Seyfert galaxies.

### 7.2.2 Available data

We have constructed a sample of nearby Low Luminosity AGNs (LLAGN), imaged with HST in the near-UV, from the catalogue presented in Ho et al. (1997), HFS97 hereafter. From the original sample of HFS97, all the LLAGN which had archival WFPC2 images at optical wavelengths (F606W, F555W or F547M) and NICMOS observations at F160W, were included in the proposal 10548 (P.I. González Delgado) for the cycle 14 of the HST. This observations were made with the Advanced Camera for Surveys (ACS) in its High Resolution Configuration, and with the filter F330W. Due to technical problems during the snapshot program only 11 out of the proposed 59 galaxies could be successfully observed. We complemented our sample with other LLAGNs imaged with ACS/HRC from the proposal 9454 (P.I. Maoz), what added 14 more galaxies to the set. The objects imaged in the proposal 9454, but classified as Seyfert galaxies by HFS97 were rejected, which are M 81, M 106, and NGC 3486. We then checked for which objects listed in HFS97 as LINER or Transition Objects (TO) existed available HST archival data with the filters F300W, F330W or F336W. We found 16 more objects that had near-UV images, all but one (NGC 6384) imaged with WFPC2. The final list of 41 objects is listed in Table 7.1. Our subsequent studies will be based in this reference sample. This is perhaps a too heterogeneous selection of data and objects, and therefore it may be necessary to construct subsamples from it for each particular study.

### 7.2.3 Photometry of a sample of Low Luminosity AGN

We have carried out a preliminary photometric and morphological study of a sample of LLAGN, similar to that presented in Chapter 3 and published in Muñoz Marín et al. (2007). The sample is extracted from the one presented in last section, with the requirement for the galaxies of being imaged with the same configuration that was used for our Seyfert study, what allows for a more straightforward comparison. This sample is thus composed of 26 objects (those from the proposals 10548 and 9454, plus NGC 6384), of which 18 galaxies (69%) are classified as LINER, and the other 8 (31%) as TO, assuming the classification of Ho et al. (1997). All the galaxies possess HST images in near-UV (ACS), optical (WFPC2), and near-IR (NICMOS).

The properties of the resultant 26 objects are listed in table 7.2. We have compared the distance from NED corrected for a Virgo infall model with the distances given in Ho et al. (1997). For those objects with very different values of distance in both sources we have checked the bibliography to find a more robust measurement. In the case of NGC 404 Tonry et al. (2001) give a distance of $3.26 \pm 0.15$ Mpc, based in the surface brightness fluctuations method. This is confirmed by Karachentsev et al. (2002), who calculated a value of $3.06 \pm 0.37$ Mpc through the tip of the giant branch method. The resultant mean distance to the objects is 19 Mpc. Therefore these galaxies are closer on average than the Seyfert sample.

The proposal 9454 was intended for checking the possible near-UV variability of LINER nuclei. As a consequence, each object possesses several images of short exposure time and taken with different pointings. The absolute pointing of HST has an accuracy of 1 arcsecond, and thus these images had to be carefully registered and combined using the IRAF package 'Pydrizzle'. This requires a bit of extra work, but for the rest the procedure for this analysis is similar to that explained in Chapter 3.

Table 7.3 show the results for this sample of the measurements analogous to those for Seyferts. In our first results, LLAGN show similar values of compactness and absolute magnitudes in the inner 300 pc, to those of Sy2 (see Fig. 7.2). No difference is seen, when considering TOs and LINER separately. We find a conspicuous unresolved nucleus in about 25% of the objects, in good agreement with previous results (Maoz et al., 1995; Barth et al., 1998). These results however are preliminary and have to be completed with an extended and deeper analysis, using also the available data in other bands.

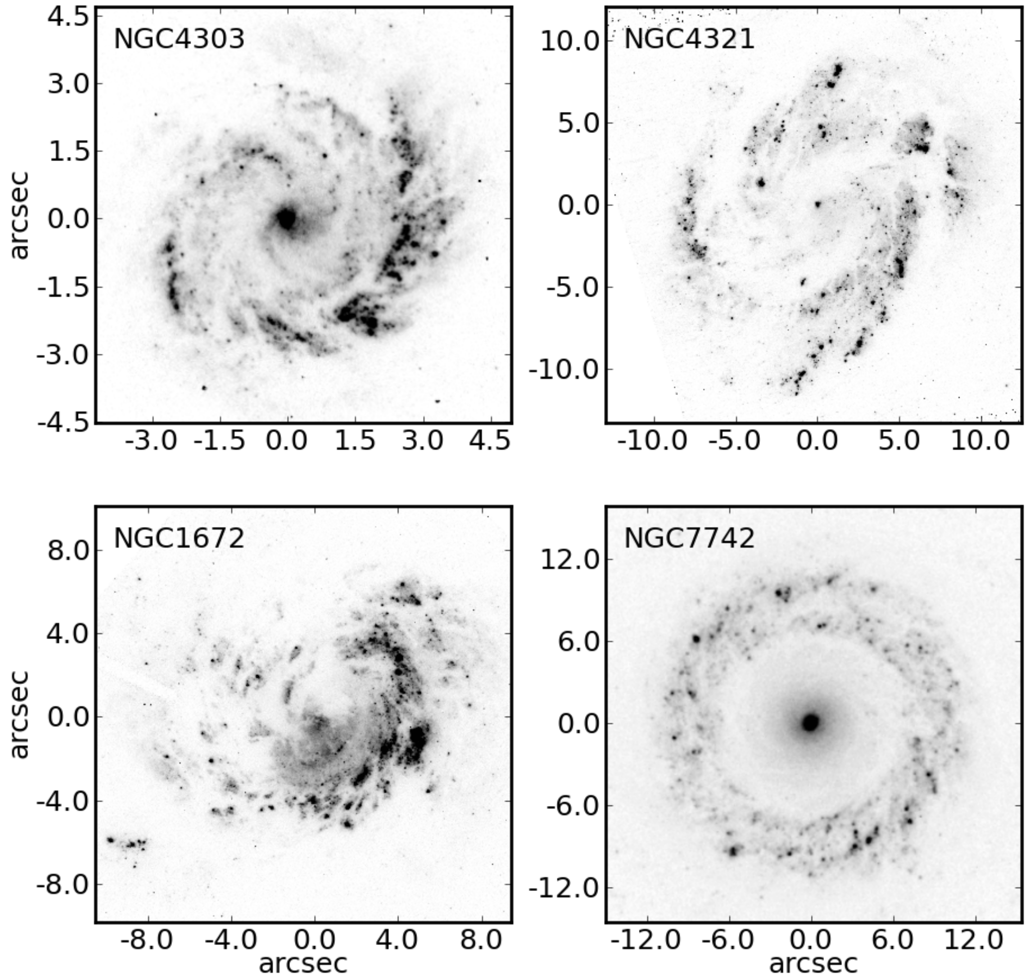

Figure 7.1: These four panels show near-UV images of selected active galaxies of different activity type with an abundant population of circumnuclear star clusters. They will serve as a starting point for an extension of the analysis in Chapter 5. See discussion in text.

Table 7.1: Data of the images for the whole LLAGN sample

| Galaxy Name | Filter | Instrument and chip | Total exposure time (s) | Proposal ID |
|---|---|---|---|---|
| NGC 404 | F330W | HRC | 300 | 9454 |
| NGC 428 | F300W | WFALL | 1000 | 9124 |
| NGC 488 | F330W | HRC | 1200 | 10548 |
| NGC 524 | F330W | HRC | 1200 | 10548 |
| NGC 1052 | F330W | HRC | 300 | 9454 |
| NGC 2336 | F330W | HRC | 1200 | 10548 |
| NGC 2681 | F300W | PC1 | 1000 | 8632 |
| NGC 2685 | F330W | HRC | 1200 | 10548 |
| NGC 2787 | F330W | HRC | 1200 | 10548 |
| NGC 3368 | F330W | HRC | 600 | 9454 |
| NGC 3507 | F300W | PC1 | 1000 | 8632 |
| NGC 3608 | F300W | WF3 | 3000 | 9676/9679 |
| NGC 3642 | F330W | HRC | 1200 | 9454 |
| NGC 3898 | F300W | PC1 | 1000 | 8632 |
| NGC 3900 | F300W | PC1 | 1000 | 8632 |
| NGC 3998 | F330W | HRC | 300 | 9454 |
| NGC 4111 | F330W | HRC | 1200 | 10548 |
| NGC 4203 | F330W | HRC | 1500 | 9454 |
| NGC 4278 | F300W | PC1 | 2000 | 5381 |
| NGC 4314 | F336W | PC1 | 3700 | 6265 |
| NGC 4321 | F330W | HRC | 1200 | 10548 |
| NGC 4486 | F330W | HRC | 600 | 9454 |
| NGC 4552 | F330W | HRC | 1500 | 9454 |
| NGC 4569 | F330W | HRC | 240 | 9454 |
| NGC 4579 | F330W | HRC | 600 | 9454 |
| NGC 4589 | F300W | PC1 | 1000 | 8632 |
| NGC 4594 | F330W | HRC | 900 | 9454 |
| NGC 4636 | F300W | PC1 | 800 | 6355 |
| NGC 4736 | F330W | HRC | 1200 | 9454 |
| NGC 4772 | F300W | PC1 | 800 | 6355 |
| NGC 5055 | F330W | HRC | 1500 | 9454 |
| NGC 5195 | F330W | HRC | 1200 | 10548 |
| NGC 5322 | F330W | HRC | 1200 | 10548 |
| NGC 5377 | F300W | PC1 | 800 | 6355 |
| NGC 5746 | F336W | PC1 | 2500 | 9046 |
| NGC 5982 | F330W | HRC | 1200 | 10548 |
| NGC 5985 | F330W | HRC | 1200 | 10548 |
| NGC 6384 | F330W | HRC | 2580 | 9395 |
| NGC 6500 | F330W | HRC | 1200 | 9454 |
| NGC 7177 | F300W | PC1 | 1000 | 8632 |
| NGC 7742 | F336W | WF3 | 2100 | 6276 |

Col. (1): Galaxy name; Col. (2): Filter used for the observations; Col. (3): Chip and configuration used for each image-set. HRC for the High Resolution Configuration of the ACS camera, or PC1, WF3 or WFALL depending on the WFPC2 chip used; Col. (4): Exposure time for each object; Col. (5): HST proposal ID; Col. (6): archival key for each image used.

Table 7.2: Basic data of the LLAGN ACS subsample

| Galaxy Name | Alternative Name | Spectral Class (NED) | Spectral Class (HFS97) | Hubble Type | T | Distance [Mpc](NED) | Distance [Mpc] (HFS97) | Scale pc/″ | B_T [mag] | E(B–V) [mag] | axial ratio (b/a) |
|---|---|---|---|---|---|---|---|---|---|---|---|
| NGC 404 | | LINER | L2 | SA(s)0-: | -3 | 0.88 | 2.4 | 12 | 11.21 | 0.059 | 1 |
| NGC 488 | | | T2:: | SA(r)b | 3 | 30.6 | 29.3 | 142 | 11.15 | 0.031 | 0.75 |
| NGC 524 | | | T2: | SA(rs)0+ | -1 | 32.3 | 32.1 | 156 | 11.3 | 0.083 | 1 |
| NGC 1052 | | LINER/Sy2 | L1.9 | E4 | -5 | 18.7 | 17.8 | 86 | 12.08 | 0.027 | 0.7 |
| NGC 2336 | | Sy2 | L2/S2 | SAB(r)bc | 4 | 33.6 | 33.9 | 164 | 11.05 | 0.033 | 0.55 |
| NGC 2685 | | Sy2 | S2/T2: | (R)SB0+ pec | -1 | 14.7 | 16.2 | 79 | 12.12 | 0.062 | 0.51 |
| NGC 2787 | | LINER | L1.9 | SB(r)0+ | -1 | 12.7 | 13 | 63 | 11.82 | 0.131 | 0.625 |
| NGC 3368 | M 96 | LINER/Sy | L2 | SAB(rs)ab | 2 | 12.7 | 8.1 | 39 | 10.11 | 0.025 | 0.68 |
| NGC 3642 | | LINER | L1.9 | SA(r)bc: | 4 | 25.0 | 27.5 | 133 | 12.6g | 0.011 | 0.87 |
| NGC 3998 | | LINER/Sy1 | L1.9 | SA(r)00̂? | -2 | 17.5 | 21.6 | 105 | 11.61 | 0.016 | 0.81 |
| NGC 4111 | | LINER/HII | L2 | SA(r)0+: sp | -1 | 13.9 | 17 | 82 | 11.63 | 0.015 | 0.22 |
| NGC 4203 | | LINER | L1.9 | SAB0-: | -3 | 17.3 | 9.7 | 47 | 11.8 | 0.012 | 0.94 |
| NGC 4321 | M 100 | LINER/HII | T2 | SAB(s)bc | 4 | 13.1 | 16.8 | 81 | 10.05 | 0.026 | 0.85 |
| NGC 4486 | M 87 | NLRG/Sy | L2 | E+0-1 pec | -4 | 13.1 | 16.8 | 81 | 9.59 | 0.022 | 0.80 |
| NGC 4552 | M 89 | LINER/HII | T2: | E | -5 | 6.01 | 16.8 | 81 | 10.73 | 0.041 | 0.92 |
| NGC 4569 | M 90 | LINER/Sy | T2 | SAB(rs)ab | 2 | – | 16.8 | 81 | 10.26 | 0.046 | 0.46 |
| NGC 4579 | M 58 | LINER/Sy1.9 | S1.9/L1.9 | SAB(rs)b | 3 | 13.1 | 16.8 | 81 | 10.48 | 0.041 | 0.80 |
| NGC 4594 | M 104 | LINER/Sy1.9 | L2 | SA(s)a | 1 | 13.8 | 20 | 97 | 8.98 | 0.051 | 0.40 |
| NGC 4736 | M 94 | LINER/Sy2 | L2 | (R)SA(r)ab | 2 | 7.21 | 4.3 | 21 | 8.99 | 0.018 | 0.81 |
| NGC 5055 | M 63 | LINER/HII | T2 | SA(rs)bc | 4 | 10.09 | 7.2 | 35 | 9.31 | 0.018 | 0.57 |
| NGC 5195 | M 51b | LINER | L2: | SB0_1 pec | 90 | 9.82 | 9.3 | 45 | 10.45 | 0.036 | 0.79 |
| NGC 5322 | | LINER | L2:: | E3-4 | -5 | 27.9 | 31.6 | 153 | 11.14 | 0.014 | 0.66 |
| NGC 5982 | | LINER | L2:: | E3 | -5 | 45.5 | 38.7 | 188 | 12.04 | 0.018 | 0.73 |
| NGC 5985 | | LINER/Sy1 | L2 | SAB(r)b | 3 | 38.7 | 39.2 | 190 | 11.87 | 0.017 | 0.54 |
| NGC 6384 | | LINER | T2 | SAB(r)bc | 4 | 25.3 | 26.6 | 129 | 11.14 | 0.123 | 0.66 |
| NGC 6500 | | LINER | L2 | SAab: | 1.7 | 44.3 | 39.7 | 192 | 13.05 | 0.090 | 0.73 |

All the quantities are extracted from NED database, except when HFS97 (Ho et al., 1997) is stated. It is assumed $H_o = 73$ km/sec/Mpc, Omega(matter) = 0.27, and Omega(vacuum) = 0.73. Distances from NED are given after correcting for a Virgo Infall model.

Table 7.3: Aperture photometry of the LLAGN ACS subsample

| Galaxy Name (1) | m(0.3″) (2) | m(1″) (3) | m($R_{max}$) (4) | m(100 pc) (5) | m(300 pc) (6) | $\mu$(0.3″) (7) | $\mu$(1″) (8) | $\mu_{50}$ (9) | $R_{20}$ [pc (″)] (10) | $R_{50}$ [pc (″)] (11) | $R_{80}$ [pc (″)] (12) | $R_{max}$ [pc (″)] (13) | C (14) |
|---|---|---|---|---|---|---|---|---|---|---|---|---|---|
| NGC 404 | 16.22 | 15.38 | 14.73 | – | – | 15.88 | 17.73 | 17.60 | 3 (0.22) | 10 (0.88) | 21 (1.79) | 33 (2.82) | 4.58 |
| NGC 488 | 19.32 | 17.35 | 15.03 | 17.87 | 16.33 | 18.09 | 19.07 | 20.10 | 216 (1.52) | 456 (3.21) | 694 (4.89) | 876 (6.17) | 2.53 |
| NGC 524 | 18.94 | 17.20 | 14.80 | 17.78 | 16.27 | 17.70 | 18.84 | 19.88 | 246 (1.58) | 509 (3.27) | 764 (4.91) | 957 (6.15) | 2.46 |
| NGC 1052 | 18.27 | 16.66 | 15.14 | 16.46 | 15.11 | 17.30 | 18.40 | 18.97 | 73 (0.84) | 153 (1.78) | 234 (2.71) | 290 (3.36) | 2.53 |
| NGC 2336 | 19.60 | 17.80 | 16.27 | 18.51 | 17.05 | 18.55 | 19.53 | 20.29 | 140 (0.85) | 308 (1.87) | 481 (2.93) | 598 (3.64) | 2.68 |
| NGC 2787 | 18.04 | 16.50 | 14.17 | 16.01 | 14.82 | 17.26 | 18.35 | 19.95 | 111 (1.76) | 277 (4.40) | 416 (6.60) | 510 (8.08) | 2.87 |
| NGC 3368 | 17.42 | 16.34 | 14.49 | 15.46 | 14.04 | 16.86 | 18.36 | 19.71 | 43 (1.11) | 122 (3.12) | 179 (4.56) | 212 (5.40) | 3.07 |
| NGC 3642 | 17.95 | 16.88 | 15.77 | 17.19 | 16.11 | 17.47 | 18.87 | 19.57 | 72 (0.54) | 195 (1.47) | 334 (2.51) | 412 (3.09) | 3.34 |
| NGC 3998 | 15.87 | 15.19 | 14.49 | 15.23 | 14.29 | 16.35 | 17.52 | 17.46 | 12 (0.11) | 98 (0.94) | 181 (1.73) | 238 (2.28) | 5.89 |
| NGC 4111 | 17.64 | 15.86 | 12.84 | 15.54 | 13.90 | 16.69 | 17.35 | 18.98 | 181 (2.20) | 397 (4.82) | 702 (8.52) | 1001 (12.15) | 2.94 |
| NGC 4203 | 17.33 | 16.32 | 14.48 | 15.45 | 14.33 | 17.39 | 18.27 | 19.24 | 51 (1.09) | 121 (2.57) | 195 (4.15) | 251 (5.35) | 2.91 |
| NGC 4321 | 17.96 | 17.24 | 12.57 | 17.02 | 15.32 | 18.24 | 19.40 | 19.12 | 423 (5.20) | 617 (7.58) | 772 (9.48) | 1016 (12.47) | 1.31 |
| NGC 4486 | 17.14 | 16.21 | 15.16 | 16.07 | 15.10 | 17.80 | 17.51 | 19.38 | 45 (0.55) | 128 (1.57) | 233 (2.86) | 285 (3.50) | 3.59 |
| NGC 4552 | 18.20 | 15.94 | 13.32 | 15.63 | 14.24 | 16.90 | 17.53 | 19.26 | 151 (1.85) | 350 (4.30) | 585 (7.19) | 786 (9.65) | 2.95 |
| NGC 4569 | 13.93 | 13.55 | 13.36 | 13.48 | 13.24 | 14.54 | 16.88 | 13.09 | 5 (0.06) | 15 (0.19) | 67 (0.82) | 149 (1.83) | 5.65 |
| NGC 4579 | 17.02 | 15.82 | 13.92 | 15.58 | 14.40 | 16.85 | 17.68 | 18.96 | 92 (1.13) | 229 (2.81) | 373 (4.58) | 468 (5.75) | 3.03 |
| NGC 4594 | 17.46 | 15.61 | 12.23 | 15.56 | 13.87 | 16.58 | 17.15 | 18.88 | 277 (2.86) | 605 (6.24) | 966 (9.92) | 1228 (12.66) | 2.70 |
| NGC 4736 | 16.09 | 14.55 | 11.16 | 12.44 | 11.24 | 15.22 | 16.35 | 18.17 | 72 (3.45) | 150 (7.18) | 245 (11.76) | 336 (16.13) | 2.66 |
| NGC 5055 | 16.47 | 15.61 | 14.94 | 15.04 | 14.21 | 16.13 | 18.28 | 17.97 | 8 (0.23) | 30 (0.87) | 77 (2.22) | 118 (3.38) | 4.93 |
| NGC 5985 | 20.03 | 18.49 | 16.80 | 19.32 | 17.85 | 19.23 | 20.24 | 20.67 | 182 (0.96) | 370 (1.95) | 521 (2.74) | 624 (3.28) | 2.29 |
| NGC 6384 | 19.97 | 17.59 | 14.98 | 18.04 | 16.24 | 18.67 | 19.04 | 20.08 | 215 (1.67) | 431 (3.34) | 655 (5.08) | 814 (6.31) | 2.42 |

Col. (1): Galaxy name; Col. (2): Magnitude within 0.3″ radius. Col. (3): Magnitude within 1″ radius. Col. (4): Magnitude within the maximum radius. Col. (5): Magnitude within a projected radius of 100 pc. Col. (6): Magnitude within 300 pc. Col. (7) & (8): Differential surface brightness at 0.3″ and 1″ respectively. Col. (9): Differential surface brightness at the half-light radius. Col. (10): Computed maximum radius in parsecc and arcsec in brackets. Col. (11), (12) & (13): Radius enclosing 80%, 50% and 20% of the flux within $R_{max}$, in parsecc (same in arcsec in brackets). Col. (14): Compactness, as defined in Chapter 3.

All the magnitudes are calculated in the STMAG system, for the F330W filter, and corrected for galactic extinction.

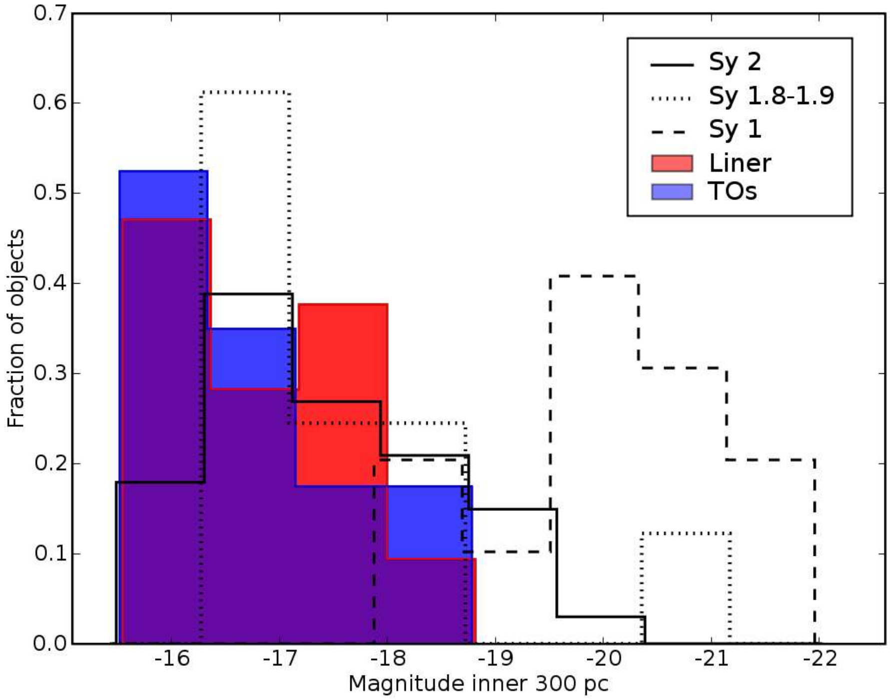

Figure 7.2: Distribution of the central magnitude (inner 300 pc), comparing different activity types. Sy1 (dashed line) are brighter due to the AGN nuclear contribution. No clear difference can be seen between Sy2 (full line) and LINER (shaded in red) or TO (shaded in blue). This is a example of the kind of photometrical analysis that could be performed with these data.

## 7.3 Nuclear clusters in Low Luminosity AGN

### 7.3.1 Motivation and summary

Massive and compact star clusters are common in galactic centers. These nuclear clusters are found all across the Hubble sequence in around 70% of the galaxies (Böker et al., 2002; Carollo et al., 1997; Côté et al., 2006). Recent studies indicate that nuclear clusters follow the same scaling relation than SMBH (Ferrarese et al., 2006; Rossa et al., 2006). They also enclose roughly the same fraction of the total bulge mass than SMBH do (Côté et al., 2006). Therefore, it seems that there exists a common formation mechanism for these objects. In this sense we can relate SMBH and nuclear clusters and talk instead about a Compact Massive Object occurring in the center of the potential well of galaxies. SMBH populate the most massive bulges, while clusters occur in less massive ones. Within the former picture remain some open questions. Do these clusters evolve and collapse into a SMBH when they grow in mass? Is a nuclear cluster a requisite for the occurrence of a SMBH or are these grown from primordial BH seeds? In some galaxies, as NGC 4395 (Filippenko & Ho, 2003), we know from spectroscopy or direct observation that there is a central compact star cluster coexisting with an AGN, and thus a SMBH. However it is not yet well established how these objects fall in the $\mathrm{M}_{BH}$–$\sigma$ relation.

Our primary motivation is to identify compact emission (AGN or stellar nuclei) in Low Luminosity AGN, and to obtain measurements of their size and brightness. More precisely, the main goals of this work are: 1) to construct the surface brightness profiles and extract their fundamental parameters; 2) to determine the fraction of LINER and TO which posses a central compact object; 3) to measure colors and sizes of these objects thus determining their true nature, AGN or cluster; 4) combining these results with STIS spectra (when available), placing them in the $M_{CMO}$-$\sigma$ relation; and 5) making a high resolution map of the dust distribution in several wavelengths.

In order to do this, we will work on the whole LLAGN sample presented in Section 7.2.2. We will fit the galactic profiles to a Sérsic (Sersic, 1968) or core-Sérsic law (Graham et al., 2003) plus a King core, which will yield the required parameters. This profiles are widely accepted and used throughout the literature. We will use for reference the work of Ferrarese et al. (2006) and Graham et al. (2003). Also, we will keep the core-Sérsic approach over the alternative Nuker-law profiles (Lauer et al., 1995), as these last may pose some convergence and numerical problems (Cid Fernandes in private communication).

### 7.3.2 Extracting the surface brightness profiles

The near-UV morphology of these objects, as it can be appreciated in our data, is in general much smoother than for Seyfert galaxies, what is specially true for LINER. This is in agreement with a study of the circumnuclear dust in LLAGN by González Delgado et al. (2008), where they find that the dust in LINER galaxies tend to be more settled in nuclear disks than it does for Seyfert galaxies or young-TOs. This fact will allow us to model better the extended emission and the dust morphology by conducting the surface brightness analysis with elliptical isophotal fitting. We use the IRAF task 'ellipse' to construct the surface brightness profiles and get the position angle and ellipticity of the isophotes. We perform an iterative fitting and comparison with the original image in order to create a map of the dust distribution and to obtain a *clean* profile, free of clumpy dust obscuration. An example can be seen in Fig. 7.3. This study in the near-UV will allow us to resolve better the nuclear structure and extract the parameters of the possible central cluster. However, in this band it is hard to get good signal to noise ratio, and the dust obscuration may become a serious problem. For these reasons we need to perform a multi-band analysis, many times doing the isophotal fitting in longer wavelength images first, and then using the parameters of the fit with the near-UV image, assuming the same morphology. This allows us to create a first estimation of the dust distribution and to get a better fit.

### 7.3.3 Profile fitting and parameter extraction

The main issue is to perform a robust fitting of the profiles, and check how confident is the determination of the parameters of the nuclei. There are many problems to address. Some are the coupling of the parameters and the degeneracy of models. Using a chi-square minimisation algorithm to fit the data can lead to a wide interval for the parameters or family of models with a very similar $\chi^2$. A possible approach could be a grid of models, in which we would have an idea of how robust is the parameter determination, just as we have done for the clusters and SSP models in Chapter 5. Another issue to address is that adding a nucleus or a core in a Sérsic profile, seem to have the same role in helping to fit the profile reducing the $\chi^2$. In addition, we will have to determine whether a King nucleus is needed or not in order to fit a certain profile.

One of our collaborators, Roberto Cid Fernandes, has already dealt with many of these and other issues. He has written, and kindly offered to us, a code to perform this task called `SBPfits`. Although the code is not completed but in a testing phase, it may well serve as a starting point for this work.

At this point it is worth mention than the election of the PSF chosen to convolve with the King profile is critical, in order to derive the correct value of the profile parameters. We have been testing the PSF for ACS created by Anderson & King (2004). Comparing it with the PSF generated by TiniTim, it seems that the Anderson-King PSF reproduces better the core of the PSF, while TinyTim fits better the wings. The differences are very small, and therefore changing the PSF wouldn't affect the outcome of our previous work. However, we think that Anderson-King PSF may be more appropriate for this delicate analysis.

### 7.3.4 Complementary data

Preliminary tests fitting the surface brightness profiles showed that, in some cases, the small field of view of the images may be a serious limitation for a good determination of the parameters. We thus have decided to complement our data with ground based or lower resolution data covering larger galactic radii. The photometry in these data will be joined to the HST data, allowing us to construct extended profiles which will constrain better the Sérsic parameters.

With the former aim, we have performed a series of observations with the 2.5 m Nordic Optical Telescope at Observatorio Roque de Los Muchachos (La Palma). We used the instrument MOSCA, which is a 16 Megapixel mosaic CCD camera., offering a scale plate of $0.11''$/pixel and good near-UV sensitivity. We have been able to get images at U and V bands with good S/N for our porpose of the next objects: M 89, NGC 524, NGC 2336, NGC 2685, NGC 2787, NGC 3998, NGC 4203, and NGC 5982. The data have been reduced, combined and mosaicked, and are ready to be analyzed. Our intention is to use SDSS data, which are available for other objects of the sample, in order to complement this set.

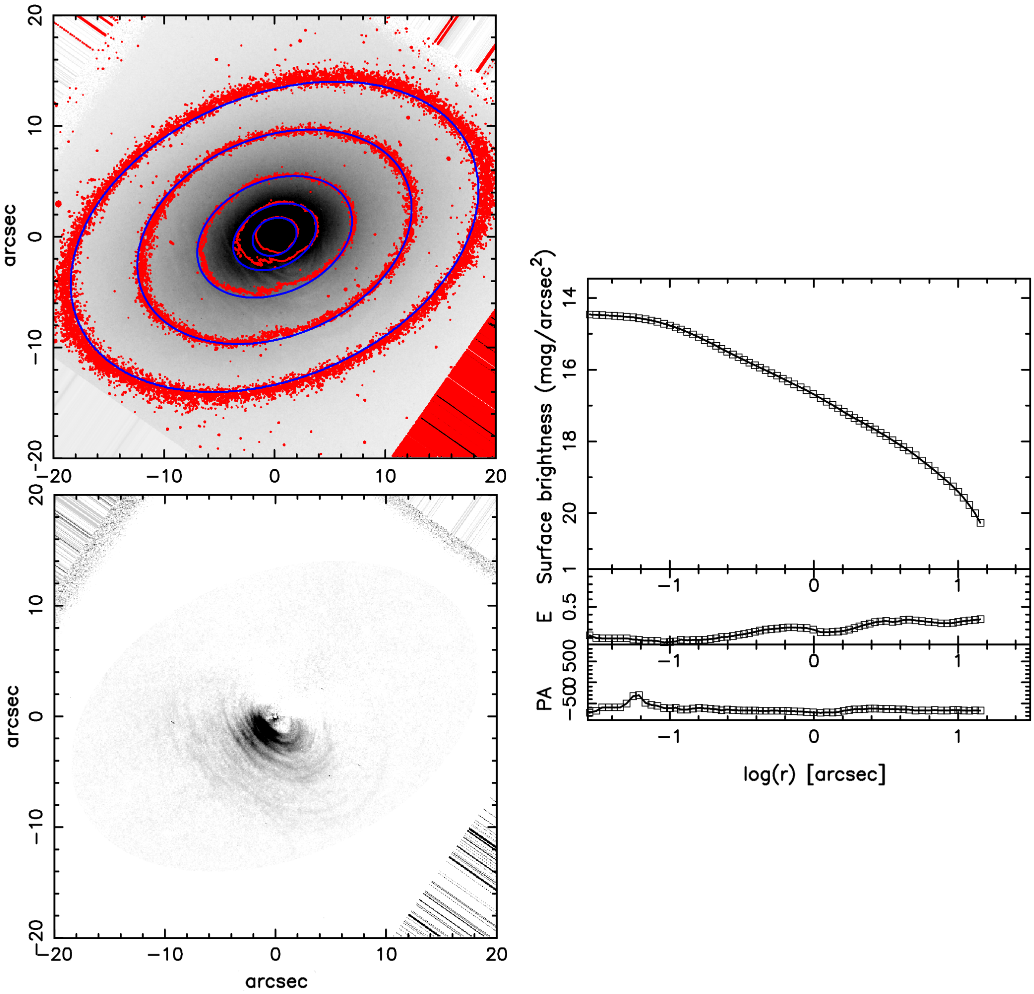

Figure 7.3: Example of the elliptical fitting analysis, showing the galaxy NGC 2787. The data are from WFPC2 in the filter F814W (~I band). In the upper-left panel, contours of the model and the isophotes corresponding to those contours over the gray scale image. Lower-left panel shows the image of the dust distribution. Right panel: the calculated surface brightness profile and the ellipticity and position angle parameters.

# Acknowledgments

This research has been funded by the Spanish Research Council (CSIC) under the I3P grant program, and partially supported by the Spanish Ministerio de Educación y Ciencia under grants AYA 2007-64712 and AYA2004-02703. This work was carried out in part at Instituto de Física of Universidade Federal do Rio Grande do Sul (Porto Alegre), and at Universidade Federal de Santa Catarina (Florianópolis).

This research has made use of the NASA/IPAC Extragalactic Database (NED) which is operated by the Jet Propulsion Laboratory, California Institute of Technology, under contract with the National Aeronautics and Space Administration.

Pretender reducir una tesis al desarrollo profesional, o incluso intelectual, sería pura ceguera. Pensar que uno ha sido el principal agente de esta creación sería pura vanidad. Intentar nombrar siquiera todo lo que me ha traído y acompañado hasta aquí sería necesariamente incompleto, injusto, y un juicio innecesario. Yo estoy esparcido por 510 millones de kilómetros cuadrados; vosotros vivís en menos de medio litro.

# Bibliography

Alonso-Herrero, A., Quillen, A. C., Rieke, G. H., Ivanov, V. D., & Efstathiou, A. 2003, AJ, 126, 81 30

Anders, P., Bissantz, N., Fritze-v. Alvensleben, U., & de Grijs, R. 2004, MNRAS, 347, 196 159

Anderson, J., & King, I. R. 2004, Multi-filter PSFs and Distortion Corrections for the HRC, Tech. rep., Space Telescope Science Institue 201

Anderson, K. S. 1970, ApJ, 162, 743 106

Antonucci, R. 1993, ARA&A, 31, 473 2

Antonucci, R. R. J., & Miller, J. S. 1985, ApJ, 297, 621 2, 113

Baan, W. A. 1985, Nature, 315, 26 39

Barth, A. J., Ho, L. C., Filippenko, A. V., & Sargent, W. L. W. 1998, ApJ, 496, 133 194

Bastian, N., Trancho, G., Konstantopoulos, I. S., & Miller, B. W. 2009, ApJ, 701, 607 142

Bedregal, A. G., Colina, L., Alonso-Herrero, A., & Arribas, S. 2009, ApJ, 698, 1852 173, 175

Bershady, M. A., Jangren, A., & Conselice, C. J. 2000, AJ, 119, 2645 90, 92

Böker, T., Laine, S., van der Marel, R. P., Sarzi, M., Rix, H., Ho, L. C., & Shields, J. C. 2002, AJ, 123, 1389 4, 200

Bruzual, G., & Charlot, S. 2003, MNRAS, 344, 1000 23, 24, 116, 122, 124, 125, 148, 159

Capetti, A., Macchetto, F., Axon, D. J., Sparks, W. B., & Boksenberg, A. 1995, ApJ, 452, L87+ 113

Cardelli, J. A., Clayton, G. C., & Mathis, J. S. 1989, ApJ, 345, 245 81, 112, 123, 139, 147, 160

Carollo, C. M., Stiavelli, M., de Zeeuw, P. T., & Mack, J. 1997, AJ, 114, 2366 200

Carollo, C. M., Stiavelli, M., Seigar, M., de Zeeuw, P. T., & Dejonghe, H. 2002, AJ, 123, 159 4

Cerviño, M., & Mas-Hesse, J. M. 1994, A&A, 284, 749 24

Chandar, R., Leitherer, C., Tremonti, C. A., Calzetti, D., Aloisi, A., Meurer, G. R., & de Mello, D. 2005, ApJ, 628, 210 5, 104

Chandar, R., et al. 2010, ApJ, 719, 966 142

Chiaberge, M., Lim, P. L., Kozhurina-Platais, V., Sirianni, M., & Mack, J. 2009, Updated CTE photometric correction for WFC and HRC, Tech. rep., Space Telescope Science Institute 149

Cid Fernandes, R., Gu, Q., Melnick, J., Terlevich, E., Terlevich, R., Kunth, D., Rodrigues Lacerda, R., & Joguet, B. 2004a, MNRAS, 355, 273 5, 137

Cid Fernandes, R., Heckman, T., Schmitt, H., González Delgado, R. M., & Storchi-Bergmann, T. 2001, ApJ, 558, 81 5, 127, 132, 133, 137

Cid Fernandes, R., et al. 2004b, ApJ, 605, 105 193

Colina, L., García Vargas, M. L., González Delgado, R. M., Mas-Hesse, J. M., Pérez, E., Alberdi, A., & Krabbe, A. 1997, ApJ, 488, L71 5

Colina, L., González Delgado, R. M., Mas-Hesse, J. M., & Leitherer, C. 2002, ApJ, 579, 545 44, 193

Conselice, C. J. 1997, PASP, 109, 1251 90

Côté, P., et al. 2006, ApJS, 165, 57 4, 200

Crenshaw, D. M., Kraemer, S. B., Filippenko, A. V., & Peterson, B. M. 1998, in ESA Special Publication, Vol. 413, Ultraviolet Astrophysics Beyond the IUE Final Archive, ed. W. Wamsteker, R. Gonzalez Riestra, & B. Harris, 605–+ 106

Cruz-González, I., Carrasco, L., Serrano, A., Guichard, J., Dultzin-Hacyan, D., & Bisiacchi, G. F. 1994, ApJS, 94, 47 29, 106

Dahari, O., & De Robertis, M. M. 1988, ApJS, 67, 249 29

Davies, R. I., Müller Sánchez, F., Genzel, R., Tacconi, L. J., Hicks, E. K. S., Friedrich, S., & Sternberg, A. 2007, ApJ, 671, 1388 5

de Grijp, M. H. K., Keel, W. C., Miley, G. K., Goudfrooij, P., & Lub, J. 1992, A&AS, 96, 389 29, 106

Díaz-Santos, T., Alonso-Herrero, A., Colina, L., Packham, C., Levenson, N. A., Pereira-Santaella, M., Roche, P. F., & Telesco, C. M. 2010, ApJ, 711, 328 4

Díaz-Santos, T., Alonso-Herrero, A., Colina, L., Packham, C., Radomski, J. T., & Telesco, C. M. 2008, ApJ, 685, 211 173

Dokuchaev, V. I., & Eroshenko, Y. N. 2003, Astronomical and Astrophysical Transactions, 22, 727 4

Dolphin, A. E. 2000, PASP, 112, 1397 149, 151

Dultzin-Hacyan, D., Krongold, Y., Fuentes-Guridi, I., & Marziani, P. 1999, ApJ, 513, L111 2

Dunn, J. P., et al. 2010, ApJ, 709, 611 5

Ercolano, B., & Storey, P. J. 2006, MNRAS, 372, 1875 109

Falcke, H., Wilson, A. S., & Simpson, C. 1998, ApJ, 502, 199 29

Fall, S. M., Chandar, R., & Whitmore, B. C. 2005, ApJ, 631, L133 5

Fath, E. A. 1909, Lick Observatory Bulletin, 5, 71 1

Ferland, G. 1995, in The Analysis of Emission Lines: A Meeting in Honor of the 70th Birthdays of D. E. Osterbrock & M. J. Seaton, ed. R. Williams & M. Livio, 83 111

Ferland, G. J., Korista, K. T., Verner, D. A., Ferguson, J. W., Kingdon, J. B., & Verner, E. M. 1998, PASP, 110, 761 111

Ferrarese, L., & Ford, H. 2005, Space Science Review, 116, 523 2

Ferrarese, L., & Merritt, D. 2000, ApJ, 539, L9 3

Ferrarese, L., et al. 2006, ApJ, 644, L21 4, 200

Ferruit, P., Wilson, A. S., & Mulchaey, J. 2000, ApJS, 128, 139 29

Feruglio, C., Maiolino, R., Piconcelli, E., Menci, N., Aussel, H., Lamastra, A., & Fiore, F. 2010, A&A, 518, L155 5

Filippenko, A. V., & Ho, L. C. 2003, ApJ, 588, L13 200

Fioc, M., & Rocca-Volmerange, B. 1997, A&A, 326, 950 23

Freedman, W. L., et al. 1994, ApJ, 427, 628 27

Freeman, K. C. 1970, ApJ, 160, 811 64

Freeman, K. C., Karlsson, B., Lynga, G., Burrell, J. F., van Woerden, H., Goss, W. M., & Mebold, U. 1977, A&A, 55, 445 27

Gebhardt, K., et al. 2000, ApJ, 539, L13 3

Girardi, L., Bertelli, G., Bressan, A., Chiosi, C., Groenewegen, M. A. T., Marigo, P., Salasnich, B., & Weiss, A. 2002, A&A, 391, 195 23

Goddard, Q. E., Bastian, N., & Kennicutt, R. C. 2010, MNRAS, 405, 857 170

Gondoin, P. 2004, Nuclear Physics B Proceedings Supplements, 132, 181 39

González Delgado, R. M., Cerviño, M., Martins, L. P., Leitherer, C., & Hauschildt, P. H. 2005, MNRAS, 357, 945 24

González Delgado, R. M., & Cid Fernandes, R. 2010, MNRAS, 403, 797 24

González Delgado, R. M., Cid Fernandes, R., Pérez, E., Martins, L. P., Storchi-Bergmann, T., Schmitt, H., Heckman, T., & Leitherer, C. 2004, ApJ, 605, 127 193

González Delgado, R. M., Heckman, T., & Leitherer, C. 2001, ApJ, 546, 845 5, 132

González Delgado, R. M., Heckman, T., Leitherer, C., Meurer, G., Krolik, J., Wilson, A. S., Kinney, A., & Koratkar, A. 1998, ApJ, 505, 174 5, 45, 173, 176

González Delgado, R. M., & Pérez, E. 1996a, MNRAS, 278, 737 106

—. 1996b, MNRAS, 280, 53 108, 137

González Delgado, R. M., Pérez, E., Cid Fernandes, R., & Schmitt, H. 2008, AJ, 135, 747 4, 200

Graham, A. W., Erwin, P., Caon, N., & Trujillo, I. 2001, ApJ, 563, L11 3

Graham, A. W., Erwin, P., Trujillo, I., & Asensio Ramos, A. 2003, AJ, 125, 2951 200

Graham, A. W., & Li, I. 2009, ApJ, 698, 812 3

Greenhill, L. J., Kondratko, P. T., Lovell, J. E. J., Kuiper, T. B. H., Moran, J. M., Jauncey, D. L., & Baines, G. P. 2003, ApJ, 582, L11 41

Gu, Q., Melnick, J., Cid Fernandes, R., Kunth, D., Terlevich, E., & Terlevich, R. 2006, MNRAS, 366, 480 29

Haehnelt, M. G., & Kauffmann, G. 2000, MNRAS, 318, L35 4

Hasinger, G., Lehmann, I., Schmidt, M., Gunn, J. E., Schneider, D. P., Giacconi, R., Trümper, J., & Zamorani, G. 2000, New Astronomy Reviews, 44, 497 106

Heckman, T. M., González-Delgado, R., Leitherer, C., Meurer, G. R., Krolik, J., Wilson, A. S., Koratkar, A., & Kinney, A. 1997, ApJ, 482, 114 5, 42

Ho, L. C., Filippenko, A. V., & Sargent, W. L. 1995, ApJS, 98, 477 40

Ho, L. C., Filippenko, A. V., & Sargent, W. L. W. 1997, ApJS, 112, 315 29, 43, 192, 193, 194, 197

Huchra, J., & Burg, R. 1992, ApJ, 393, 90 30

Humphrey, A., Villar-Martín, M., Sánchez, S. F., Martínez-Sansigre, A., Delgado, R. G., Pérez, E., Tadhunter, C., & Pérez-Torres, M. A. 2010, MNRAS, 408, L1 5

Inglis, M. D., Brindle, C., Hough, J. H., Young, S., Axon, D. J., Bailey, J. A., & Ward, M. J. 1993, MNRAS, 263, 895 114, 135

Joseph, R. D. 1999, Ap&SS, 266, 321 4

Karachentsev, I. D., et al. 2002, A&A, 389, 812 194

Kay, L. E. 1994, ApJ, 430, 196 114

Kazantzidis, S., et al. 2005, ApJ, 623, L67 3

Kewley, L. J., Groves, B., Kauffmann, G., & Heckman, T. 2006, MNRAS, 372, 961 193

Kharb, P., O'Dea, C. P., Baum, S. A., Colbert, E. J. M., & Xu, C. 2006, ApJ, 652, 177 126

King, A. R. 2010, MNRAS, 408, L95 4

Kinney, A. L., Bohlin, R. C., Calzetti, D., Panagia, N., & Wyse, R. F. G. 1993, ApJS, 86, 5 84, 86, 87

Kishimoto, M., Kay, L. E., Antonucci, R., Hurt, T. W., Cohen, R. D., & Krolik, J. H. 2002a, ApJ, 567, 790 113

—. 2002b, ApJ, 565, 155 113

Kondratko, P. T., et al. 2006, ApJ, 638, 100 43

Kormendy, J., & Richstone, D. 1995, ARA&A, 33, 581 3

Kormendy, J., & Sanders, D. B. 1992, ApJ, 390, L53 4

Koski, A. T. 1978, ApJ, 223, 56 108, 110, 112

Koulouridis, E., Chavushyan, V. H., Plionis, M., Dultzin, D., Krongold, Y., Goudis, C., & Chatzichristou, E. 2008, Memorie della Società Astronomica Italiana, 79, 1185 3

Krug, H. B., Rupke, D. S. N., & Veilleux, S. 2010, ApJ, 708, 1145 5

Lada, C. J., & Lada, E. A. 2003, ARA&A, 41, 57 5

Larsen, S. S., & Richtler, T. 2000, A&A, 354, 836 171

Lauer, T. R., et al. 1995, AJ, 110, 2622 64, 200

Lawrence, A. 1987, PASP, 99, 309 1

Lawrence, A., & Elvis, M. 2010, ApJ, 714, 561 3

Leitherer, C., et al. 1999, ApJS, 123, 3 24, 116

Levenson, N. A., Weaver, K. A., Heckman, T. M., Awaki, H., & Terashima, Y. 2004, ApJ, 602, 135 173, 176

Lipovetsky, V. A., Neizvestny, S. I., & Neizvestnaya, O. M. 1988, Soobshcheniya Spetsial'noj Astrofizicheskoj Observatorii, 55, 5 29

Luridiana, V., Pérez, E., & Cerviño, M. 2003, in Revista Mexicana de Astronomia y Astrofisica Conference Series, Vol. 18, Revista Mexicana de Astronomia y Astrofisica Conference Series, ed. M. Reyes-Ruiz & E. Vázquez-Semadeni, 60–62 113

Magorrian, J., et al. 1998, AJ, 115, 2285 3

Maiolino, R., & Rieke, G. H. 1995, ApJ, 454, 95 30, 31, 42

Malkan, M. A., Gorjian, V., & Tam, R. 1998, ApJS, 117, 25 2, 27, 42

Malkan, M. A., & Oke, J. B. 1983, ApJ, 265, 92 106

Maoz, D., Filippenko, A. V., Ho, L. C., Rix, H.-W., Bahcall, J. N., Schneider, D. P., & Macchetto, F. D. 1995, ApJ, 440, 91 194

Marconi, A., & Hunt, L. K. 2003, ApJ, 589, L21 3

Marconi, A., Moorwood, A. F. M., Salvati, M., & Oliva, E. 1994, A&A, 291, 18 41

Martel, A. R. 1996, PhD thesis, , Univ. California at Santa Cruz, (1996) 129

Mathur, S., Fields, D., Peterson, B. M., & Grupe, D. 2011, ArXiv e-prints 3

McLeod, K. K., & Rieke, G. H. 1995, ApJ, 441, 96 30

Mediavilla, E., Guijarro, A., Castillo-Morales, A., Jiménez-Vicente, J., Florido, E., Arribas, S., García-Lorenzo, B., & Battaner, E. 2005, A&A, 433, 79 41

Meurer, G. R., Heckman, T. M., Leitherer, C., Kinney, A., Robert, C., & Garnett, D. R. 1995, AJ, 110, 2665 5, 99, 171

Miller, J. S., & Goodrich, R. W. 1990, ApJ, 355, 456 2, 114

Miller, J. S., Goodrich, R. W., & Mathews, W. G. 1991, ApJ, 378, 47 113

Miyoshi, M., Moran, J., Herrnstein, J., Greenhill, L., Nakai, N., Diamond, P., & Inoue, M. 1995, Nature, 373, 127 40

Moles, M., Marquez, I., & Perez, E. 1995, ApJ, 438, 604 31

Morris, S. L., & Ward, M. J. 1988, MNRAS, 230, 639 29, 108, 110, 112

Muñoz Marín, V. M., González Delgado, R. M., Schmitt, H. R., Cid Fernandes, R., Pérez, E., Storchi-Bergmann, T., Heckman, T., & Leitherer, C. 2007, AJ, 134, 648 26, 194

Muñoz Marín, V. M., Storchi-Bergmann, T., González Delgado, R. M., Schmitt, H. R., Spinelli, P. F., Pérez, E., & Cid Fernandes, R. 2009, MNRAS, 399, 842 104

Mulchaey, J. S., Wilson, A. S., & Tsvetanov, Z. 1996, ApJS, 102, 309 29

Nelson, C. H., MacKenty, J. W., Simkin, S. M., & Griffiths, R. E. 1996, ApJ, 466, 713 63

Ogle, P. M., Cohen, M. H., Miller, J. S., Tran, H. D., Fosbury, R. A. E., & Goodrich, R. W. 1997, ApJ, 482, L37+ 137

Oliva, E., Origlia, L., Maiolino, R., & Moorwood, A. F. M. 1999, A&A, 350, 9 2

Oliva, E., Salvati, M., Moorwood, A. F. M., & Marconi, A. 1994, A&A, 288, 457 29

Osterbrock, D. E. 1981, ApJ, 249, 462 29

—. 1989, Astrophysics of gaseous nebulae and active galactic nuclei (University Science Books) 111, 112, 122

Osterbrock, D. E., & Dahari, O. 1983, ApJ, 273, 478 44

Panessa, F., & Bassani, L. 2002, A&A, 394, 435 2

Pérez, E., González-Delgado, R., Tadhunter, C., & Tsvetanov, Z. 1989, MNRAS, 241, 31P 2

Prieto, M. A., Marco, O., & Gallimore, J. 2005, MNRAS, 364, L28 175

Puccetti, S., Fiore, F., Risaliti, G., Capalbi, M., Elvis, M., & Nicastro, F. 2007, MNRAS, 377, 607 3

Quataert, E. 2001, in Astronomical Society of the Pacific Conference Series, Vol. 224, Probing the Physics of Active Galactic Nuclei, ed. B. M. Peterson, R. W. Pogge, & R. S. Polidan, 71–+ 193

Quillen, A. C., McDonald, C., Alonso-Herrero, A., Lee, A., Shaked, S., Rieke, M. J., & Rieke, G. H. 2001, ApJ, 547, 129 26, 127

Ramos Almeida, C., et al. 2011, ArXiv 1101.3335 3

Rossa, J., van der Marel, R. P., Böker, T., Gerssen, J., Ho, L. C., Rix, H., Shields, J. C., & Walcher, C. 2006, AJ, 132, 1074 4, 200

Salviander, S., Shields, G. A., Gebhardt, K., & Bonning, E. W. 2006, in Astronomical Society of the Pacific Conference Series, Vol. 352, New Horizons in Astronomy: Frank N. Bash Symposium, ed. S. J. Kannappan, S. Redfield, J. E. Kessler-Silacci, M. Landriau, & N. Drory, 277 4

Sanders, D. B. 1999, Ap&SS, 266, 331 4

Sanders, D. B., & Mirabel, I. F. 1996, ARA&A, 34, 749 29

Sanders, D. B., Soifer, B. T., Elias, J. H., Neugebauer, G., & Matthews, K. 1988, ApJ, 328, L35 4

Schawinski, K., Virani, S., Simmons, B., Urry, C. M., Treister, E., Kaviraj, S., & Kushkuley, B. 2009, ApJ, 692, L19 5

Scheepmaker, R. A., Haas, M. R., Gieles, M., Bastian, N., Larsen, S. S., & Lamers, H. J. G. L. M. 2007, A&A, 469, 925 147

Schmitt, H. R., Donley, J. L., Antonucci, R. R. J., Hutchings, J. B., & Kinney, A. L. 2003, ApJS, 148, 327 29, 104, 105, 136

Schmitt, H. R., & Kinney, A. L. 1996, ApJ, 463, 498 39, 105

Sersic, J. L. 1968, Atlas de galaxias australes (Córdoba, Argentina: Observatorio Astronómico) 200

Seyfert, C. K. 1943, ApJ, 97, 28 1

Silk, J., & Rees, M. J. 1998, A&A, 331, L1 4

Sirianni, M., et al. 2005, PASP, 117, 1049 81, 97, 112

Smith, J. E., Young, S., Robinson, A., Corbett, E. A., Giannuzzo, M. E., Axon, D. J., & Hough, J. H. 2002, MNRAS, 335, 773 113, 129, 135

Soifer, B. T., Cohen, J. G., Armus, L., Matthews, K., Neugebauer, G., & Oke, J. B. 1995, ApJ, 443, L65 108

Soifer, B. T., Neugebauer, G., & Houck, J. R. 1987, ARA&A, 25, 187 39

Spinelli, P. F., Storchi-Bergmann, T., Brandt, C. H., & Calzetti, D. 2006, ApJS, 166, 498 18, 108

Stasińska, G., Vale Asari, N., Cid Fernandes, R., Gomes, J. M., Schlickmann, M., Mateus, A., Schoenell, W., & Sodré, Jr., L. 2008, MNRAS, 391, L29 193

Storchi-Bergmann, T., Bica, E., & Pastoriza, M. G. 1990, MNRAS, 245, 749 29

Storchi-Bergmann, T., González Delgado, R. M., Schmitt, H. R., Cid Fernandes, R., & Heckman, T. 2001, ApJ, 559, 147 2

Storchi-Bergmann, T., Kinney, A. L., & Challis, P. 1995, ApJS, 98, 103 84, 86, 87, 108, 110

Storchi Bergmann, T., & Pastoriza, M. G. 1989, ApJ, 347, 195 29

Storchi-Bergmann, T., Raimann, D., Bica, E. L. D., & Fraquelli, H. A. 2000, ApJ, 544, 747 5

Storchi-Bergmann, T., Wilson, A. S., Mulchaey, J. S., & Binette, L. 1996, A&A, 312, 357 108

Tadhunter, C., Dickson, R., Morganti, R., Robinson, T. G., Wills, K., Villar-Martin, M., & Hughes, M. 2002, MNRAS, 330, 977 137

Tadhunter, C., & Tsvetanov, Z. 1989, Nature, 341, 422 2

Terlevich, R., Melnick, J., Masegosa, J., Moles, M., & Copetti, M. V. F. 1991, A&AS, 91, 285 29

Tonry, J. L., Dressler, A., Blakeslee, J. P., Ajhar, E. A., Fletcher, A. B., Luppino, G. A., Metzger, M. R., & Moore, C. B. 2001, ApJ, 546, 681 194

Tran, H. D. 1995, ApJ, 440, 597 114, 135

—. 2001, ApJ, 554, L19 2, 127

Tran, H. D., Miller, J. S., & Kay, L. E. 1992a, ApJ, 397, 452 42, 43, 45

Tran, H. D., Osterbrock, D. E., & Martel, A. 1992b, AJ, 104, 2072 3

Tremaine, S., et al. 2002, ApJ, 574, 740 3

Tremonti, C. A., Calzetti, D., Leitherer, C., & Heckman, T. M. 2001, ApJ, 555, 322 5, 104

Tremonti, C. A., Moustakas, J., & Diamond-Stanic, A. M. 2007, ApJ, 663, L77 5

Trump, J. R., et al. 2011, ArXiv e-prints 3

Tully, R. B. 1988, Nearby galaxies catalog (Cambridge University Press) 27

Urry, C. M., & Padovani, P. 1995, PASP, 107, 803 2

Vázquez, G. A., & Leitherer, C. 2005, ApJ, 621, 695 116, 122

Veilleux, S., Cecil, G., & Bland-Hawthorn, J. 2005, ARA&A, 43, 769 5

Vernet, J., Fosbury, R. A. E., Villar-Martín, M., Cohen, M. H., Cimatti, A., di Serego Alighieri, S., & Goodrich, R. W. 2001, A&A, 366, 7 122

Walcher, C. J., Böker, T., Charlot, S., Ho, L. C., Rix, H., Rossa, J., Shields, J. C., & van der Marel, R. P. 2006, ApJ, 649, 692 4

Whitmore, B. C., Zhang, Q., Leitherer, C., Fall, S. M., Schweizer, F., & Miller, B. W. 1999, AJ, 118, 1551 142

Whittle, M. 1992, ApJS, 79, 49 29, 106

Wild, V., Heckman, T., & Charlot, S. 2010, MNRAS, 405, 933 5

Wilson, A. S., Ward, M. J., & Haniff, C. A. 1988, ApJ, 334, 121 2

Wilson, C. D., Harris, W. E., Longden, R., & Scoville, N. Z. 2006, ApJ, 641, 763 97

Zepf, S. E., Ashman, K. M., English, J., Freeman, K. C., & Sharples, R. M. 1999, AJ, 118, 752 171

APPENDIX A

# Visual Atlas of the Sample

An image-atlas of all the objects is presented. We show the whole field of view of the near-UV images in Figs. A.1-A.3. In most cases these figures show additional and complementary information to that of Figs. 3.7-3.9.

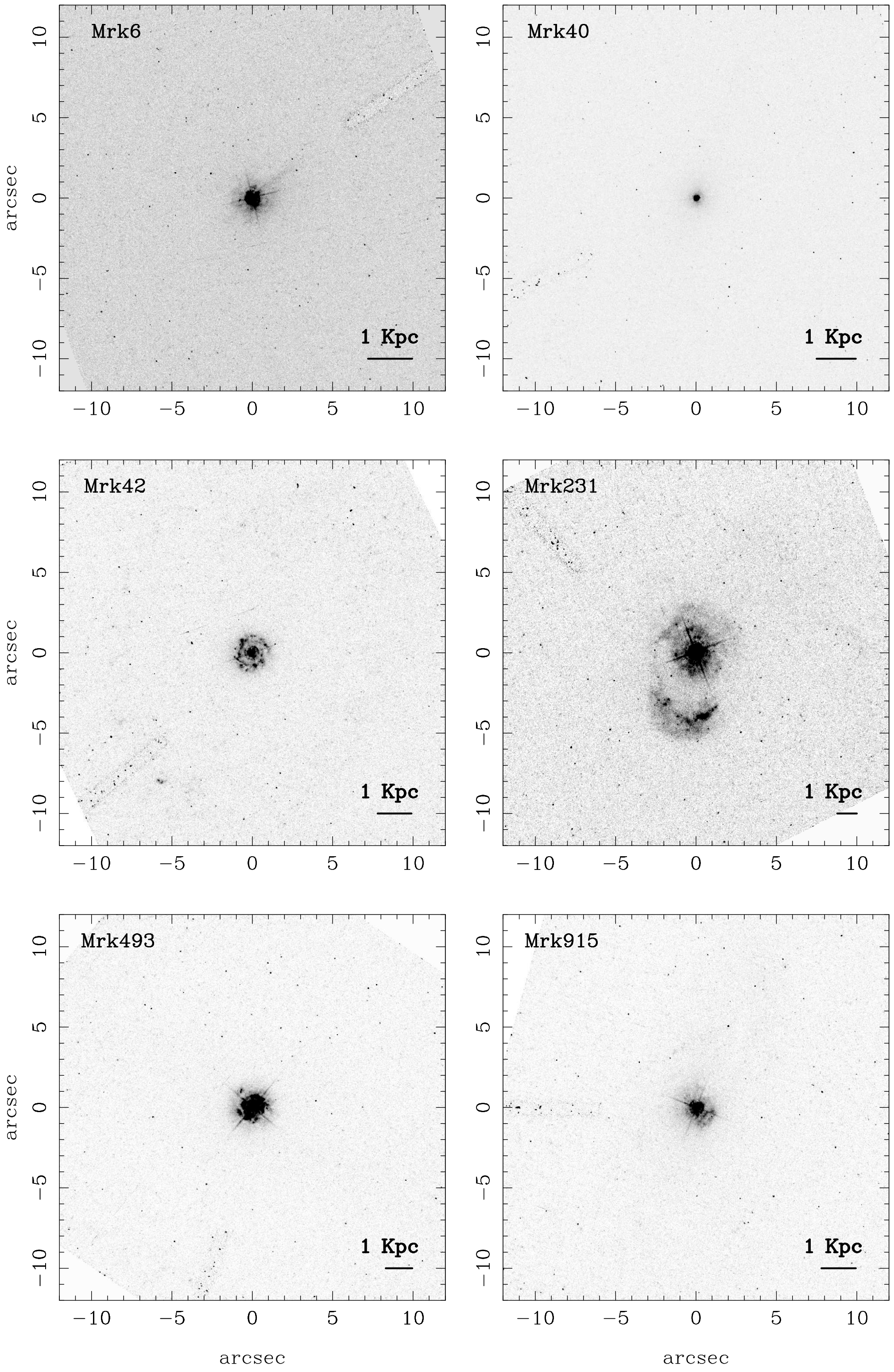

Figure A.1: Field of view (FoV) images of the Sy1 galaxies of the sample. North is up and East to the left in all the figures

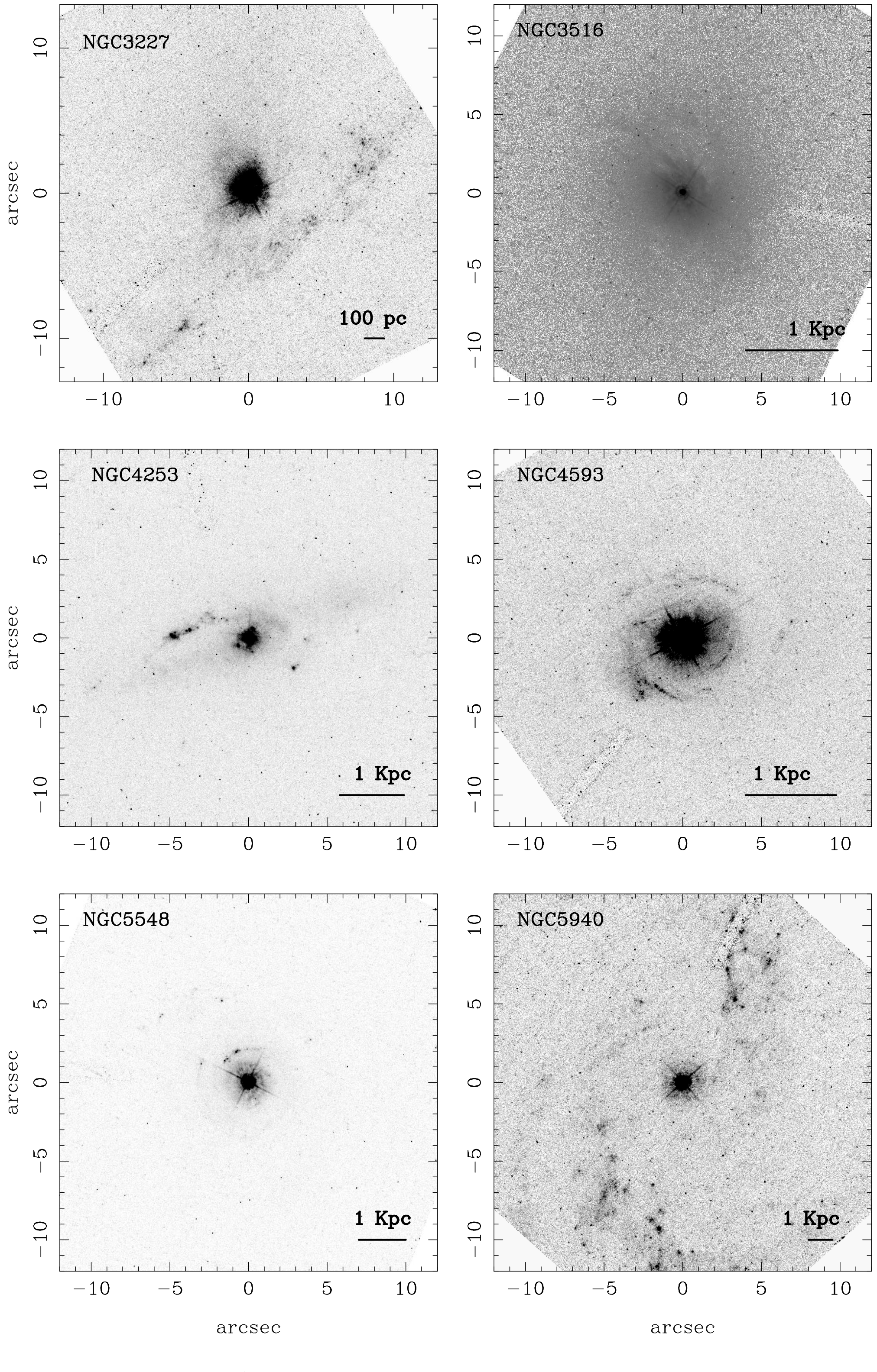

Figure A.1: FoV images of the Sy1 galaxies –continued.

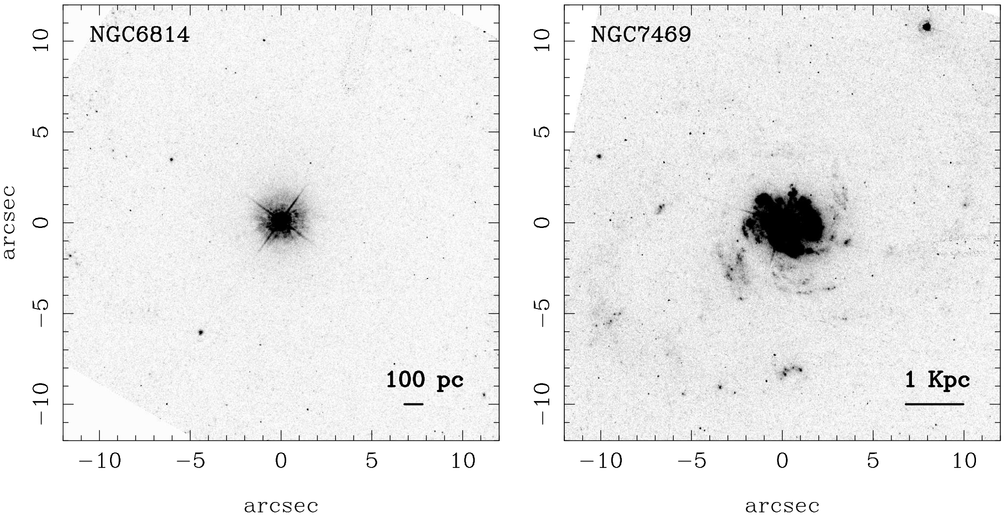

Figure A.1: FoV images of the Sy1 galaxies –continued.

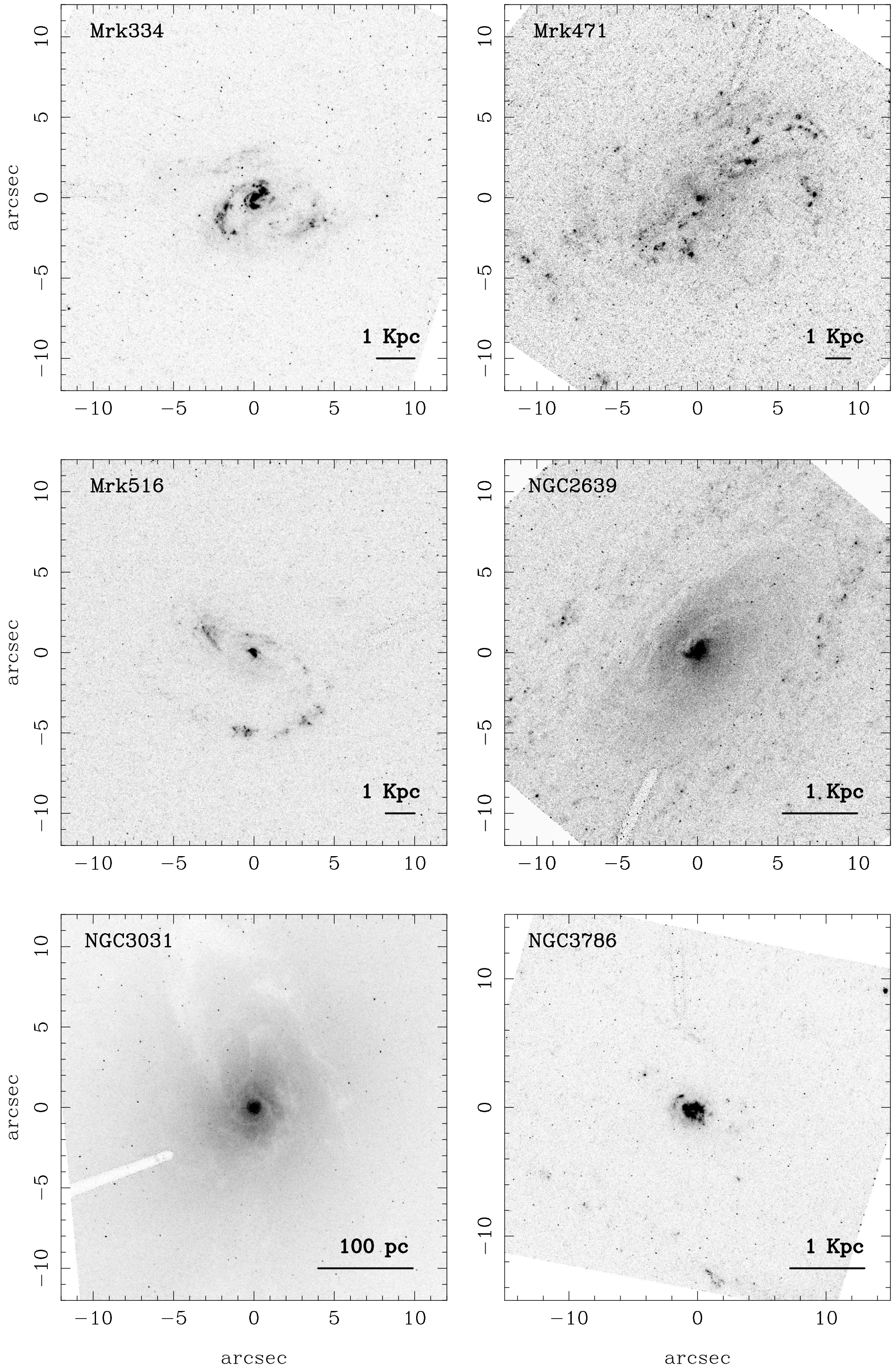

Figure A.2: FoV images of intermediate Sy type (Sy1.8-1.9)

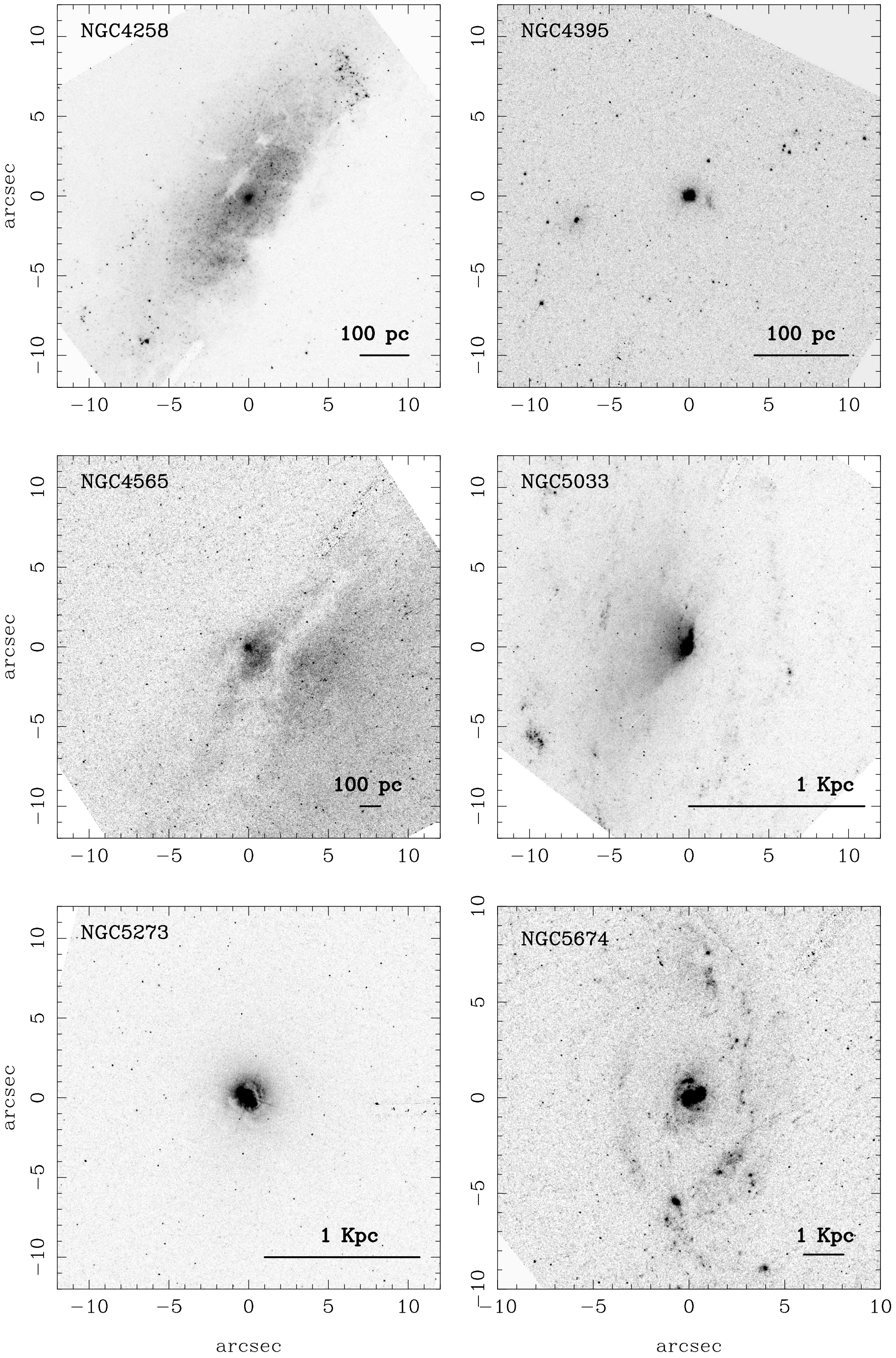

Figure A.2: FoV images of Sy1.8-1.9 –continued.

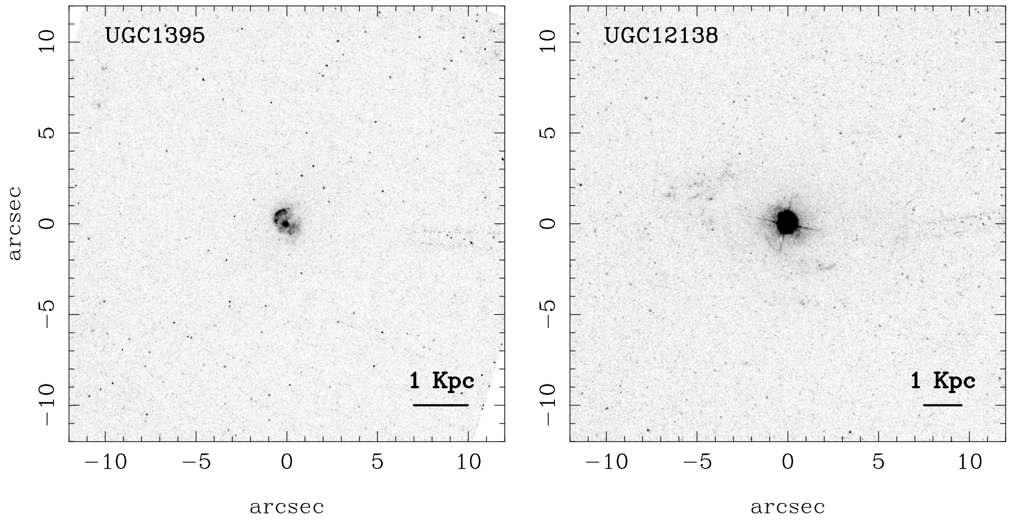

Figure A.2: FoV images of Sy1.8-1.9 –continued.

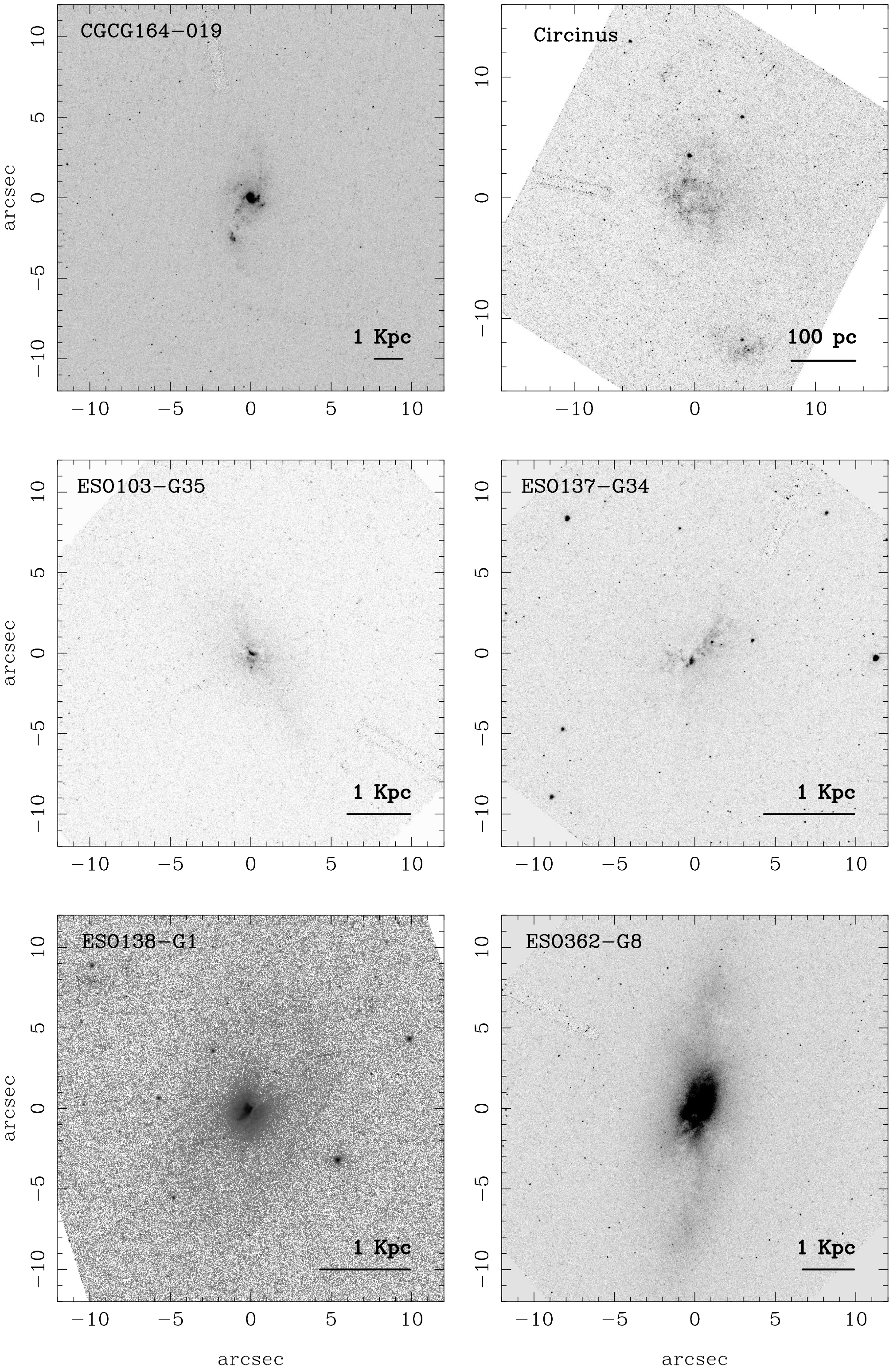

Figure A.3: FoV images of the Sy2 galaxies

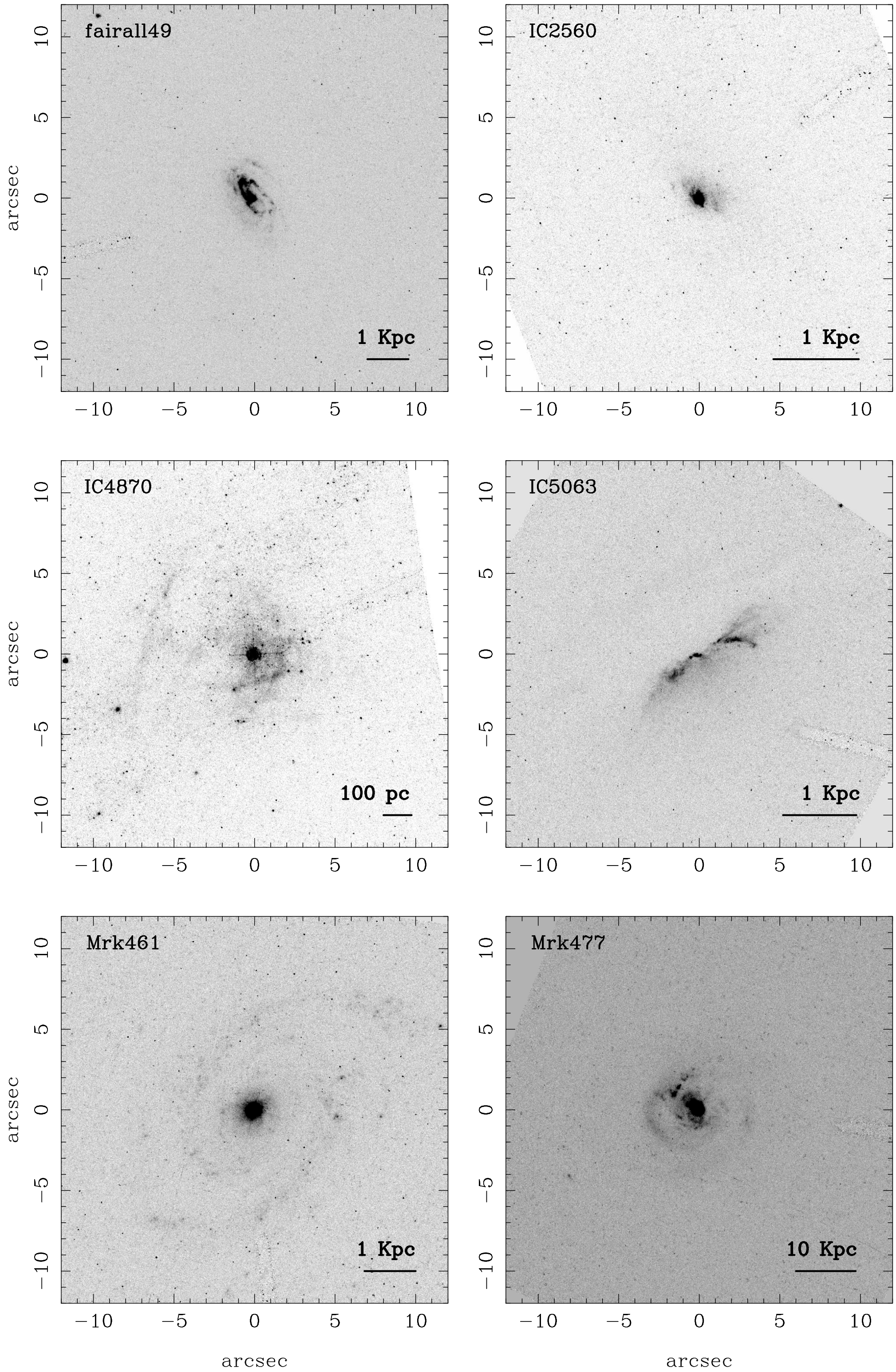

Figure A.3: FoV images of the Sy2 –continued.

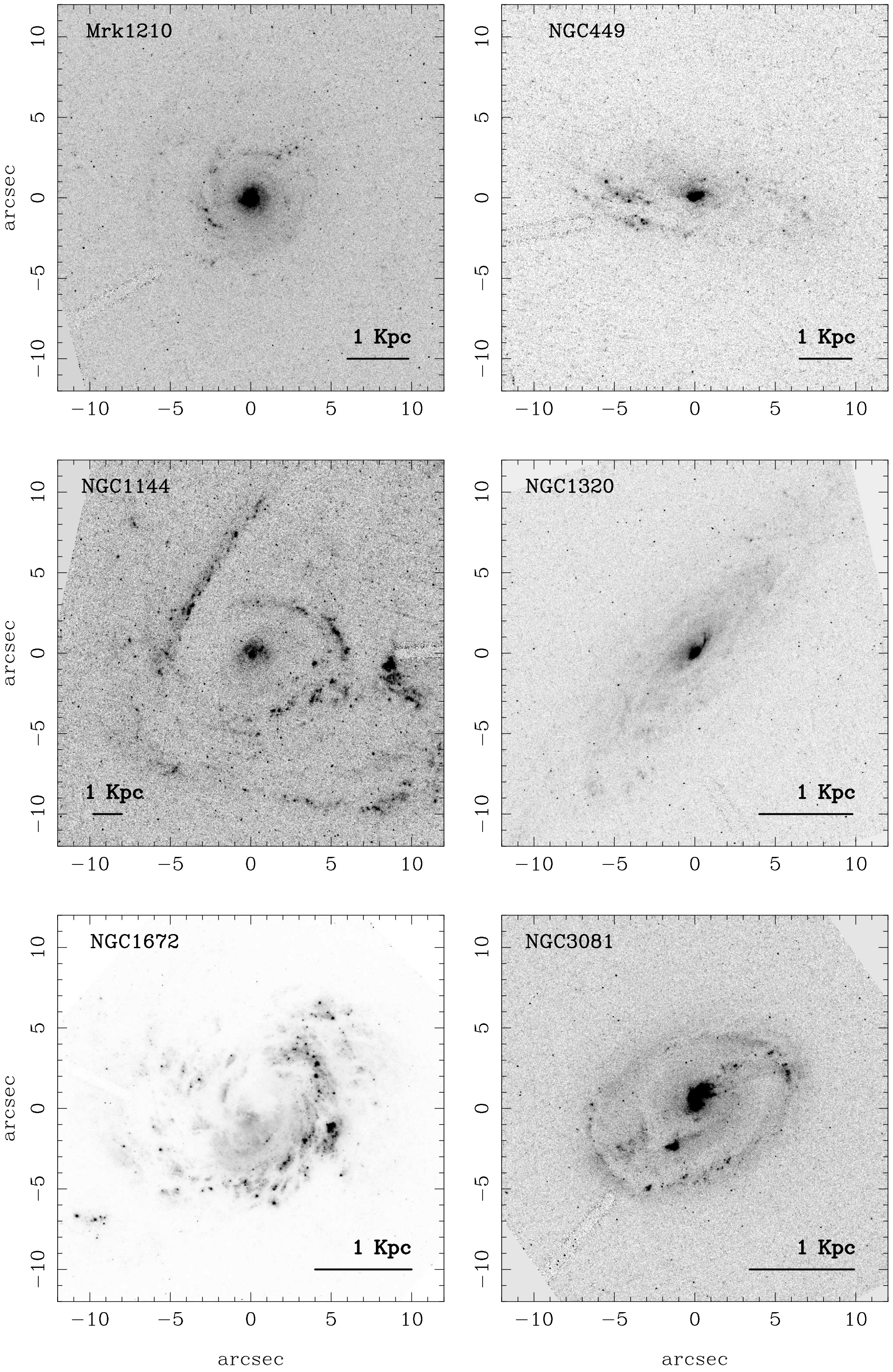

Figure A.3: FoV images of the Sy2 –continued.

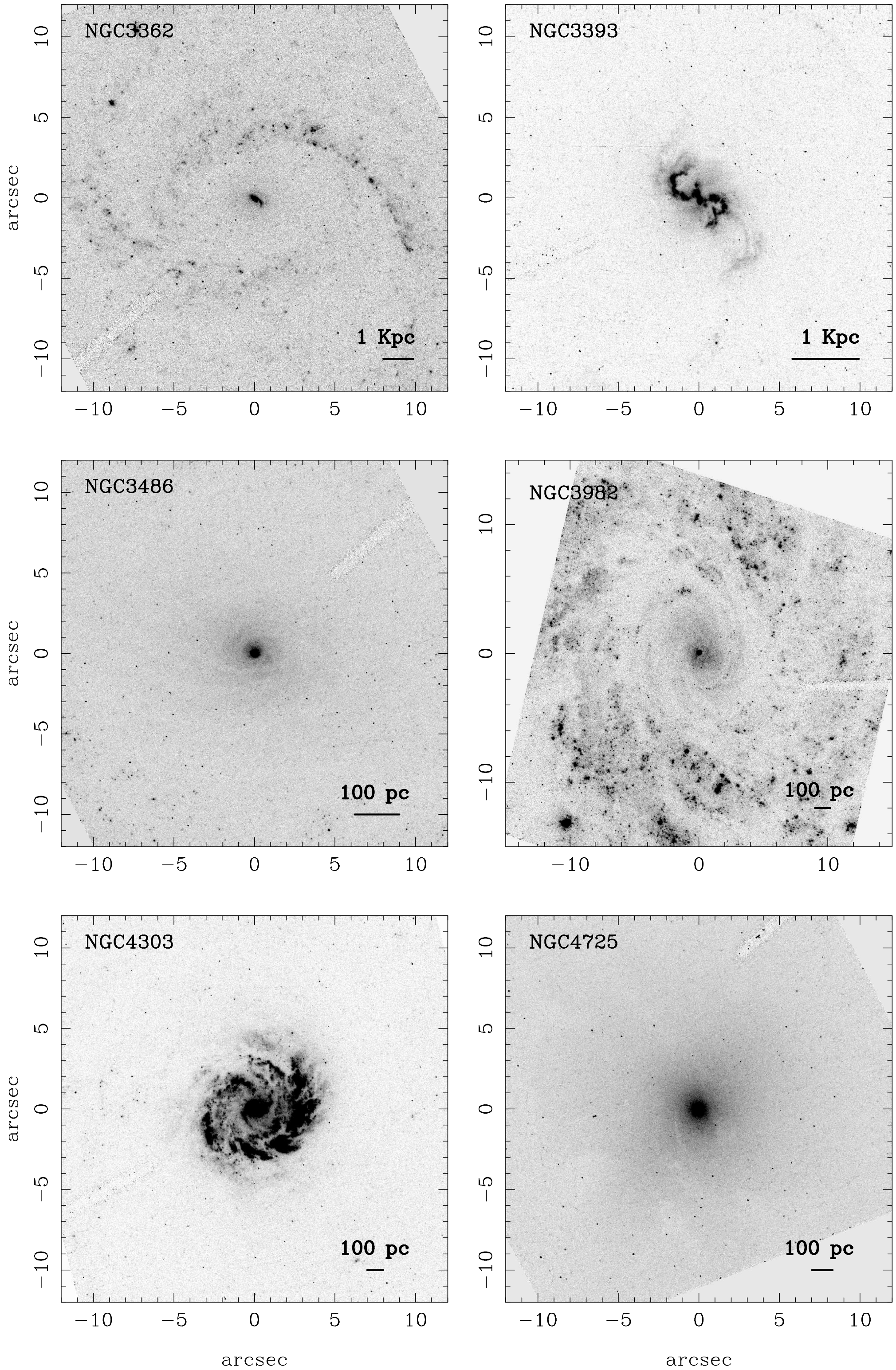

Figure A.3: FoV images of the Sy2 –continued.

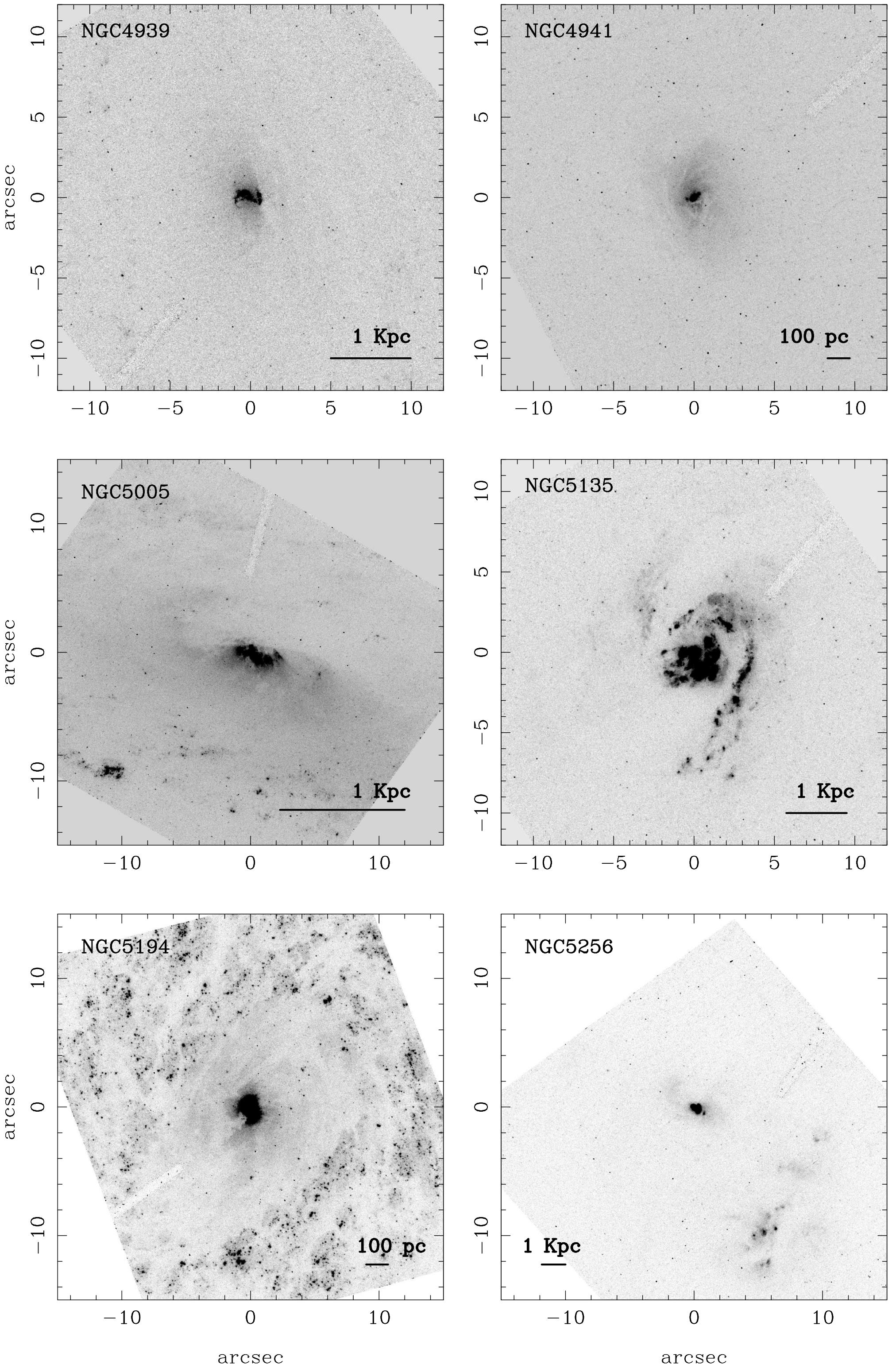

Figure A.3: FoV images of the Sy2 –continued.

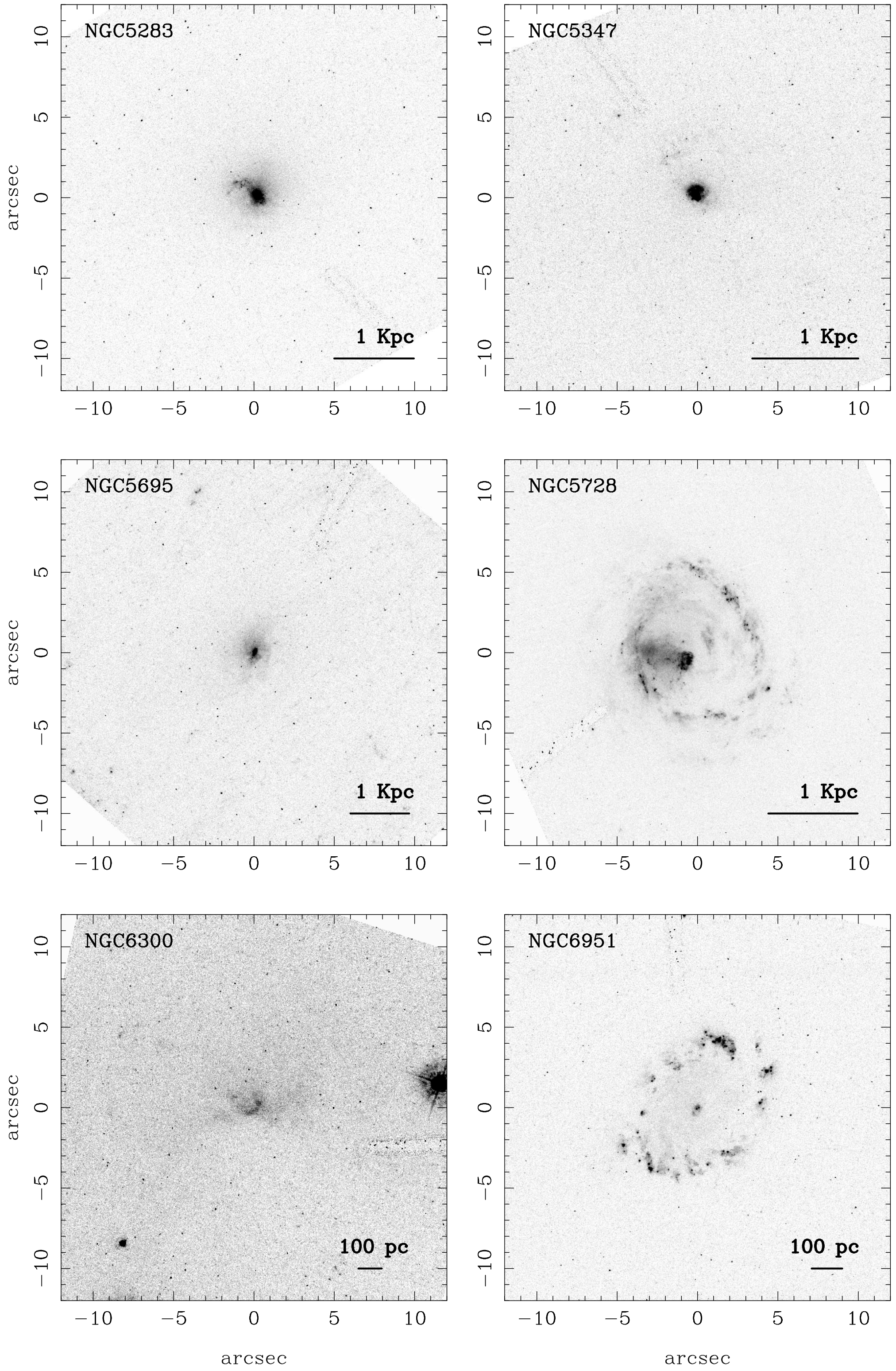

Figure A.3: FoV images of the Sy2 –continued.

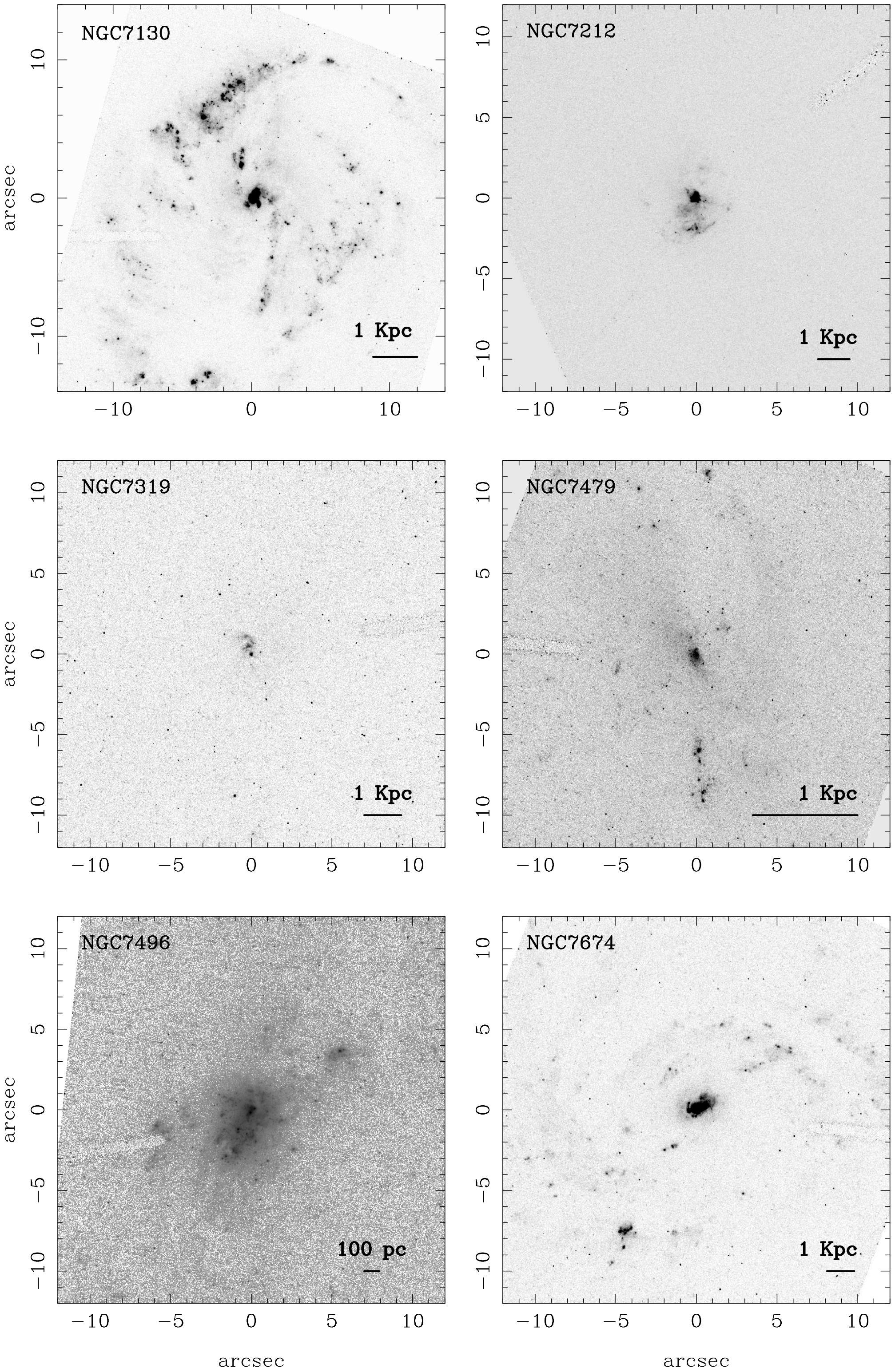

Figure A.3: FoV images of the Sy2 –continued.

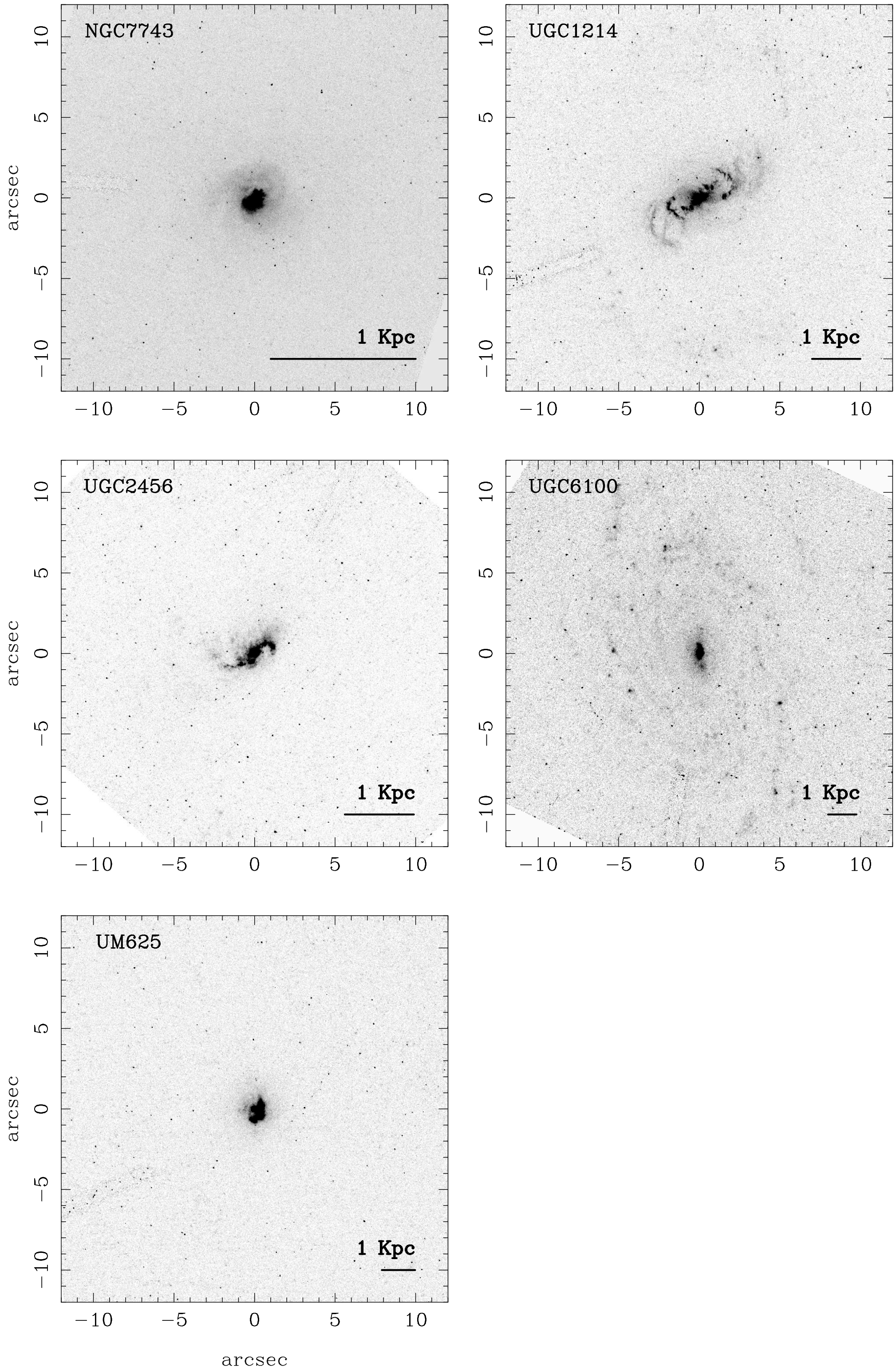

Figure A.3: FoV images of the Sy2 –continued.

# Appendix B

# Acronyms

---

**ACS** Advanced Camera for Surveys

**AGN** Active Galactic Nucleus/-i

**BLR** Broad Line Region

**CCD** Charge-Coupled Device

**CfA** Center for Astrophysics (galaxy sample)

**COSTAR** Corrective Optics Space Telescope Axial Replacement

**CR** Cosmic Rays

**CTE** Charge Transfer Efficiency

**DN** Data Numbers (counts in digital units)

**ENLR** Extended Narrow Line Region

**ESA** European Space Agency

**FIR** Far-Infrared

**FOC** Faint Object Camera

**FoV** Field of View

**FTP** File Transfer Protocol

**FWHM** Full Width at Half Maximum

| | |
|---|---|
| **HRC** | High Resolution Channel |
| **HST** | Hubble Space Telescope |
| **IFU** | Integral Field Unit |
| **IMF** | Initial Mass Function |
| **IPAC** | Infrared Processing and Analysis Center |
| **IR** | Infrared |
| **IRAS** | Infrared Astronomical Satellite |
| **ISR** | Instrument Science Report |
| **IUE** | International Ultraviolet Explorer |
| **LINER** | Low Ionization Nuclear Emission-line Region |
| **LIRG** | Luminous Infrared Galaxy |
| **LLAGN** | Low Luminosity Active Galactic Nucleus |
| **MJD** | Modified Julian Date |
| **NASA** | National Agency for the Space and the Aeronautics |
| **NC** | Nebular Continuum |
| **NED** | NASA/IPAC Extragalactic Database |
| **NICMOS** | Near Infrared Camera and Multi-Object Spectrometer |
| **NLR** | Narrow Line Region |
| **NLRG** | Narrow Line Radio Galaxy |
| **P.I.** | Principal Investigator |
| **PSF** | Point Spread Function |

**QSO** Quasi-Stellar Object

**RC3** Third Reference Catalogue of Bright Galaxies

**RN** Read-out Noise

**RSA** Revised Shapley-Ames Catalog (galaxy sample)

**SED** Spectral Energy Distribution

**SF** Star Formation

**SMBH** Super Massive Black Hole

**S/N** Signal to Noise Ratio

**SSP** Single Stelar Population

**STIS** Space Telescope Imaging Spectrograph

**STSDAS** Space Telescope Data Analysis System

**TO** Transition Object

**ROSAT** Röntgen Satellite

**ULIRG** Ultra Luminous Infrared Galaxy

**UV** Ultraviolet

**VLA** Very Large Array

**WFPC2** Wide Field Planetary Camera 2

# APPENDIX C

# Publications

Our work during this thesis has led to a number of publications which we list in this appendix.

## Publications in refereed journals

**“An Atlas of the Circumnuclear Regions of 75 Seyfert Galaxies in the Near-Ultraviolet with the Hubble Space Telescope Advanced Camera for Surveys”** Muñoz Marín, V. M.; González Delgado, R. M.; Schmitt, H. R.; Cid Fernandes, R.; Pérez, E.; Storchi-Bergmann, T.; Heckman, T.; Leitherer, C., Astronomical Journal, 134, pp. 648-667 (2007).

**“On the nature of the near-UV extended light in Seyfert galaxies”** Muñoz Marín, V. M.; Storchi-Bergmann, T.; González Delgado, R. M.; Schmitt, H. R.; Spinelli, P. F.; Pérez, E.; Cid Fernandes, R., Monthly Notices of the Royal Astronomical Society, 399, pp. 842-860 (2009)

## Contribution to conference proceedings

**“The starburst-AGN connection: the role of stellar clusters in AGNs”** González Delgado, R. M.; Muñoz Marín, V. M.; Pérez, E.; Schmitt, H. R.; Cid Fernandes, R., Astrophysics and Space Science, 320, pp. 61-67 (2009)

**“Stellar clusters in the nuclear regions of AGN with the Advanced Camera for Surveys”** Muñoz Marín, V. M.; González Delgado, R. M.; Schmitt, H. R.; Cid Fernandes, R.; Pérez, E., Astrophysics and Space Science, 324, pp. 253-258 (2009)

**“Origin of the Near-UV Light in the Circumnuclear Regions of Seyfert Galaxies”** Muñoz Marín, V. M., Storchi-Bergmann, T., González Delgado, R. M., Schmitt, H. R., & Spinelli, P., Highlights of Spanish Astrophysics V, Astrophysics and Space Science Proceedings, p. 321 (2010)

**"Near-UV Study of Active Galactic Nuclei with Advanced Camera for Surveys"** Muñoz Marín, V. M., González Delgado, R. M., Schmitt, H. R., Cid Fernandes, R., & Pérez, E., The Impact of HST on European Astronomy, Astrophysics and Space Science Proceedings, p. 259 (2010)

**"Stellar Populations in Luminous and Ultraluminous Infrared Galaxies"** González Delgado, R. M., Cid Fernandes, R., Pérez, E., Rodríguez-Zaurín, J., Tadhunter, C., Dors, O., Muñoz Marín, V. M., & Villar-Martín, M., IAU Symposium, 262, pp. 341-342 (2010)

## Outreach articles

**"Agujeros negros en núcleos galácticos. AGN y formación estelar"** Muñoz Marín, V. M., Información y Actualidad Astronómica, 30, p. 22 (2010)

**"La luz ultravioleta de las galaxias Seyfert"** Muñoz Marín, V. M., Investgación y Ciencia, 414, pp. 10-11 (2011)

## Other publications

**"GRB 080207: optical observations"** Muñoz Marín, V. M., Sabater, J., Castro-Tirado, A. J., Gorosabel, J., Jelinek, M., & de Ugarte Postigo, A., GRB Coordinates Network, Circular Service, 7291 (2008)